UNIVERSITY OF CALIFORNIA,
IRVINE

Understanding and Tailoring Intrinsic Self-Healing in Cementitious Materials

DISSERTATION

submitted in partial satisfaction of the requirements for the degree of

DOCTOR OF PHILOSOPHY

in Civil Engineering

by

Shuai Fan

Dissertation Committee:
Assistant Professor Mo Li, Chair
Professor Lizhi Sun
Associate Professor Timothy J. Rupert

2017

DEDICATION

To

my parents Jianming Fan and Ling Li for making me be who I am,

and my wife Cheng Shi for supporting me all the way.

TABLE OF CONTENTS

LIST OF FIGURES

LIST OF TABLES

ACKNOWLEDGMENTS

I would like to express the deepest appreciation to my committee chair, Professor Mo Li, who has continually and convincingly conveyed a spirit of creativity in regard to research, and an excitement in regard to teaching. Without her guidance and persistent help this dissertation would not have been possible.

I would like to thank my committee members, Professor Lizhi Sun and Professor Timothy J. Rupert, whose criticisms and suggestions are of vital importance to the completion of this dissertation. In addition, a thank you to Professor Yong Yuan of Tongji University, who introduced me to Civil Engineering, and whose enthusiasm and encouragement had lasting effect.

My sincere gratitude also goes to my colleagues whose assistance are crucial to this research, including but not limited to Mr. Xiaopeng Li, Mr. Yunchen Wu, Dr. Prakash Bhat, Mr. Mengyang Jia, Mr. Jingming Cai, Ms. Ing Lim, Dr. Qian Li, Dr. Guang Yang, and Dr. Botong Zheng.

Finally, I would like to thank my family for all their love and encouragement. For my parents who raised me with a love of science and supported me in all my pursuits. And most of all for my loving, supportive, encouraging, and patient wife Dr. Cheng Shi whose faithful support during this Ph.D. is so appreciated. Thank you.

CURRICULUM VITAE

Shuai Fan

2005-2009	B.S. in Civil Engineering, Tongji University, China
2009-2012	M.S. in Civil Engineering, Tongji University, China
2013-2017	Ph.D. in Civil Engineering, University of California, Irvine
2013-2017	Research Assistant, University of California, Irvine
2016-2017	Teaching Assistant, University of California, Irvine

FIELD OF STUDY

High performance concrete material and structures

PUBLICATIONS

Cao, B., Fan, S., Tan, X., Li, M., & Hu, Y. (2017). Cementitious Materials Modified with Hematite Nanoparticles for Enhanced Cement Hydration and Uranium Immobilization. Environmental Science: Nano.

Fan, S., & Li, M. (2015). X-ray computed microtomography of three-dimensional microcracks and self-healing in engineered cementitious composites. Smart Materials and Structures, 24(1), 015021.

Fan, S., Li, X., & Li, M. Electrical Impedance Spectroscopy of Damage and Self-Healing in Strain-Hardening Cementitious Composites, Cement and Concrete Research, In press.

Fan, S., & Li, M. Damage-Tolerant Geopolymer, Journal of the American Ceramics Society, under review.

ABSTRACT OF THE DISSERTATION

Understanding and Tailoring Intrinsic Self-Healing in Cementitious Materials

By

Shuai Fan

Doctor of Philosophy in Civil Engineering

University of California, Irvine, 2017

Professor Mo Li, Chair

Damage tolerance and self-healing are naturally occurring phenomena found in many biological systems, optimized through millennia of evolution. Man-made materials, however, generally do not possess such attributes. Concrete is the most heavily used man-made material, but is inherently brittle and inevitably suffers from cracking under various mechanical and environmental loading conditions. Cracking impairs concrete mechanical properties, causing local stress concentration, and stiffness and strength reduction in structural members. Cracking also compromises concrete transport properties, accelerating other deterioration mechanisms such as chloride diffusion, moisture penetration, and reinforcement corrosion. These challenges can be potentially addressed by a new generation of self-healing cementitious materials, which can autogenously regain its transport property as well as mechanical capacity after damage.

While self-healing phenomena has been observed in cementitious materials, questions arise as to whether robust self-healing can occur reliably. The goal of this dissertation is to generate fundamental understandings of the chemical, physical and environmental mechanisms that control the self-healing process in cementitious materials. It is hypothesized that these mechanisms determine what, how and to what extent healing products form along crack walls.

Understanding these mechanisms will lead to new material tailoring strategies to achieve robust and intrinsic self-healing in cementitious materials.

In this dissertation, we first establish an experimental framework to accurately probe the level and quality of self-healing within a crack, to analyze the chemical composition of the healing products, and to quantify the recovery of material transport and mechanical properties. Through experiments, we uncover and quantify the nonhomogeneous self-healing volume and varying chemical compositions along the crack depth. Second, we formulate a coupled transport-thermodynamics model to predict crack profile evolution with time due to self-healing. The model captures three mechanisms that dynamically control the healing process: the advective transport of ions as reactants caused by the flow of the aqueous solution, the molecular diffusion of dissolved reactants due to the concentration gradient, and the kinetics of chemical reactions occurring at the water-material interfaces controlled by thermodynamics. We test and validate the model through a set of designed experiments with well-controlled chemical and physical parameters. Third, we extend the experimental framework and the model to study the effects of different chemical variables (e.g. binder chemistry, age, ion concentration), physical properties (e.g. crack width, geometry, transport properties), and environmental conditions (e.g. wet and dry, flow rate, pH) on the self-healing extent and properties. The results elucidate the healing mechanisms and governing parameters, laying the groundwork for designing robust self-healing in cementitious materials. Fourth, we develop new self-healing cementitious composite materials by satisfying a combination of criteria: (a) the presence of a multitude of essential chemical species or ions can react with natural actuators upon cracking, (b) distributed damage behavior that sequentially and spatially activates healing reactants, and (c) self-controlled tight crack width that can promote robust self-healing without consuming a large amount of healing

reactants. The experiments validate the improved three-dimensional healing extent of the new materials, and the recovery of transport and mechanical properties. Finally, the dissertation explores the multifunctionality of new cementitious materials by coupling the cracking and healing processes with the electrical properties.

CHAPTER 1 INTRODUCTION

1.1 Background

The infrastructure of the United States - its transportation, energy, water, and building systems - is vital to the quality of life and economic well-being of its citizens. Each year, the nationwide network of roads and bridges alone transports over 75% of goods across the US [1], accounting for over 30% of GDP [2]. As the economy expands, nearly tripling in size over the past 20 years, and the population grows [3], the importance of a reliable infrastructure system for economic growth and public safety, only looks to increase into the future.

While the importance of infrastructure to national prosperity is clear, its level of disrepair is alarming. Much of American infrastructure was built with technology of the mid-1900s, and has now poorly deteriorated (e.g. aging, corrosion, and fatigue). Specifically, Concrete as the most widely used man-made materials, has been recognized for being responsible for many deterioration problems due to its brittle nature in tension. The American Society of Civil Engineer's 2013 Report Card for America's Infrastructure assigned a national grade of "D+" to the US infrastructure with a total investment of $2.6 trillion needed by 2020 for repairs [4]. Aside from direct repair costs borne by government agencies, user costs such as $101 billion annual burden on drivers for wasted time and fuel further emphasize the need for improved infrastructure system [5]. While the current problems encountered in the aging civil infrastructure are overwhelming, they only look to get worse into the future. Although funding sources such as the 2005 Transportation Equity Act [6] are unarguably important for maintenance, repair and rehabilitation of existing structures, a long-term fundamental solution to the apparent lack of durability and sustainability in concrete must be sought.

Engineering materials before were mostly developed based on the ‘damage prevention’ paradigm [7]. This design philosophy led to stronger and stiffer materials by assembling as many atoms with a high bond strength to neighboring atoms in as small a volume as possible, and by processing the material to minimize defects [8]. Therefore, the traditional way to improve the durability of reinforced concrete is typically associated with a dense concrete matrix, i.e. a very compact microstructure expected to lower permeability and reduce transport of corrosives to the embedded steel [9]. This approach is best exemplified by “Macro defect-free materials” designed by a combination of polymer additives serving as “lubricants” and externally applied pressure during processing for tight packing of cement grains [10][11]. Other attempts to reduce flaw sizes in concrete include well-graded particle size distribution, optimized packing density, and low water/cement ratios [12][13]. These concepts, however, rely upon the concrete to remain uncracked within a structure throughout its expected lifetime to resist the transport of water, chloride ions, oxygen, etc. through its dense microstructure. In this presumed uncracked state, numerous concrete materials have shown promising durability in laboratory tests [14][15]. However, such materials have been proved ineffective at eliminating cracks in field conditions due to increased brittleness despite their high strength [16]. Indeed, structures made of stronger materials can have delayed damage initiation time, but once damage is initiated, the damage level usually increases to the level of failure. This is especially true for brittle materials such as concrete.

In reality, concrete infrastructure cracking is inevitable, and can be the result of one or a combination of factors such as restrained shrinkage, thermal effect, fatigue, stress concentration, and embedded steel corrosion [17][21]. These cracks provide pathways for the penetration of aggressive ions to cause concrete deterioration. Aggressive agents can migrate through cracks and ultimately lead to corrosion of reinforcement. Although the uncracked concrete between

adjacent cracks can be extremely dense and nearly impermeable, the presence of cracks results in a high overall permeability and unhindered access of corrosives to reinforcing steels, causing the loss of mechanical capacity and structural integrity [22][27]. The periodic inspection and external maintenance and repairs of cracked structure result in intensive life cycle costs and environmental impacts. Therefore, controlling and repairing cracks in concrete structure is one of the top issues in the field of civil engineering [28][30]. These challenges can be potentially addressed by innovative self-healing cementitious materials, which can autogenously regain material transport properties as well as mechanical characteristics after the crack/healing process.

1.2 Emerging Self-Healing Technologies for Engineering Materials

The inspiration for the development of self-healing materials originally comes from biological systems. Biological materials are evolutionarily optimized functional systems [31]. Since the origin of life on earth about 3.8 billion years ago, live beings have evolved and developed fascinating material properties to survival through a vast variety of environmental conditions and selective pressures. The ability of autonomic repair and regeneration of function upon the infliction of damage, which is termed self-healing, is one of the most important survival features in nature at every level of biological organization, ranging from the molecule level like the repair of DNA [32], to the organ level such as the closure of injured blood vessels [33] or merging of broken bones [34]. In sharp contrast, this self-healing process has generally not been found or applied in man-made materials.

Very recently, the self-healing materials, as a new emerging concept of ‘damage management’ [7], has attracted increasing attention in the area of materials science. This design philosophy is based on the notion that the formation of damage is not problematic as long as it is counteracted by a subsequent process of damage sensing and self-repair, thus, demonstrating

continuous renewal its performance. Different strategies and approaches to devise self-healing materials in a wide range of material classes have been investigated, including polymers, metals, ceramics, and cementitious materials [35][36]. For all these materials with different properties, the self-healing function is achieved based upon the similar general principle and underlying concept, as summarized in **Figure 1.1**. Firstly, damage in a material is allowed to occur. Failure of a material is not regarded as a yes/no state, but much more as the gradual process. While damage is being introduced by an action, a recovery reaction against this action should be triggered to start the healing process. This trigger mechanism needs both location and time dependent. Once a healing process is being initiated, some sort of physical or chemical reaction is required in order to counteract the damage. It should be emphasized that, in general, it is the functionality rather than the exact internal or external structure to be recovered [36]. If the self-healing concept can be realized from idea to practice, it is undisputed that this kind of property would offer enormous possibilities to improve the safety, lifetime, energy and environmental efficiency of man-mad materials, in particular for applications where long-term reliability is critical as well as in poorly accessible areas.

In light of these requirements and opportunities, from the last decade, studies about self-healing materials have been intensely devoted, accompanied by a significant increase in the number of scientific publications (from <20 in 2001 to >300 in 2013) [37]. Throughout the development of this new type of smart materials, self-healing materials can be generally divided into two classes: extrinsic and intrinsic [35][37], depending on the nature of the material matrix and the respective healing process, as illustrated in **Figure 1.2** [38].

The extrinsic method relies on the damage-triggered release of healing agents stored within discrete capsules [39][52], tubes [54][61] or interconnected vascular networks [62][67] to fill the

crack and restore the material functionality. Capsules or capillary based self-healing materials sequester the healing agent in discrete components (**Figure 1.2(a)**). After release, the local region is usually depleted of healing materials, leading to only a singular healing event. Vascular self-healing materials embed the healing agents into a network which is connected until damage (**Figure 1.2(b)**). After the vasculature is damaged and the first delivery of healing agent occurs, the network may be refilled by an external source or from an undamaged but connected region of the vasculature. This refilling action might allow for multiple local healing events. The healing agents for extrinsic healing can be a monomer that will be released after mechanical damage [41]. With the help of a catalyst, the monomer polymerizes in the crack plane to rebind the crack surfaces. Other healing agents include epoxy resins [44], linseed oil [45], pure solvents (e.g. chlorobenzene) [46], isocyanates [47], combination of reactive monomers [48], polydimethylsiloxane and polydiethoxysiloxane [49]. For concrete materials, the embedment of immobilized bacteria as biomineralized healing agent has been explored [51][53]. The principle of this microbial healing relies on the precipitation of calcium carbonate by the growth and metabolism of certain types of bacteria. These carbonate-precipitating bacteria can be added into concrete during the process of mixing. When cracks appear, dormant bacteria in the crack zone will be activated. Dense layers of calcium carbonate are produced by bacterial conversion of an incorporated mineral precursor compound, such as calcium lactate, calcium glutamate, yeast extract, and peptone [53].

The advantage of extrinsic self-healing method is the straightforward mechanism, and the instant actuation of the healing process once crack breaks through the capsules. However, several issues such as the survivability of the healing agents, the repeatability for re-damage condition, the workability for large-scale processing, more importantly the prohibitively high costs, are remain significantly challenging. For example, concrete as the bulk building materials is usually

used for large-scale construction, where the material cost accounts for one of the largest part of the initial project budget. The complex processing and extremely high cost of the encapsulation technique will sharply raise the materials cost, which could easily offset the later benefits from the reduction of repair frequency, resulting in a total life-cycle cost that is almost impossible to compete with the traditional materials and maintenance strategy. Furthermore, the singular healing event of the capsulation method poses great challenges when the concrete structures along with continued deterioration under service loading conditions. While the repeatable healing of vascular system has been proved in organic polymers, it is unfeasible for designing and processing cementitious materials with such complicated vascular network.

Different from the extrinsic healing, the other method requires no sequestered healing agents, but relies on the intrinsic healing capacity of the materials themselves (**Figure 1.2(c)**), such as hydrogen bonding, molecular diffusion and entanglement, ionic interaction and arrangements, thermally reversible reactions, or reversible polymerizations, that can be activated by damage or by external stimulus [68][87]. For organic polymers, for instance, the higher temperatures can cause diffusion of the polymer chains followed by formation of secondary chemical bonds, resulting in the closure of the crack [68]. For concrete materials, when water exists in fractured concrete, the water-concrete interactions can cause dissolution of minerals from the porous media. Once the dissolved cations and anions in the water reach the saturation equilibrium, insoluble ionic solid products, such as calcite ($CaCO_3$), portlandite ($Ca(OH)_2$), and C-S-H, start precipitating in cracks, leading to localized alteration of crack apertures [88][93]. This intrinsic self-healing process, also termed autogenous healing, has been demonstrated in cementitious materials under various conditions [92]~[110]. Although the overall contribution of different physical parameters (e.g. crack width and depth), chemical species (e.g ingredients and

proportion), and environmental exposures (e.g. pH, temperature, wet/dry cycles, and chloride environment) remains a matter of debate, based on the limited knowledge, researchers have dedicated to redesign the cementitious materials to promote the autogenous healing capacity in the past decade. Li and coworkers firstly proposed to use the fiber reinforced engineered cementitious composite (ECC) to restrict the crack width and thus improve autogenous healing [94][97]. ECC is a family of materials featuring a strain-hardening behavior accompanied by multiple microcracking, which is in contrast with the localized cracking or fracture in conventional concrete materials or fiber reinforced cementitious materials with 'tension-softening' behavior [111]. As a result, the microcrack width in ECC during strain-hardening is intrinsically controlled to be at micrometer scale, which is offering one of the most important conditions for autogenous healing. From the view of another potential improvement factor -- the supply of water, several researchers investigated the possibility to mix super absorbent polymers (SAP) [98][100], or other water reservoirs [101][102] into ECC to provide additional water for continued hydration and carbonation. Different supplementary cementitious materials, such as fly ash and slag, have been incorporated into concrete matrix to study their influence on self-healing properties [103][110].

While typically slower acting than encapsulation techniques, the intrinsic method offers potential for repeatable self-healings and relatively low costs. Nevertheless, the effectiveness and feasibility of intrinsic healing method is often questionable as they rely heavily on the material inherent properties and the environmental conditions. The first and major obstacle for designing robust self-healing cementitious materials has been the lack of comprehensive understanding about the basic healing mechanism [91][93]. This is largely due to that the physical and chemical

interactions between water and concrete inside cracks are extremely complex. Furthermore, measurement of these interactions inside opaque concrete is prohibitively difficult.

The change of crack profile (i.e. the dissolution and deposition) in porous medium is contributed by a wide range of microscale processes, which are usually coupled. For cementitious materials, the interplay of different processes can be mainly related to the mass transport mechanisms (both advection and diffusion), reaction kinetics at mineral surfaces (hydration degree, local mineralogy, supersaturation, salinity, precipitation rate, temperature, pH, etc.), and the changing properties of the fracture microstructures (the feedback between permeability and precipitation). Such a complex system controls the local autogenous healing rate at various temporal and spatial scales. Understanding these coupled hydro-thermodynamic processes is fundamental to the interpretation of autogenous healing in cementitious materials, and to the further optimization for robust self-healing concrete.

1.3 Research Objectives and Dissertation Outline

Based on the previous discussions focused on emerging self-healing technologies for cementitious materials, there remains the need for mechanistic studies about basic healing mechanism and the ability to spur self-healing performance with robustness under varying environmental conditions. Thus, two of the primary objectives of this dissertation are: (1) to gain a clear understanding of how autogenous healing works; (2) to realize a new generation of "concrete" materials with designed physical and chemical characteristics that favor robust and repeatable self-healing. To achieve these goals, the following studies were conducted and the structure of different chapters are schematically presented in **Figure 1.3**.

Chapter 2 describes the development of characterization method used to probe the self-healing behavior within a three-dimensional cementitious crack. Specifically, X-Ray Computed

Micro-Tomography (μCT) technique was adopted to quantitatively characterize the microstructure evolution of cracks during the healing process. The CT method allowed imaging, phase segmentation, quantification, and monitoring of the interior characteristics of the healing behavior in cementitious materials. Additionally, other imaging or chemical analysis techniques including SEM (scanning electron microscopy), EDX (energy-dispersive X-ray spectroscopy), XRD (X-ray diffraction), and Raman spectroscopy have been used to characterize the morphology and mineralogy of the healing products.

Upon the characterization method established in Chapter 2, Chapter 3 focuses on the experimental investigation to understand the fundamental mechanism that control the quantities and qualities of the intrinsic healing performance, as well as the feedback between mineral precipitation and crack transmissibility. Aside from the healing mechanisms in Portland cement, the addition of replacement materials of industrial by-products, like silica fume (SF), fly ash (FA), and ground granulated blast-furnace slag (GGBS), brings additional complexity to the kinetics of healing reaction. The influence of such additives on the healing extent and healing products composition were also explored in this chapter. The experiments provide quantitative measurement of the intrinsic healing induced crack aperture alterations. However, the complicated and various boundary conditions, the time-prohibitive nature of the mineral growth process, and small length-scale of the experiments, limit our ability to interpret and quantify the complex healing process. Therefore, Chapter 4 seeks to build a hydro-thermodynamic model to promote the mechanistic understanding about the complex autogenous healing behavior and the influence of different chemical, physical, and environmental parameters, such as the crack geometry, sample age, supersaturation condition, and flow rate. Gaining a clear understanding of

how self-healing works allows us to further design the materials in a more intelligent route and thereby increase the likelihood for material design success.

In Chapter 5, guided by the mechanistic knowledge obtained from previous chapters, new cementitious composites were assembled with designed physical (e.g. cracking behavior) and chemical (e.g. ingredient) characteristics to boost the self-healing capacity. The robust self-healing in cementitious materials can be possibly achieved by meeting a combination of conditions: (a) the material exhibits a self-controlled, distributed damage process; (b) a multitude of healing compounds are present that can be randomly triggered by each damage event, and react with natural actuators present in the environment; and (c) the healing process and reaction kinetics can lead to the formation of high strength and high toughness healing products with sufficiently large volume, leading to recovery of both mechanical and transport properties.

Chapter 6 presents the multifunctionality of the self-healing materials toward damage self-sensing. The frequency-dependent electrical behavior of these materials was studied by the 4-point AC electrical impedance spectroscopy (EIS) and equivalent circuit model analysis. Finally, Chapter 7 concludes this dissertation by summarizing the overall conclusions and identifying potential areas for future research.

Figures

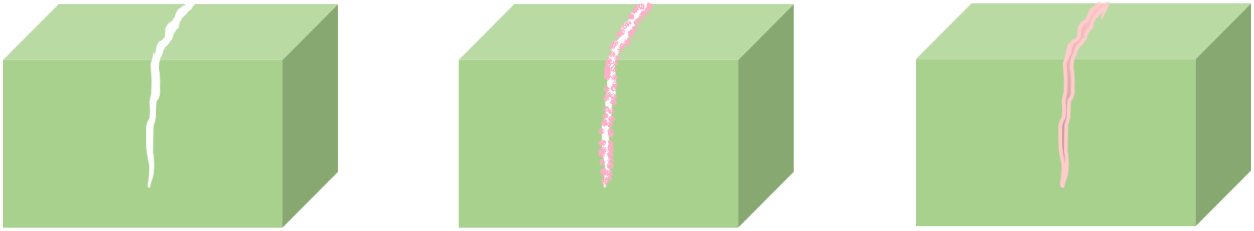

Figure 1.1 Basic principle of self-healing materials: (a) a crack is induced; (b) a healing reaction is initiated; (c) closure of the crack by the reaction products.

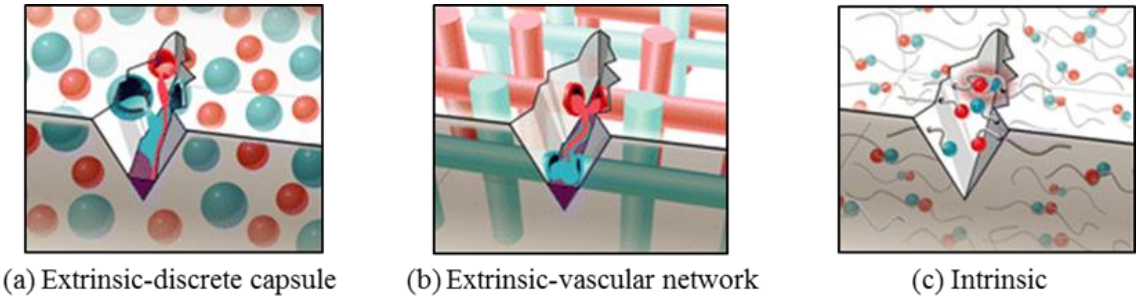

Figure 1.2 Schematic diagram of approaches to self-healing [38]: (a) extrinsic self-healing by capsule based method; (b) extrinsic self-healing by vascular network; (c) Intrinsic self-healing.

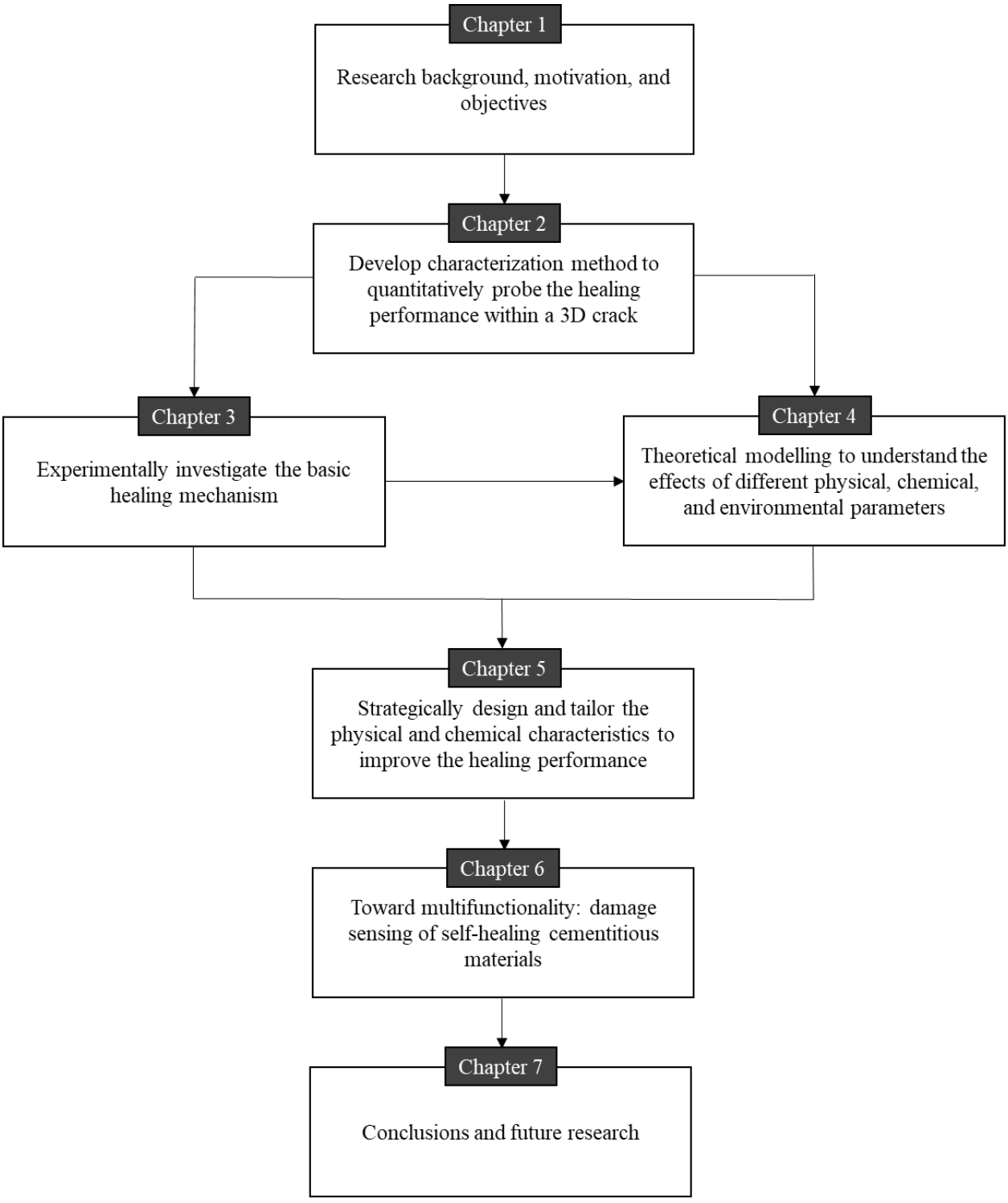

Figure 1.3 A schematic outline of the major topics presented in this dissertation.

References

[1] U.S. Department of Commerce, Bureau of Economic Analysis. Industry Economic Accounts. 2014.

[2] U.S. Department of Commerce, Bureau of Economic Analysis. National Income and Product Accounts. 2014.

[3] U.S. Census Bureau. Summary Population and Housing Characteristics (Decennial Census). 2014.

[4] American Society of Civil Engineers. Report card for America's Infrastructure. 2013.

[5] American Society of Civil Engineers. Report Card for America's Infrastructure – Roads. 2013.

[6] U.S. Library of Congress, Text of HR3 "The Safe, AccTransportation Equity Act: A Legacy for Users" 2005.

[7] Zwaag, S. (Ed.). (2008). Self-healing materials: an alternative approach to 20 centuries of materials science. Springer Science+ Business Media BV.

[8] Gordon, J. E. (1968). The new science of strong materials, or why you don't fall through the floor. Princeton University Press, Princeton.

[9] Oh, B. H., Cha, S. W., Jang, B. S., & Jang, S. Y. (2002). Development of high-performance concrete having high resistance to chloride penetration. Nuclear Engineering and Design, 212(1), 221-231.

[10] Drabik, M., & Slade, R. C. (2004). Macrodefect-free materials: modification of interfaces in cement composites by polymer grafting. Interface Science, 12(4), 375-379.

[11] Mojumdar, S., Chowdhury, B., Varshney, K., & Mazanec, K. (2004). Synthesis, moisture resistance, thermal, chemical and SEM analysis of macro-defect-free (MDF) cements. Journal of thermal analysis and calorimetry, 78(1), 135-144.

[12] de Larrard, F., & Sedran, T. (1994). Optimization of ultra-high-performance concrete by the use of a packing model. Cement and Concrete Research, 24(6), 997-1009.

[13] Aïtcin, P. C. (2011). High performance concrete. CRC Press.

[14] Okamura, H. (1997). Self-compacting high-performance concrete. Concrete international, 19(7), 50-54.

[15] de Larrard, F., & Sedran, T. (1994). Optimization of ultra-high-performance concrete by the use of a packing model. Cement and Concrete Research, 24(6), 997-1009.

[16] Shah, S.P., K. Wang, W.J.Weiss. (2000). Is high strength concrete durable?" concrete techniology for a sustainale development in the 21th century, Eds. O.E. Gjorv and K. Sakai. 2000, 102-114

[17] Wittmann, F. H. (2002). Crack formation and fracture energy of normal and high strength concrete. Sadhana, 27(4), 413-423.

[18] Mehta, P. K., & Gerwick, B. C. (1982). Cracking-corrosion interaction in concrete exposed to marine environment. Concrete International, 4(10), 45-51.

[19] Vaysburd, A. M., Brown, C. D., Bissonnette, B. E. N. O. I. T., & Emmons, P. H. (2004). Realcrete" versus" Labcrete. Concrete International-Detroit, 26(2), 90-94.

[20] Lawler, J. S., Zampini, D., & Shah, S. P. (2002). Permeability of cracked hybrid fiber-reinforced mortar under load. Materials Journal, 99(4), 379-385.

[21] Vaysburd, A. M., Emmons, P. H., McDonald, J. E., Poston, R. W., & Kesner, K. (2000). Selecting Durable Repair Materials, Performance Criteria/Field Studies. Concrete International, 22(12), 39-45.

[22] Hearn, N. (1999). Effect of shrinkage and load-induced cracking on water permeability of concrete. Materials Journal, 96(2), 234-241.
[23] Elsener, B. (2002). Macrocell corrosion of steel in concrete–implications for corrosion monitoring. Cement and concrete composites, 24(1), 65-72.
[24] Gerard, B., Reinhardt, H. W., & Breysse, D. (1997). Measured transport in cracked concrete. Rilem report, 265-324.
[25] Stanish, K. D., Hooton, R. D., & Thomas, M. D. A. (2000). Testing the chloride penetration resistance of concrete: a literature review. Toronto, Ontario, Canada: Department of Civil Engineering, University of Toronto.
[26] Aldea, C. M., Shah, S. P., & Karr, A. (1999). Effect of cracking on water and chloride permeability of concrete. Journal of materials in civil engineering, 11(3), 181-187.
[27] Neville, A. (1995). Chloride attack of reinforced concrete: an overview. Materials and Structures, 28(2), 63.
[28] ACI Committee 224R-2001, Control of cracking in concrete structures, ACI Manual of Concrete Practice, Part 3, American Concrete Institute, Farmington Hills, Michigan, 2001.
[29] Mehta, P. K. (1997). Durability--Critical issues for the future. Concrete international, 19(7), 27-33.
[30] Mihashi, H., & Leite, J. P. D. B. (2004). State-of-the-art report on control of cracking in early age concrete. Journal of Advanced Concrete Technology, 2(2), 141-154.
[31] Meyers, M. A., Chen, P. Y., Lin, A. Y. M., & Seki, Y. (2008). Biological materials: structure and mechanical properties. Progress in Materials Science, 53(1), 1-206.
[32] Lindahl, T. (2013). My journey to DNA repair. Genomics, proteomics & bioinformatics, 11(1), 2-7.
[33] L'heureux, N., Pâquet, S., Labbé, R., Germain, L., & Auger, F. A. (1998). A completely biological tissue-engineered human blood vessel. The FASEB Journal, 12(1), 47-56.
[34] Einhorn, T. A. (1998). The cell and molecular biology of fracture healing. Clinical orthopaedics and related research, 355, S7-S21.
[35] Ghosh, S. K. (Ed.). (2009). Self-healing materials: fundamentals, design strategies, and applications. John Wiley & Sons.
[36] Hager, M. D., Greil, P., Leyens, C., van der Zwaag, S., & Schubert, U. S. (2010). Self-healing materials. Advanced Materials, 22(47), 5424-5430.
[37] Van Tittelboom, K., & De Belie, N. (2013). Self-healing in cementitious materials—A review. Materials, 6(6), 2182-2217.
[38] Blaiszik, B. J., Kramer, S. L. B., Olugebefola, S. C., Moore, J. S., Sottos, N. R., & White, S. R. (2010). Self-healing polymers and composites. Annual Review of Materials Research, 40, 179-211.
[39] Dry, C. (1994). Matrix cracking repair and filling using active and passive modes for smart timed release of chemicals from fibers into cement matrices. Smart Materials and Structures, 3(2), 118.
[40] Dry, C. M. (2000). Three designs for the internal release of sealants, adhesives, and waterproofing chemicals into concrete to reduce permeability. Cement and Concrete Research, 30(12), 1969-1977.
[41] White, S. R., Sottos, N. R., Geubelle, P. H., Moore, J. S., Kessler, M., Sriram, S. R., ... & Viswanathan, S. (2001). Autonomic healing of polymer composites. Nature, 409(6822), 794-797.

[42] Brown, E. N., White, S. R., & Sottos, N. R. (2005). Retardation and repair of fatigue cracks in a microcapsule toughened epoxy composite—Part II: In situ self-healing. Composites Science and Technology, 65(15), 2474-2480.
[43] Sanada, K., Yasuda, I., & Shindo, Y. (2006). Transverse tensile strength of unidirectional fibre-reinforced polymers and self-healing of interfacial debonding. Plastics, rubber and composites, 35(2), 67-72.
[44] Yin, T., Zhou, L., Rong, M. Z., & Zhang, M. Q. (2007). Self-healing woven glass fabric/epoxy composites with the healant consisting of micro-encapsulated epoxy and latent curing agent. Smart Materials and Structures, 17(1), 015019.
[45] Suryanarayana, C., Rao, K. C., & Kumar, D. (2008). Preparation and characterization of microcapsules containing linseed oil and its use in self-healing coatings. Progress in organic coatings, 63(1), 72-78.
[46] Caruso, M. M., Blaiszik, B. J., White, S. R., Sottos, N. R., & Moore, J. S. (2008). Full recovery of fracture toughness using a nontoxic solvent-based self-healing system. Advanced Functional Materials, 18(13), 1898-1904.
[47] Blaiszik, B. J., Caruso, M. M., McIlroy, D. A., Moore, J. S., White, S. R., & Sottos, N. R. (2009). Microcapsules filled with reactive solutions for self-healing materials. Polymer, 50(4), 990-997.
[48] Patel, A. J., Sottos, N. R., Wetzel, E. D., & White, S. R. (2010). Autonomic healing of low-velocity impact damage in fiber-reinforced composites. Composites Part A: Applied Science and Manufacturing, 41(3), 360-368.
[49] Cho, S. H., Andersson, H. M., White, S. R., Sottos, N. R., & Braun, P. V. (2006). Polydimethylsiloxane-Based Self-Healing Materials. Advanced Materials, 18(8), 997-1000.
[50] Samadzadeh, M., Boura, S. H., Peikari, M., Kasiriha, S. M., & Ashrafi, A. (2010). A review on self-healing coatings based on micro/nanocapsules. Progress in Organic Coatings, 68(3), 159-164.
[51] Jonkers, H. M., Thijssen, A., Muyzer, G., Copuroglu, O., & Schlangen, E. (2010). Application of bacteria as self-healing agent for the development of sustainable concrete. Ecological engineering, 36(2), 230-235.
[52] Van Tittelboom, K., De Belie, N., De Muynck, W., & Verstraete, W. (2010). Use of bacteria to repair cracks in concrete. Cement and Concrete Research, 40(1), 157-166.
[53] Wang, J. Y., Soens, H., Verstraete, W., & De Belie, N. (2014). Self-healing concrete by use of microencapsulated bacterial spores. Cement and Concrete Research, 56, 139-152.
[54] Dry, C. (1996). Procedures developed for self-repair of polymer matrix composite materials. Composite Structures, 35(3), 263-269.
[55] Dry, C., & McMillan, W. (1996). Three-part methylmethacrylate adhesive system as an internal delivery system for smart responsive concrete. Smart materials and structures, 5(3), 297.
[56] Li, V. C., Lim, Y. M., & Chan, Y. W. (1998). Feasibility study of a passive smart self-healing cementitious composite. Composites Part B: Engineering, 29(6), 819-827.
[57] Bleay, S. M., Loader, C. B., Hawyes, V. J., Humberstone, L., & Curtis, P. T. (2001). A smart repair system for polymer matrix composites. Composites Part A: Applied Science and Manufacturing, 32(12), 1767-1776.
[58] Pang, J. W. C., & Bond, I. P. (2005). 'Bleeding composites'—damage detection and self-repair using a biomimetic approach. Composites Part A: Applied Science and Manufacturing, 36(2), 183-188.

[59] Williams, G., Trask, R., & Bond, I. (2007). A self-healing carbon fibre reinforced polymer for aerospace applications. Composites Part A: Applied Science and Manufacturing, 38(6), 1525-1532.
[60] Trask, R. S., Williams, G. J., & Bond, I. P. (2007). Bioinspired self-healing of advanced composite structures using hollow glass fibres. Journal of the royal society Interface, 4(13), 363-371.
[61] Abdullayev, E., Abbasov, V., Tursunbayeva, A., Portnov, V., Ibrahimov, H., Mukhtarova, G., & Lvov, Y. (2013). Self-healing coatings based on halloysite clay polymer composites for protection of copper alloys. ACS applied materials & interfaces, 5(10), 4464-4471.
[62] Bejan, A., Lorente, S., & Wang, K. M. (2006). Networks of channels for self-healing composite materials. Journal of Applied Physics, 100(3), 033528.
[63] Toohey, K. S., Sottos, N. R., Lewis, J. A., Moore, J. S., & White, S. R. (2007). Self-healing materials with microvascular networks. Nature materials, 6(8), 581-585.
[64] Williams, H. R., Trask, R. S., & Bond, I. P. (2007). Self-healing composite sandwich structures. Smart Materials and Structures, 16(4), 1198.
[65] Williams, H. R., Trask, R. S., Knights, A. C., Williams, E. R., & Bond, A. I. (2008). Biomimetic reliability strategies for self-healing vascular networks in engineering materials. Journal of the Royal Society Interface, 5(24), 735-747.
[66] Hansen, C. J., Wu, W., Toohey, K. S., Sottos, N. R., White, S. R., & Lewis, J. A. (2009). Self-healing materials with interpenetrating microvascular networks. Advanced Materials, 21(41), 4143-4147.
[67] Patrick, J. F., Hart, K. R., Krull, B. P., Diesendruck, C. E., Moore, J. S., White, S. R., & Sottos, N. R. (2014). Continuous self-healing life cycle in vascularized structural composites. Advanced Materials, 26(25), 4302-4308.
[68] Chen, X., Dam, M. A., Ono, K., Mal, A., Shen, H., Nutt, S. R., ... & Wudl, F. (2002). A thermally re-mendable cross-linked polymeric material. Science, 295(5560), 1698-1702.
[69] Chung, C. M., Roh, Y. S., Cho, S. Y., & Kim, J. G. (2004). Crack healing in polymeric materials via photochemical cycloaddition. Chemistry of materials, 16(21), 3982-3984.
[70] Kersey, F. R., Loveless, D. M., & Craig, S. L. (2007). A hybrid polymer gel with controlled rates of cross-link rupture and self-repair. Journal of the royal society interface, 4(13), 373-380.
[71] Kalista Jr, S. J., Ward, T. C., & Oyetunji, Z. (2007). Self-healing of poly (ethylene-co-methacrylic acid) copolymers following projectile puncture. Mechanics of advanced materials and structures, 14(5), 391-397.
[72] Plaisted, T. A., & Nemat-Nasser, S. (2007). Quantitative evaluation of fracture, healing and re-healing of a reversibly cross-linked polymer. Acta Materialia, 55(17), 5684-5696.
[73] Cordier, P., Tournilhac, F., Soulié-Ziakovic, C., & Leibler, L. (2008). Self-healing and thermoreversible rubber from supramolecular assembly. Nature, 451(7181), 977-980.
[74] Bergman, S. D., & Wudl, F. (2008). Mendable polymers. Journal of Materials Chemistry, 18(1), 41-62.
[75] Varley, R. J., & van der Zwaag, S. (2008). Towards an understanding of thermally activated self-healing of an ionomer system during ballistic penetration. Acta Materialia, 56(19), 5737-5750.
[76] Corten, C. C., & Urban, M. W. (2009). Repairing polymers using oscillating magnetic field. Advanced Materials, 21(48), 5011-5015.

[77] Tian, Q., Yuan, Y. C., Rong, M. Z., & Zhang, M. Q. (2009). A thermally remendable epoxy resin. Journal of Materials Chemistry, 19(9), 1289-1296.
[78] Burnworth, M., Tang, L., Kumpfer, J. R., Duncan, A. J., Beyer, F. L., Fiore, G. L., ... & Weder, C. (2011). Optically healable supramolecular polymers. Nature, 472(7343), 334-337.
[79] Peterson, A. M., Jensen, R. E., & Palmese, G. R. (2011). Thermoreversible and remendable glass–polymer interface for fiber-reinforced composites. Composites Science and Technology, 71(5), 586-592.
[80] Pratama, P. A., Peterson, A. M., & Palmese, G. R. (2012). Diffusion and Reaction Phenomena in Solution-Based Healing of Polymer Coatings Using the Diels–Alder Reaction. Macromolecular Chemistry and Physics, 213(2), 173-181.
[81] Chen, Y., Kushner, A. M., Williams, G. A., & Guan, Z. (2012). Multiphase design of autonomic self-healing thermoplastic elastomers. Nature chemistry, 4(6), 467-472.
[82] Chen, Y., & Guan, Z. (2013). Self-assembly of core–shell nanoparticles for self-healing materials. Polymer Chemistry, 4(18), 4885-4889.
[83] Zhang, M. Q., & Rong, M. Z. (2013). Intrinsic self-healing of covalent polymers through bond reconnection towards strength restoration. Polymer Chemistry, 4(18), 4878-4884.
[84] Mozhdehi, D., Ayala, S., Cromwell, O. R., & Guan, Z. (2014). Self-healing multiphase polymers via dynamic metal–ligand interactions. Journal of the American Chemical Society, 136(46), 16128-16131.
[85] Kuhl, N., Bode, S., Bose, R. K., Vitz, J., Seifert, A., Hoeppener, S., ... & Schubert, U. S. (2015). Acylhydrazones as Reversible Covalent Crosslinkers for Self-Healing Polymers. Advanced Functional Materials, 25(22), 3295-3301.
[86] Roy, N., Bruchmann, B., & Lehn, J. M. (2015). DYNAMERS: dynamic polymers as self-healing materials. Chemical Society Reviews, 44(11), 3786-3807.
[87] Cash, J. J., Kubo, T., Bapat, A. P., & Sumerlin, B. S. (2015). Room-Temperature Self-Healing Polymers Based on Dynamic-Covalent Boronic Esters. Macromolecules, 48(7), 2098-2106.
[88] C.A. Clear, The effects of autogenous healing upon the leakage of water through cracks in concrete, Cement and Concrete Association Technical Report No.559, 1985.
[89] N. Hearn, Self-sealing, autogenous healing and continued hydration: what is the difference? Materials and Structures, 31(201) (1998), 563-567.
[90] C. Edvardsen, Water permeability and autogenous healing of cracks in concrete, ACI Materials Journal, 96(4) (1999), 448-454.
[91] Neville, A. (2002). Autogenous healing—a concrete miracle? Concrete International, 24(11), 76-82.
[92] Van Tittelboom, K., Gruyaert, E., Rahier, H., & De Belie, N. (2012). Influence of mix composition on the extent of autogenous crack healing by continued hydration or calcium carbonate formation. Construction and Building Materials, 37, 349-359.
[93] Snoeck, D., & De Belie, N. (2015). From straw in bricks to modern use of microfibers in cementitious composites for improved autogenous healing–A review. Construction and Building Materials, 95, 774-787.
[94] Yang, Y., Lepech, M. D., Yang, E. H., & Li, V. C. (2009). Autogenous healing of engineered cementitious composites under wet–dry cycles. Cement and Concrete Research, 39(5), 382-390.

[95] Kan, L. L., Shi, H. S., Sakulich, A. R., & Li, V. C. (2010). Self-healing characterization of engineered cementitious composite materials. ACI Materials Journal, 107(6), 617.
[96] Li, M., & Li, V. C. (2011). Cracking and healing of engineered cementitious composites under chloride environment. ACI Materials Journal, 108(3), 333-340.
[97] Herbert, E. N., & Li, V. C. (2013). Self-healing of microcracks in engineered cementitious composites (ECC) under a natural environment. Materials, 6(7), 2831-2845.
[98] Lee, H. X. D., Wong, H. S., & Buenfeld, N. R. (2010). Potential of superabsorbent polymer for self-sealing cracks in concrete. Advances in Applied Ceramics, 109(5), 296-302.
[99] Snoeck, D., Steuperaert, S., Van Tittelboom, K., Dubruel, P., & De Belie, N. (2012). Visualization of water penetration in cementitious materials with superabsorbent polymers by means of neutron radiography. Cement and Concrete Research, 42(8), 1113-1121.
[100] Snoeck, D., Van Tittelboom, K., Steuperaert, S., Dubruel, P., & De Belie, N. (2014). Self-healing cementitious materials by the combination of microfibres and superabsorbent polymers. Journal of Intelligent Material Systems and Structures, 25(1), 13-24.
[101] Qian, S. Z., Zhou, J., & Schlangen, E. (2010). Influence of curing condition and precracking time on the self-healing behavior of engineered cementitious composites. Cement and concrete composites, 32(9), 686-693.
[102] Janssen, D. (2011). Water encapsulation to initiate self-healing in cementitious materials (Doctoral dissertation, Master Thesis, Delft University of Technology, Delft, The Netherlands).
[103] Yang, E. H., Yang, Y., & Li, V. C. (2007). Use of high volumes of fly ash to improve ECC mechanical properties and material greenness. ACI Materials Journal, 104(6), 620-628.
[104] Termkhajornkit, P., Nawa, T., Yamashiro, Y., & Saito, T. (2009). Self-healing ability of fly ash–cement systems. Cement and Concrete Composites, 31(3), 195-203.
[105] Qian, S., Zhou, J., De Rooij, M. R., Schlangen, E., Ye, G., & Van Breugel, K. (2009). Self-healing behavior of strain hardening cementitious composites incorporating local waste materials. Cement and Concrete Composites, 31(9), 613-621
[106] Ahn, T. H., & Kishi, T. (2010). Crack self-healing behavior of cementitious composites incorporating various mineral admixtures. Journal of Advanced Concrete Technology, 8(2), 171-186.
[107] Na, S. H., Hama, Y., Taniguchi, M., Katsura, O., Sagawa, T., & Zakaria, M. (2012). Experimental investigation on reaction rate and self-healing ability in fly ash blended cement mixtures. Journal of Advanced Concrete Technology, 10(7), 240-253.
[108] Sisomphon, K., Copuroglu, O., & Koenders, E. A. B. (2013). Effect of exposure conditions on self-healing behavior of strain hardening cementitious composites incorporating various cementitious materials. Construction and Building Materials, 42, 217-224.
[109] Sahmaran, M., Yildirim, G., & Erdem, T. K. (2013). Self-healing capability of cementitious composites incorporating different supplementary cementitious materials. Cement and Concrete Composites, 35(1), 89-101.
[110] Huang, H., Ye, G., & Damidot, D. (2014). Effect of blast furnace slag on self-healing of microcracks in cementitious materials. Cement and concrete research, 60, 68-82.
[111] Li, V. C. (2003). On engineered cementitious composites (ECC). Journal of advanced concrete technology, 1(3), 215-230.

CHAPTER 2 PROBE SELF-HEALING IN CEMENTITIOUS MATERIALS BY THREE-DIMENSIONAL X-RAY COMPUTED MICROTOMOGRAPHY

2.1 Introduction

For the understanding of the healing mechanism and the development of robust self-healing cementitious materials it is crucial to precisely characterize the damage (e.g. microcracks) volume evolution during the self-healing process under various environmental conditions. In the precious researches, a number of self-healing characterization techniques have been adopted, including: water permeability and signal transmission tests to characterize transport properties[1-6], ultrasonic echoing and dynamic modulus measurement to characterize both transport and mechanical properties [6-9], destructive tests such as bending, compression, uniaxial tension and stiffness measurements [10-18]. Additionally, analysis techniques of self-healing products including SEM (scanning electron microscopy) and AEM (analytical electron microscopy) imaging, EDX (energy-dispersive X-ray spectroscopy), FTIR (Fourier transform infrared spectroscopy), and XRD (X-ray diffraction) chemical analysis have been used to characterize the morphology and mineralogy of the healing products [6][7][15][19]. These methods have been effective for verifying self-healing in cementitious materials at the bulk composite material level, or to analyze self-healing products present at the sample surface. However, little knowledge is available on the change in the three-dimensional internal microstructure of cementitious materials due to self-healing. The current methods are not suitable for directly measuring the self-healing potential of a three-dimensional crack with certain initial shape and geometry at specified environmental exposure conditions. To date, the validation and direct quantification of

through-depth self-healing of microcracks of cementitious materials have remained unaddressed. This knowledge, however, is critical for establishing a rational and quantitative relation between self-healing extent with different physical, chemical, and environmental parameters.

To fill this knowledge gap, this study adopts 3D X-Ray Computed Micro-Tomography (μCT) techniques that are commonplace in the biomedical and geophysics fields. As a non-destructive imaging technique, μCT provides a means of obtaining 3D maps of the internal structure of a material based on X-ray absorption of different phases or elements [19]. μCT was used in a number of studies to characterize the microstructure of concrete [20][24], but has rarely been employed to study cracking and self-healing in cementitious materials [25]. This study established a new systematic method for characterizing the change in 3D microstructure and cracks in cementitious composites before and after self-healing. The CT method allowed imaging, phase segmentation, quantification, and monitoring of the interior characteristics of cementitious materials. Besides the tomography, microscopy and SEM were also applied to visualize the morphological characteristics of the healing products. In addition, EDX, XRD, FTIR, and Raman spectroscopy were utilized as the chemical analysis tools to investigate the mineralogy information of the healing products. Through this integrated multiscale characterization system, more precise quantification of 3D self-healing extent and quality can be realized, which allow us to systematically study the complex autogenous healing mechanism.

2.2 Material and Methods

2.2.1 Material and Specimen Preparation

In this study, type I ordinary Portland cement (OPC) was used in all specimens. The neat cement pastes were prepared at a fixed water to cement ratio (by weight) of 0.4. The

cementitious ingredients and their hydration products together formed the matrix, while a small amount of polyvinyl alcohol (PVA) fibers (volume fraction of 2.0%) were incorporated into the matrix to control the cracking behavior. The PVA fibers were 8 mm long and 39 μm in diameter, with nominal tensile strength of 1620 MPa and density of 1300 kg/m^3. The fiber/matrix interfacial micro-parameters were tailored so that the fiber bridging vs. crack opening relation and maximum fiber bridging stress satisfy the strain-hardening criteria.

The mix design is listed in **Table 2.1** and the chemical compositions of cement are given in **Table 2.2**. The fresh mixture was cast into a series of coupon specimens with dimensions of 300×100×12.5 mm. The specimens were covered with plastic sheets and cured in laboratory air with a temperature of 20±1°C and relative humidity of 45%±5 until the age of demold. The demolded specimens were thoroughly cured in water until the age of 4 month for mechanical loading to induce cracks. The long curing time allowed cement hydration to stabilize. The coupon specimens were loaded using a servo-hydraulic testing system with a 25 kN load cell with a fixed cross head displacement rate of 0.001 mm/s to simulate a quasi-static lading condition. The four-point bending test setup is shown in **Figure 2.1**. The bending test, rather than the direct uniaxial tensile test, was intentionally adopted in this study to generate "V-shape" 3-dimensional cracks (i.e. crack width varies with crack depth) that are most common in real structures. Also, these "non-flat" cracks can better reveal the capacity of μCT for characterizing three-dimensional damage, and the effect of both crack depth and width on self-healing. After unloading, the crack pattern of the specimen was examined under an optical microscope. Then, two representative regions were selected and cut from the specimen, with dimensions of 10×10×11 mm - namely sample-A and sample-B. The maximum opening of each crack on the top surface was measured by optical microscopy, summarized in **Table 2.3**. Sample-A contains 4

microcracks with average surface crack width of 31 μm. Sample-B contains 3 microcracks with average surface crack width of 102 μm (**Figure 2.2**). These two samples were then used for micro-CT, SEM and EDS examination.

The samples were exposed to water-dry cycles to allow potential self-healing to occur. For each cycle, the samples were firstly submersed into water at 20°C for 24h, and then naturally dried in ambient air at 20±1°C and 45%±5 RH for 24h to simulate the rain/dry outdoor environments. The water was changed after each cycle to prevent it from becoming saturated with leached particles.

2.2.2 μCT Procedure

X-ray micro-tomographic scanning was conducted on the samples before self-healing and after 1, 5 and 10 wet/dry cycles of environmental exposure. The principle of X-ray computed tomography is based on the 3D computed reconstruction of a sample from 2D projections acquired at different angles around its axis of rotation [26]. When an X-ray beam illuminates and translates through the sample, the beam intensity will be attenuated after absorption by the different phases and components of the material. Generally, a unit with higher density will absorb more X-ray. The intensity of the transmitted X-ray beam is recorded by a digital detector and the value of the attenuation coefficient for each voxel is transformed into CT numbers according to the Hounsfield scale [27] given by:

$$CT\ Number = \frac{1000(\mu_X - \mu_{water})}{\mu_{water}} \tag{2.1}$$

where, μ_X and μ_{water} are the linear attenuation coefficients of the sample material and water, respectively. After raw data collection, a set of gray-scale 2D cross sections that map the density variation within the sample can be calculated and constructed. These 2D images are then

mathematically re-constructed to create a 3D map of the interior structure of the sample based on the variation in X-ray absorption [28]. Finally, A great deal of two or three-dimensional morphological parameters (e.g. surface area and volume) of the object can be analyzed through these image data. It should be noted that the resolution that can be achieved by the μCT system is one of the most significant parameters which directly affects the accuracy of the analysis. Resolution is normally defined by the dimensions of the data voxels: the z resolution corresponds to the spacing between 2D slice planes, which is usually equal to or slightly below the slice thickness. The x–y resolution is typically the sample cross-sectional diameter divided by the image pixel dimension, depending primarily on the number of detector channels and geometric factors.

The μCT facility used in this study was a high energy microtomography scanner for large and dense objects, which consisted of a newly developed 130 kV X-ray source with improved stability of focal spot position, and a distortion-free flat panel detector with maximum 4000 × 2648 resolution. For each scanning process, the ECC sample was fixed on an embedded micro-positioning stage and scanned in air with 80 kV tube voltage and 125 μA tube current. A total of 2200 slice images were stored while the sample was rotated with an angle step of 0.3º. The thickness and resolution of each slice were 5 μm and 2400 × 2400, respectively, which means the voxel size of the reconstructed 3D volume rendering was 5 μm × 5 μm × 5 μm. Because of various reasons such as instability of the detector and the construction procedure, all of the CT images contained noise. In order to obtain a more realistic image, the wavelet analysis-based denoising technique [29] was performed on each slice image to suppress the noise. Additionally, a median filter method [30] was also applied to remove the non-physical presence of random noise surrounding the air voids. After these specific noise-reduction corrections, a package of software

was used for 3D visualization based on the filtered back-projection procedure for Feldkamp cone-beam reconstruction for circular and spiral acquisition [31].

2.2.3 Image Processing and Analysis

The images obtained from μCT method were analyzed in order to separate the crack phase from the air pore phase and the solid phase, and to quantify the changes in the crack phase after different cycles of self-healing. To our knowledge, this has not been conducted on cementitious materials to study self-healing. The data obtained from μCT scanning were mathematically regarded as a four-dimensional set. Each pixel was represented by Cartesian coordinates (X, Y and Z) and corresponding density. This allowed for the application of image processing methods based on the quantitative information extracted from the μCT. **Figure 2.3(a)** and **(b)** show the typical cross sectional raw images of sample-A and sample-B. Each raw image contains a 2D array of contiguous squares (i.e. pixels) consisting of 256 possible levels (0-255) of gray intensity. The gray level of each pixel in the images represents a density value that corresponds to the linear attenuation coefficient of the element contained in that pixel. The lower density element appears darker colored, while the higher density element appears lighter colored. These raw images generally contain two phases: (1) gas phase including air pores and cracks, which appear black and (2) solid phase including the cementitious binder and fine aggregates, which appear as a lighter grey. Within the solid phase, the unhydrated clinker has higher density than the fine aggregates (sand) and hydration products (i.e. C-S-H and C-H), thus absorbing most of the X-ray and appearing as slightly brighter pixels in the images. It was also observed that some white dots exist in the μCT images. The most likely sources for these spots are the high-density metal impurities in the cementitious matrix.

In order to focus on the specific component in the non-homogeneous material, image segmentation was then carried out to separate the digital image into multiple phases. An accurate and accessible image segmentation method is also in high demand for skeletonizing 3D models. For demonstrating the segmentation process, a volume of interest, abbreviated VOI, was extracted with dimension 1 × 1 × 1 mm from the sample-B as shown in **Figure 2.4**. First, a global thresholding method was needed to convert the grey-scale images to binary images. By examining all the voxels in each gray-scale VOI, a histogram representing the frequency distribution of each intensity level was generated, as shown in **Figure 2.5**. The Otsu's method was then applied to calculate the threshold values: T_1 separates the gas phase from the solid phase; T_2 further divide the solid phase by separating the hydrates and aggregates from unhydrated particles. Otsu's method [32] of image segmentation selects an optimum threshold by maximizing the between-class variance (intra-class variance) in a gray image. However, this method becomes very time-consuming when extended to a multi-level threshold problem since a particularly large number of iterations are required for computing the cumulative probability and the mean of a class. To improve the efficiency of computation, a faster algorithm proposed by Liao [33] was used in this study to quickly determine the modified between-class variance and the associated thresholds.

To verify the accuracy of the obtained threshold values T_1 and T_2, we selected three other VOIs that did not contain any cracks to calculate the cumulative volume fraction of pores based on the segmented histogram. We then compared the calculated average porosity with the porosity experimentally determined by other researchers using mercury intrusion method [34]. The µCT-based result (22.6%) was comparable with the experimental result (23.7%), thus confirming that the threshold value that separates the gas phase from the solid phase was reliable.

Next, the threshold intensity values were applied to all the pixels of the gray-scale images. The target pixels (i.e. the component of interest) were isolated and colored white; otherwise they were colored black. By these means, binary images were generated, as shown in **Figure 2.6**. The gas phase, for instance, was determined as all the pixels with intensity smaller than T_1, and were segregated and colored white (**Figure 2.6(a)**). The unhydrated particles, were identified as the dispersed aggregation of pixels with intensity larger than T_2, and were colored white in **Figure 2.6(b)**. After thresholding segmentation, a series of binary images were combined into a 3D matrix of voxels. The 3D renderings of the different phases are shown in **Figure 2.7**.

To further separate the cracks from the air pore network, a mathematically morphological method was employed. Mathematical morphology is a theory as well as a technique that can be applied to graphs, digital images and spatial structures, for mathematically studying geometric structures and shape elements [35][36]. In a binary image (**Figure 2.6(a)**), a pixel can either have a value of '1' when it is part of the gas phase (foreground), or '0' when it is part of the solid phase (background). In order to identify cracks, we first partitioned the gas phase of the binary image into different connected components, also called clusters, by means of pixel connectivity. Pixel connectivity describes the way pixels are connected to their neighbors. In this study, a three-dimensional 18-connected labeling method proposed by Lumia [38] was adopted. 18-connectivity is defined as when every two adjacent voxels sharing the same face or edge are considered "connected", as illustrated in **Figure 2.8**. Based on this definition, the gas phase in the binary images were scanned. Every maximally connected cluster was identified as a group of 18-connected pixels with a value of "1", and then was labeled with a distinct integer.

Morphological operations were then conducted to take measurements from the labeled clusters, based on the basic mathematical principles introduced by Serra [35]. Plenty of 2D and 3D

geometry-topology characteristics were acquired, such as volume, surface area, cross sectional area and perimeter, thickness, connectivity, convexity, structure model index (SMI), etc. With two of these topological parameters, volume and SMI, we were able to recognize if a cluster was a pore or a crack. For lessening the calculation, we first removed the small capillary pores by setting a 0.001 mm^{-3} volume filter to the clusters, so that only larger pores and crack remained (**Figure 2.9**). Subsequently, we calculated the structure model index for each of the rest clusters. SMI is a parameter indicating the topology characteristic of a homogeneous random closed set, similar to the isoperimetric shape factors used for compact sets [38]. The calculation was based on the dilation of the 3D voxel model first suggested by Hildebrand and Rüegsegger [39] for quantifying plate- or rod-like bone microarchitecture. SMI is defined as follows:

$$SMI = 6 \cdot \frac{VS'}{S^2} \tag{2.2}$$

where, V is the initial undilated volume of the cluster, S is the surface area before dilation, and the derivative of S is taken with respect to the shift of the structure surface in the direction perpendicular to that surface caused by dilation. Following Equation (2.2), an ideal plate has a SMI value of 0. A cylinder and a sphere have SMI values of 3 and 4, respectively. For the clusters in **Figure 2.9**, the SMI of each cluster was calculated and the result was shown in **Figure 2.10**. It can be seen that the crack has a much lower SMI and is distinguishable from the pores. Thus, the gas phase was finally subdivided into cracks and pores (see different colors in **Figure 2.9**), allowing us to measure and quantify self-healing within the cracks.

2.3 Results and Discussion

The reconstructed 3D renderings as well as the corresponding orthogonal cross sections for the damaged samples are shown in **Figure 2.11**. The image data was reoriented so that the

edges of the sample block were parallel to the orthogonal planes. The surface (Z = 0) where the cracks cross the whole section was labeled as “top”; the top surface also corresponds to the tensile side surface of the original bending specimen. The other two orthogonal planes were labeled as “front” and “side”. During the image analysis, the selection of the VOI for both samples started from the “top” surface and continued through the depth until the end of the cracks. **Figure 2.11** shows the top, front, and side views of a crack, clearly defining the 3D geometry of the crack. Through the image analysis described in Section 3, the geometrical characteristics of the cracks for each sample can be obtained and parts of them were summarized in **Table 2.4**. Based on these geometrical parameters, the evolution of cracks under cyclic wet/dry exposure was quantitatively presented.

The total crack volume change ratios over different self-healing cycles were calculated (**Figure 2.12**), indicating the effect of crack width as well as the number of cycles on the self-healing extent and rate. For sample-A, the average width of the 4 cracks on the top surface was 31 μm, while the average width of the total volumetric cracks was 15 μm. After 1, 5 and 10 wet/dry cycles, the total crack volume decreased by 13.2%, 37.3% and 43.1% respectively due to self-healing. For sample-B, the average width of the 3 cracks on the top surface was 102 μm, and the average width of the total volumetric cracks was 75 μm. The total crack volume decreased by only 2.4%, 7.2% and 10.8% due to self-healing after 1, 5 and 10 wet/dry cycles. A visualized comparison of the 3D microstructure of the cracks within sample-A and sample-B before and after 5 cycles of self-healing is shown in **Figure 2.13** with a 30% opacity. The lighter color regions were the cracks; part of which turned darker just as the background matrix color after the self-healing process. The results clearly revealed the strong effect of crack width on 3D self-healing extent (i.e. how much has been healed) and rate (i.e. how fast did self-healing occur

between cycles). The smaller cracks healed faster volumetrically than larger cracks, with the presence of the same chemical species and equal environmental exposure conditions. However, it was found that change in the total crack volume for sample-A and sample-B were on the same scale (i.e. 2.255 mm^3 for Sample A and 1.715 mm^3 for Sample B after 10 cycles).

Figure 2.14 shows the change in crack area with respect to the distance from the top surface after 5 cycles, based on the μCT image analysis results. The left axis specifies crack area, which accounts for the multiple microcracks within each sample at a fixed distance from the top surface; the right axis specifies normalized crack width, which was calculated by dividing the crack area by the number of cracks and the total length of the sample size. The first important finding was that self-healing not only occurred at crack top surface, but also through the crack depth for both samples with different average crack width.

We also observed a significant difference in self-healing extent between the crack region close to the top surface and the crack region deeper inside the samples. From **Figure 2.14(c)**, it can be seen that from the top surface to 0.05~0.15 mm depth, 95% of the cracks in sample-A was healed, which was significantly higher than the 37.3% healing of total crack volume (**Figure 2.12**). Even for large cracks in sample-B, a similar region of 0.05-0.15 mm below the top surface was healed as high as approximately 30%, compared to the 7.2% healing of total crack volume. Beyond this shallow region, the self-healing extent had a dramatic drop – 33.4% was healed for smaller cracks in sample-A and 2.1% was healed for larger cracks in sample-B. In order to better distinguish the self-healing phenomenon occurred at these two different regions, we divided the crack into the exterior part and the interior part. **Figure 2.15** provides the representative cross-section mages extracted from 0.05 and 2mm depth from the top surface for visualized comparison of the healing extent in these two regions. The images clearly showed that the

exterior region of the cracks was healed to a greater extent, despite that the interior region of the cracks tends to have smaller crack width than the exterior region (due to the "V" shape of the cracks). The findings indicated that although self-healing extent greatly depends on the crack width measured from the top surface, as discussed in the last section, it also greatly depends on the crack depth. Smaller cracks favor self-healing, but the deeper region of a same crack tends to have a much lower self-healing extent than the shallower region despite that the latter has wider crack width. The non-homogenous through-depth self-healing of a crack strongly indicates a change in the self-healing mechanism. The results further suggested that characterizing self-healing only from the surface is not sufficient to evaluate or verify the true self-healing condition of the entire crack within a cementitious material.

SEM and EDX results were used to further investigate the self-healing mechanisms within the crack exterior and interior regions, as shown in **Figure 2.16** and **Figure 2.17**. **Figure 2.16(a)** shows the image taken at 1000X magnification of a microcrack from sample-A surface. The red dash lines marked the original crack top surface lines. The self-healing products had filled in the crack after 5 cycles. These healing products were mainly irregular crystals with a variety of shapes including acute to obtuse rhombohedra, tabular forms or prism, and almost fully "sealed" the crack surface. EDX results showed that the chemical composition of these crystals had three dominating ingredients (**Figure 2.16(b)**): carbon, oxygen, and calcium, suggesting that calcium hydroxide ($Ca(OH)_2$) together with calcium carbonate ($CaCO_3$) were possibly formed. This finding partially supported the mechanism proposed by previous studies Error! Reference source not found.**[1]** that self-healing of cementitious materials is largely attributed to the dissolution and re-deposition of calcium hydroxide, or calcite formed from the carbonation of calcium hydroxide. However, this conclusion from previous studies was derived based on the

observation from sample surface and on the assumption that the self-healing mechanism is uniform along the crack depth, Interestingly, the 3D μCT results from our study revealed that the mixture of $Ca(OH)_2$ and $CaCO_3$ were largely found within a shallow region of approximately 0.15 mm deep below the crack top surface. The possible reason for this phenomenon was that the crystalline precipitates, once formed, physically sealed the crack top surface region. This fast-occurring process isolated the crack interior region from the surroundings environment. It thus became difficult for carbon dioxide or water present in the environment to transport through the sealed area and reach the interior region of the crack. Instead, the continued hydration and pozzolanic reaction also contribute to the self-healing process of the interior region. The unhydrated cement particles reacted with water, forming calcium silicate hydrate (C-S-H) and calcium hydroxide. C-S-H is also a main reaction product of cement hydration, and is the main source of mechanical strength of cementitious materials. This was verified through the SEM and EDX results. **Figure 2.17(a)** shows the SEM image of the crack interior region after self-healing. The healing products within the crack appeared quite similar as the surrounding uncracked area, suggesting that the self-healing products were similar as the cement hydration and pozzolanic reaction products. The EDX analysis (**Figure 2.17(b)**) showed that more silicon element was present (12.84% ± 1.5% for interior vs. 1.94 % ± 0.32% for exterior), suggesting the significant presence of calcium silicate hydrate.

Compared with the dissolution, re-deposition and carbonation process fast occurred at sample surface, the kinetics and crystal growth rate of further cement hydration and pozzolanic reaction are relatively slow. This explains the significant difference in the self-healing extent and rate between the exterior and interior regions, which were observed by μCT. Apparently, within the interior region the self-healing extent was still influenced by crack width and depth. For

sample-A with an average crack width of 31 μm, the self-healed area generally decreased with increasing depth (**Figure 2.14(a)**). In contrast, a more uniform formation of self-healing products along the crack depth was observed for sample-B with an average crack width of 102 μm (**Figure 2.14(b)**). This difference can be explained by the larger initial crack width in sample-B, which allowed faster transport of water into the interior of crack to form self-healing product in a deeper crack region. In Sample-A, the trend of decreasing crack area with increasing crack depth became less linear after self-healing; the non-uniform self-healing profile can be attributed to a combination of factors, including the non-uniform presence of the chemical species (e.g. unhydrated cement, fly ash, calcium hydroxide) along the crack surface with increasing depth, and the time it took for water (governed by permeability) or carbon dioxide (governed by diffusion) to transport through the crack to activate the self-healing process. Finally, it was shown that the self-healing extent in sample-B was much lower, indicating the importance in limiting crack width to a very small value at micrometer scale to promote robust and reliable self-healing.

The beauty of the μCT method established in this study is two-fold: First, it can quantitatively characterize 3D self-healing extent, the effect of crack depth and width, and allow direct study of each individual crack as discussed above. Second, it can fully isolate the effect of environmental conditions on the change in material pore structure from the self-healing of cracks, which cannot be achieved from other bulk material characterization techniques. As shown in **Table 2.5**, the change in porosity and unhydrated particles ratio were calculated before and after self-healing. A similar reduction in porosity in sample-A (0.90%) and sample-B (0.93%) was found. The reduction in unhydrated particles ratio was also at a similar level for the two samples after 5 cycles of self-healing. This is reasonable as the two samples were taken from the same

specimen with the same mixture composition. The reduction in porosity and unhydrated particles ratio can be attributed to the continued hydration and pozzolanic reaction as a high amount of fly ash is present in the mixture.

Finally, it should be noted that the spatial resolution of μCT is limited in that it depends on the energy of the X-ray, the dimensions of the samples and the technology of the detector. Inferences can be made only about structures bigger than the individual pixel. In this study the measured geometry and topological properties, especially for micro-pore structure, depend on the image resolution. A finer resolution could provide more accurate evidence, but at the expense of reduced sample size.

2.4 Summary

In this study, the three-dimensional morphological microstructure of cracks before and after self-healing in cementitious materials was investigated by x-ray computed microtomography (μCT) technology. This work showed that μCT is an effective technique to directly and quantitatively characterize self-healing extent in three dimensions. This is extremely important when the healing kinetic is not uniform along the crack depth. The CT method allowed imaging, phase segmentation, quantification, and monitoring of the interior characteristics of cementitious materials. Scanning Electron Microscope (SEM) and Energy Dispersive X-ray Spectroscopy (EDX) were also adopted to morphologically and chemically analyze the healing products. The integrated characterization method enables us to attempt at answering the following scientific questions:

- While self-healing has been observed in cementitious materials from the crack top surface, does self-healing really occur below the surface and deep inside the crack?

- How much and how fast can self-healing occur within a three-dimensional crack? And what self-healing products tend to form at different depth inside the crack?
- How small of a crack is sufficiently small to promote robust and reliable 3D autogenous healing in cementitious materials?
- What are the different parameters that can influence the elf-healing extent, rate, mechanism, and chemical products?
- Are surface characterization method (e.g. SEM, EDX) and bulk material testing methods (e.g. mechanical testing, resonance frequency test) sufficient in understanding the self-healing quality, extent, rate and mechanism within cementitious materials?
- How can we design the cementitious material physical parameters (e.g. crack width and depth), chemical species (e.g. ingredients and proportion) under certain environmental exposure (e.g. wet/dry cycles, chloride environment) to promote pervasive (i.e. through-depth and three-dimensional) self-healing within a crack with robust self-healing products favoring recovery of both transport properties and mechanical characteristics?

Tables

Table 2.1 Mixture proportion of cement pastes.

Mix	Cement	Water/Binders	Fiber
OPC	1	0.4	2% vol.

Table 2.2 Chemical compositions of cement.

Chemical composition, %	Cement
SiO_2	19.68
Al_2O_3	5.23
CaO	60.57
Fe_2O_3	2.47
MgO	1.12
SO_3	3.81
Na_2O	0.22
K_2O	1.25

Table 2.3 Crack width on the surface of the samples.

Sample-Atop surface crack width (μm)				Sample-top surface crack width (μm)		
Crack #1	Crack #2	Crack #3	Crack #4	Crack #1	Crack #2	Crack #3
25	33	35	30	110	108	89
Average = 31				Average = 102		

Table 2.4 μCT image analysis results.

Parameters	Unit	Sample-A	Sample-B
ROI Volume	mm^3	466.257	878.793
Volume of Each Crack	mm^3	#A1 : 0.481 #A2 : 1.052 #A3 : 0.884 #A4 : 0.669	#B1 : 5.310 #B2 : 5.951 #B3 : 4.622
Total Crack Volume	mm^3	3.086	15.883
Crack Volume/ROI Volume	%	0.662	1.498
Total Crack Surface	mm^2	271.360	890.379
Ave.of Total Cross-sectional Crack Width	μm	15	75
Ave.of Total Cross-sectional Crack Area	mm^2	0.514	1.536
Ave.of Total Cross-sectional Crack Perimeter	mm	27.414	57.069
Ave.of Crack Width on the Top Surface	μm	31	102

Table 2.5 The volume percentage change of pores and unhydrated particles.

	Sample A		Sample B	
	Porosity	Unhydrated particles ratio	Porosity	Unhydrated particles ratio
Before self-healing	21.05%	21.11%	20.84%	22.29%
After self-healing	20.15%	19.50%	19.91%	21.18%

Figures

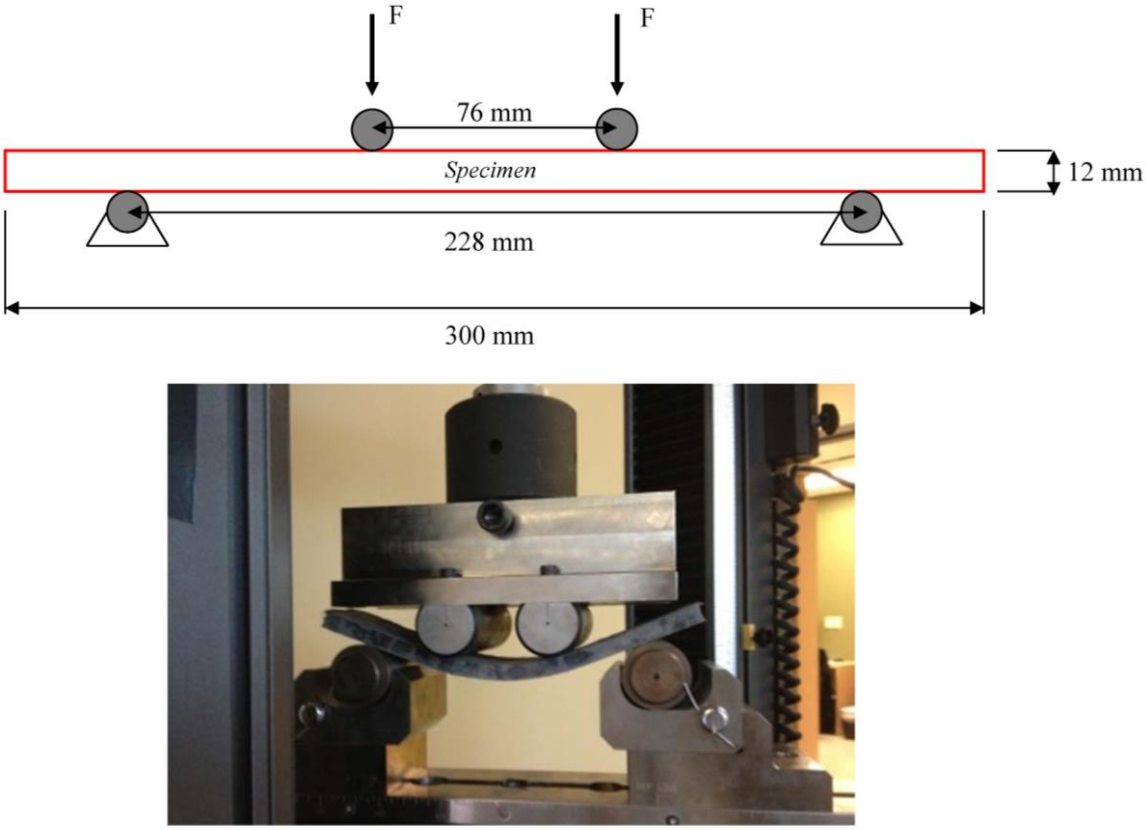

Figure 2.1 Four-point bending test setup and specimen geometry.

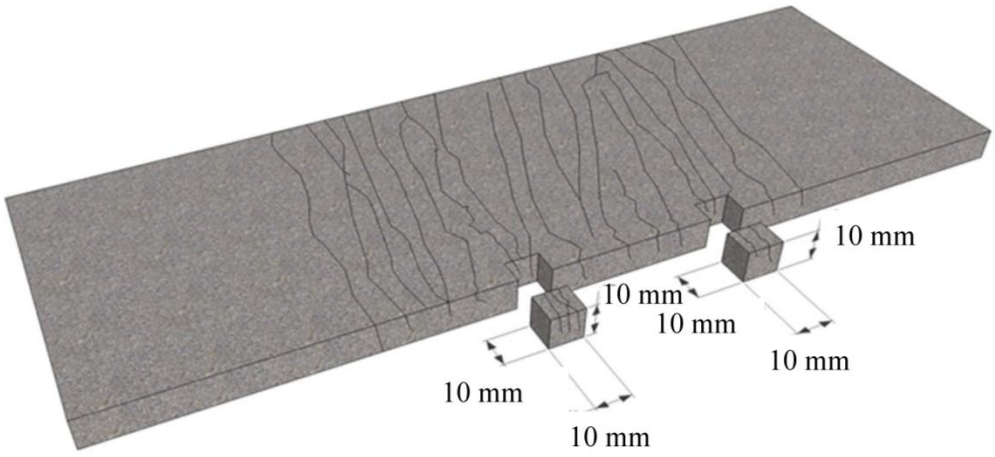

(a)

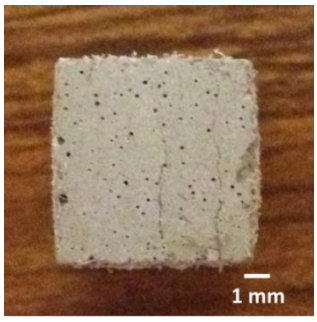

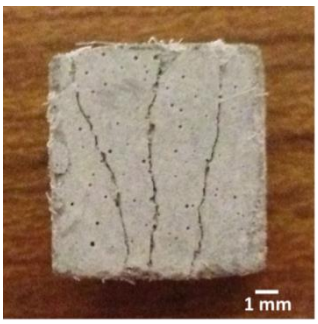

(b) (c)

Figure 2.2 (a) Cubic sample preparation, (b) Sample-A (avg. crack width 31 μm), (c) Sample-B (avg. crack width 102 μm).

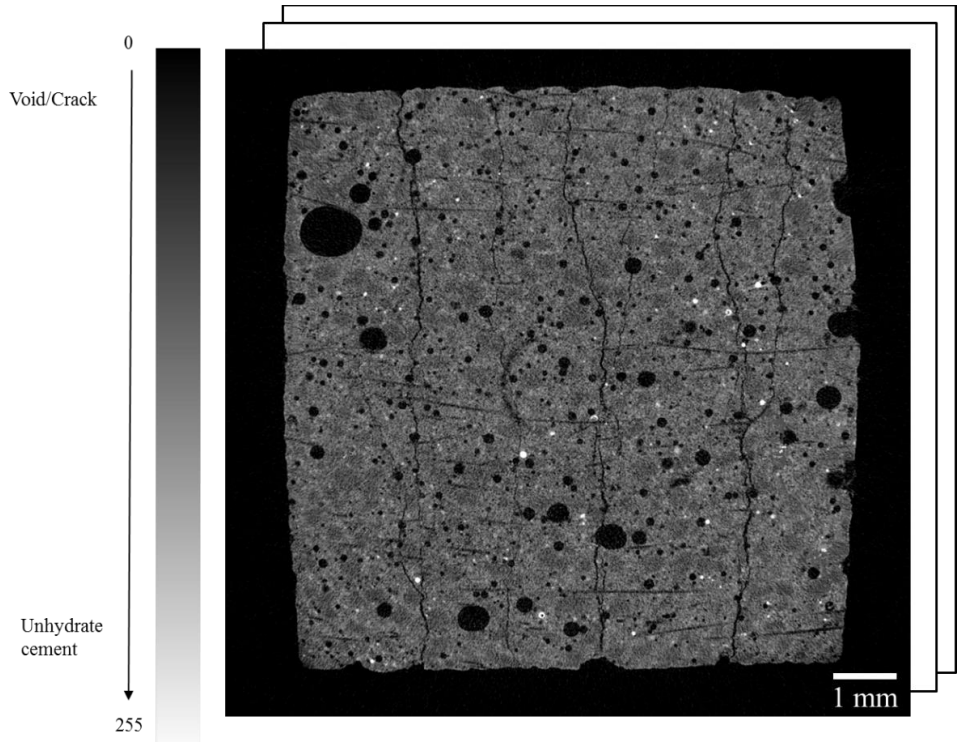

(a) Sample-A before self-healing

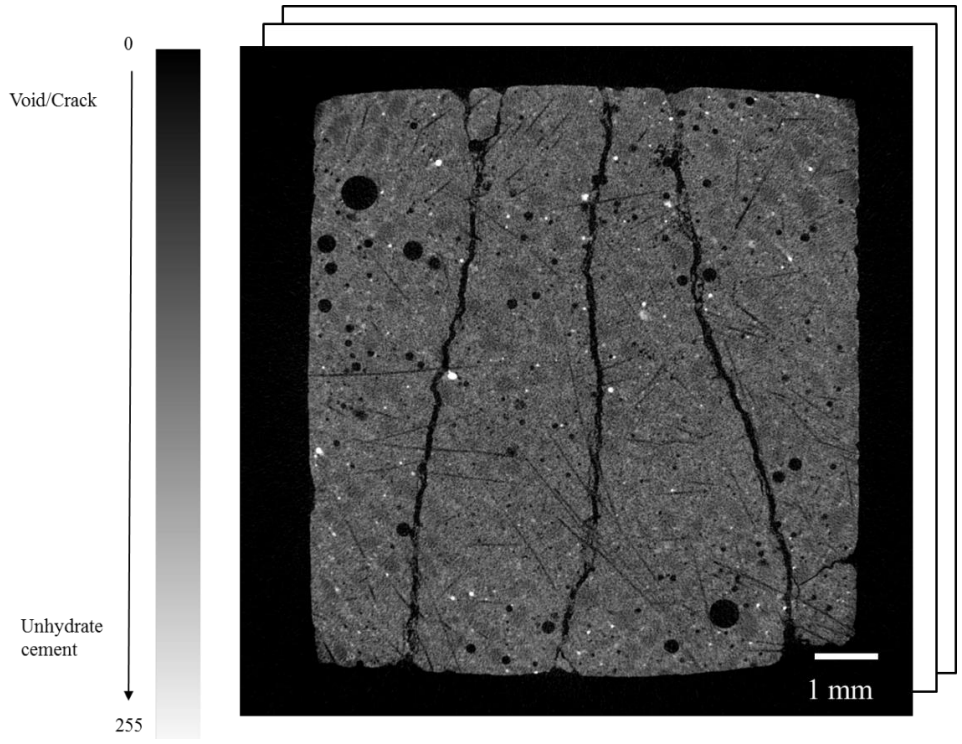

(b) Sample-B before self-healing

Figure 2.3 Examples of μCT 2D raw images.

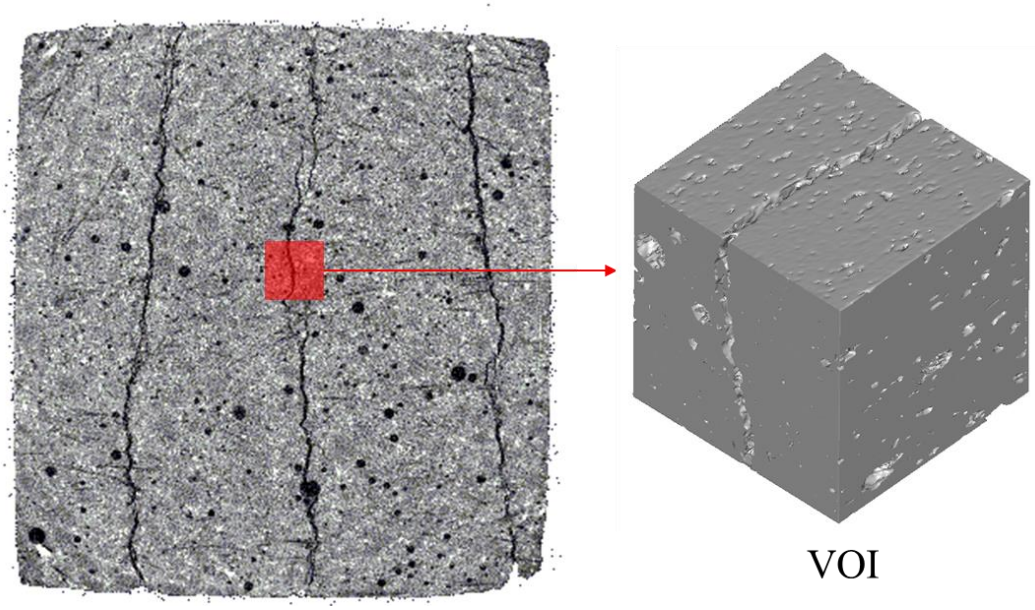

Figure 2.4 Volume of interest (VOI) selected from sample-B.

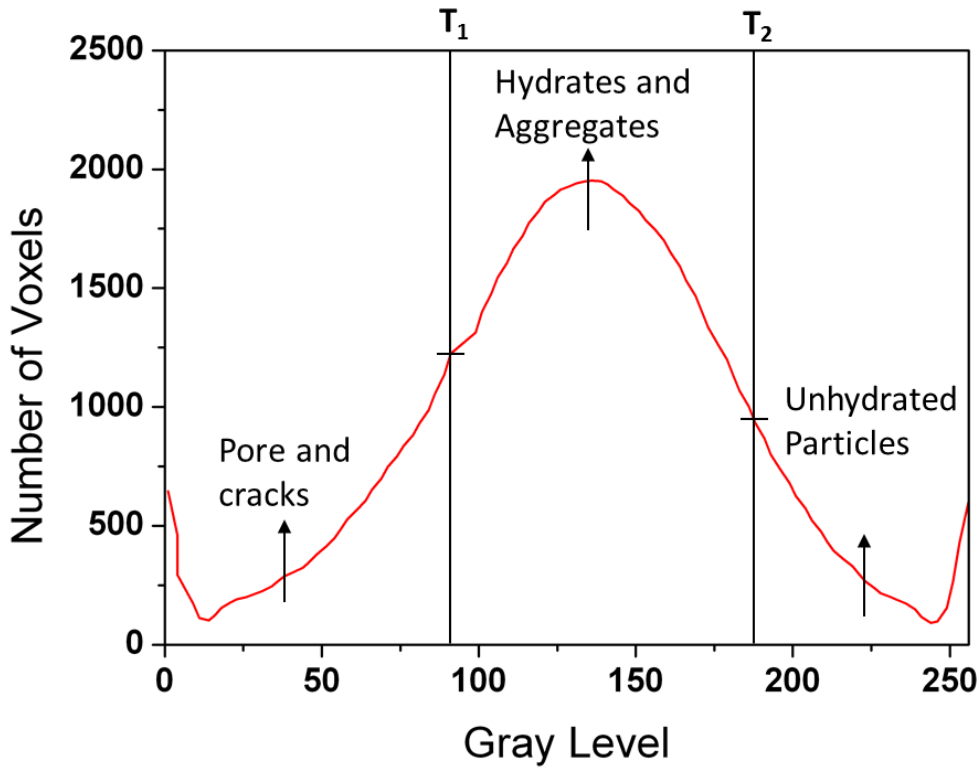

Figure 2.5 Gray level histogram of VOI and threshold values.

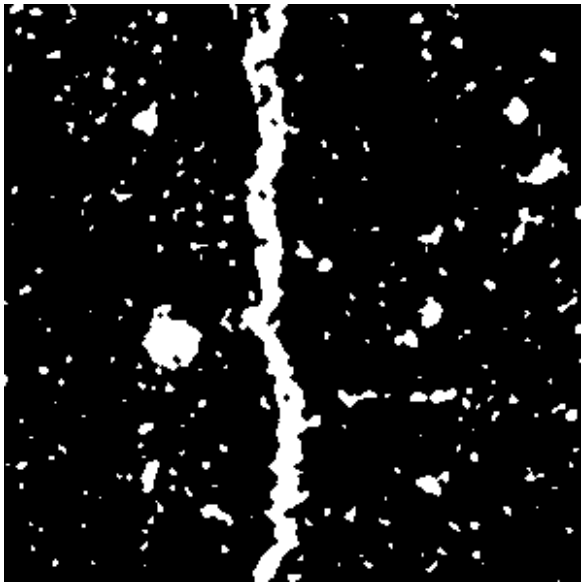

(a) Gas phase (white color)

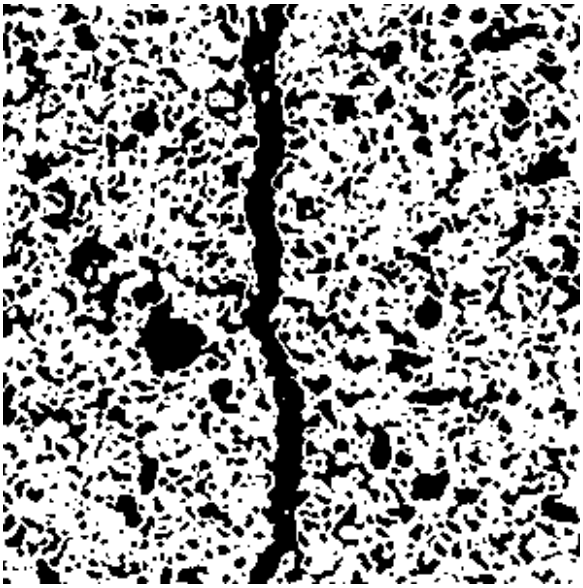

(b) Hydrates and aggregates (white color)

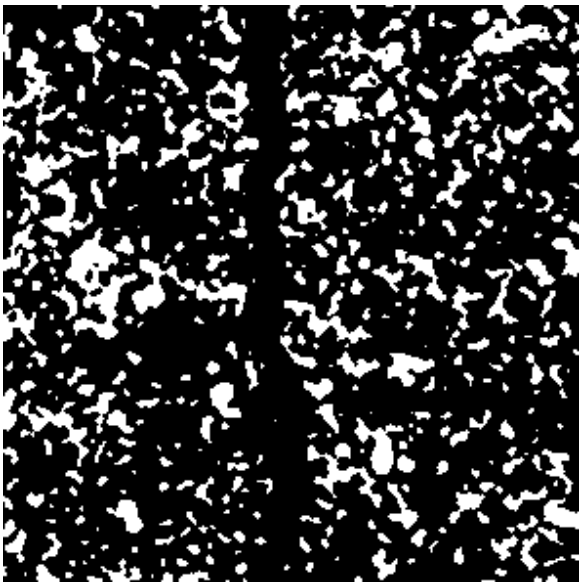

(c) Unhydrated particles (white color)

Figure 2.6 2D Binary results of thresholding segmentation for VOI.

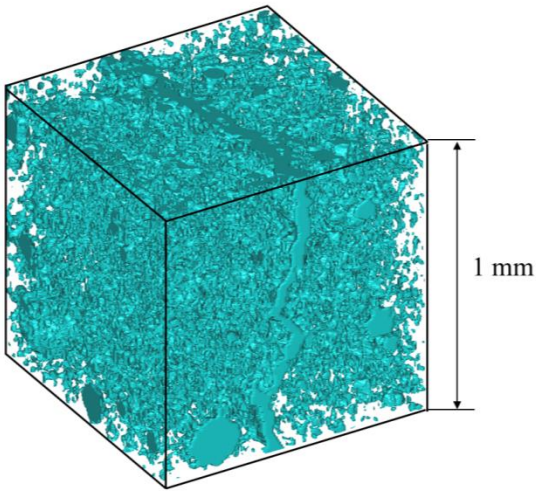

(a) Air pores and cracks

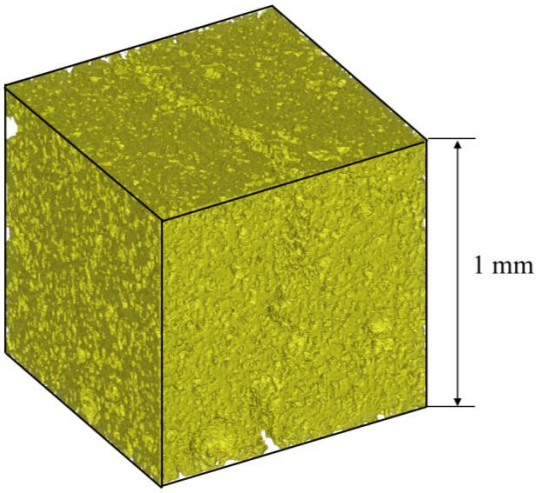

(b) Hydrates and aggregates

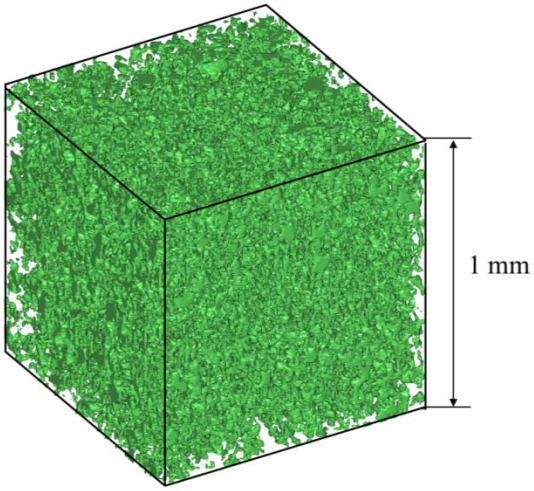

(c) Unhydrated particles

Figure 2.7 Reconstructed 3D images of VOI.

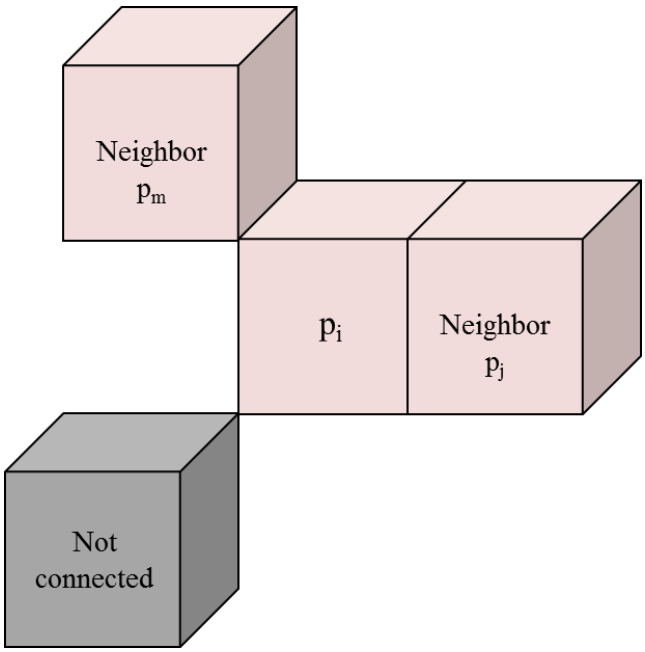

Figure 2.8 Configuration of adjacent voxels by 18-connectivity definition.

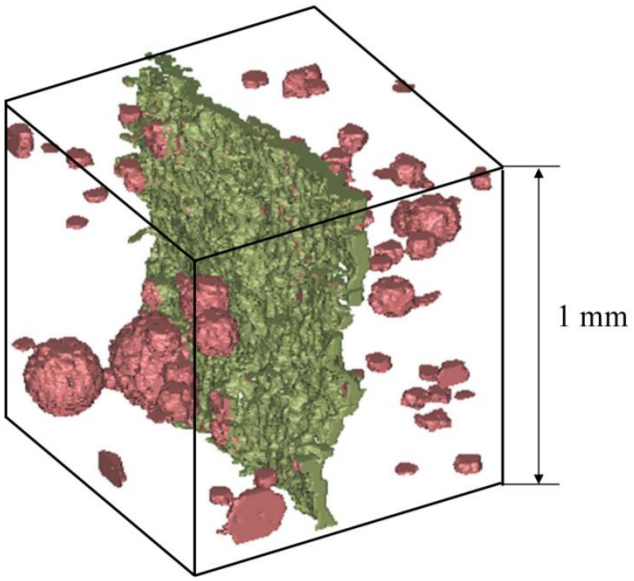

Figure 2.9 Separation of the crack (green) from the large pores (red).

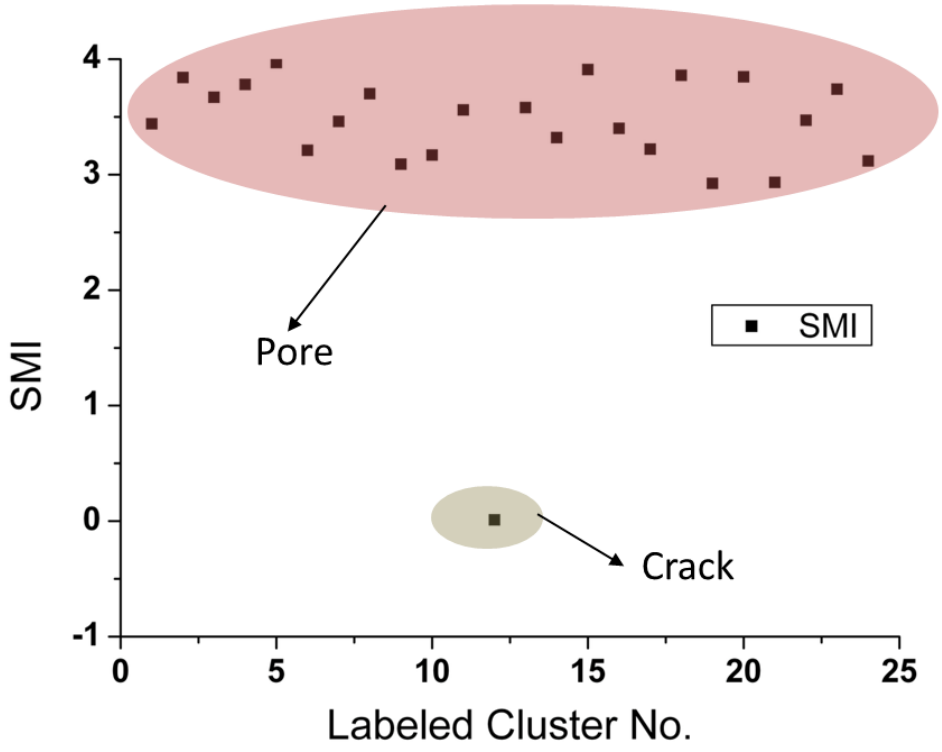

Figure 2.10 Structure model index (SMI) for the clusters in Figure 2.9.

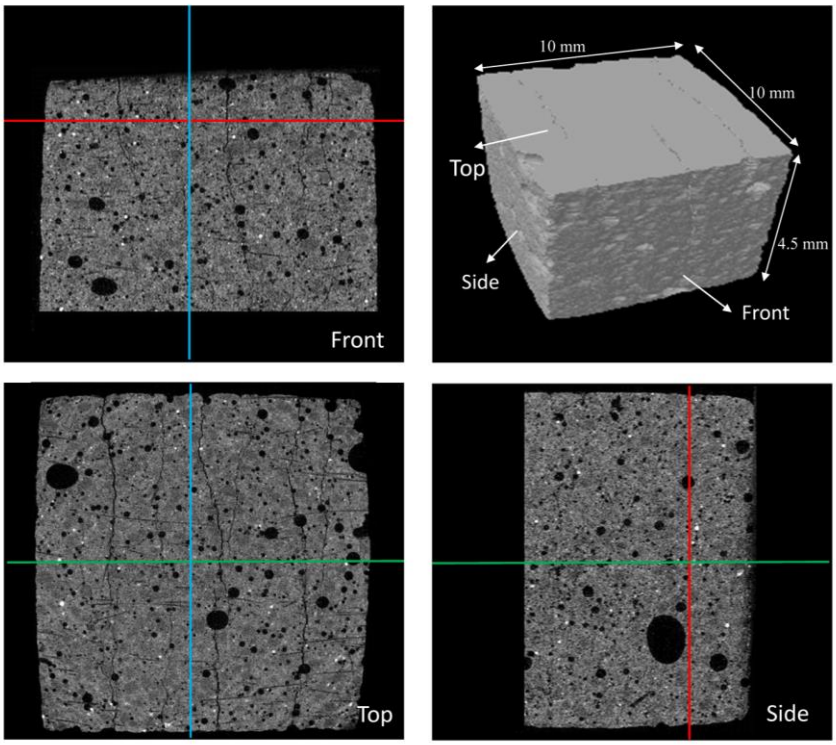

(a) Sample-A

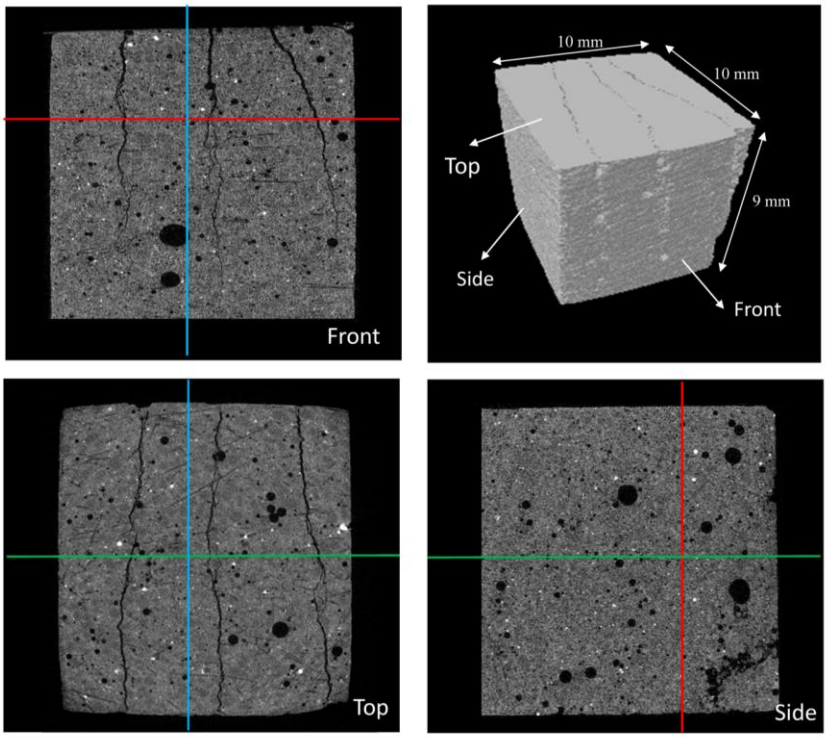

(b) Sample-B

Figure 2.11 Reconstructed 3D renderings and orthogonal cross-section images of VOI.

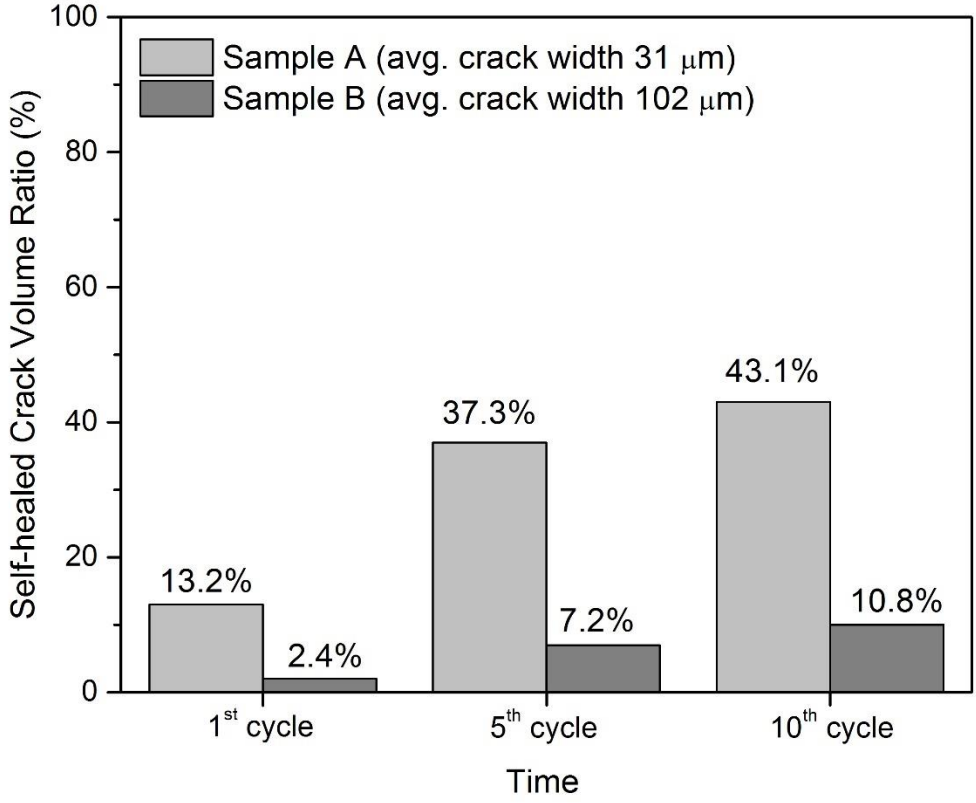

Figure 2.12 Total crack volume change ratio after different cycles of self-healing (Self-healed crack volume / initial crack volume before healing).

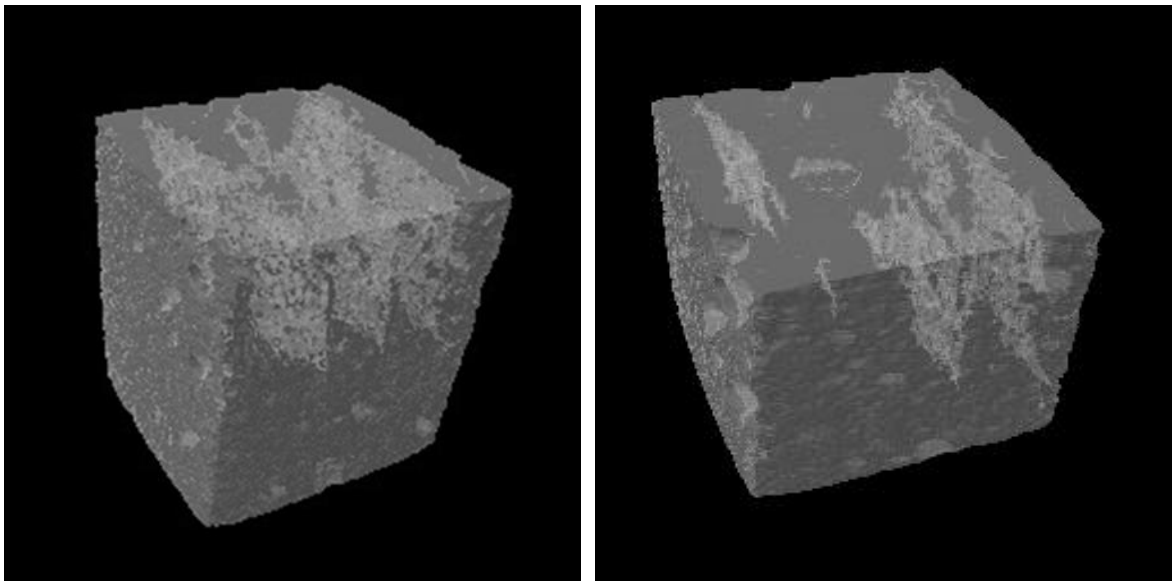

(a) Sample-A before self-healing (b) Sample-A after 5 cycles self-healing

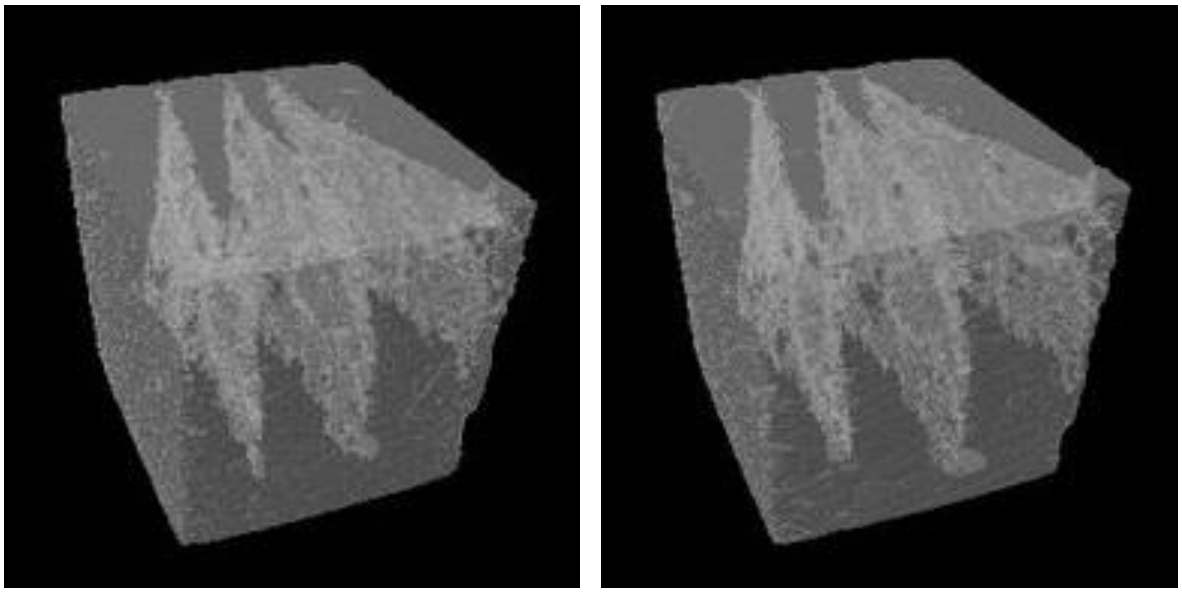

(c) Sample-B before self-healing (d) Sample-B after 5 cycles self-healing

Figure 2.13 Self-healing effect on the 3D microstructure of cracks.

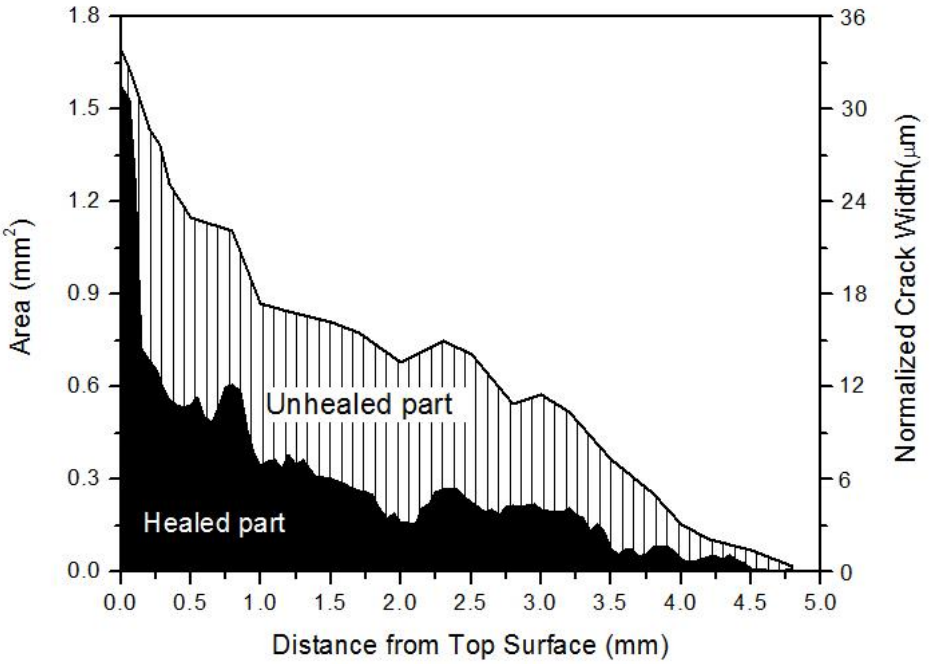

(a) Sample-A

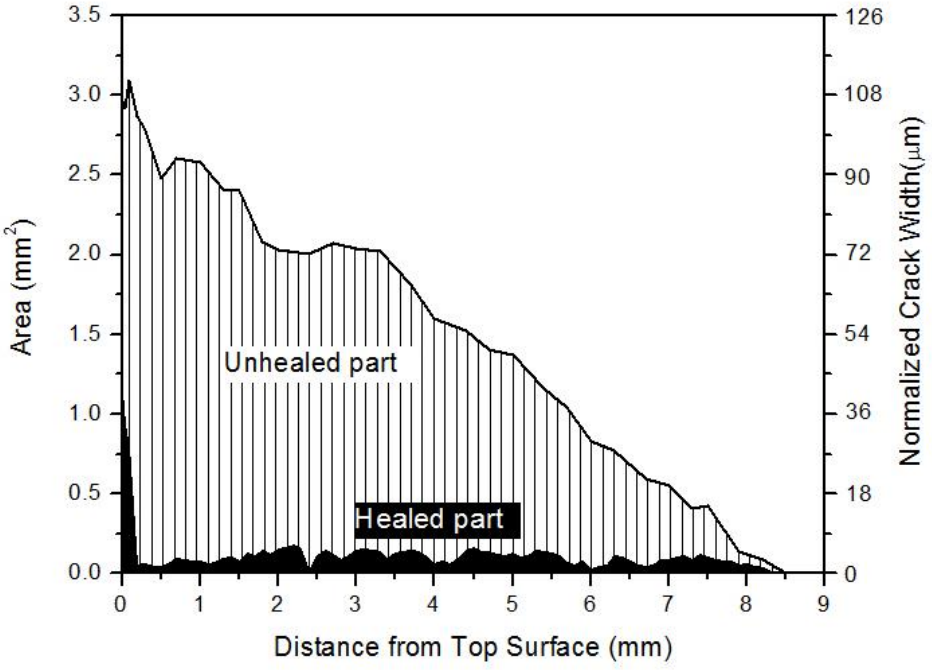

(b) Sample-B

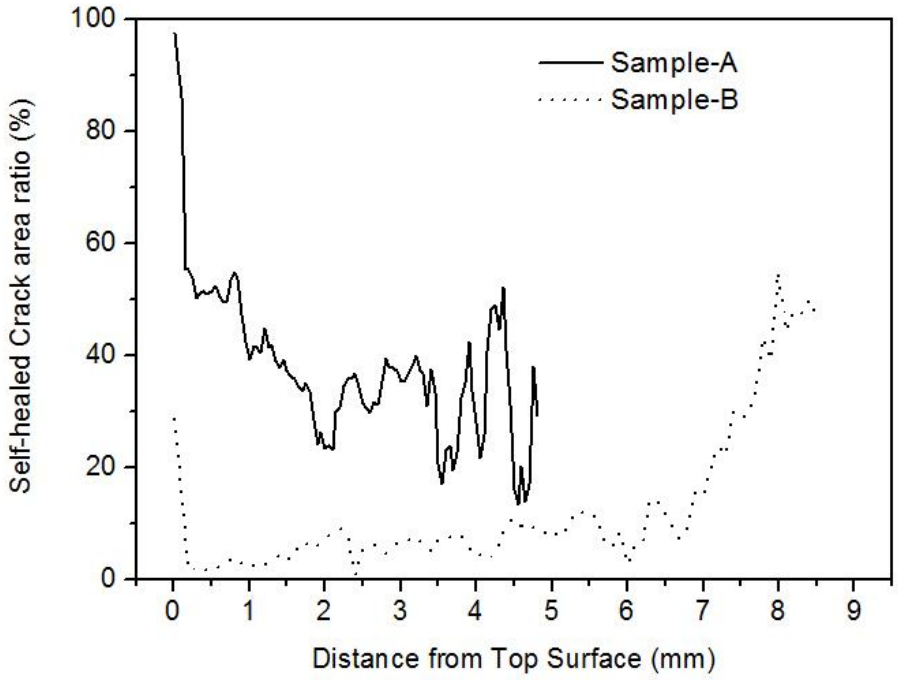

(c) Self-healed crack area ratio (Self-healed crack area / initial crack area before healing)

Figure 2.14 Cracks area change after 5 cycles healing vs. distance from the top surface.

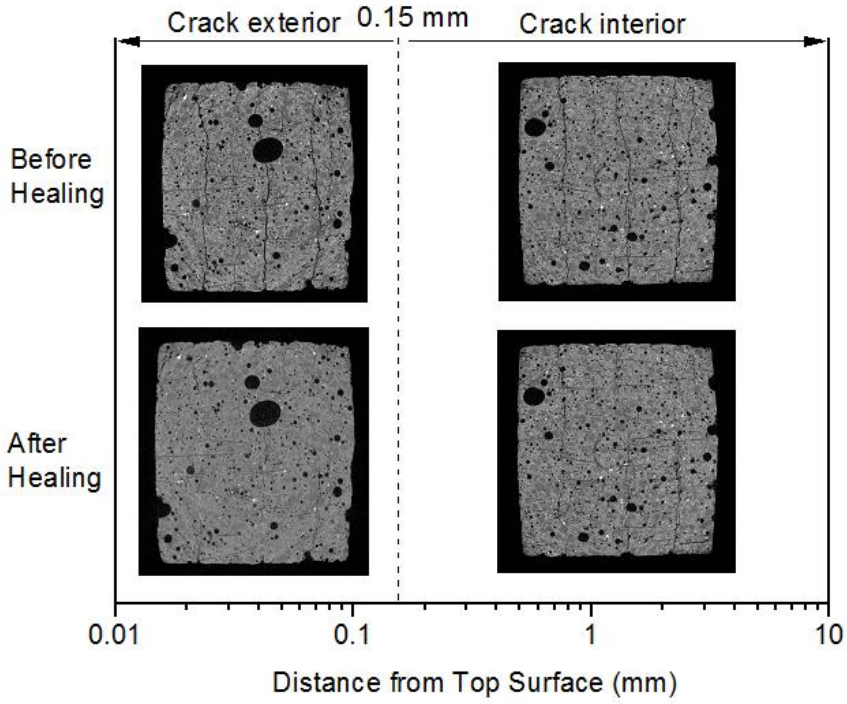

(a) Sample-A

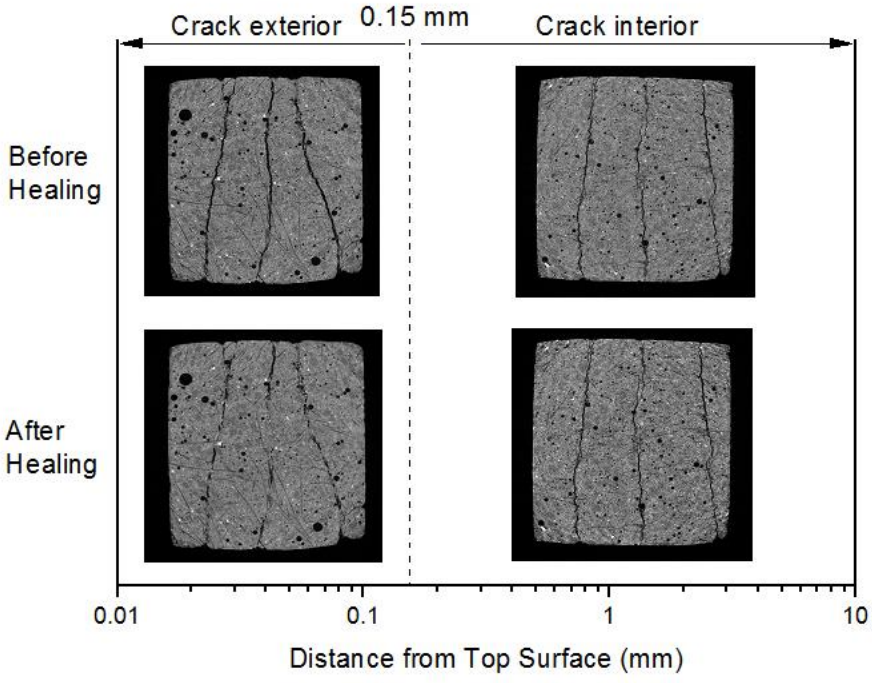

(b) Sample-B

Figure 2.15 Comparison of CT images corresponding to different depth (0.05 mm and 2 mm, respectively).

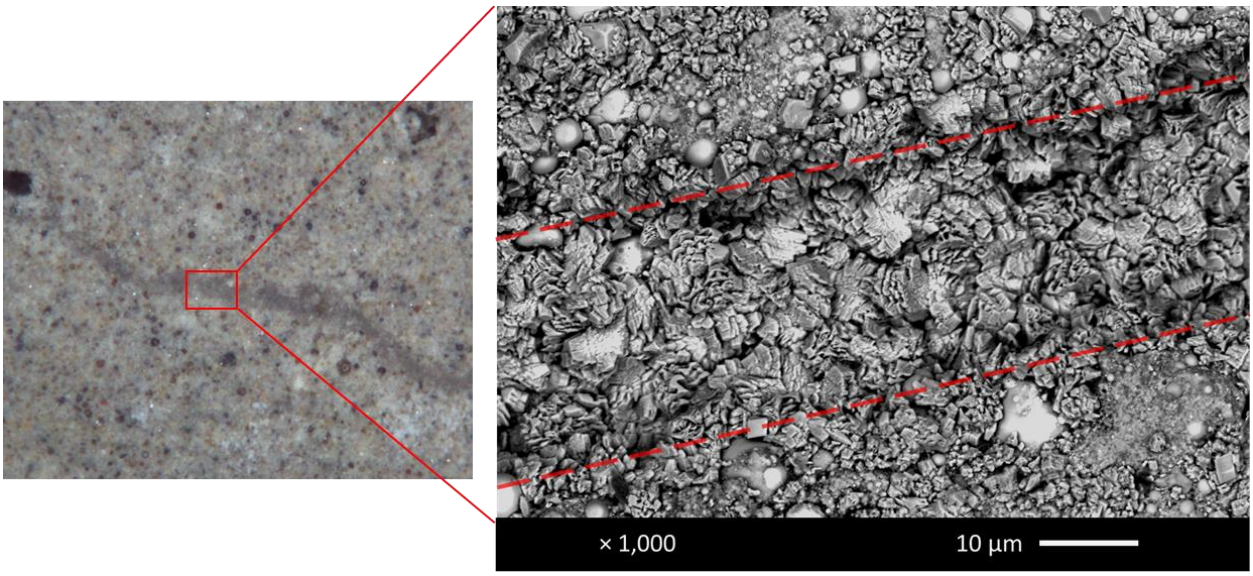

(a) SEM

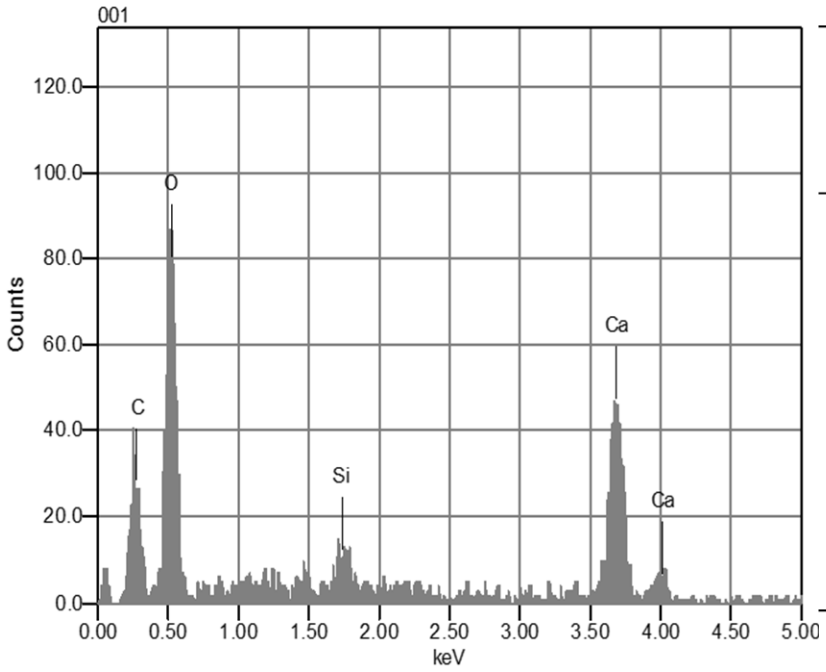

Chemical formula	Mass (%)	
	Avg. of 6 points	Standard Deviation
C	9.56	1.04
O	42.83	2.47
Al	0.61	0.42
Si	1.94	0.32
Ca	45.06	5.45

(b) EDX spectrum and element proportion analysis

Figure 2.16 SEM image and EDX results of self-healing products for crack exterior part.

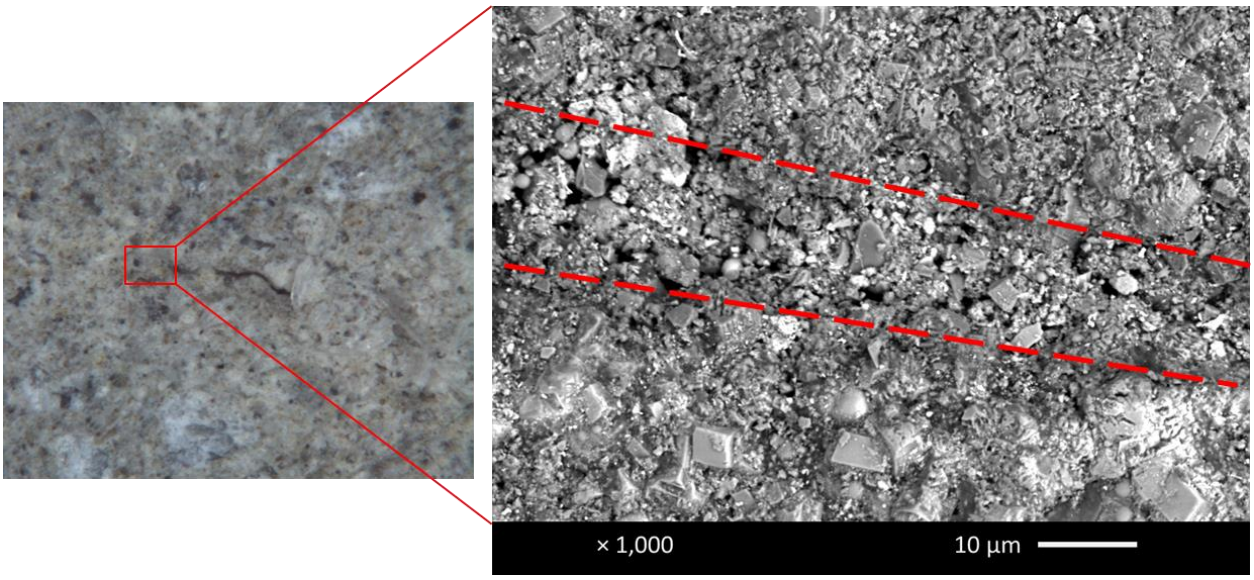

(a) SEM

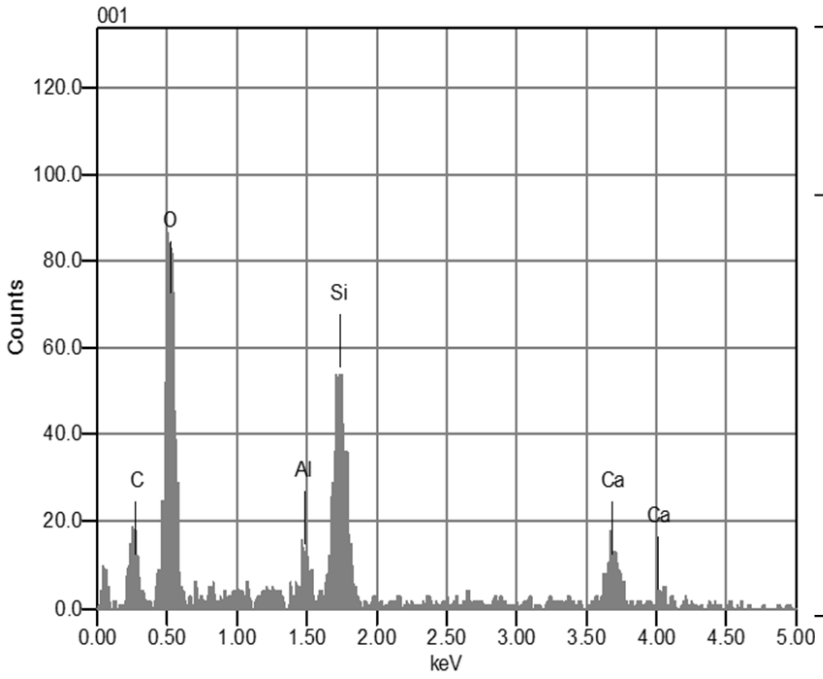

Chemical formula	Mass (%)	
	Avg. of 6 points	Standard Deviation
C	10.67	2.94
O	42.25	4.60
Al	3.89	1.06
Si	12.82	1.50
Ca	30.37	3.87

(b) EDX spectrum and element proportion analysis

Figure 2.17 SEM image and EDX results of self-healing products for crack interior part.

References

[1] Hearn, N. (1998). Self-sealing, autogenous healing and continued hydration: What is the difference?. Materials and Structures, 31(8), 563-567.

[2] Edvardsen, C. (1999). Water permeability and autogenous healing of cracks in concrete. Materials Journal, 96(4), 448-454.

[3] Aldea, C. M., Song, W. J., Popovics, J. S., & Shah, S. P. (2000). Extent of healing of cracked normal strength concrete. Journal of materials in civil engineering, 12(1), 92-96.

[4] Reinhardt, H. W., & Jooss, M. (2003). Permeability and self-healing of cracked concrete as a function of temperature and crack width. Cement and Concrete Research, 33(7), 981-985.

[5] Granger, S., Loukili, A., Pijaudier-Cabot, G., & Chanvillard, G. (2007). Experimental characterization of the self-healing of cracks in an ultra-high performance cementitious material: Mechanical tests and acoustic emission analysis. Cement and Concrete Research, 37(4), 519-527.

[6] Yang, Y., Lepech, M. D., Yang, E. H., & Li, V. C. (2009). Autogenous healing of engineered cementitious composites under wet–dry cycles. Cement and Concrete Research, 39(5), 382-390.

[7] Kan, L. L., Shi, H. S., Sakulich, A. R., & Li, V. C. (2010). Self-Healing Characterization of Engineered Cementitious Composite Materials. ACI Materials journal, 107(6).

[8] Jacobsen, S., Marchand, J., & Boisvert, L. (1996). Effect of cracking and healing on chloride transport in OPC concrete. Cement and Concrete Research, 26(6), 869-881.

[9] Jacobsen, S., & Sellevold, E. J. (1996). Self healing of high strength concrete after deterioration by freeze/thaw. Cement and Concrete Research, 26(1), 55-62.

[10] Li, M., & Li, V. C. (2011). Cracking and Healing of Engineered Cementitious Composites under Chloride Environment. ACI Materials Journal, 108(3).

[11] Herbert, E. N., & Li, V. C. (2013). Self-healing of microcracks in engineered cementitious composites (ECC) under a natural environment. Materials, 6(7), 2831-2845.

[12] Hannant, D. J., & Keer, J. G. (1983). Autogenous healing of thin cement based sheets. Cement and Concrete Research, 13(3), 357-365.

[13] Mangat, P. S., & Gurusamy, K. (1987). Permissible crack widths in steel fibre reinforced marine concrete. Materials and structures, 20(5), 338-347.

[14] Gray, R. J. (1984). Autogenous healing of fibre/matrix interfacial bond in fibre-reinforced mortar. Cement and Concrete Research, 14(3), 315-317.

[15] Homma, D., Mihashi, H., & Nishiwaki, T. (2009). Self-healing capability of fibre reinforced cementitious composites. Journal of Advanced Concrete Technology, 7(2), 217-228.

[16] Qian, S. Z., Zhou, J., & Schlangen, E. (2010). Influence of curing condition and precracking time on the self-healing behavior of engineered cementitious composites. Cement and concrete composites, 32(9), 686-693.

[17] Sahmaran, M., Yildirim, G., & Erdem, T. K. (2013). Self-healing capability of cementitious composites incorporating different supplementary cementitious materials. Cement and Concrete Composites, 35(1), 89-101.

[18] Snoeck, D., Van Tittelboom, K., Steuperaert, S., Dubruel, P., & De Belie, N. (2014). Self-healing cementitious materials by the combination of microfibres and superabsorbent polymers. Journal of Intelligent Material Systems and Structures, 25(1), 13-24.

[19] Huang, H., Ye, G., & Damidot, D. (2014). Effect of blast furnace slag on self-healing of microcracks in cementitious materials. Cement and concrete research, 60, 68-82.
[20] Landis, E. N., & Keane, D. T. (2010). X-ray microtomography. Materials characterization, 61(12), 1305-1316.
[21] Bentz, D. P., Mizell, S., Satterfield, S., Devaney, J., George, W., Ketcham, P., ... & Sallee, H. (2002). The visible cement data set. Journal of Research of the National Institute of Standards and Technology, 107(2), 137.
[22] Landis, E., Petrell, A., Lu, S., & Nagy, E. (2000). Examination of pore structure using three dimensional image analysis of microtomographic data. Concrete Sci. Eng., 2(8).
[23] Lu, S., Landis, E. N., & Keane, D. T. (2006). X-ray microtomographic studies of pore structure and permeability in Portland cement concrete. Materials and Structures, 39(6), 611-620.
[24] Gallucci, E., Scrivener, K., Groso, A., Stampanoni, M., & Margaritondo, G. (2007). 3D experimental investigation of the microstructure of cement pastes using synchrotron X-ray microtomography (μCT). Cement and Concrete Research, 37(3), 360-368.
[25] Zhang, M., He, Y., Ye, G., Lange, D. A., & van Breugel, K. (2012). Computational investigation on mass diffusivity in Portland cement paste based on X-ray computed microtomography (μCT) image. Construction and Building Materials, 27(1), 472-481.
[26] Fukuda, D., Nara, Y., Kobayashi, Y., Maruyama, M., Koketsu, M., Hayashi, D., ... & Kaneko, K. (2012). Investigation of self-sealing in high-strength and ultra-low-permeability concrete in water using micro-focus X-ray CT. Cement and Concrete Research, 42(11), 1494-1500.
[27] Flannery, B. P., Deckman, H. W., Roberge, W. G., & d'Amico, K. L. (1987). Three-dimensional X-ray microtomography. Science, 237(4821), 1439-1444.
[28] Brooks, R. A. (1977). A quantitative theory of the Hounsfield unit and its application to dual energy scanning. Journal of computer assisted tomography, 1(4), 487-493.
[29] Landis, E. N. (2013). Emerging imaging techniques applied to concrete durability. In Proceedings of the FraMCoS-8/30GEF Workshop.
[30] Chang, S. G., Yu, B., & Vetterli, M. (2000). Adaptive wavelet thresholding for image denoising and compression. IEEE transactions on image processing, 9(9), 1532-1546.
[31] Bentz, D. P., Martys, N. S., Stutzman, P., Levenson, M. S., Garboczi, E. J., Dunsmuir, J., & Schwartz, L. M. (1994). X-ray microtomography of an ASTM C109 mortar exposed to sulfate attack. MRS Online Proceedings Library Archive, 370.
[32] Feldkamp, L. A., Davis, L. C., & Kress, J. W. (1984). Practical cone-beam algorithm. JOSA A, 1(6), 612-619.
[33] Otsu, N. (1979). A threshold selection method from gray-level histograms. IEEE transactions on systems, man, and cybernetics, 9(1), 62-66.
[34] Liao, P. S., Chen, T. S., & Chung, P. C. (2001). A fast algorithm for multilevel thresholding. J. Inf. Sci. Eng., 17(5), 713-727.
[35] Şahmaran, M., Özbay, E., Yücel, H. E., Lachemi, M., & Li, V. C. (2011). Effect of fly ash and PVA fiber on microstructural damage and residual properties of engineered cementitious composites exposed to high temperatures. Journal of Materials in Civil Engineering, 23(12), 1735-1745.
[36] Serra, J. (1982). Image analysis and mathematical morphology, v. 1. Academic press.
[37] Mathematical Morphology: From Theory to Applications, Laurent Najman and Hugues Talbot (Eds). ISTE-Wiley. ISBN 978-1-84821-215-2, 2010.

[38] Lumia, R. (1983). A new three-dimensional connected components algorithm. Computer Vision, Graphics, and Image Processing, 23(2), 207-217.
[39] Ohser, J., Redenbach, C., & Schladitz, K. (2011). Mesh free estimation of the structure model index. Image Analysis & Stereology, 28(3), 179-185.
[40] Hildebrand, T. O. R., & RÜEGSEGGER, P. (1997). Quantification of bone microarchitecture with the structure model index. Computer Methods in Biomechanics and Bio Medical Engineering, 1(1), 15-23.

CHAPTER 3 EXPERIMENTAL STUDY OF THE QUANTITIES AND QUALITIES OF INTRINSIC SELF-HEALING IN CEMENTITIOUS MATERIALS

3.1 Introduction

The intrinsic self-healing, also termed autogenous healing, of small crack is a ubiquitous feature in cementitious materials when they are exposed to water. Water-concrete interactions within cracks can lead to dissolution and precipitation at crack surfaces and local alteration of crack apertures, potentially modifying the transport and mechanical properties of fractured concrete. Quantifying the mechanisms that control self-healing in cementitious cracks, the focus of the present study, is fundamental to the understanding of the intrinsic self-healing process in concrete. However, the water-concrete interactions taking placing in cracks are extremely complex. It is a combination of physio-chemical process involving a series steps such as fluid diffusion or advection, mineral dissolution and precipitation, and additional hydration.

Developing a quantitative understanding of how different chemical, physical, and environmental parameters influence mineral precipitation and crack evolution requires detailed experiment investigation. Despite numerous investigations about autogenous healing in cement based materials [1], most experimental studies have tended to emphasize the healing results, such as by verifying the transport and mechanical properties recovery at composite level, rather than the exploration about the physico-chemical driving forces behind the healing phenomenal. Several studies dedicated in healing mechanism have shown a range of behaviors due to differences in experimental conditions, which poses challenges for interpreting the relative influence of different parameters. Moreover, these studies were mostly based on scanning

electron microscopy or chemical analysis from top surface of the sample, very few quantitative diagnoses of the microstructural information inside a singular 3D crack can be found [2][4]. Aside from the understanding of the healing mechanisms in Portland cement, the addition of replacement materials of industrial by-products, like silica fume (SF), fly ash (FA), and ground granulated blast-furnace slag (GGBS), brings additional complexity to the kinetics of healing process. Although there are some publications considering the self-healing ability of fly ash or slag-cement systems at the composite material level in terms of the recoveries of mechanical and transport properties [5][12], no study has directly probe the healing extent within a three-dimensional crack, and gain insight into the morphology and mineralogy of the healing products in the blended cementitious system.

Based on the characterization methods established in last chapter, the present study aims to elucidate the fundamental healing mechanism within a three-dimensional cementitious crack. X-ray computed microtomography (μCT) was applied to accurately probe the entire crack volume evolution. Scanning electron microscopy (SEM), energy dispersive spectroscopy (EDS), and Raman spectroscopy were used to characterize the morphology and minerology of the healing products. In parallel, the effect of supplementary cementitious materials (SCMs), such as silica fume, fly ash, and ground granulated blast-furnace slag on the physico-chemical process of autogenous healing in blended cementitious systems were also investigated.

3.2 Experimental Program

3.2.1 Materials and Sample Preparation

Pure cement paste samples were prepared with three different variables: (1) crack width, (2) crack geometry (i.e. tension-induced flat crack or bending-induced crack), (3) material age

(i.e. 7 days or 90 days). **Table 3.1** shows the experimental matrix of neat cement paste samples. For the cement composites blended with supplementary materials, three mineral additives were investigated: Class F fly ash (FA), ground granulated blast-furnace slag (GGBS), and silica fume (SF). The blended cement mixes contained 0%, 25%, 50%, and 75% of pozzolanic additives to replace cement by weight were prepared to study the influence of replacement dosage on the autogenous healing mechanism. Each mix is labeled according to its replacement ratio and is listed in **Table 3.2**. The chemical compositions of cement and pozzolanic materials are given in **Table 3.3**. The neat and blended pastes were prepared at a fixed water to solids ratio (by weight) of 0.4.

The cementitious ingredients and their hydration products together formed the matrix, while a small amount of polyvinyl alcohol (PVA) fibers (volume fraction of 2.0%) were incorporated into the matrix to control the cracking behavior, leading to a strain-hardening composites with distributed crack widths from micro to millimeter. The fresh mixture was cast into a series of coupon specimens with dimensions of 152×50×12.5 mm. The specimens were covered with plastic sheets and cured in laboratory air with a temperature of 20±1°C and relative humidity of 45%±5 until the age of demold. The demolded specimens were thoroughly cured in water until the age of 7 days or 90 days for mechanical loading to induce cracks. The coupon specimens were loaded using a servo-hydraulic testing system with a 25 kN load cell with a fixed cross head displacement rate of 0.001 mm/s to simulate a quasi-static lading condition. A number of microcracks with width ranging from 20 to 300μm were induced in the specimens, as shown in **Figure 3.1**. The crack widths were measured from the specimen surface using a polarizing digital microscope with 5.0-megapixel resolution and 180×magnification. Afterwards,

~4×4×4mm cubic samples containing multiple cracks were carefully sawed off from coupon specimens for μCT scan and other chemical examination.

3.2.2 Environmental Treatment

Two types of environmental exposure conditions were considered in this study: naturally wet/dry cycles and controlled advective fluid saturated with $CaCO_3$, as shown in **Table 3.1**. For the first condition, the samples were exposed to water-dry cycles to allow potential self-healing to occur, as shown in **Figure 3.2**. For each cycle, the samples were firstly submersed into water at 20°C for 24h, and then naturally dried in ambient air at 20±1°C and 45%±5 RH for 24h to simulate the rain/dry outdoor environments.

The mineral resource (e.g. Ca^{2+}, CO_3^{2-}) for autogenous healing in natural environment are mostly supplied by the dissolve of carbon dioxide in water, and the leaching of concrete matrix. However, the rate and extent of these reactions are usually too low to produce significant grains to study the details of microstructural evolution at laboratory timescales. Also, it is very difficult to quantitively control the initial dissolving condition in the solution. Therefore, in this study, we designed analogue experiments by using advective fluid saturated with $CaCO_3$ through the natural concrete crack. The supersaturated fluid can provide constant and controllable chemical supplies, resulting in significant precipitation over relatively short timescales.

Figure 3.3 shows the experimental setup. The cube-size cementitious sample containing a crack was placed into a cylindrical tube with an inner diameter of 6 mm, and sealed with removeable and waterproof sealant so that the flow only passes through the crack. Deionized water saturated with Ca^{2+} and CO_3^{2-} ions was slowly injected into the reaction tube by a syringe pump at 50 μl/h, which corresponds to an initial flow velocity of about 1 μm/s. This simulates the condition that Ca^{2+} ion has dissolved and leached out from cementitious matrix, and a small

fraction of the dissolved CO_2 has converted to carbonate anions. The relative supersaturation index, denoted as *SI*, is calculated as:

$$SI = \log_{10}\left(\frac{\{Ca^{2+}\}\{CO_3^{2-}\}}{K_{sp}}\right) \quad (3.1)$$

where $\{Ca^{2+}\}\{CO_3^{2-}\}$ is the ion activity product, K_{sp} is the thermodynamic solubility product, which is 3.16×10^{-9} for $CaCO_3$ at 25 °C [13]. The supersaturation conditions, $SI = 1.2$, was adopted to simulate the natural concentration of ions in the interstitial liquid containing leached calcium and dissolved carbon dioxide. The solution was prepared by mixing calcium chloride solution ($CaCl_2$) (10 mM) with sodium bicarbonate solution ($NaHCO_3$) (1 mM). After mixing, the solution was brought to a pH of 10, which represents the typical pH value for concrete leachates [14], through the controlled addition of potassium hydroxide solution (KOH). This designed reactive transport-healing experiment enables the accurate control of flow flux by adjusting pumping rate at crack inlet, and the ion supersaturation condition in the flow by adjusting the initial concentration of reagents. Such well-controlled experimental conditions are crucial for understanding the effects of controlled parameters.

3.2.3 μCT

The crack profile evolution was measured by X-ray microtomography (μCT) before and after self-healing. The μCT method addresses the challenges faced by other indirect methods by directly measuring the three-dimensional microstructure of a crack and quantifying crack apertures and self-healing extents along crack depth. The details of μCT technique and image processing method to quantify crack self-healing in cementitious materials were reported in chapter 1. In this study, the Micro-CT facility used was SkyScan 1173 system, which consisted of a 130 kV x-ray source with improved stability of focal spot position for large and dense

objects, and a distortion-free flat panel detector with maximum 4000 × 2648 resolution. For each scanning process, the cementitious sample was fixed on an embedded micro-positioning stage, and scanned in air with 80kV tube voltage and 125 μA tube current. After raw data collection, a set of gray-scale two-dimensional cross-sectional images that map the density variation within the cementitious samples were constructed. A total of 2000 slices of images were collected while the sample was rotated with an angle step of 0.3º. Each image represents a slice with 2 μm thickness and 2000 × 2000 resolution. These two-dimensional images (**Figure 3.4(a)**) were then mathematically re-constructed to create the three-dimensional mapping of the interior structure of the cementitious sample (**Figure 3.4(b)**). The voxel size of the reconstructed three-dimensional rendering was 2μm × 2μm × 2μm.

A global thresholding method was used to convert the grey-scale images to binary images. The Otsu's method was applied to calculate the threshold intensity values to separate the gas phase from the solid phase, and to further divide the solid phase to separate unhydrated particles from the hydrates and aggregates. The threshold intensity values were applied to all the pixels of the gray-scale images to isolate the phase of interest from other phases. To further isolate the cracks from the air pore network, a mathematically morphological method was employed. This method uses topological parameters, volume and structure model index, to recognize if a cluster of air phase is a crack or a pore. The reconstructed 3D renderings of different phases are shown in **Figure 3.4(c)**.

3.2.4 Scanning Electron Microscopy (SEM) with Energy Dispersive X-ray Spectroscopy (EDS)

SEM and EDS were performed to characterize the morphology and chemical composition of self-healing products within the shallow (Z = 0 mm) and deep (Z = 2mm) region of the crack.

After the healing experiments and micro-CT scanning, the cementitious samples were carefully cut and cleaned in ultrasonic bath for 1 minute, then dried in vacuum chamber to remove the vapor inside the pore space. The sample surfaces were coated with a layer gold under vacuum to increase conductivity. SEM (FEI Quanta Dual Beam) was performed on the samples under low vacuum condition at 10 kV voltage and probe current of 180 pA using back-scattered electron signal. EDS (INCA, Oxford Instruments) mapping was performed to analyze five elements (C, O, Al, Si, Ca) for a total of 500 data points (50×10 rectangular area, 1μm increments). The atomic ratios were used for quantitative analysis of the chemical composition of self-healing products.

3.2.5 Raman Spectroscopy

To identify and quantify the mineral structures of the reaction products in cracks, Raman spectroscopy analysis was conducted in this study. In comparison to other vibrational spectroscopy methods, such as FT-IR and NIR, Raman has several major advantages. For example, it is non-destructive and requires little to no sample preparation, which can help us continuously monitor the evolution of healing reaction. Also because the intensity of a Raman band is directly proportional to the number of molecules giving rise to the band, then the Raman band can be used to provide a measure of the concentration of a molecule for quantitative analysis. Raman scattering spectra of the samples were acquired under the following steps and parameters: a continuous-wave titanium sapphire laser (Spectra-Physics 3900S) provides an output laser beam of 785nm which is filtered by a laser-line filter (Semrock LL01-785-12.5). The output is then fed through the back port of an inverted microscope (Olympus IX71). A dichroic mirror (Semrock LPD01-785RU-25) is placed in the microscope turret for epi-Raman acquisition via a microscope objective (Olympus UPLSAPO 60XW). The Raman light is redirected out via

the microscope side port, filtered by a long-wave pass filter (Semrock LP02-785RS-25), and sent into a spectrograph (Acton SpectroPro 300i) with a thermal-electrically cooled CCD camera (Princeton Instruments 400BR-excelon). The spectral resolution of the system is ~8cm^{-1} by comparing spectra taken by this system and a calibrated confocal Raman system, respectively.

During the test, the laser spot was about 1 μm^2, and the measured power at the sample was kept less than 10 mW in order to avoid any damage to the material. Several spectra were recorded at different points for the same sample in order to evaluate the homogeneity and reproducibility of the main spectral features. After the raw data acquisition, a series of software packages, such as SpecTools and MatLab were utilized for post-processing of the spectrum, including spike removal, smoothing/denoising, background correlation, baseline normalization, and spectral calibration.

3.3 Results and Discussion

3.3.1 The Crack Depth Dependent Autogenous Healing Mechanism

In order to verify the in-depth self-healing in cement paste, the visualized 3D CT images of cracks evolution during self-healing process is shown in **Figure 3.5** with a 30% opacity. **Figure 3.5(a)** shows the rendering images of the original crack before any healing treatment. The lighter color regions represent the cracks, while the background voxels with darker color are the cement paste matrix. It can be seen that, after 3 cycles water/dry exposure, only few part of the cracks turned darker (**Figure 3.5(b)**), where the healing products should fully bridge the crack. Based on the quantitative analysis of the μCT slides, **Figure 3.6** provides the calculated crack healing ratio vs. the distance from the top surface after different cycles healing. The self-healing ratio η in this study is defined by:

$$\eta = \frac{\text{Crack volume change}}{\text{Initial crack volume}} \tag{3.2}$$

The first important finding was that the self-healing extent had a sufficient difference between the crack region close to the top surface and the crack region deeper inside the samples. After 3 cycles, about 70% of the crack area at the crack shallow region had already been closed, that was significantly higher than the deep region where healing ratio was only about 10% (**Figure 3.7**). The thickness for this quickly sealed region was around 50~200 μm.

After 14 cycles, more voxels of the original crack turned into black color (**Figure 3.5(c)**), which proved that there were new healing products continuously precipitated inside the crack, leading to the crack roughly appeared as a net-like structure. However, the non-homogeneity of healing extent through-depth were yet obvious. As shown in **Figure 3.7**, the healing ratio at the deep region increased from around 8% after 3 cycles to 23% after 14 cycles. Meanwhile, at the shallow region the healing ratio was almost constant about 70 %, but still much greater than the total crack healing extent. The results strongly indicate a change in the self-healing mechanisms along the crack deep direction. It further suggested that characterizing self-healing only from the surface is not sufficient to evaluate or verify the true healing condition of the entire crack within a cementitious material. The healing ratio calculated by surface observation may result in a considerable overestimation of the real healing behavior.

The comparison between the initial and final aperture field reveals the three-dimensional self-healing extent of the crack. A pervasive self-healing along the crack walls and reduction in crack apertures were observed, but the extent of self-healing was larger near to the crack inlet than deep inside the crack. This nonhomogeneous healing phenomenon suggests varying precipitation of healing products along crack depth. As the ion-containing flow (e.g. Ca^{2+} and

CO_3^{2-}) travels through the crack, the continued precipitation process leads to a decline in the flow supersaturation and the associated growth rate along the crack depth. This progressive depletion of solute in the moving fluid causes the crack to evolve towards nonhomogeneous healing, faster at crack shallower region and slower at deeper region. The quick sealing of crack shallow region further reduces the local transport properties, making it more difficult for the ions to transport to the crack deeper region, enhancing the nonhomogeneous healing along crack depth. This negative feedback between mineral precipitation and local alteration of transport properties is a crucial mechanism of intrinsic self-healing in cementitious materials.

SEM, EDS, and Raman Spectroscopy were conducted to further investigate the morphology and mineralogy of healing products within the crack shallow and deep regions, as respectively shown in **Figure 3.8** and **Figure 3.9**. **Figure 3.8(a)** exhibits the SEM image taken from the top surface of a microcrack. It can be seen that irregular crystals had greatly filled up the crack shallow region after only 3 cycles. EDS results showed that the chemical composition of these crystals had three dominating ingredients (**Figure 3.8(b)**): carbon, oxygen, and calcium, which suggests that the precipitates are primarily calcium carbonate. The Raman spectroscopy (**Figure 3.8(c)**) gave more information on the mineralogy of the reaction products. For the spectra of healing products at shallow region, the most significant peak was a broad band in the range of 1050~1100 cm-1, which is attributed to a ν_1 [CO_3^{2-}] mode. Such particular compound is characteristic of calcium carbonate hydrate **[15]**. Another weak band in the spectrum was at ~720 cm-1, which also represents the carbonate phase and could be assigned to the ν_4 [CO_3^{2-}] mode **[16]**. This result confirms that amorphous calcium carbonate ($CaCO_3 \cdot xH_2O$) were the main healing productions at crack shallow region.

The SEM image of crack deep region, after 14 cycles of healing, is shown in **Figure 3.9(a)** by carefully cutting the sample. It is clearly seen that the composition of healing products in this area was more completed. Besides large calcium carbonate crystals, tapered needle-liked and flake or foil-liked structures were found as well. The EDS results (**Figure 3.9(b)**) revealed that more silicon and aluminum elements were present, indicating the possibility of formation of calcium silicate hydrate, calcium aluminate hydrate as well as ettringite. In order to further verify this assumption, Raman spectroscopy was performed to identify the molecule structures of healing products at crack deep region. **Figure 3.9(c)** shows the spectra recorded from the cross section immediately after cut and exposure to the atmosphere. By comparing with **Figure 3.8(c)**, the bands corresponding to carbonate were still obvious. However, other major peaks were also apparent, such as the symmetrical bending (SB) band of Si-O-Si near 600~700 cm^{-1} and the internal deformations of Si-O band at 450 cm^{-1}, both of which were relative to C-S-H. In addition, two peaks attributed to Ca-O lattice vibration at 325 cm^{-1} assigned for C-S-H and at 350 cm^{-1} assigned for portlandite [17] can be observed as well. Moreover, there was also a clear band at about 985 cm^{-1} in the spectra which is attributed to the ν_1 [SO_4^{2-}] in sulfate phase such as ettringite (AFt) and monosulfate (AFm) [18]. Based on the chemical analysis above, it is found that the healing products formed at the crack shallow region is dominated by the calcium carbonate hydrate. These crystalline precipitates mostly occur at the sample surface area, once formed, quickly seal the crack and isolate the crack deep region from the surroundings environment. It thus became difficult for carbon dioxide to transport through the sealed area and reach the interior region of the crack. As a result, the continued hydration, leaching and recrystallization of portlandite and ettringite became another resource for healing reaction at

crack deep region. But both the rate and extent of these reactions are very limited compared with the carbonation at sample surface.

EDS mapping for a total of 467 compositions within the cement paste, 489 compositions from the healing products of crack shallow region, and 466 compositions of crack deep region are plotted as atomic percentages in the Al/Ca against Si/Al diagram in **Figure 3.10**. Besides silicon and calcium, aluminum is considered here because it greatly exits in the AFt and AFm. In addition, it is generally considered the most significant substituent of silicon in CSH phases. For neat cement paste (**Figure 3.10(a)**), bulk of the data points closed to one cluster dominated by CSH or CS(A)H with average Si/Ca ratio about 0.6 and Al/Ca ratio about 0.08. Others were scattered in two general directions. The first connected the composition of CSH to that of portlandite or calcium carbonate, marked as CH and CC. The second general direction was towards the composition of two sulfate-containing phases, ettringite (AFt) and monosulfate (AFm). **Figure 3.10(b)** shows the compositional data for healing products at crack shallow region. the bulk of the data points aggregated close to one corner, which confirms that the main component of the healing products at crack shallow region are $CaCO_3$. **Figure 3.10(c)** provides the distribution of mapping data for healing products in deep region. Besides the main group close to the CC(CH) vertex, large amount of analyses was located near the CSH phase region and aluminum sulfate phases region. It can be seen that the fraction of AFt and AFm in healing products inside the crack was much larger than that in the bulk cement paste, indicating that there might be more sulfate phase precipitated. But It should be mentioned that these ingredients in the bulk paste are mostly surrounded by CSH, while those formed in cracks as healing products might not be finely intermixed. Thus, it is easier for EDS to detect them separately in crack than in the paste. From Figure 8, it can be also noticed that for the C-S(A)-H phase, the

Si/Ca ratio in healing products was much lower than that in cement paste, while the Al/Ca ratio in healing products was slightly higher. For cement paste, the Si/Ca ratio of CSH phase ranged from ~0.4 to ~0.8 with a mean value of ~0.6. This ratio range had a noticeable shift to left (between ~0.3 to ~0.6 with a mean of ~0.45) for the CSH formed in healing products. Regarding the Al uptake in CSH, the peak value of Al/Ca ratio for healing products was about 0.1~0.12, which was generally higher than that for cement paste around 0.06~0.08.

Figure 3.11 illustrates the Si/Ca and Al/Ca atom ratio frequency histograms incorporating individual EDS microanalyses to quantify the differences between cement paste and healing products. For cement paste, the Si/Ca ratio of C-S-H phase ranged from ~0.42 to ~0.79 with a mean value of ~0.61. This ratio range had a noticeable shift to left (between ~0.3 to ~0.64 with a mean of ~0.44) for the C-S-H formed in healing products. Regarding the Al uptake in C-S-H (Figure 9(b)), it is notable that the peak value of Al/Ca ratio for healing products was about 0.1~0.12, which was generally higher than that for cement paste around 0.6~0.8. These differences indicate that the chemical composition and microstructures of newly formed C-S-H in crack are different from the original hydration products. In the crack system, once there is water, ions, such as Ca^{2+}, OH^{-}, SO_4^{2-}, $SiO_2(aq)$, Al^{3+}, etc., can diffuse out from bulk paste. The exchange of ions takes place and when the concentrations reach saturation condition, healing products are able to deposit in the crack. According to cement chemistry **[19]**, the diffusion coefficient of Si is smaller than the Ca and Al, therefore, the amount of Si in the crack solution system might be relatively lower than Ca and Al ions, resulting in the C-S-H formed in the crack has a lower Ca/Si ratio and contains more Al.

3.3.2 The Influence of Crack Width and Geometry

The influence of crack width on the autogenous healing extent was investigated under natural environmental condition and controlled reactive flow. For natural wet/dry cycles, 12 samples containing total of 29 cracks with different crack widths ranging from ~10 μm to ~140 μm were scanned using micro CT before and after 3 and 14 cycles of healing. **Figure 3.12(a)** and **(b)**, focusing on crack shallow region, provides the experimental data for healing ratio vs.. crack width. As can be seen, the healing ratio roughly followed a nonlinear decline trend as the crack width increased. Smaller cracks had a larger healing extent, with the presence of same chemical species and equal environmental exposure conditions. **Figure 3.12(c)** and **(d)** present the crack width dependency of the healing ratio at crack deep region after 3 and 14 cycles, respectively. Similar as the shallow region, the total crack healing ratio exhibited a rapid decay. For crack width between 10~20 microns, the average healing ratio was above 20% after 14 cycles. It quickly decreased to about 5% beyond 40 microns and retained only around 2% after 80 microns.

It should be noticed that the healing ratio is determined not only by the amount of healing products, but also the original crack width. In order to compare the absolute healing extent which is directly related to the healing mechanism, the total healing products volume after 14 cycles for each crack was calculated and plotted in **Figure 3.13**. Despite scattering of the data, it still can be interestingly seen that the volume of newly precipitated healing products increased as the crack width became larger. This behavior might be explained by the fact that the sealing of surface region takes longer time for large crack than small crack, which means there are higher chances for a larger amount of reactants to precipitate into the crack deep region. For the smaller crack,

however, the total mass flux through the crack has been significantly limited by the quickly sealed surfaced region.

In order to further prove this hypothesis, reactive flow experiment was conduct to quantitatively control the initial healing environments. **Figure 3.14(a-c)** show the crack profiles before and after healing, and the self-healing ratios of T1, T2 and T3 samples with different initial crack widths. The healing ratios for all of these three samples show similar decreasing trend along crack depth. After 10 days of mineral precipitation, the crack inlet region was almost closed. The healing ratio at sample surface was above 90%. As the solution transports ions through the crack, the precipitation first accumulates near the crack inlet. At the time of crack sealing near surface region, which caused the significant reduction in fracture transmissibility, large portions of the downstream end of the crack remained devoid of precipitated minerals. This result indicated that long-range flux was unable to deliver enough dissolved minerals to uniformly fill the crack before the flow channel had been obstructed. By comparing the healing profiles for different samples with various crack widths (**Figure 3.14(d)**), we can observe that the larger crack showed a greater and more homogenous healing potential, while the healing ratio in smaller crack dropped more rapidly. The cause for this phenomenon can be mainly due to the different fracture sealing time. When all the other conditions are the same and there is sufficient mineral input, seemingly it takes longer time for precipitates to fill up a wider crack, which means there are higher chances for a larger amount of solute to travel into the crack deep region. However, it has to be kept in mind that for concrete structure in nature environment, the precipitated minerals come from the dissolution of concrete material itself, so it is very difficult to maintain the ambient conditions especially the supersaturation condition as our laboratory experiments. Although a larger crack increases the potential to be healed homogenously, it needs

very large fluid volume and time scale to produce enough precipitated materials. Therefore, for the samples N1~12 which exposed to nature water/dry condition, the narrower cracks show higher healing ratio.

Figure 3.15 shows the effects of crack geometry on the healing extent. Sample B2 contains a nearly linear bending crack, which has the similar initial crack volume as the nearly flat tension crack in sample T2. The crack aperture at surface for B2 approximately doubles that of T2. It can be seen that the general trend of the healing profile was still decreasing, but due to the larger crack open mouth, the close of the transportation path for bending crack experienced longer duration, leading to a higher healing ratio at deep region of the crack comparing with the tension crack.

3.3.3 The Influence of Sample Age

Figure 3.16 shows the effects of material age on crack healing profile and healing ratio along crack depth. Sample T1Y has a similar surface crack width as T1, but a younger age (7 days vs. 90 days). Higher healing extents and healing ratios were observed in the younger sample along crack depth. This indicates the continued hydration did contribute to the crack aperture evolution. The younger sample containing higher ratio of unhydrated cement particles shows higher healing potential (**Figure 3.16(b)**). However, even for the 7-day sample with small surface crack width of 48 μm, 80% of the crack deep region remained unhealed after 10 days of environmental treatment. This further proved the hypothesis that the intrinsic healing potential under the crack surface is limited by the accessibility to fluid containing dissolved ions. In addition, it suggests that the hydration product growth outside of the original reacting clinkers is very limited. For old sample, especially with larger crack width, the contribution of continued hydration to the crack volume change is negligible.

3.3.4 The Influence of Supplementary Cementitious Materials (SCMs)

The use of supplementary cementitious materials (SCMs), such as silica fume, fly ash, or blast furnace slag, represents a viable solution to partially substitute Portland cement. The chemistry of SCMs is generally characterized by lower calcium content but richer silica than ordinary cement, leading to a more complex system where the hydration of cement and pozzolanic reaction of the SCMs occur simultaneously and may also influence the reactively of each other. Numerous researchers have shown that SCMs have a significant impact on the cement reaction and formed hydrates [20][23]. It is well established, that the composition of C–S–H and portlandite in systems containing silica-rich SCMs is significantly different to that in pure cements. Qualitatively, the incorporation of silica fume will lead to a decrease of the amount of portlandite and the formation of more C–S–H with a lower C/S ratio. Similarly, blending of PC with fly ash will decrease the amount of portlandite, increase the amount of C–S–H with a lower Ca/Si and the amount of AFm phases as fly ash can contain high quantities of Al_2O_3. Blending with blast furnace slag has little effect on the amount of portlandite with respect to clinker, until high level of substitution. However, more C–S–H with a lower Ca/Si will be formed to accommodate the lower overall Ca/Si ratio of the system. All of these differences may alternatively have an impact on the self-healing kinetics in the blended systems. In addition, the pozzolanic reaction of SCMs is relatively slower than cement clinkers, there could be a larger amount of unreacted chemical species available for continued reaction, thus influencing the self-healing behavior in long term. To determine the physical and chemical effect of SCMs on self-healing in blended cement pastes, the self-healing extent as a function of healing time and SCMs replacement ratio was quantitatively investigated by means of μCT; the chemical composition of healing products was examined by EDS mapping.

SCMs-cement blended samples with several microcracks (Avg. cw=31μm) were scanned using micro CT before and after self-healing treatment. According to the CT result, **Figure 3.17** presents the depth depended healing ratio change in samples containing 50% cement and 50% SCMs. Similar as pure cement paste, the healing extent for fly ash and slag mixed systems (**Figure 3.17(a) and (b)**, respectively) still can be roughly divided into two parts: the shallow region with greater healing ratio and deep region with lower healing ratio. But it should be noticed that this difference in the silica fume-cement blends (**Figure 3.17(c)**) was no longer obvious. **Figure 3.18(a)** shows the evolution of healing ratio at crack shallow region as a function of healing time. Comparing with pure cement paste, the replacement of silica fume caused the most significant reduction in the healing ratio from ~70% to ~30%, followed by fly ash to ~50%. Slag had the least effect on healing ratio at shallow region, only about 5% decrease was observed. Based on the discussion from previous section, the healing mechanism at crack shallow region can be mainly attributed to the calcium leaching, re-deposition and carbonation. Because the silica fume and fly ash are rich of Si but containing no or very litter Ca, and the presence of these SCMs can consume large amount of portlandite during hydration and secondary reaction, all of which will result in less dissolved OH^- and Ca^{2+} available in the crack system. The low pH condition makes the transformation of carbonic acid to carbonate ions become more difficult. Therefore, the ion activity $\{Ca^{2+}\}\{CO_3^{2-}\}$ corresponding to carbonation reaction to form large calcite crystal in the cement/silica fume or fly ash composites is lower than the pure cement system. Slag contains more CaO than fly ash and silica fume (**Table 3.3**), thus provided similar healing extent as pure cement sample at crack shallow region.

Figure 3.18(b) gives the healing ratio evolution at crack deep region. After 28 cycles of healing, pastes containing silica fume had a lower healing ratio than pure cement pastes, while

the fly ash and slag systems showed an enhanced healing extent. It is also noted that, for pure cement and silica fume-cement mixed pastes, the healing ratio increased rapidly in the first 7 cycles and flattened after 14 cycles. For the binary mixes with 50% fly ash or 50% slag, although the healing extent was much lower than pure cement pastes at early healing age (before 7 cycles), it kept increasing through all the healing cycles. This result indicates, in the presence of moderate amounts of fly ash or slag, the pozzolanic reactions could contribute to the self-healing at long term. Since the reactivity of fly ash or slag is slower than cement clinkers, there will be a large amount of unreacted fly ash or slag available on the crack surfaces, but it usually takes longer time to further react and release the healing potential.

Figure 3.19 shows the effect of SCMs type and replacement ratio on the healing extent. For the crack shallow region (**Figure 3.19(a)**), generally as the SCMs replacement level increases, the healing extent drops in a roughly liner way. For the deep region (**Figure 3.19(b)**), The healing extent increases with moderate slag replacement ratio, but then starts to decline after 50%. Similar trend is observed for in pastes containing fly ash. But this upward trend is not observed in pastes containing any amount of silica fume.

The chemical compositional data for healing products in three different types of SCMs-cement systems with 50% replacement ratio have been determined from EDS mapping and are shown in **Figure 3.20(a-c)**. The large set of data can illustrate the extent of compositional variation possible for healing products present deep inside the crack. In order to facilitate comparison, a graphic representation of the C-S-H formed in the healing products of different systems is shown in **Figure 3.20(d)**. Based on the EDS mapping data, **Figure 3.21(a)** and **(b)** illustrate the frequency distributions for Si/Ca and Al/Ca ratios from different blends, respectively. For fly ash-cement blends, the C-S-H cluster can be clearly observed. Besides the

C-S-H phase, there are still significant number of analyses distributed towards to the AFt and AFm phases in a quite scattering way. By the comparison with healing products in pure cement paste, qualitatively it can be seen that the blending of cement with fly ash leads to a decrease of the amount of portlandite and calcite, and the formation of more C-S-H with higher Si/Ca and Al/Ca ratios. This could be interpreted as being due to the significant amount of SiO_2 and Al_2O_3 phases in fly ash, which could greatly facilitate the release of silicon and aluminum ions into the crack. They react with calcium ions in the solution, forming hydrates like C-S-H and calcium aluminate with lower Ca ratio. The composition of healing products in slag-cement system was very similar to that in pure cement system. Blending with slag has little effect on the change of portlandite and calcite phases inside the crack. However, because of the higher overall Si/Ca ratio of the system, more C-S-H with higher Si/Ca was formed, which is linked with significant similarity as fly ash. Blending of silica fume with cement greatly decreased the amount of portlandite, calcite, and sulfate phases, increased the amount of C-S-H with much higher Si/Ca ratio and larger variation.

3.4 Summary

In this chapter, autogenous healing of cracks in cementitious materials due to the precipitation of reactive solutes transporting through the crack was experimentally investigated. μCT was applied to quantitatively characterize the mineral precipitation and healing patterns in natural, rough-walled, water-saturated concrete cracks. The morphology and minerology of the healing products were analyzed as well. The influences of different parameters, such as crack widths, crack shapes, anhydrate cement ratios, supplementary cementitious materials types as well as the replacement levels, on the self-healing extent and the composition of reaction products were investigated. The main conclusions drawn from this study are listed as follows:

(1) For cementitious materials, the intrinsic self-healing through depth shows different behaviors at crack shallow region and deep region. The healing mechanism is strongly controlled by the relative rates of dissolved ion transport and reaction kinetics at the fractural surfaces. Because the mass flux (e.g. CO_3^{2-} and Ca^{2+}) at the sample surface is large to the advective flux through the crack, precipitation is found to mainly focused near the crack inlet. At the time of crack surface sealing, large portions of the deep region of the crack remains devoid of healing products, which suggest that the quickly sealing part significantly reduces long range fluxes to deliver enough dissolved minerals to uniformly fill the crack downstream. The thickness of this quickly sealed region is about 50~200 microns.

(2) When concrete is exposed to water, the dissolution of solid calcium from cement hydrates can quickly occur. The concentration gradients lead to the diffusion of main ionic species, such as alkalis, calcium, hydroxides, etc., from concrete system to the external environment. The presence of CO_2 in the air can also dissolve in water forming H_2CO_3. Once the concentration reaches the equilibrium criteria for precipitation, large crystals, mainly the mixture of $Ca(OH)_2$ and $CaCO_3$, can be formed and deposit at the sample surface as well as the crack shallow region.

(3) The healing products which quickly seal the crack shallow region will further reduce the transport of water or carbon dioxide into crack deeper region. Besides $Ca(OH)_2$ and $CaCO_3$, the chemical analysis results indicate that the healing products at deep region contain significant amount of C-S-H and sulfate phases. However, the Si/Ca ratio in healing products was much lower than that in cement paste, while the Al/Ca ratio in healing products was slightly higher.

(4) The extent of intrinsic self-healing at crack both sallow region and deep region strongly depends on the initial crack width, assuming the presence of the same chemical species

and equal environmental exposure conditions. Although a larger crack increases the potential to be healed homogenously because the longer period for surface sealing, it needs more significant fluid volume and time scale to produce enough precipitated materials. However, for concrete structures in nature environment, the healing resources come from the dissolution of atmospheric CO_2 and concrete material itself, so it is very difficult to maintain the ambient conditions especially the ions supersaturation condition as our laboratory experiments. Therefore, under natural water/dry exposure and limited healing time, as the crack width increases, a sharp reduction of healing ratio can be observed.

(5) The contribution of the continued hydration on the crack volume change is depending on the unhydrated cement ratio. But even for very young sample (7 days), the healing ratio change due to hydration products growth is still insignificant.

(6) Comparing with pure cement paste, the supplementary cementitious materials generally have negative effect on the healing extent, especially at the crack shallow region. The replacement of 50% silica fume caused the most significant reduction from ~70% to ~30%, followed by fly ash to ~50%. Slag had the least effect on healing ratio at shallow region, only about 5% decrease was observed. For the healing ratio at crack deep region. after 28 cycles of healing, pastes containing silica fume showed a lower healing extent than pure cement pastes, while the fly ash and slag systems showed a slightly enhanced healing extent.

(7) The chemical compositional data for healing products in three different types of SCMs-cement systems with 50% replacement ratio have been determined from EDS mapping. The blending of cement with fly ash or silica fume leads to a decrease of the amount of portlandite and calcite, and the formation of more C-S-H with higher Si/Ca and Al/Ca ratios. Blending with slag has little effect on the change of portlandite and calcite phases inside the

crack. However, because of the higher overall Si/Ca ratio of the system, more C-S-H with higher Si/Ca was formed.

Tables

Table 3.1 Summary of experimental conditions for neat cement paste samples.

	Sample					
	T1	T2	T3	T1Y	B2	N1~12
Crack type	Tension	Tension	Tension	Tension	Bending	Tension
Material age (day)	90	90	90	7	90	90
Surface crack width (μm)	44	108	190	48	210	9~144
Crack volume (mm^3)	0.564	1.21	2.57	0.593	1.428	0.124~1.106
Exposure condition	Reactive flow	Reactive flow	Reactive flow	Reactive flow	Reactive flow	Water/dry

Table 3.2 Mixture proportion of healing materials.

Mix	Cement	Fly ash	Slag	Silica fume	Water/Binders	Fiber
OPC	1	-	-	-	0.4	2% vol.
FA1	0.75	0.25	-	-	0.4	2% vol.
FA2	0.5	0.5	-	-	0.4	2% vol.
FA3	0.25	0.75	-	-	0.4	2% vol.
GGBS1	0.75	-	0.25	-	0.4	2% vol.
GGBS2	0.5	-	0.5	-	0.4	2% vol.
GGBS3	0.25	-	0.75	-	0.4	2% vol.
SF1	0.75	-	-	0.25	0.4	2% vol.
SF2	0.5	-	-	0.5	0.4	2% vol.
SF3	0.25	-	-	0.75	0.4	2% vol.

Table 3.3 Chemical compositions of raw materials.

Chemical composition, %	Cement	Fly ash	Slag	Silica fume
SiO_2	19.68	58.93	37.49	93.47
Al_2O_3	5.23	22.52	11.03	2.04
CaO	60.57	3.24	39.36	0.45
Fe_2O_3	2.47	4.82	1.21	1.05
MgO	1.12	2.74	9.03	0.58
SO_3	3.81	0.58	0.97	0.44
Na_2O	0.22	1.18	0.65	1.03
K_2O	1.25	1.20	0.26	0.91

Figures

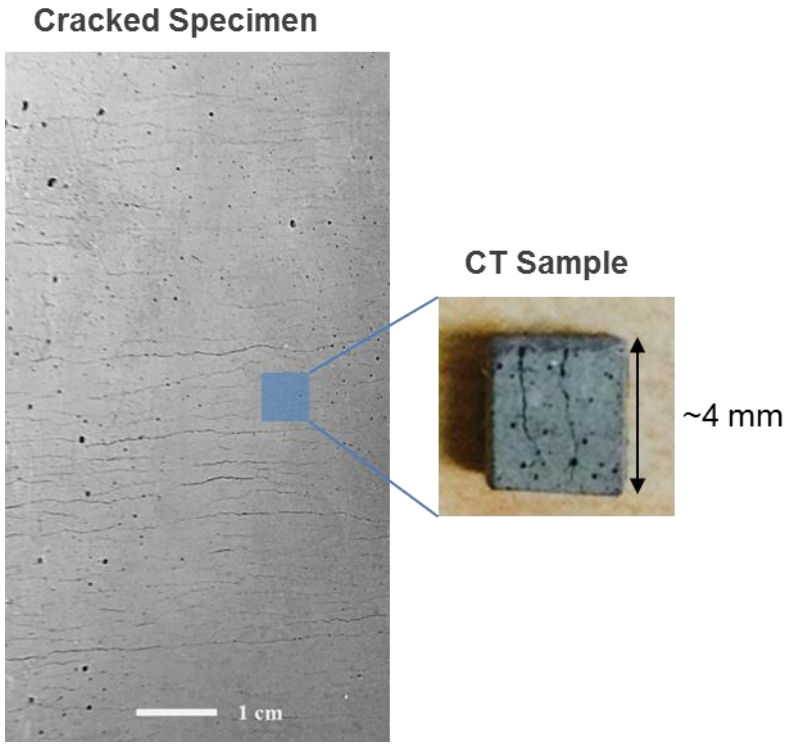

Figure 3.1 Coupon specimen after loading to induce cracks (left) and small cubic sample for CT scan (right).

Figure 3.2 Water/dry cycles for self-healing environmental treatment.

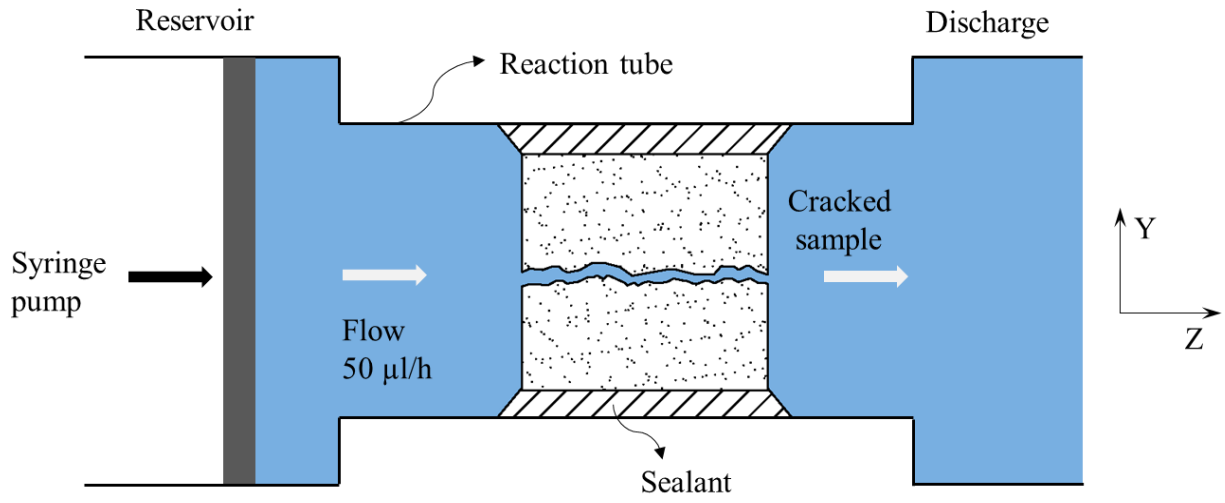

Figure 3.3 Reactive transport-healing experiment: Ion-containing fluid flows through a crack in a cementitious sample located inside a reaction tube.

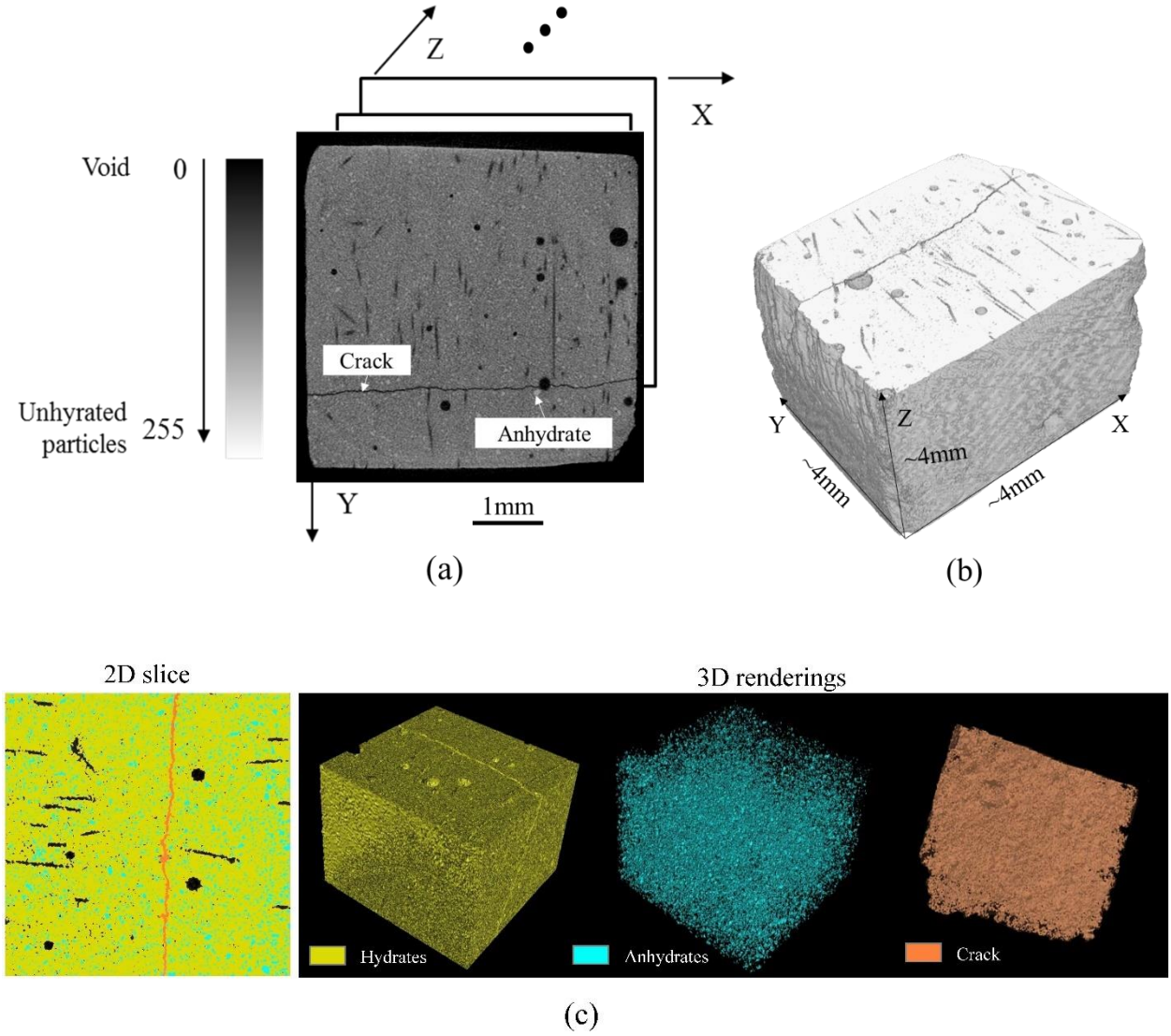

Figure 3.4 Examples of Micro-CT images: (a) 2D raw image, (b) reconstructed sample 3D rendering image, (c) phase segregation.

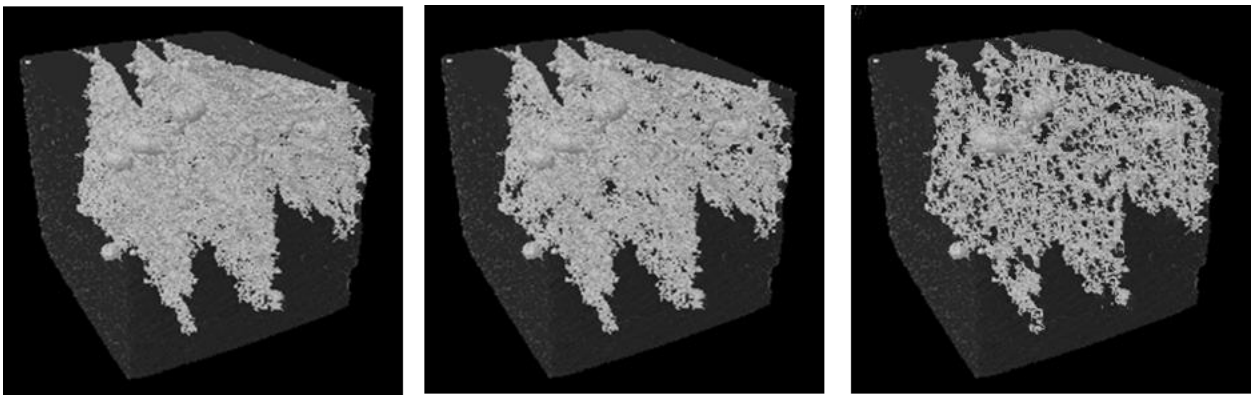

(a) virgin crack (b) after 3 cycles (c) after 14 cycles

Figure 3.5 The evolution of 3D cracks during self-healing.

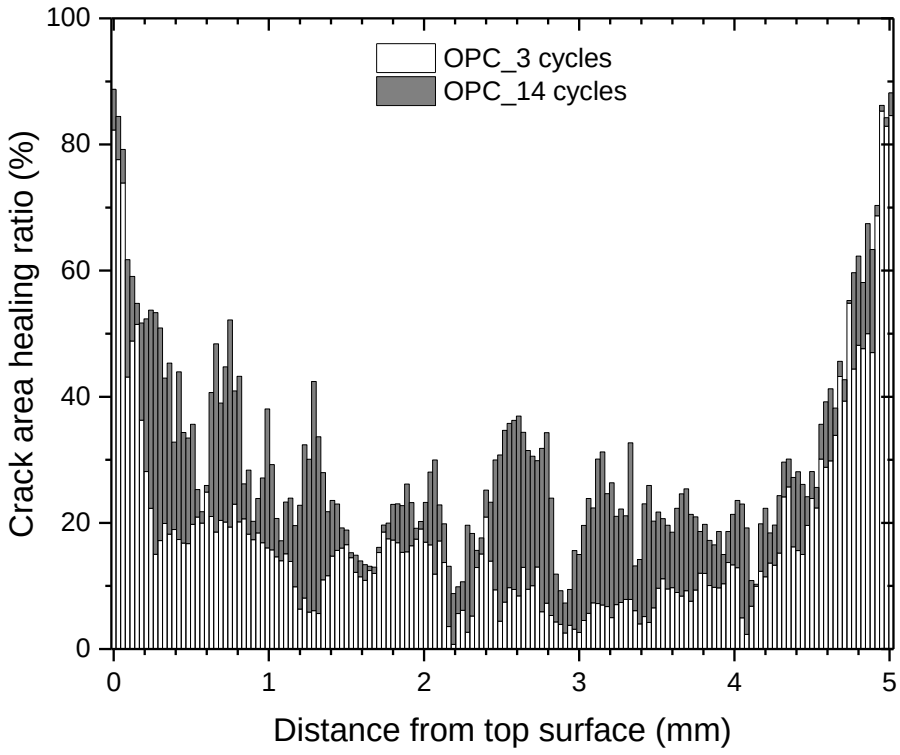

Figure 3.6 The healing ratio (crack area after healing/virgin crack area) of a typical crack in cement past vs. distance from the top surface.

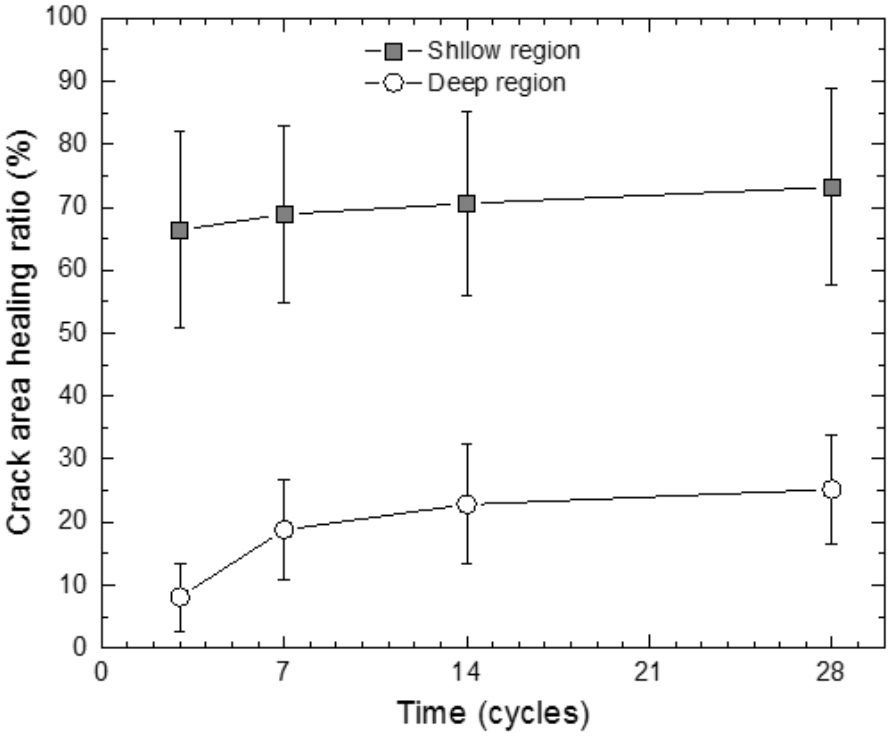

Figure 3.7 The change of crack healing ratio vs. healing time.

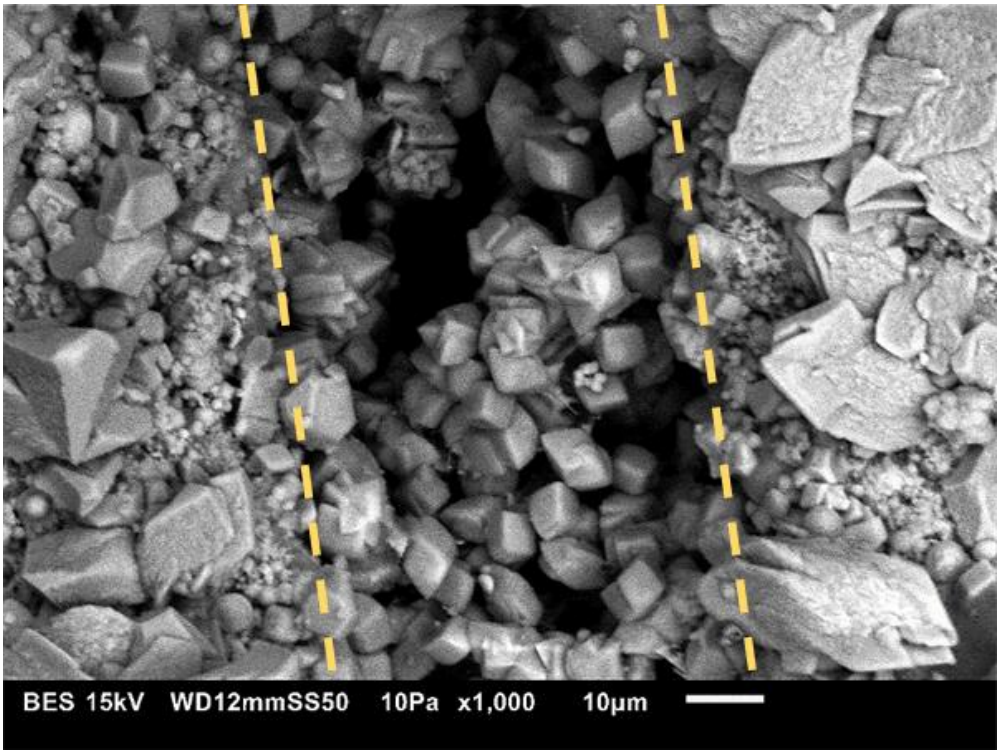
BES 15kV WD12mmSS50 10Pa x1,000 10µm

(a) SEM

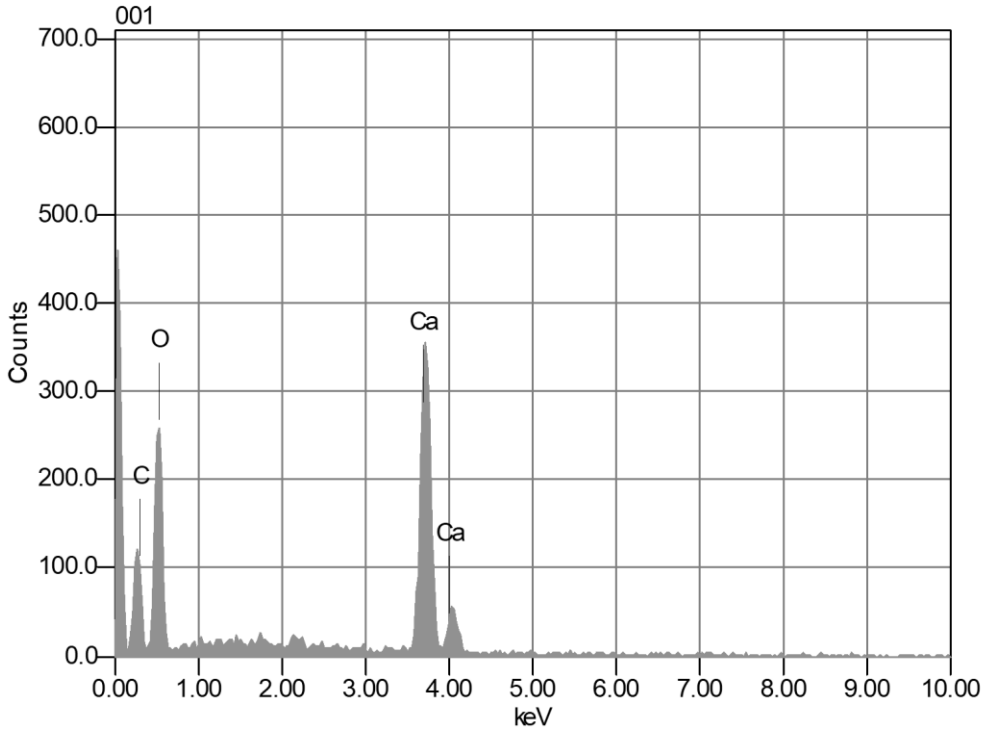
001
700.0
600.0
500.0
400.0
300.0
200.0
100.0
0.0
Counts
O
C
Ca
Ca
0.00
1.00
2.00
3.00
4.00
5.00
6.00
7.00
8.00
9.00
10.00
keV

(b) EDS

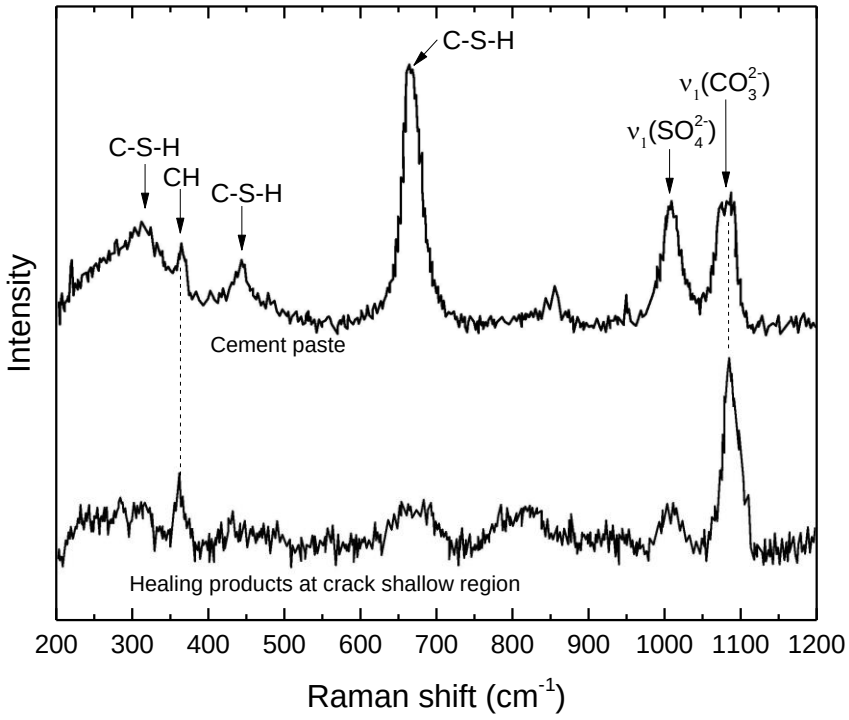

(C) Raman spectra

Figure 3.8 Typical SEM image, EDS, and Raman spectra for self-healing products at crack shallow region after 3 cycles.

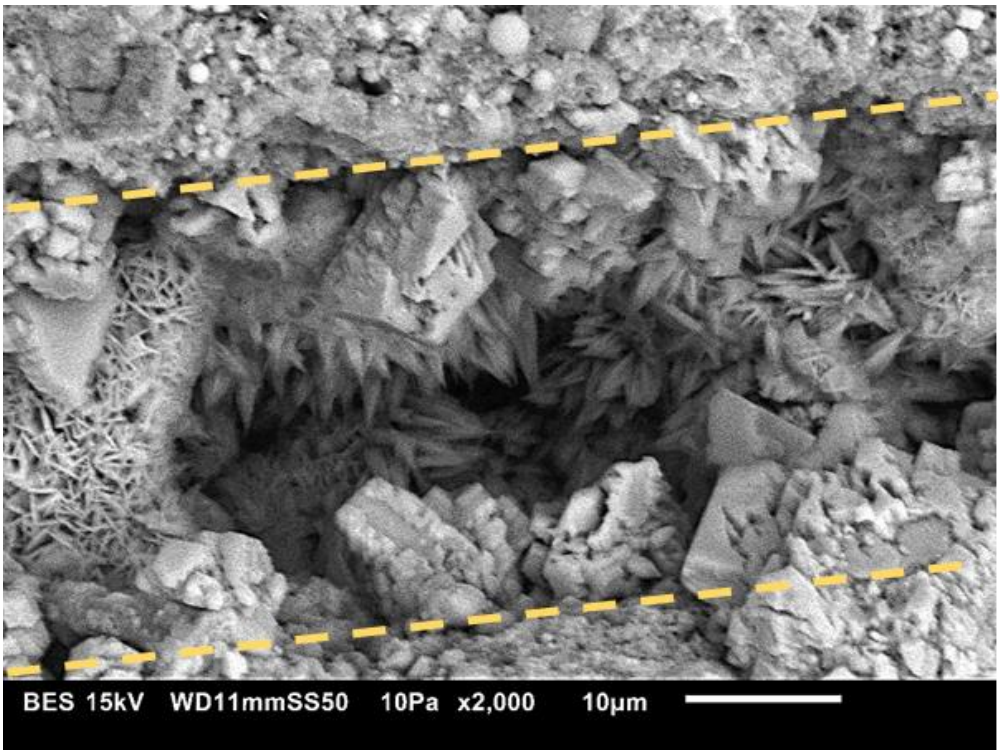
BES 15kV WD11mmSS50 10Pa x2,000 10µm

(a) SEM

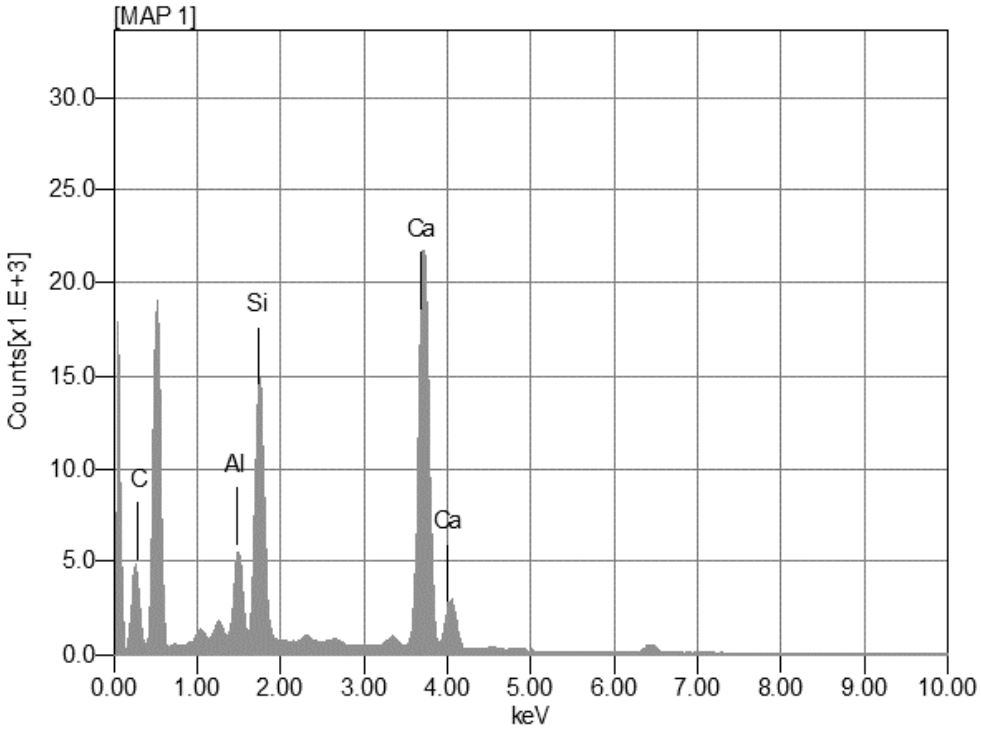
[MAP 1]
Counts[x1.E+3]
30.0
25.0
20.0
15.0
10.0
5.0
0.0
C
Al
Si
Ca
Ca
0.00
1.00
2.00
3.00
4.00
5.00
6.00
7.00
8.00
9.00
10.00
keV

(b) EDS

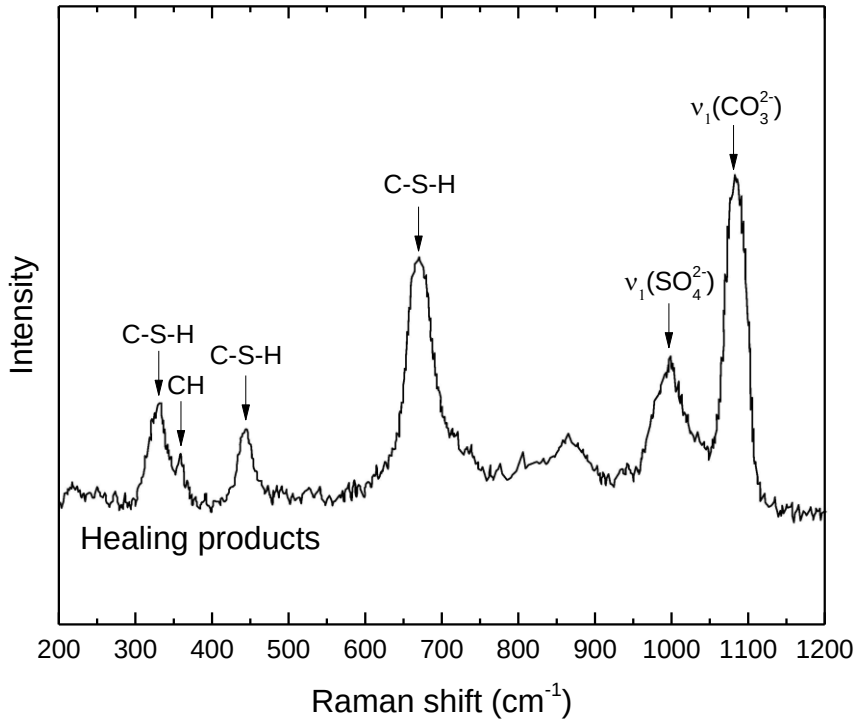

(C) Raman spectra

Figure 3.9 Typical SEM image, EDS, and Raman spectra for self-healing products at crack deep region after 14 cycles.

(a) Cement paste

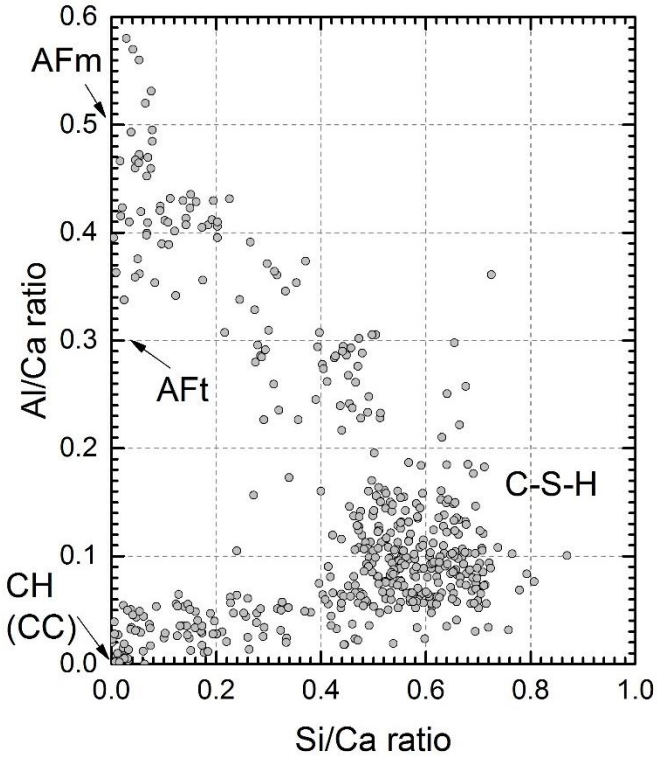

(b) Crack shallow region

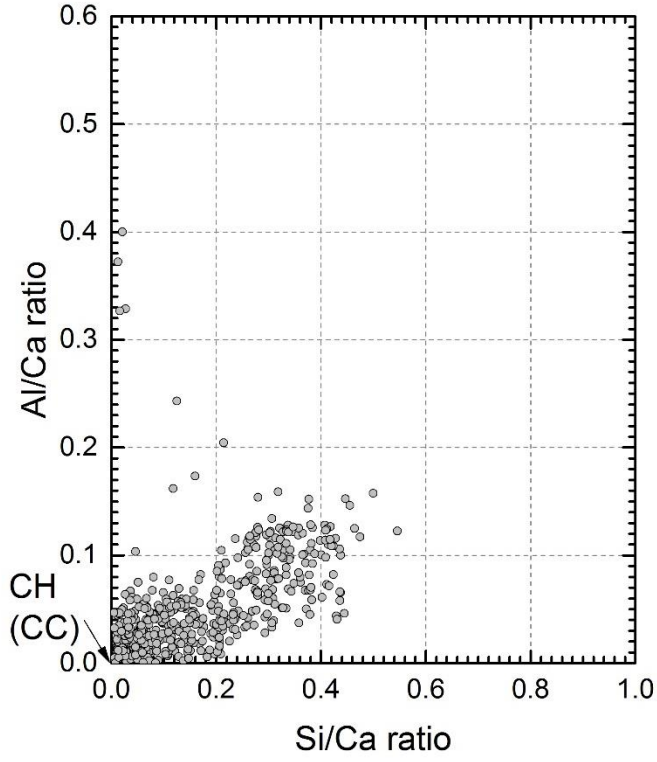

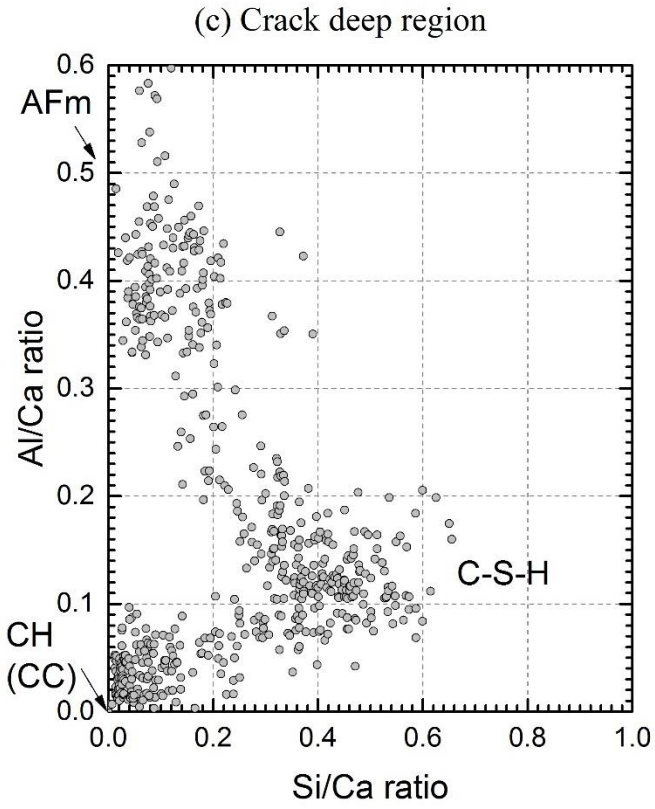

Figure 3.10 Al/Ca against Si/Al atom ratio plot for EDS mapping.

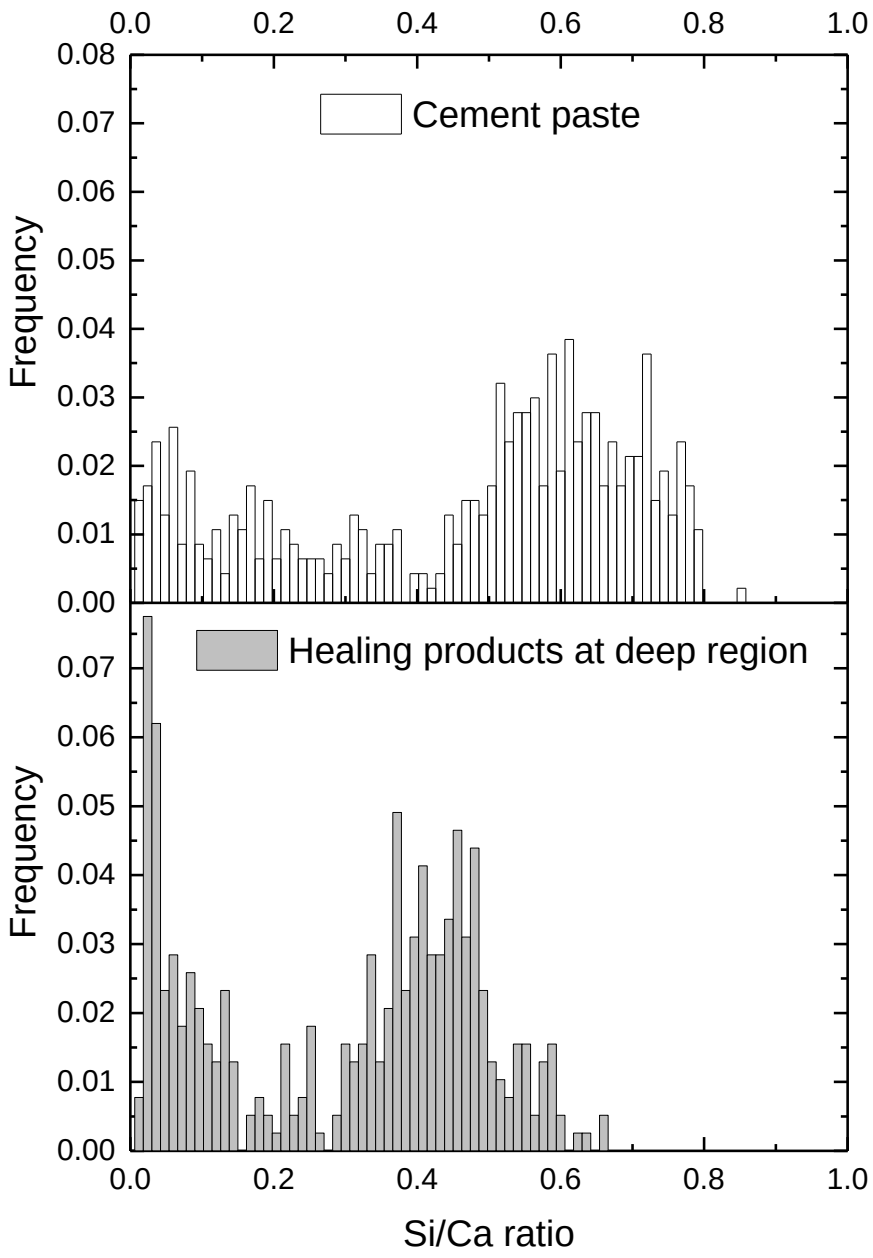

(a) Si/Ca atom ratio

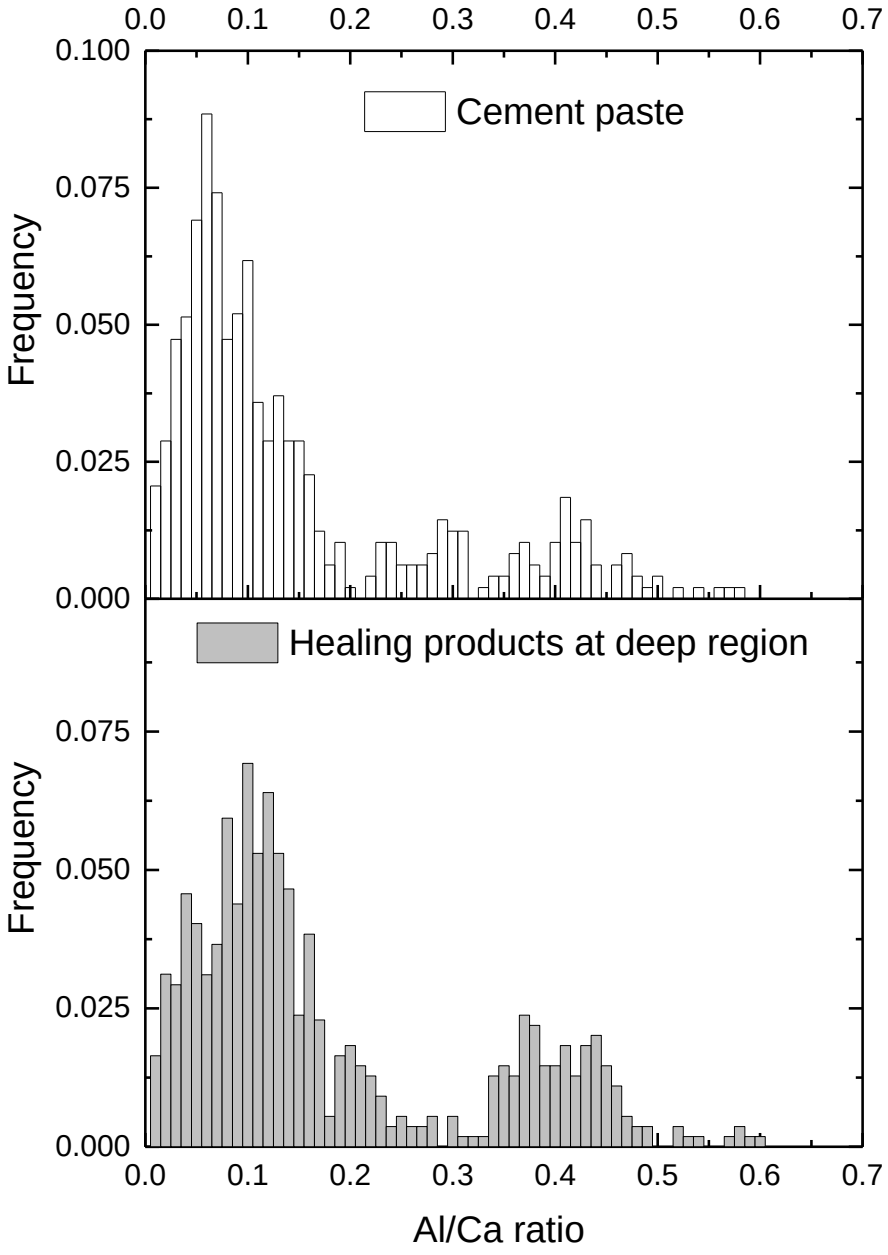

(b) Al/Ca atom ratio

Figure 3.11 Si/Ca and Al/Ca atom ratio distribution histogram for cement paste (up) and healing products at crack deep region after 14 cycles (below).

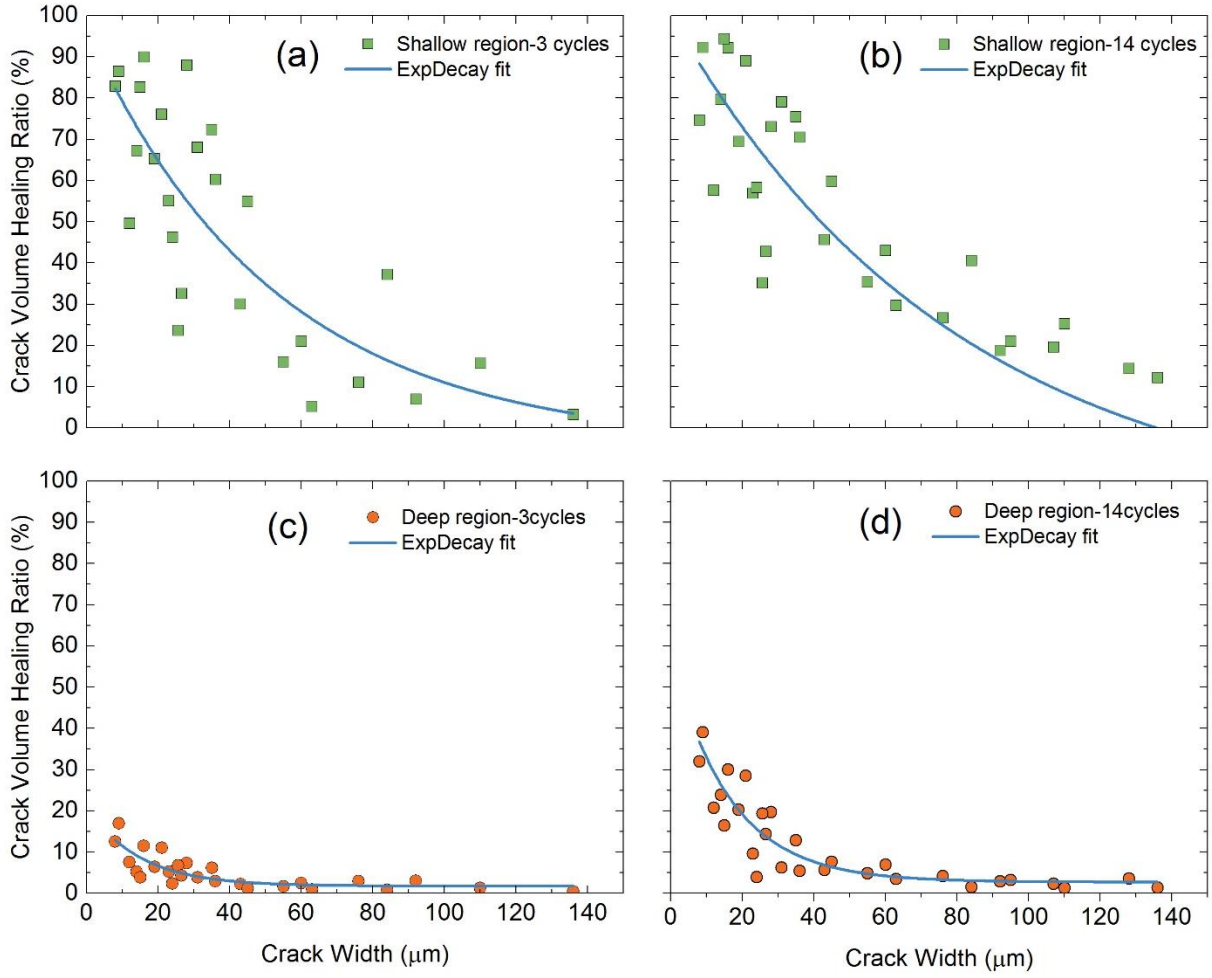

Figure 3.12 The effect of crack width on the healing ratio at (a)(b) shallow region and (c)(d) deep region.

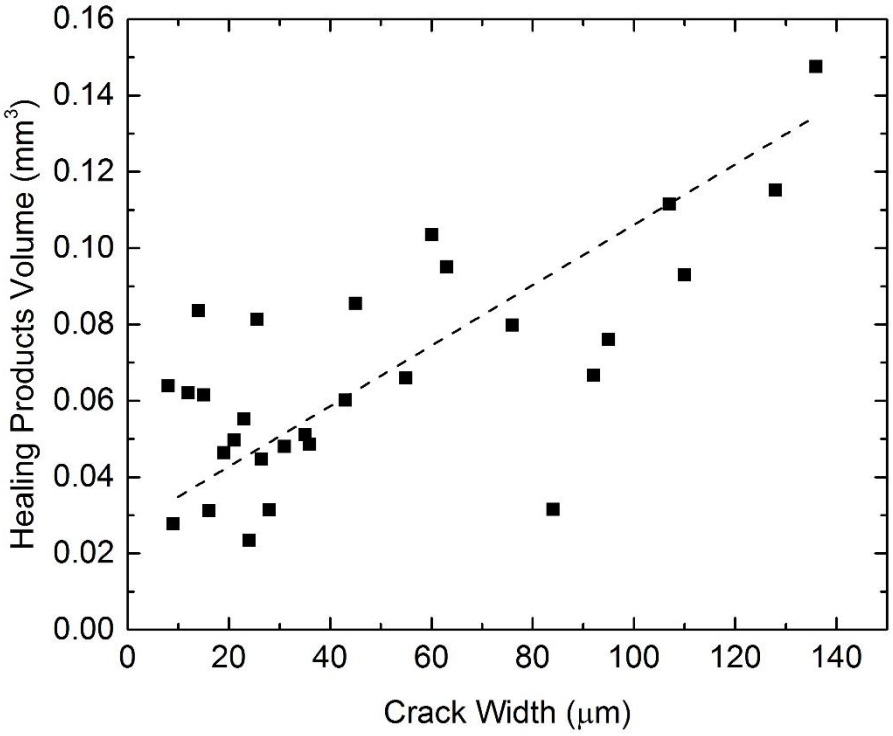

Figure 3.13 The effect of crack width on the total healing products volume after 14 cycles.

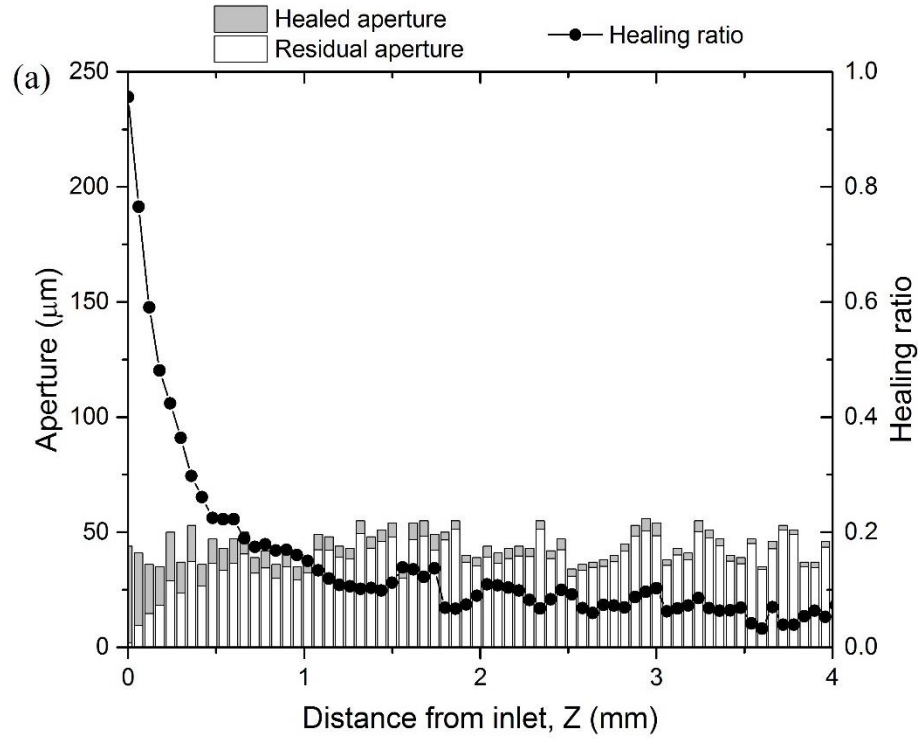
(a)
Healed aperture
Residual aperture
Healing ratio
Aperture (μm)
Healing ratio
Distance from inlet, Z (mm)
0
50
100
150
200
250
0.0
0.2
0.4
0.6
0.8
1.0
0
1
2
3
4

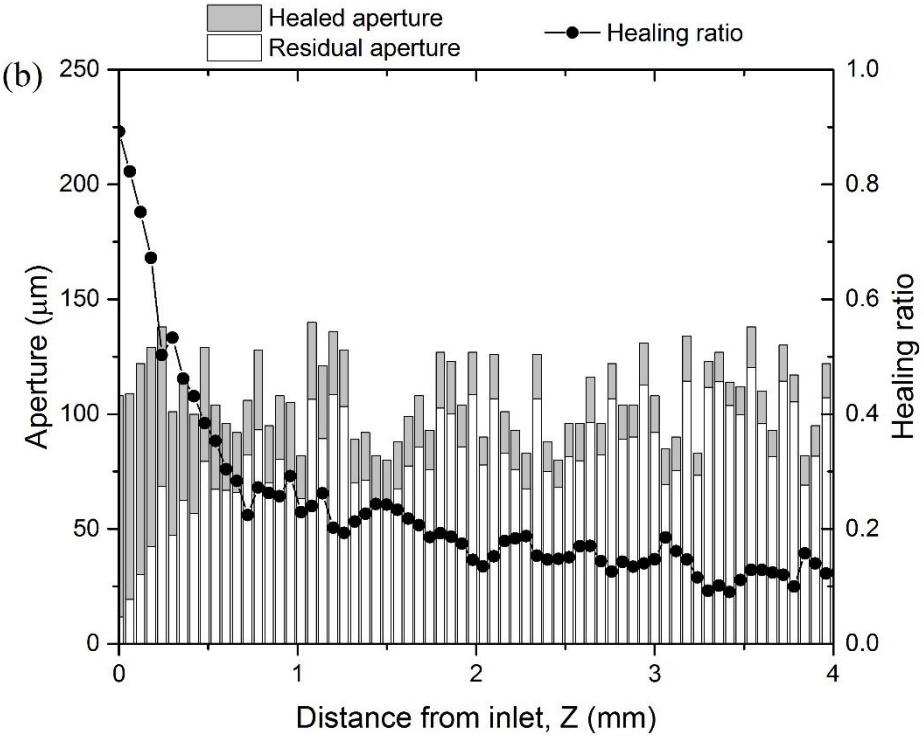
(b)
Healed aperture
Residual aperture
Healing ratio
Aperture (μm)
Healing ratio
Distance from inlet, Z (mm)
0
50
100
150
200
250
0.0
0.2
0.4
0.6
0.8
1.0
0
1
2
3
4

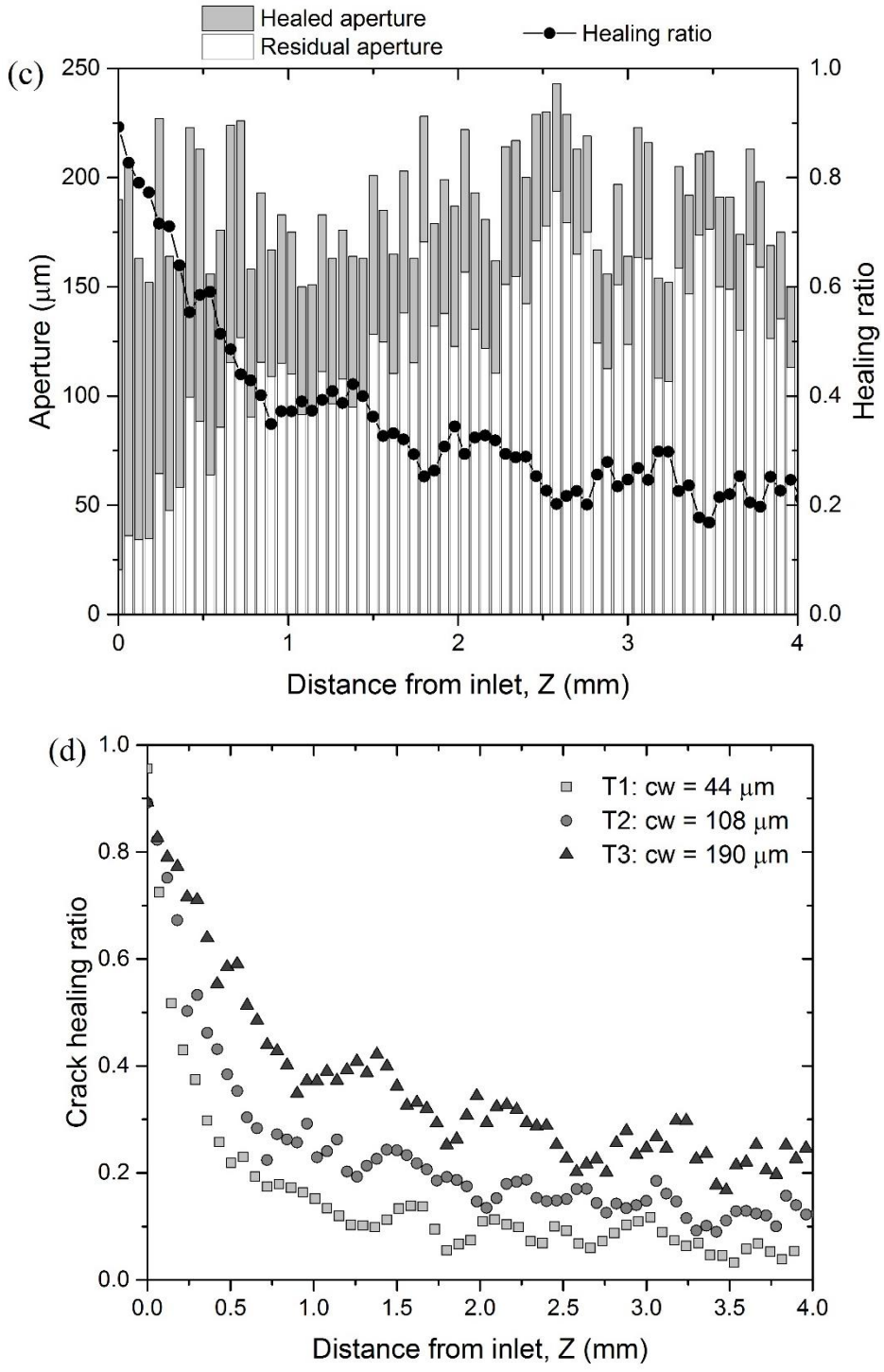

Figure 3.14 The crack healing ratio and average crack aperture along the crack depth (Z axis) for samples with different crack width: (a) crack width (T1) = 44 μm, (b) crack width (T2) = 108 μm, (c) crack widths (T3) = 190 μm, (d) The comparison of three samples.

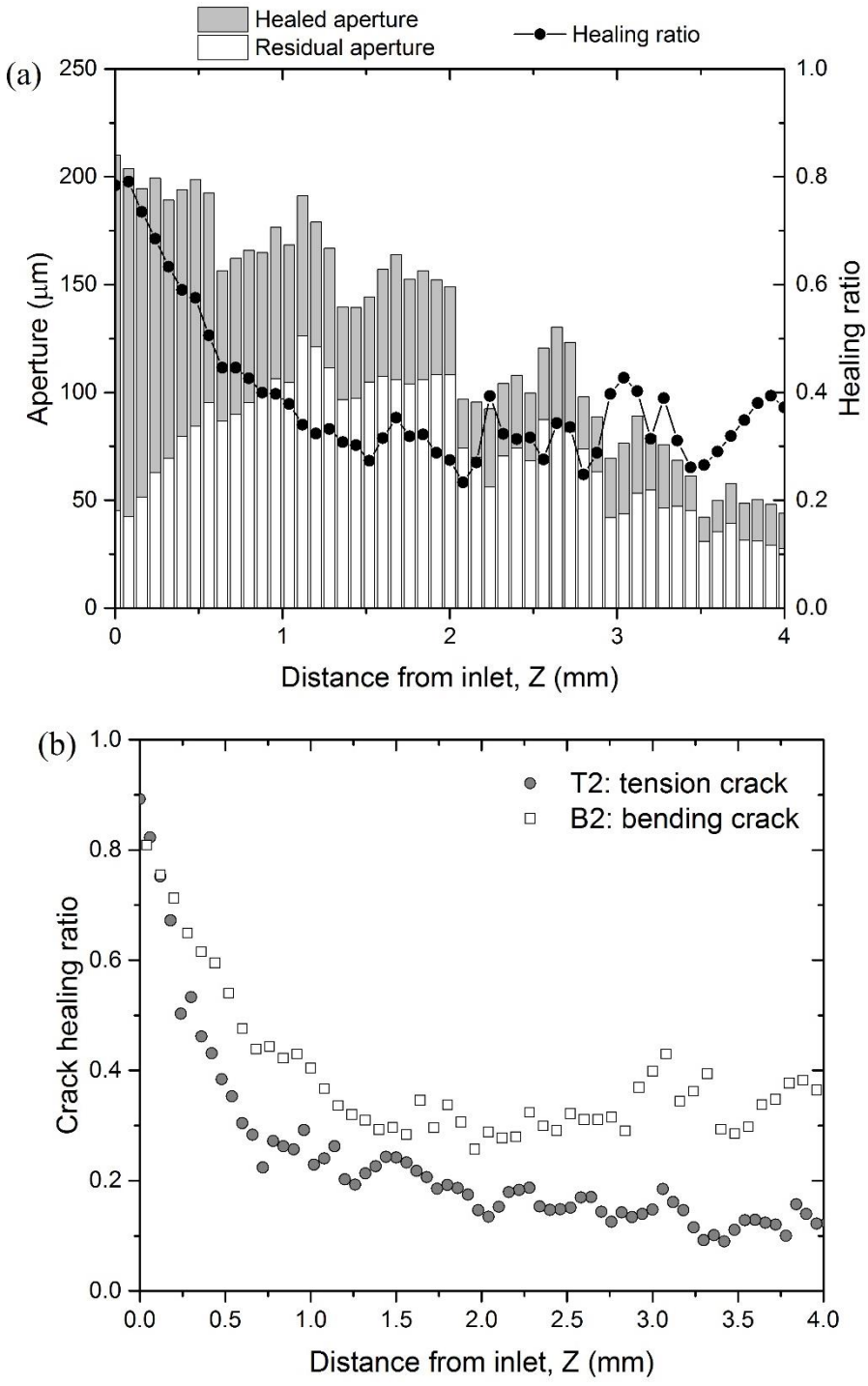

Figure 3.15 The crack healing ratio and average crack aperture along the crack depth (Z axis) for sample B2 with bending crack.

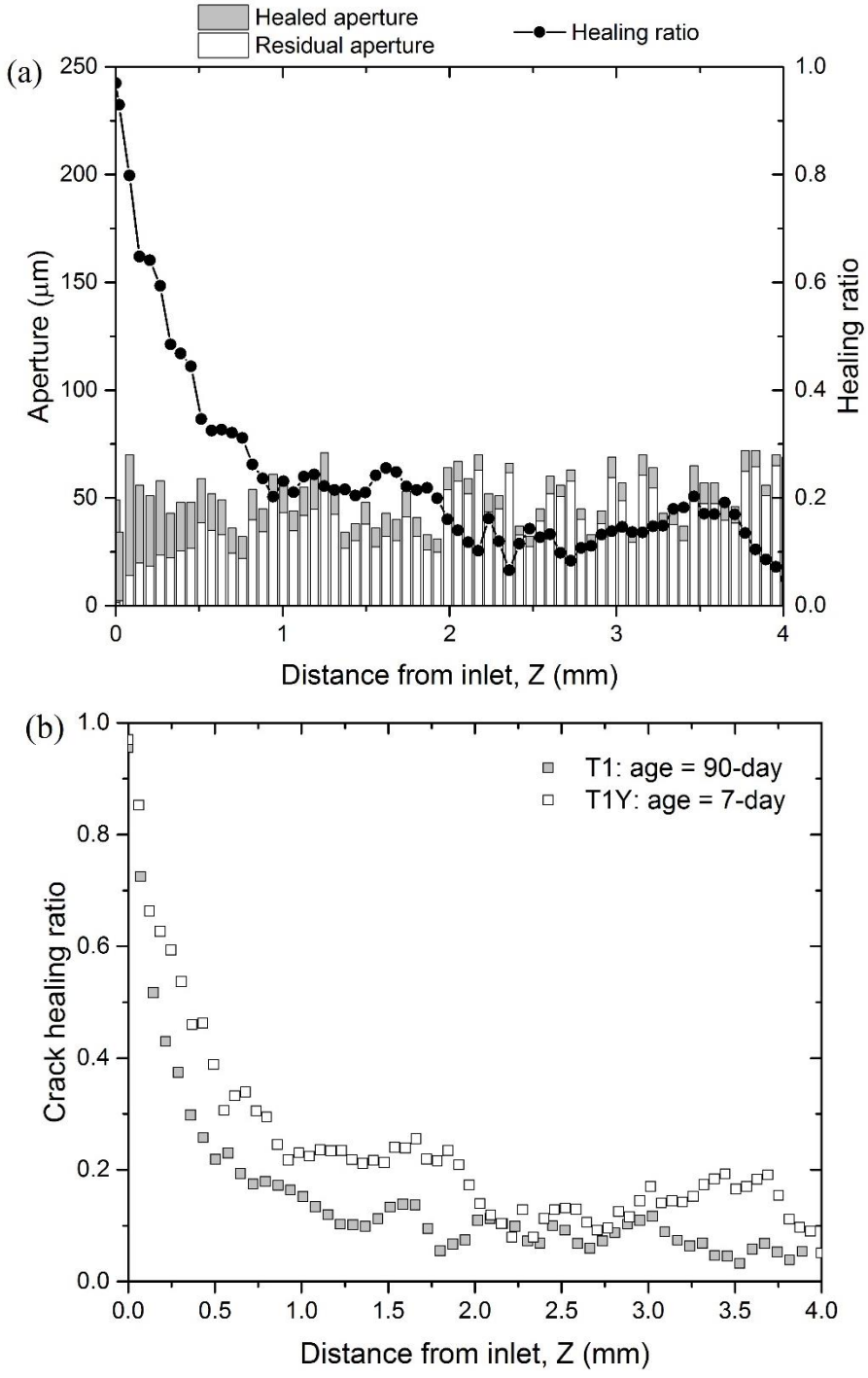

Figure 3.16 The crack healing ratio and average crack aperture along the crack depth (Z axis) for sample T1Y with young age at 7 days.

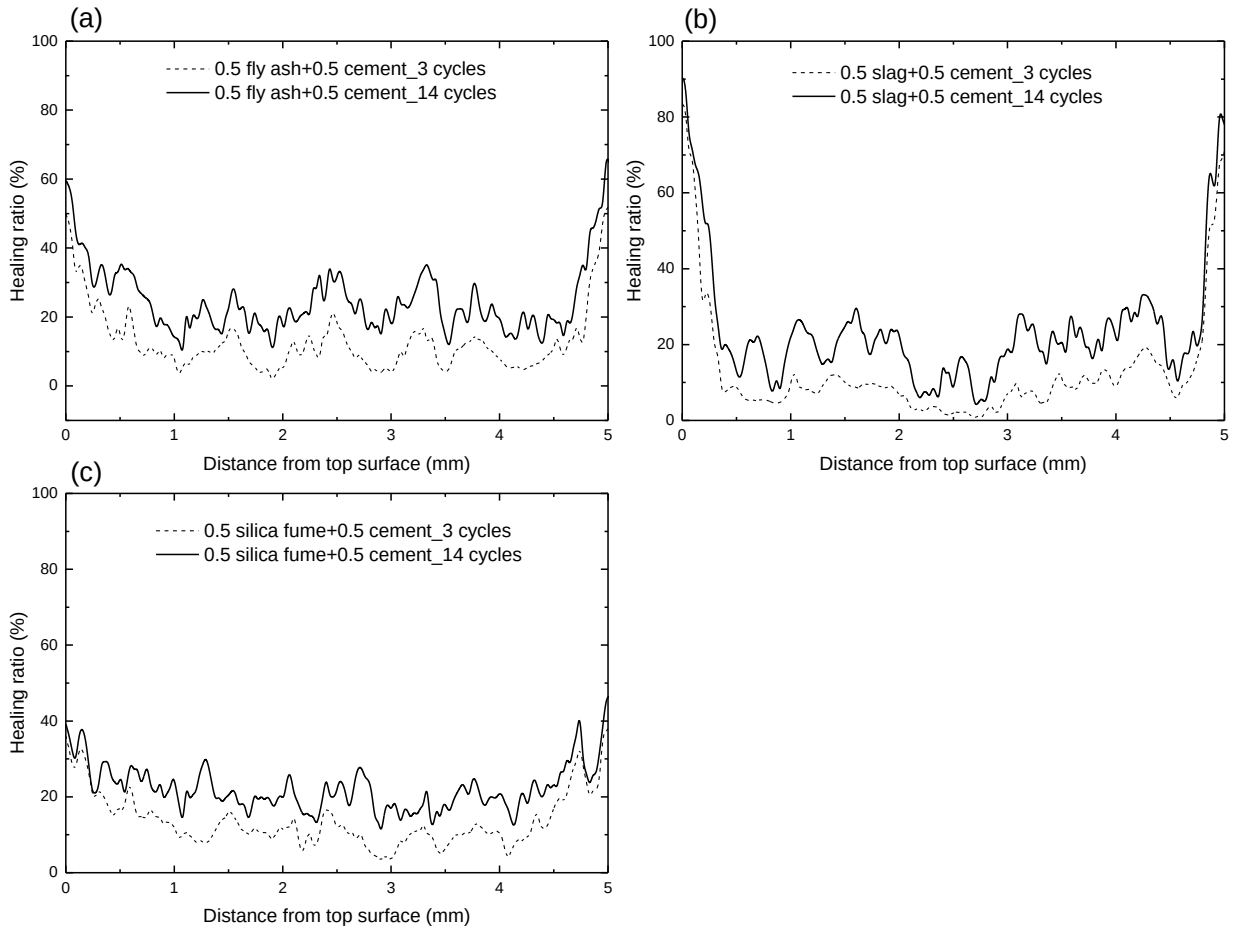

Figure 3.17 Typical crack area changes of cement-pozzolans blends after cycles healing vs. distance from the top surface: (a) fly ash, (b) slag, (c) silica fume.

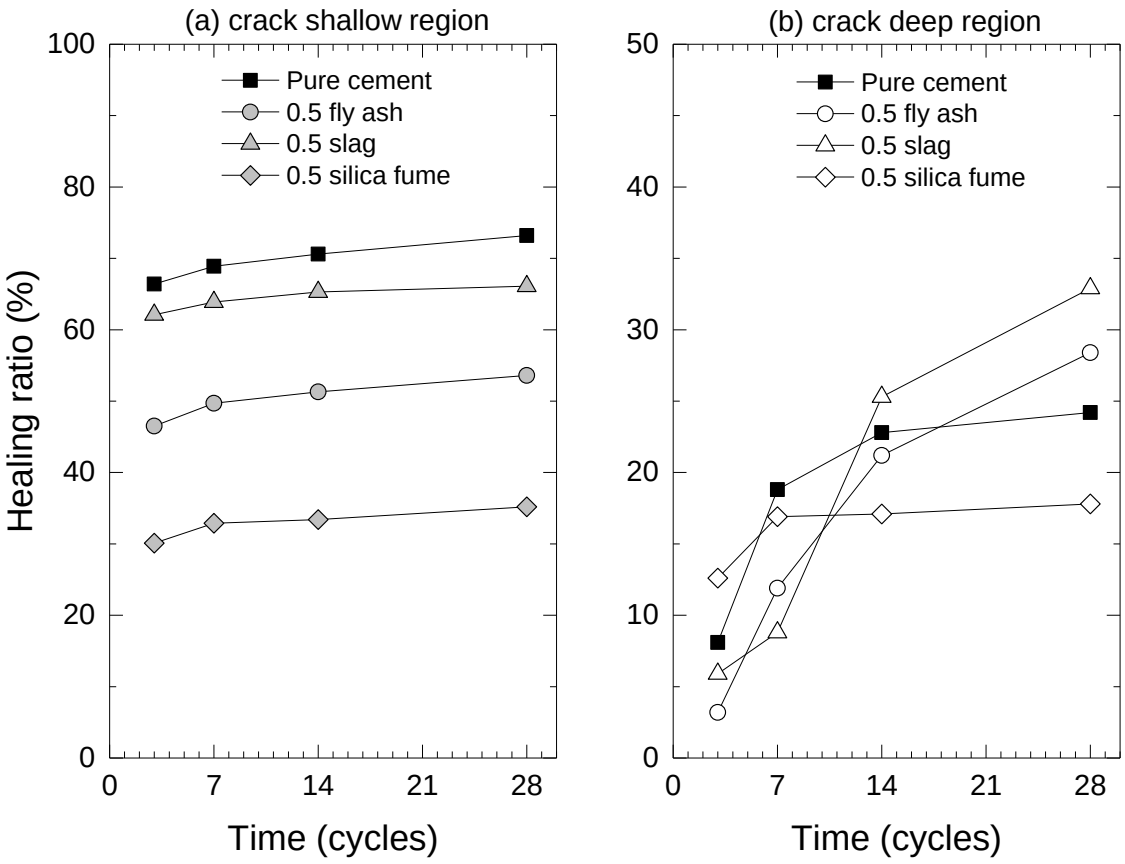

Figure 3.18 The healing ratio of SCMs-cement blends as a function of time: (a) crack shallow region, (b) crack deep region.

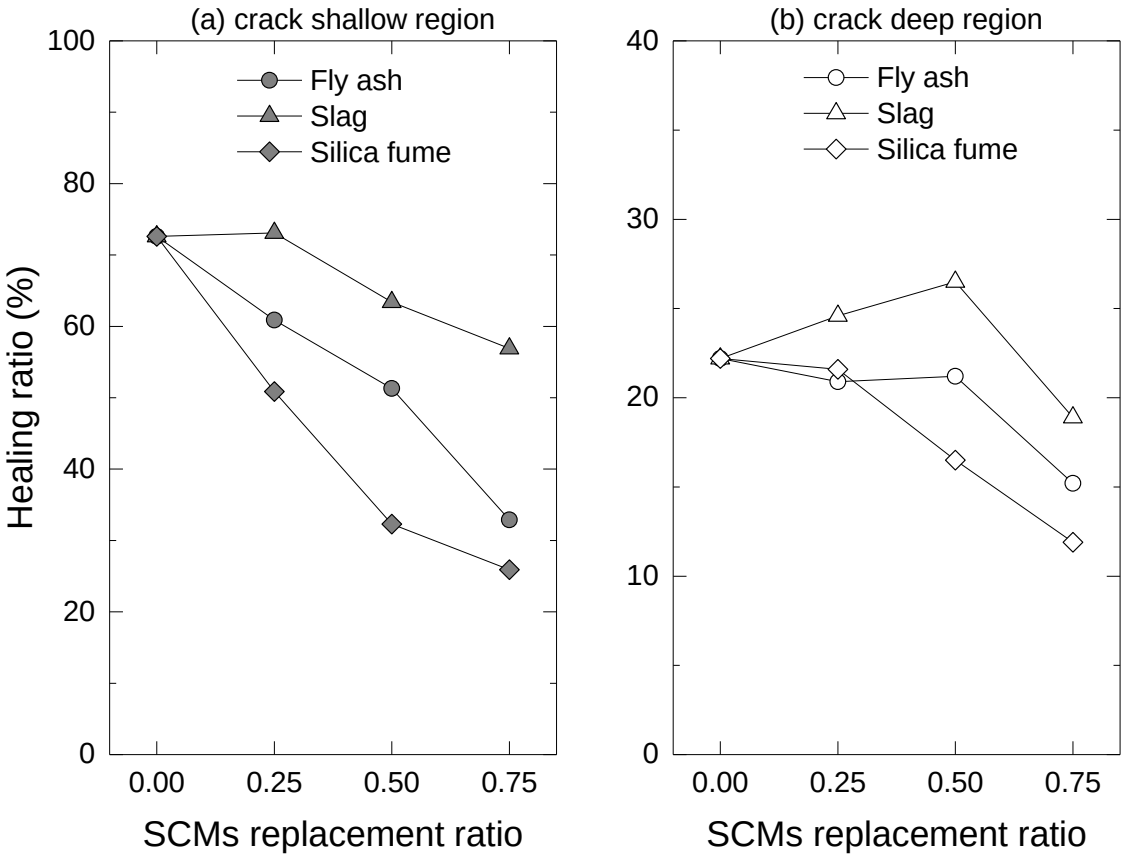

Figure 3.19 The effect of SCMs type and replacement level on the self-healing extent at 14 cycles.

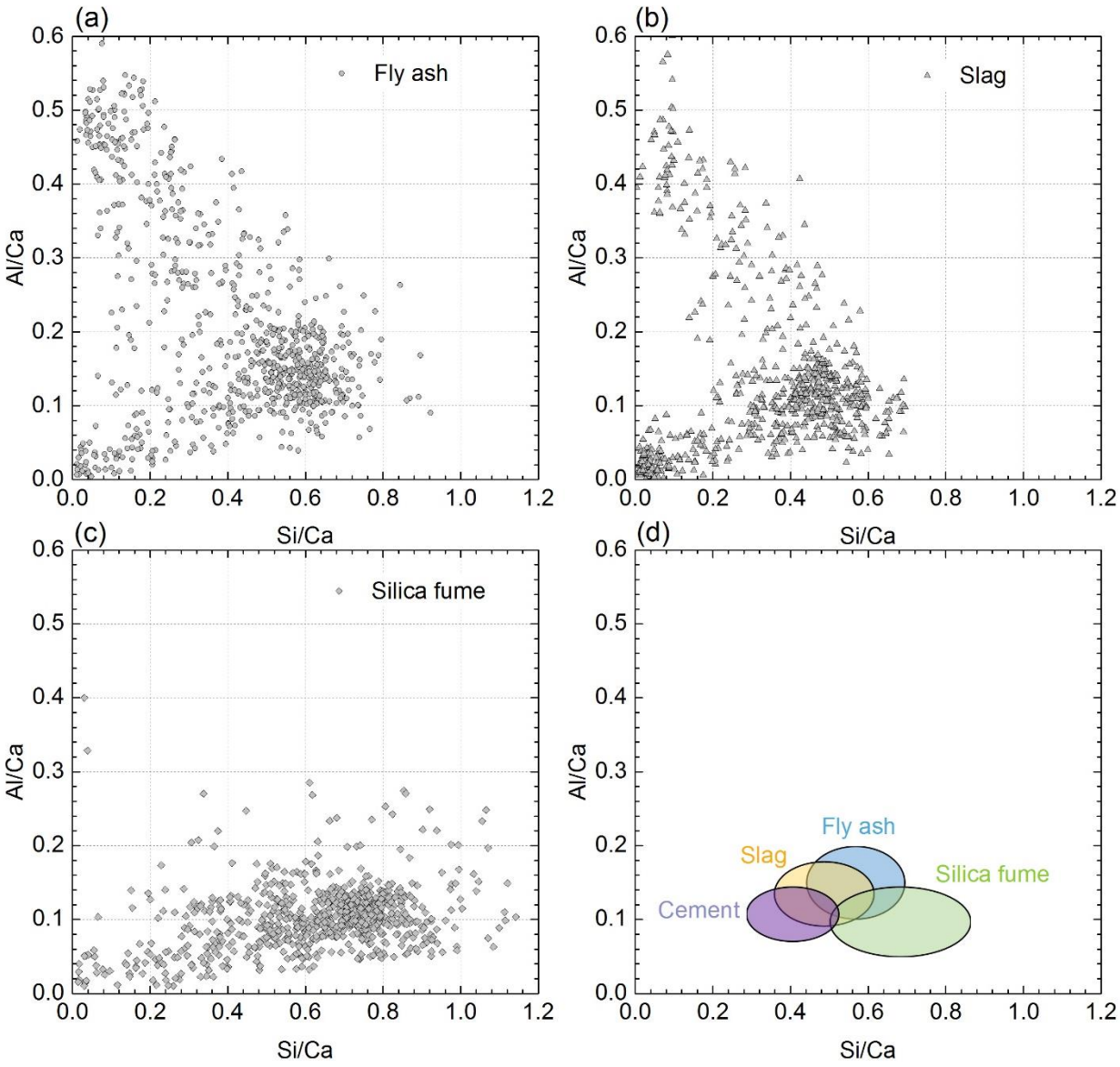

Figure 3.20 Atomic ratios of the healing products at crack deep region in SCMs-cement blends: (a) fly ash, (b) slag, (c) silica fume, (d) C-S-H phases in different systems.

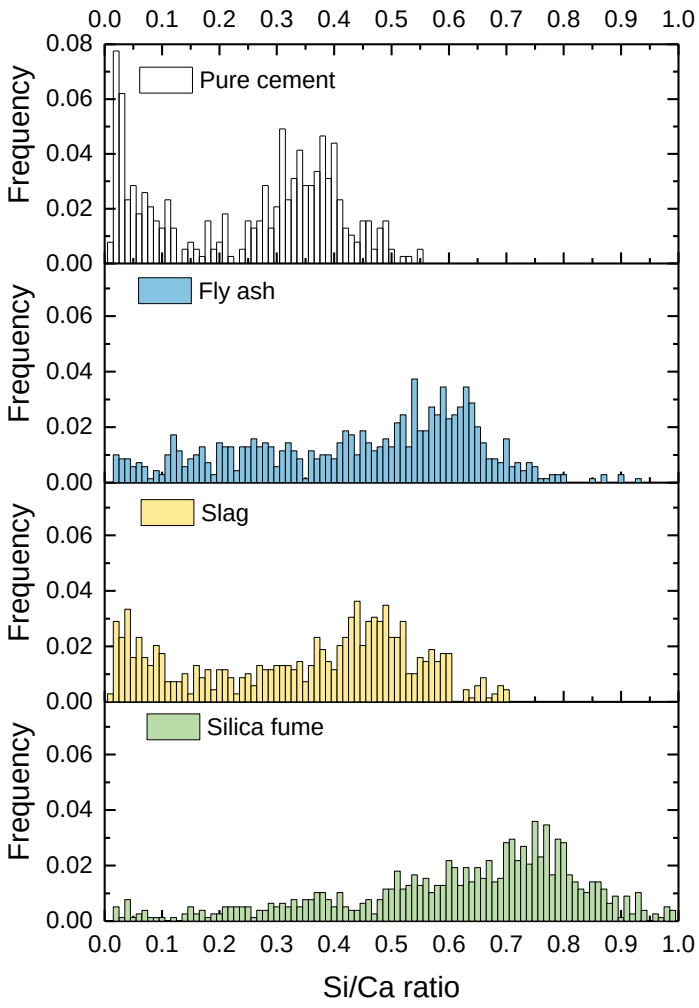

(a) Si/Ca

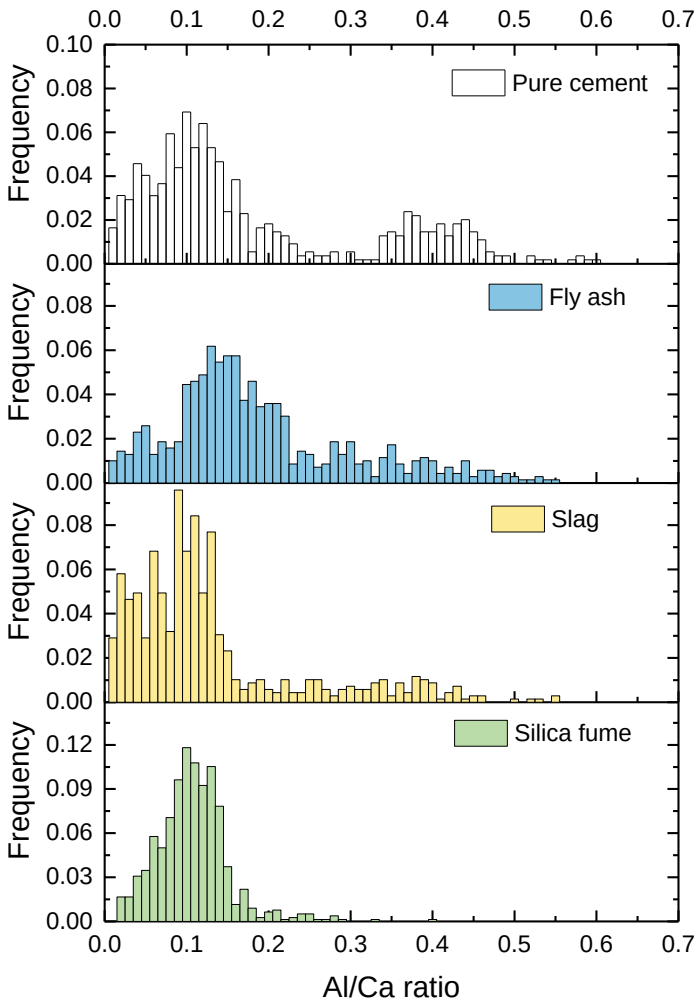

(b) Al/Ca

Figure 3.21 Si/Ca and Al/Ca atom ratio distribution histogram for healing products in different SCMs-cement blends systems.

References

[1] Snoeck, D., & De Belie, N. (2015). From straw in bricks to modern use of microfibers in cementitious composites for improved autogenous healing–A review. Construction and Building Materials, 95, 774-787.

[2] Fan, S., & Li, M. (2014). X-ray computed microtomography of three-dimensional microcracks and self-healing in engineered cementitious composites. Smart Materials and Structures, 24(1), 015021.

[3] D. Fukuda, Y. Nara, Y. Kobayashi, M. Maruyama, M. Koketsu, D. Hayashi, H. Ogawa, K. Kaneko, Investigation of self-sealing in high-strength and ultra-low-permeability concrete in water using micro-focus X-ray CT, Cement and Concrete Research, 42(11) (2012), 1494-1500.

[4] Wang, J., Dewanckele, J., Cnudde, V., Van Vlierberghe, S., Verstraete, W., & De Belie, N. (2014). X-ray computed tomography proof of bacterial-based self-healing in concrete. Cement and Concrete Composites, 53, 289-304.

[5] Yang, E. H., Yang, Y., & Li, V. C. (2007). Use of high volumes of fly ash to improve ECC mechanical properties and material greenness. ACI Materials Journal, 104(6), 620-628.

[6] Termkhajornkit, P., Nawa, T., Yamashiro, Y., & Saito, T. (2009). Self-healing ability of fly ash–cement systems. Cement and Concrete Composites, 31(3), 195-203.

[7] Qian, S., Zhou, J., De Rooij, M. R., Schlangen, E., Ye, G., & Van Breugel, K. (2009). Self-healing behavior of strain hardening cementitious composites incorporating local waste materials. Cement and Concrete Composites, 31(9), 613-621

[8] Ahn, T. H., & Kishi, T. (2010). Crack self-healing behavior of cementitious composites incorporating various mineral admixtures. Journal of Advanced Concrete Technology, 8(2), 171-186.

[9] Na, S. H., Hama, Y., Taniguchi, M., Katsura, O., Sagawa, T., & Zakaria, M. (2012). Experimental investigation on reaction rate and self-healing ability in fly ash blended cement mixtures. Journal of Advanced Concrete Technology, 10(7), 240-253.

[10] Sisomphon, K., Copuroglu, O., & Koenders, E. A. B. (2013). Effect of exposure conditions on self-healing behavior of strain hardening cementitious composites incorporating various cementitious materials. Construction and Building Materials, 42, 217-224.

[11] Sahmaran, M., Yildirim, G., & Erdem, T. K. (2013). Self-healing capability of cementitious composites incorporating different supplementary cementitious materials. Cement and Concrete Composites, 35(1), 89-101.

[12] Huang, H., Ye, G., & Damidot, D. (2014). Effect of blast furnace slag on self-healing of microcracks in cementitious materials. Cement and concrete research, 60, 68-82.

[13] Inskeep, W. P., & Bloom, P. R. (1985). An evaluation of rate equations for calcite precipitation kinetics at pCO_2 less than 0.01 atm and pH greater than 8. Geochimica et Cosmochimica Acta, 49(10), 2165-2180.

[14] Cao, B., Fan, S., Tan, X., Li, M., & Hu, Y. (2017). Cementitious Materials Modified with Hematite Nanoparticles for Enhanced Cement Hydration and Uranium Immobilization. Environmental Science: Nano.

[15] Tlili, M. M., Amor, M. B., Gabrielli, C., Joiret, S., Maurin, G., & Rousseau, P. (2002). Characterization of $CaCO_3$ hydrates by micro-Raman spectroscopy. Journal of Raman spectroscopy, 33(1), 10-16.

[16] E. E. Coleyshaw, G. Crump, and W. P. Griffith, “Vibrational Spectra of the Hydrated Carbonate Minerals Ikaite, Monohydrocalcite, Lansfordite and Nesquehonite,” Spectrochim. Acta, A 59, 2231–9 (2003).
[17] Kirkpatrick, R. J., Yarger, J. L., McMillan, P. F., Ping, Y., & Cong, X. (1997). Raman spectroscopy of CSH, tobermorite, and jennite. Advanced Cement Based Materials, 5(3), 93-99.
[18] Black, L., Breen, C., Yarwood, J., Deng, C. S., Phipps, J., & Maitland, G. (2006). Hydration of tricalcium aluminate (C_3A) in the presence and absence of gypsum—studied by Raman spectroscopy and X-ray diffraction. Journal of Materials Chemistry, 16(13), 1263-1272.
[19] Taylor, H. F. (1997). Cement chemistry. Thomas Telford.
[20] Lothenbach, B., Scrivener, K., & Hooton, R. D. (2011). Supplementary cementitious materials. Cement and Concrete Research, 41(12), 1244-1256.
[21] Juenger, M. C., & Siddique, R. (2015). Recent advances in understanding the role of supplementary cementitious materials in concrete. Cement and Concrete Research, 78, 71-80.
[22] Khatri, R. P., Sirivivatnanon, V., & Gross, W. (1995). Effect of different supplementary cementitious materials on mechanical properties of high performance concrete. Cement and Concrete Research, 25(1), 209-220.
[23] Toutanji, H., Delatte, N., Aggoun, S., Duval, R., & Danson, A. (2004). Effect of supplementary cementitious materials on the compressive strength and durability of short-term cured concrete. Cement and Concrete Research, 34(2), 311-319.

CHAPTER 4 NUMERICAL MODELING OF INTRINSIC SELF-HEALING IN CEMENTITIOUS MATERIALS

4.1 Introduction

The laboratory experiments provide quantitative measures of the precipitation induced crack aperture alterations. However, the complicated and various boundary conditions, the time-prohibitive nature of the mineral growth process, and small length-scale of the experiments, limit our ability to interpret and quantify the complex networks. Development of efficient computational models provides a potential path toward enhanced understanding of the role of mineral precipitation reactions (e.g. carbonation and further hydration) on crack revolution over a wide range of parameters and scales. Nevertheless, the number of contributions which are devoted to this topic is very limited to the best of our knowledge. Recent work by Huang et al. [1] and Chitez et al. [2] proposed hydration-based models to predict the self-healing rate as a result of the continued hydration of unreacted cementitious particles inside the crack for very young cement pastes. But these simulations did not consider the non-uniform 3D healing distribution due to the hydrothermal flow and mass transport over the crack depth. Moreover, our experimental study in last chapter and a number of literatures [3][6] have suggested that the carbonation product $CaCO_3$ rather than the hydration products is the most dominant precipitate, especially at crack top surface and in mature concrete when there is not sufficient amount of anhydrate cement.

The objective of this study is to promote the mechanistic understanding of the complex autogenous healing process in a 3D concrete crack. In order to achieve this goal, we present a hydro-thermodynamics model to mathematically predict the mineral precipitation along the

crack, together with finite difference numerical solutions. This semi-analytical model considered the coupled hydrodynamic flow, solute transport, continued hydration, precipitation process, and the feedback between crack aperture evolution and fluid transmissibility. We further present the first results of an experimental study that allow non-destructive 3D observation to visualize and quantify the healing products growth in the natural, rough-walled, water-saturated concrete crack. The dynamic behavior of the water and concrete interactions was investigated for different parameters, such as crack geometry, sample age, and supersaturation condition. The mineral resource (e.g. Ca^{2+}, CO_3^{2-}) for autogenous healing in natural environment are mostly supplied by the dissolve of carbon dioxide in water, and the leaching of concrete matrix. However, the rate and extent of these reactions are usually too low to produce significant grains to study the details of microstructural evolution at laboratory timescales. Also, it is very difficult to quantitatively control the initial dissolving condition in the solution. Therefore, in this study, we used analogue experiments by using advective fluid saturated with $CaCO_3$ through the natural concrete crack. The supersaturated fluid can provide constant and controllable chemical supplies, resulting in significant precipitation over relatively short timescales. The experimental measurements were directly used to validate the simulation results. The influences of various parameters including initial aperture variability, flow velocity, percentage of anhydrates, and relative supersaturation on the patterns of crack evolution were discussed based on a sensitivity modelling. The work generates understanding of how self-healing progresses in a crack over spatial and temporal scales, and how this healing process is influenced by various environmental, physical and chemical parameters.

4.2 A Hydro-thermodynamics Model

The intrinsic self-healing within a crack in cementitious materials involves the complex interplay of different chemo-physical processes. As illustrated in **Figure 4.1**, when water percolates through a crack in cementitious materials, the water-material interaction causes dissolution and leaching of minerals (e.g. Ca^{2+}, Na^{+}, K^{+}, $Al(OH)_4^{-}$, SO_4^{2-}, $H_3SiO_4^{-}$) from the cementitious matrix into the solution [7]. The gaseous carbon dioxide (CO_2) can also dissolve in the solution mainly as bicarbonate (HCO_3^{-}) and carbonate (CO_3^{2-}). Once the solute concentration reaches above the solubility equilibrium, precipitation of self-healing compounds occurs at the crack walls, resulting in localized changes in crack apertures along crack depth. The self-healing process is thus dynamically controlled by a combination of three mechanisms: the advective transport of ions as reactants caused by a flow of the aqueous solution, the molecular diffusion of dissolved reactants due to the concentration gradient, and the kinetics of chemical reactions occurring at the water-material interfaces controlled by thermodynamics. The relative magnitudes of the timescales associated with the advection-diffusion transport phenomena and the chemical reactions at crack walls determine the nature of intrinsic healing process and crack profile evolution.

In this study, we present a coupled hydro-thermodynamics model to simulate the evolution of crack profile along crack depth as a function of time. The model incorporates fluid flow, dissolved ion transport, and local reaction rate coefficients of calcium carbonates ($CaCO_3$) and calcium silicate hydrates (C-S-H) as major healing products. The model also considers the negative feedback between mineral precipitation and local alteration of transport properties in the crack. As illustrated in **Figure 4.1(a)**, the dissolved ions that serve as self-healing reactants can transport from outside of the crack, or from the crack walls. The first scenario is more related to

the precipitation of $CaCO_3$ as healing product. This is because calcium is abundant in Portland cement and cement hydration products; Ca^{2+} ions can leach out from the bulk cementitious matrix when it is in contact with water. CO_3^{2-} ions also come from outside of the crack due to dissolved atmospheric CO_2 in water. The second scenario is mainly related to the growth of C-S-H due to continued hydration occurring at the water-material interface in the crack. These two mechanisms were separately considered in this model. For simplicity, the growth competition between $CaCO_3$ precipitation and continued hydration was not considered.

The governing equations for ions transport, precipitation rate, and crack aperture evolution are solved using combined analytical and numerical methods [8][9]. Considering a Newtonian fluid of viscosity μ flowing through a channel between two statistically homogeneous, symmetrical plates representing two faces of a crack, as shown in **Figure 4.2**. The solute content of the fluid is described by the ion concentration c. It is assumed that the flow density and viscosity are constant, and the flow velocity $\mathbf{u}$ is so small that fluid inertia can be neglected. The Reynolds number Re is very small, because we are considering small length scales and treating flows of very small velocity (i.e. creeping flows). With the assumption of $Re \ll 1$, the Navier-Stokes equations for incompressible fluid are reduced to [10]:

$$\nabla \cdot \mathbf{u} = 0 \tag{4.1}$$

$$\mu \nabla^2 \mathbf{u} = \nabla P \tag{4.2}$$

where $\mathbf{u}$ is the velocity vector, P is the dynamic pressure, and μ is the dynamic viscosity of the fluid (i.e. water).

The mass transport of dissolved mineral ions in the incompressible fluid is described by the advection-diffusion equation [11]:

$$\frac{\partial c}{\partial t} + \nabla \cdot (c\mathbf{u} - D\nabla c) = 0 \tag{4.3}$$

where c is the volumetric solute concentration, and D is the molecular diffusion coefficient of the solute. Depending on the solute concentration and the local reaction rate coefficient, precipitation can occur on the crack walls, resulting in the local alteration of crack aperture. This in turn leads to a change in the local transmissivity of the crack, which is defined as flow rate per unit width per unit gradient. The boundary condition for the solute concentration c at the water-crack interface is described by an irreversible surface reaction [12]:

$$\frac{\partial b}{\partial t} = \frac{R^{\mathrm{CaCO_3}}(c)}{\alpha \dfrac{\rho}{MW}} \tag{4.4}$$

where b is the local half-aperture of the crack, α is the stoichiometric coefficient that represents the moles of free Ca^{2+} and CO_3^{2-} ions forming a unit mole of solid $CaCO_3$ mineral, ρ is the density of the reacting mineral ($\rho^{\mathrm{CaCO_3}} = 2.71\,\mathrm{g/cm^3}$), and MW is the mineral molecular weight ($MW^{\mathrm{CaCO_3}} = 100$ g/mol). The local reaction rate of calcite, $R^{\mathrm{CaCO_3}}(c)$, controlled by the concentrations of the Ca^{2+} and CO_3^{2-} ions in the solution, is approximated based upon idealized first-order reaction kinetics [13][16]:

$$R^{CaCO_3}(c) = k \cdot A_R \left(\frac{c\,|_{y=b}}{c_{eq}} - 1\right) \tag{4.5}$$

where k is the empirical reaction rate constant, A_R is reactive surface area per unit area of crack surface ($k \cdot A_R$ = 2.62 × 10^{-10} mol/cm^2·s [16]), and c_{eq} is the solubility equilibrium ($c_{\mathrm{eq}}^{\mathrm{CaCO_3}} = 0.013$ g/L at 25 ˚C) above which precipitation occurs. Equation (4.5) is readily modified to account for more complex nonlinear reaction kinetics. Equations (4.1-4.5) provide the mathematical

framework that describes reactive flow through a crack that leads to a crack self-healing process. The motion of the fluid is described by Equations (4.1) and (4.2). The mass balance of the solute in solution is described by Equation (4.3) and the mass balance for the solute precipitation or dissolution at the crack wall is controlled by Equations (4.4) and (4.5). The model thus couples physical transport of self-healing reactants with chemical kinetics of self-healing process to predict the change in crack profile with time due to $CaCO_3$ precipitation.

In addition to $CaCO_3$ precipitation, another major self-healing mechanism is the nucleation and growth of cement hydration products such as C-S-H and portlandite ($Ca(OH)_2$). In this study, the growth rates of cement hydration products are derived by fitting the experimental data recently measured by Grossier and Van Vliet [17] and Ferralis et al. [19]. Direct observation and quantification of cement clinker dissolution and precipitation kinetics have been a challenge. The researchers used time-lapse video microscopy to record tricalcium silicate (C_3S) particle hydration that forms C-S-H and $Ca(OH)_2$. The direct visualization data clearly show the two stages of cement hydration: the rapid growth and consolidation. The continuous and rapid growth within the first 4 hours is approximately linear with time, which is interpreted as interface-controlled kinetics. When a continuous layer of hydration product surrounds the unreacted core of cement particle, a transition from interface-limited to diffusion-limited growth is observed. The outward diffusion of dissolved ions from cement and the inward diffusion of water to reach unreacted cement cores become slower, as the layer of hydration product around the cement particles become thicker. During this consolidation stage, the growth is severely retarded or even ends. In the present model, we only consider the rapid growth stage based on the assumption that during the diffusion-limited stage the volumetric growth rate of hydration products is significantly smaller. The measured mean growth rate of hydration products formed

away from C_3S particles during the interface-controlled reaction stage [19] is fitted by least-square power law, yielding Equation (4.6). This change of half aperture of a crack due to local growth of hydration products is described by Equation (4.7). The volumetric change is averaged along the horizontal grid size (10 μm).

$$G^{\text{hydration}}(t) = 0.063t^{-0.37} \; (t \le 240\,\text{min}) \tag{4.6}$$

$$\frac{\partial b}{\partial t} = \gamma G^{\text{hydration}}(t) \tag{4.7}$$

where $G^{\text{hydration}}$ is the growth rate of hydration products (μm/min), γ is the unhydrated cement ratio that can be determined based on experiment measurement or hydration model. In this study, γ was measured using micro-CT technique as described in Section 2.2.3.

The initial conditions are given in Equations (4.8-4.13):

$$c|_{z=0} = c_{\text{in}} \tag{4.8}$$

$$\frac{\partial c}{\partial y}|_{y=0} = 0 \tag{4.9}$$

$$\frac{\partial c}{\partial t}|_{t=0} = 0 \tag{4.10}$$

$$\mathbf{u}|_{t=0} = \mathbf{u}_{\text{in}} \tag{4.11}$$

$$\mathbf{u}|_{y=\pm b} = 0 \tag{4.12}$$

$$b|_{t=0} = b_0 \tag{4.13}$$

where c_{in} is the solute concentration at the crack inlet, $\mathbf{u}_{\text{in}}$ is the fluid velocity at the crack inlet, and b_0 is the half aperture of the initial crack before self-healing occurs.

The differential equations were numerically solved using finite difference method [9][20] with a constant longitudinal grid size (10 μm) along crack depth, the element number of 1000 and the time interval of 1 minute. For the flow equation, a central finite difference discretization was used. The diffusion and advection terms in the ion transport equation were approximated by a bounded unwinding scheme [21]. The precipitation kinetics is related to the concentration field at the water-material interface in the crack. The crack profile is updated by changing the position of each elementary interfacial area according to Equations (4.4-4.5). The computation algorithm is shown in **Figure 4.3**. The indices *i* and *j* refer to the element number and the relative time of the process, respectively. The computation outputs a profile of crack aperture as functions of horizontal distance *z* and time *t*.

4.3 Simulation Results and Discussion

4.3.1 Model Validation

To evaluate the hydro-thermodynamics model, we simulated flow of the experimental fluid through the idealized initial fracture fields and directly compared the simulations to the experimentally measured crack evolution descripted in last chapter. μCT measurements and image analysis provided accurate (±2 μm) description of crack morphology and aperture field before and after 10 days of self-healing, as shown in **Figure 4.4**. The upper wall and lower wall of the crack in sample T2 were mathematically split after the crack was segregated from other phases, and are presented in **Figure 4.4(a)** and **(b)**. The heterogeneity of the crack walls was clearly visualized. After the reactive transport-healing experiment, it was observed that newly formed healing products precipitated on the crack walls, leading to increased heterogeneity of crack profile and the alteration of crack aperture field. **Figure 4.4(c)** shows the quantitative

mapping of the crack aperture field (in X-Z plane) before and after self-healing. The crack aperture is defined along the y-direction. The inlet of the crack corresponds to Z = 0. The crack aperture at each pixel is calculated as:

$$2b = Y_1 - Y_0 \tag{4.14}$$

where 2b is the crack aperture, Y_1 is the location of the crack upper wall, and Y_0 is the location of the crack lower wall. The color scale represents the magnitude of the aperture ranging from 10 μm to 100 μm.

The comparison between the initial and final aperture field reveals the three-dimensional self-healing extent of the crack. A pervasive self-healing along the crack walls and reduction in crack apertures were observed, but the extent of self-healing was larger near to the crack inlet than deep inside the crack, reflected by the transition from blue color to green and yellow along the Z axis. This nonhomogeneous healing phenomenon suggests varying precipitation of healing products along crack depth.

Figure 4.5 shows the crack healing ratios for experiments T1, T2, T3, and T1Y with the corresponding simulations. The results demonstrate a similar non-uniform, decreasing healing trend along the crack depth or flow direction. All analyses give comparable results. Both experiments and simulations indicate more rapid mineral growth at the inlet of the fracture. For all simulated cases there is a characteristic length Z^* at which the healing rate decrease steeply. In the case of T1, the characteristic length Z^* is reached at about 0.5 mm from the inlet. Changes of the input parameters have a significant effect on the healing patterns. We illustrate the sensitivity to the different parameters later.

From **Figure 4.5**, it can be also noticed that all the model calculations show a slightly stronger trend than the experimental measurements near the crack inlet region, but a lower healing ratio at the crack deep region. There are several reasons that could cause this discrepancy. First, in the model we mainly considered the calcite precipitation and simplify the calcite crystal growth as a first order liner reaction. But in reality, the fracture surface roughness, the fracture local mineral heterogeneity, and the water supersaturation condition could all affect the temporal precipitation kinetics. Another reason for the underestimation of the healing rate deep inside the crack is that our simulations stopped once the facing precipitates fronts touched. But in natural cracks flow does not stop when the crack is sealed in one spot due to its heterogeneous aperture. There are usually more tortuous paths available around the sealed spots. In addition, since the real healing products is a porous structure, the fluid flow still can penetrate through the partially sealed layer, resulting in more materials further precipitated deep inside the channel over time. Furthermore, the empirical equations that describe the unhydrated cement ratio and the continued hydration product growth rate can be another cause for the minor discrepancy. Despite these differences, the general features of all experiments are predicted quite well by the simulations. This model can satisfy our primary interest for this paper which is to elucidate the impacts of different parameters on the crack healing rates and patterns.

4.3.2 Parametric Study

Figure 4.6 shows the simulated evolution of the fracture half-aperture with control parameters u_{in} = 1 μm/s, and SI = 1.2. **Figure 4.6(a)** exhibits the tension crack with initial crack wall as a flat line, and **Figure 4.6(b)** shows the bending crack with a constricted initial crack width. The flat crack has a constant initial crack opening at 0.3 mm, while the crack opening for case (b) is linearly decreased from 0.4 mm to 0.2 mm. We compare these two cases because they

have the same initial crack volume. The red line represents the initial upper crack wall at time t = 0. Each grey line represents a certain time increment. Over time, the healing products gradually precipitate in the crack, causing the interface moving downward and finally the sealing of the inlet. The crack aperture b decreases very rapidly near inlet region, increasingly so over time t. The fracture deep inside, for example when z > 6 mm, remains almost constant at its initial value b_0 over time. By integrating the healing ratio parallel to the flow direction Z, the results show that the final healing ratio for the initially flat crack is 0.183 which is smaller than 0.307 for the initially constricted crack. This is due to the fact that the bending crack aperture b_0 at inlet is larger than the flat fracture. Therefore, the close time for flat fracture is faster than that for linearly constricted fracture and less flux can enter into the crack deep region.

Changes of the input parameters can significantly influence the fracture healing patterns. **Figure 4.7** gives the impact of initial crack width on the healing ratio. It can be seen that an increase of initial crack width b_0 results in a higher healing potential if the input saturated flow is continuously sufficient. When b_0 is larger, the precipitation can be distributed over a longer distance and the fracture can be sealed more uniformly. This is because that the precipitation takes longer time to seal the wider fracture, while narrow fracture can be sealed more rapidly. Therefore, more mineral can transport into the wider fracture, leading to a higher healing ratio even though the denominator b_0 is larger. For example, in our simulation it only takes less than 20 hour to close the crack with initial b_0 = 0.025 mm, but the closure time for sealing the crack with b_0 = 0.5 mm is more than 5400 hours. If we control the reaction stop time as the same for all apertures, for instance t_{stop} = 16.8 h as shown in **Figure 4.7(b)**, it can be seen that the healing ratio for larger crack is much lower than narrower crack. This indicates that although a larger crack increases the potential to be healed homogenously, it needs very large fluid volume and

time scale to produce enough precipitated materials. However, it has to be kept in mind that for concrete structure in nature environment, in most cases the precipitated minerals come from the dissolution of concrete material itself, so it is very difficult to maintain the ambient conditions especially the supersaturation condition as our laboratory experiments and simulations. Consequently, most of the previous experiments that observed the healing phenomena from sample surface or indirectly measured the healing ratio by permeability change found that narrower cracks are more likely to be healed.

The change of relative supersaturation has a similar effect on the fracture healing pattern. As shown in **Figure 4.8(a)**. A lower supersaturation allows more homogenous sealing over a longer distance, but requires much longer time scale to reach the sealing. The crack inlet closure time t_{stop} = 25.2 h, 227.8 h, and 7912.8 h for relative supersaturation SI = 2, 1.2, and 0.5, respectively. Equation (5) suggests that the precipitation rate is positively correlated to the relative supersaturation. An increase in supersaturation results in a faster crystal growth. As a result, the crack inlet region can be closed more rapidly and thus the crack cannot be filled over a very long distance. However, if the reaction time is controlled to be identical as shown in **Figure 4.8(b)**, higher supersaturation results in more solute precipitating and a higher healing ratio. **Figure 4.9** shows the influence of flow velocity on the fracture evolution. For high flow velocity, precipitation in the fracture is more uniform and the fracture inlet region close to throughflow less rapidly. This is because the reaction rate is relatively small comparing to the flow velocity, and thus the dominant effect is that of a faster advection, which can move the solute to a larger distance while losing the same concentration. On the contrary, smaller ratio of advection to reaction, precipitation in the fracture is highly nonuniform and the final healing ratio is much

lower. Again if we set the reaction time very short, it can be seen that the change of fracture aperture under high flow velocity can hardly be noticed.

The influence of unhydrated cement ratio or sample age on the healing ratio and healing pattern is shown in **Figure 4.10**. It can be seen that the continued hydration contributes to the entre crack, and the younger sample has a higher healing potential. Nevertheless, the hydration product growth outside of the original reacting clinkers is very limited. Even assuming with 100% unreacted cement particles on the crack wall, the increase of healing ratio due to hydration is only about 10% for a 50 μm crack. For old sample, especially with larger crack width, the contribution of continued hydration to the crack volume change is negligible.

4.4 Summary

The simulation modelling in this study is rigorously based on physical and chemical principles. The presented results may provide a mechanistic explanation and yield important information about the complex autogenous healing processes. These results can be used as a basis for the development of more complex models to fully understand water-concrete interactions in cracks. Here we list some parameters that have not been taken into account in this paper, which can be studied as future work:

- For simplicity, the precipitation reaction in this study are described by a linear kinetic surface reaction model. More complex, nonlinear models that characterize mineral precipitation are readily introduced in the simulation.
- The competition between the carbonation and continued hydration could be involved in the future study. And more parameters that might influence the hydration product growth can be considered.

- The influence of fracture aperture heterogeneity on the flow transport profile is neglected in this study. Next step the two surfaces of a random crack can be characterized mathematically and added as the initial boundary conditions.
- The dependence of reaction rate on other parameters, such as crack surface roughness and mineral distribution, can be incorporated in the model.
- The simulation ending point can be modified by considering the continued flow penetration through the porous sealing layer.

The presented results show that there is a significant decreasing trend for the healing ratio along the flow transport direction. This non-uniform healing phenomenon is because the crystal growth activity is directly related to the concentration of the solution. As the flow travels through the crack, the continued crystallization process leads to a decline in the supersaturation and the associated growth rate along the crack depth. This progressive depletion of solute in the moving fluid causes the crack to be firstly sealed at the inlet region. At the time of crack surface sealing, large portions of the deep region of the crack remains devoid of healing products, which suggest that the quickly sealing part significantly limits long range fluxes to deliver enough dissolved minerals to uniformly fill the crack downstream. The contribution of the continued hydration on the crack volume change is depending on the unhydrated cement ratio. But even for very young sample, the healing ratio change due to hydration products growth is still insignificant.

The numerical study shows that the initial crack aperture, the fluid velocity, and the supersaturation condition have profound influences on the healing patterns. A large initial crack width, low saturation content, and fast flow rate can enhance the potential to heal a crack greatly and homogenously, but require a much larger volume of mineral resource in the solution and longer temporal scale.

Figures

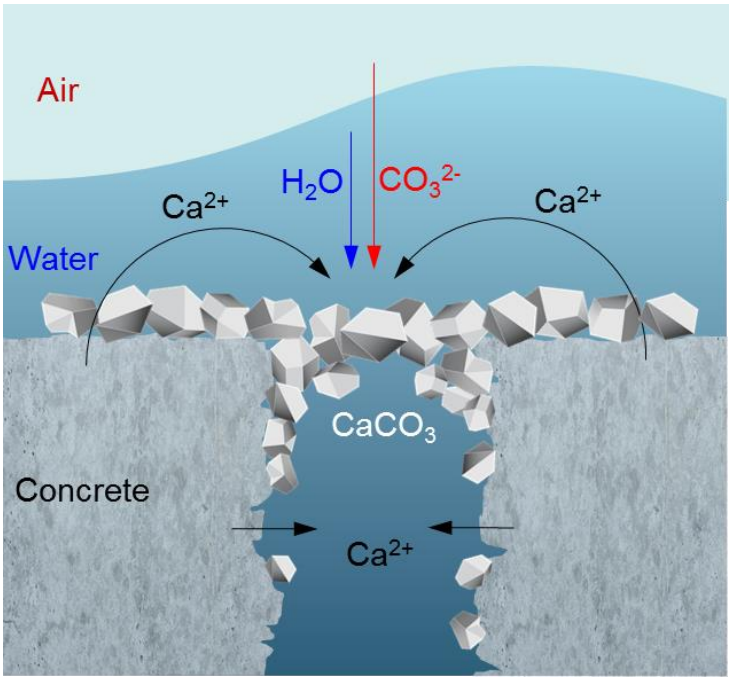

(a)

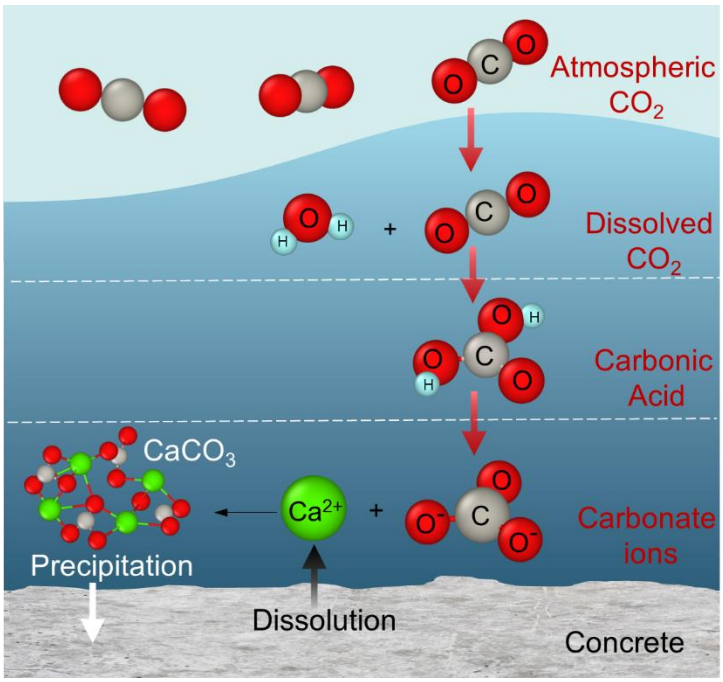

(b)

Figure 4.1 A schematic view of intrinsic self-healing mechanism in cementitious materials: (a) micro crack scale., (b) molecular scale.

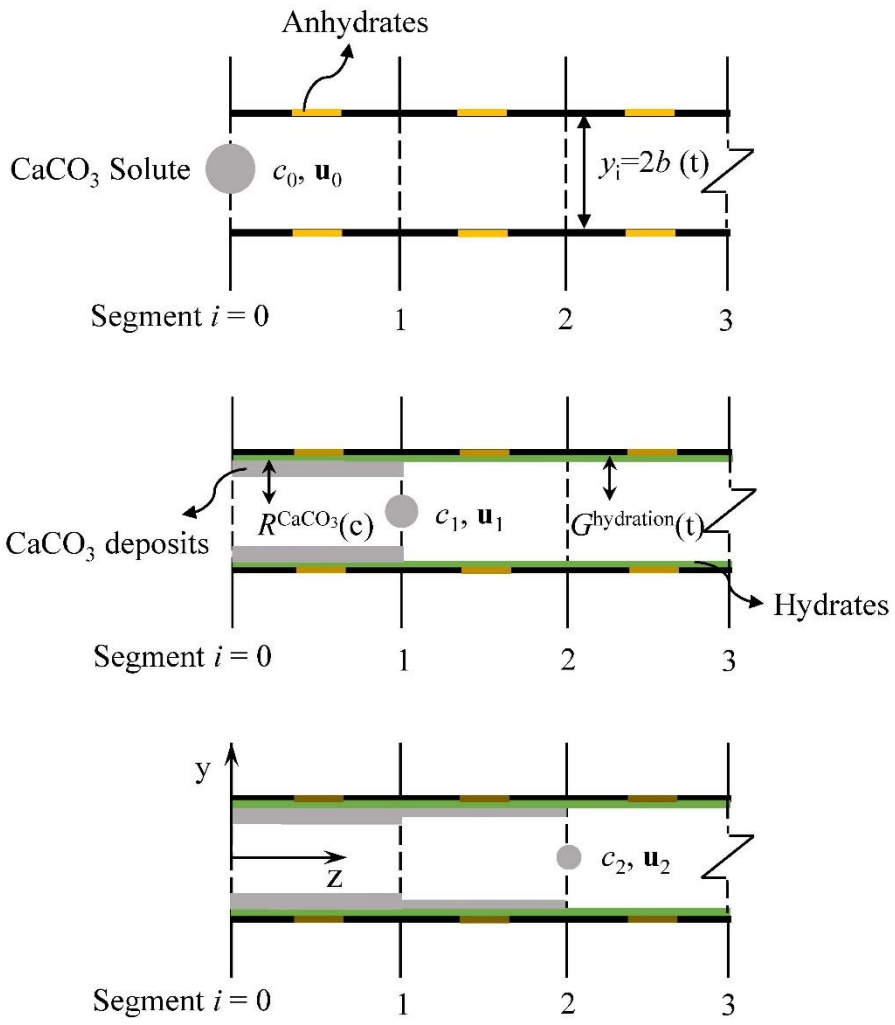

Figure 4.2 Schematic diagram of the crack-solution system for numerical simulation.

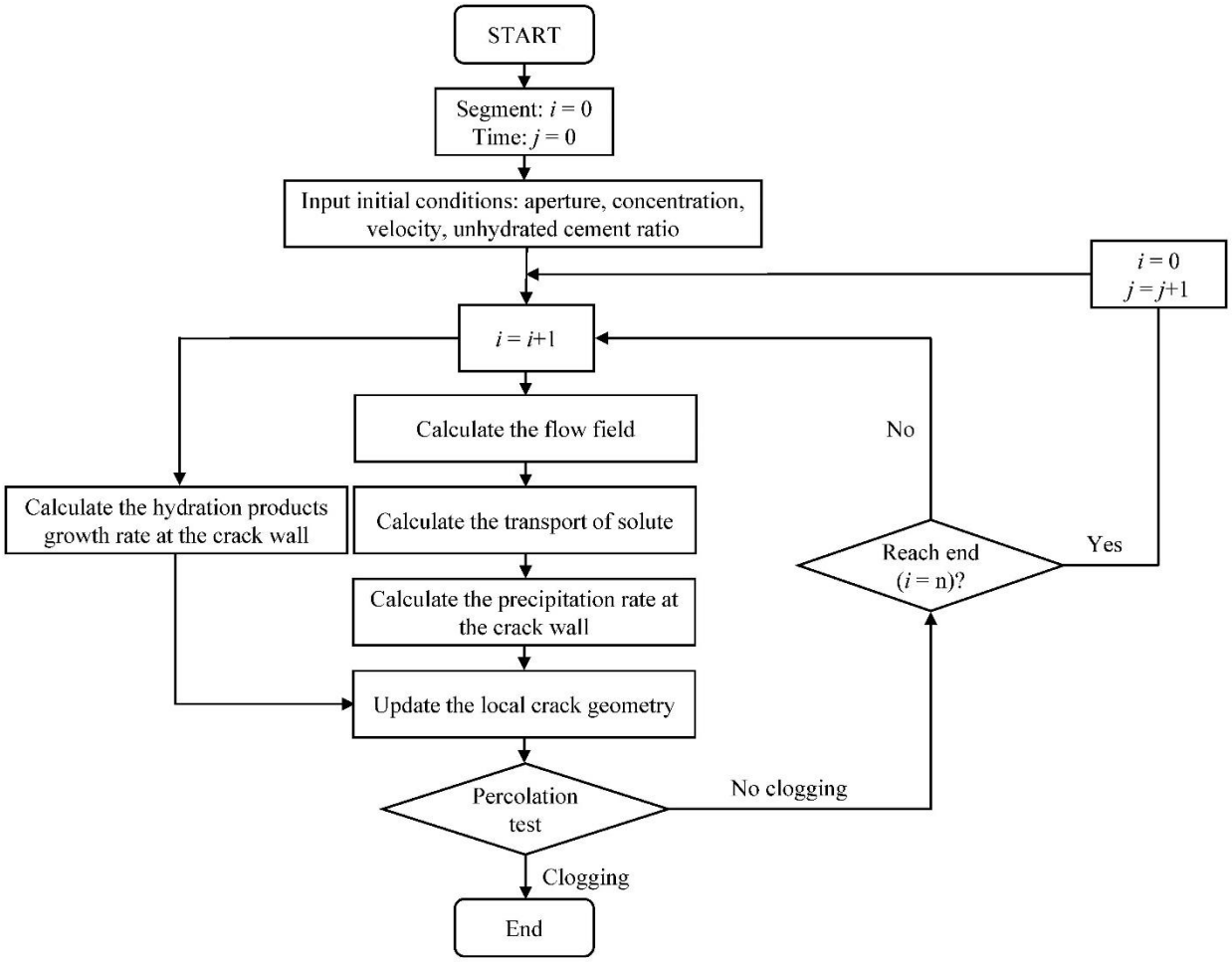

Figure 4.3 Flow chart of the numerical simulation routine.

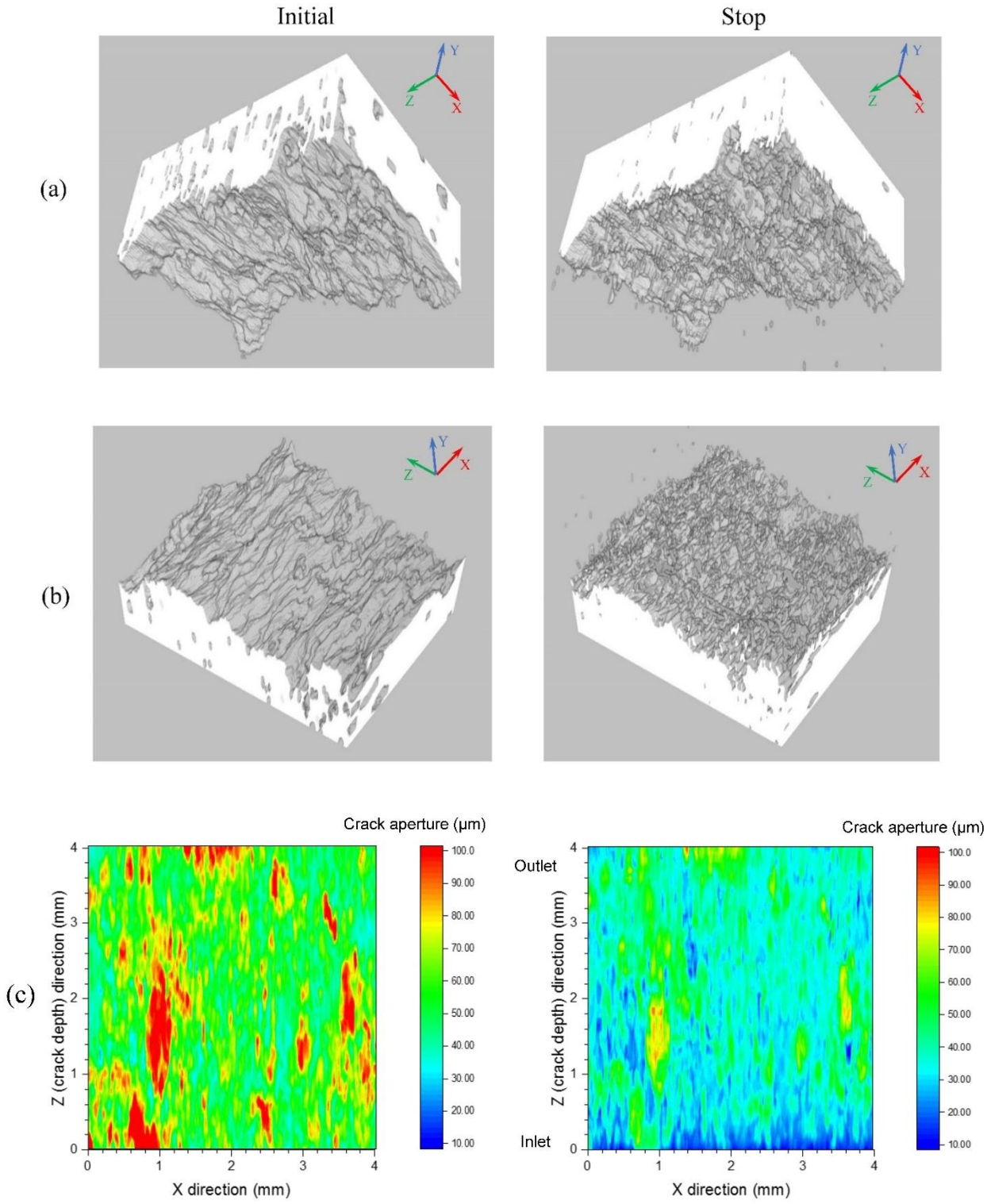

Figure 4.4 Crack morphology of sample T2 before and after self-healing: (a) crack upper wall, (b) crack lower wall, and (c) crack aperture field.

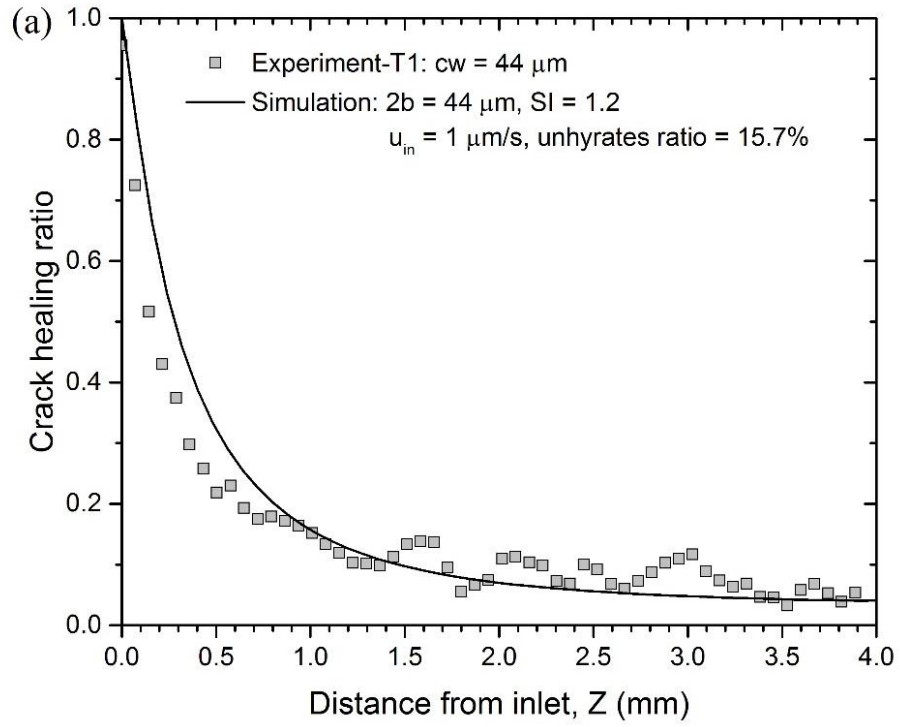
(a)
Experiment-T1: cw = 44 μm
Simulation: 2b = 44 μm, SI = 1.2
u_{in} = 1 μm/s, unhyrates ratio = 15.7%
Crack healing ratio
Distance from inlet, Z (mm)
0.0
0.2
0.4
0.6
0.8
1.0
0.0
0.5
1.0
1.5
2.0
2.5
3.0
3.5
4.0

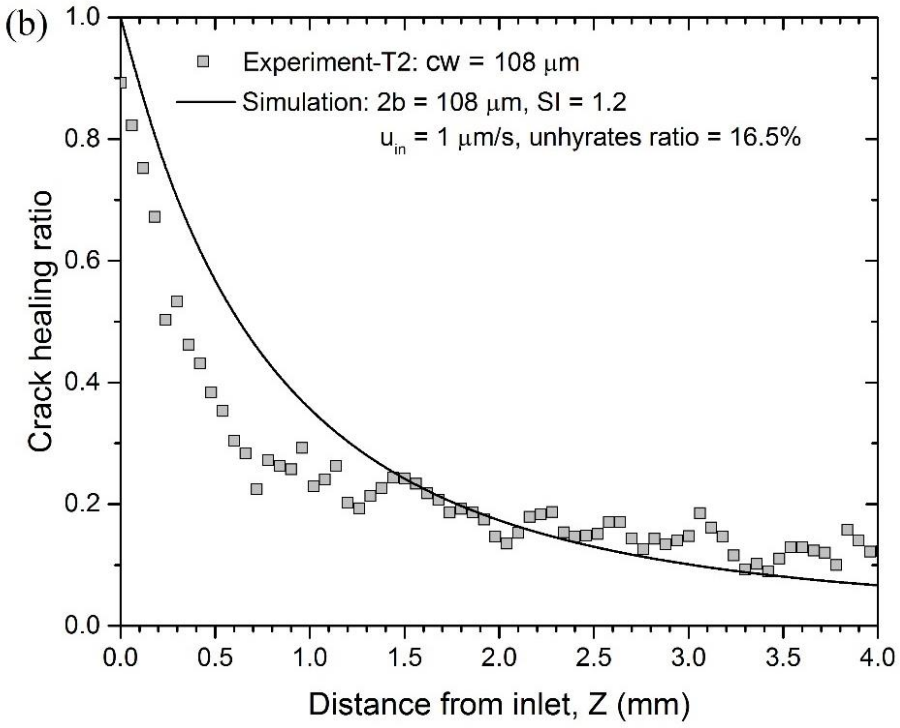
(b)
Experiment-T2: cw = 108 μm
Simulation: 2b = 108 μm, SI = 1.2
u_{in} = 1 μm/s, unhyrates ratio = 16.5%
Crack healing ratio
Distance from inlet, Z (mm)
0.0
0.2
0.4
0.6
0.8
1.0
0.0
0.5
1.0
1.5
2.0
2.5
3.0
3.5
4.0

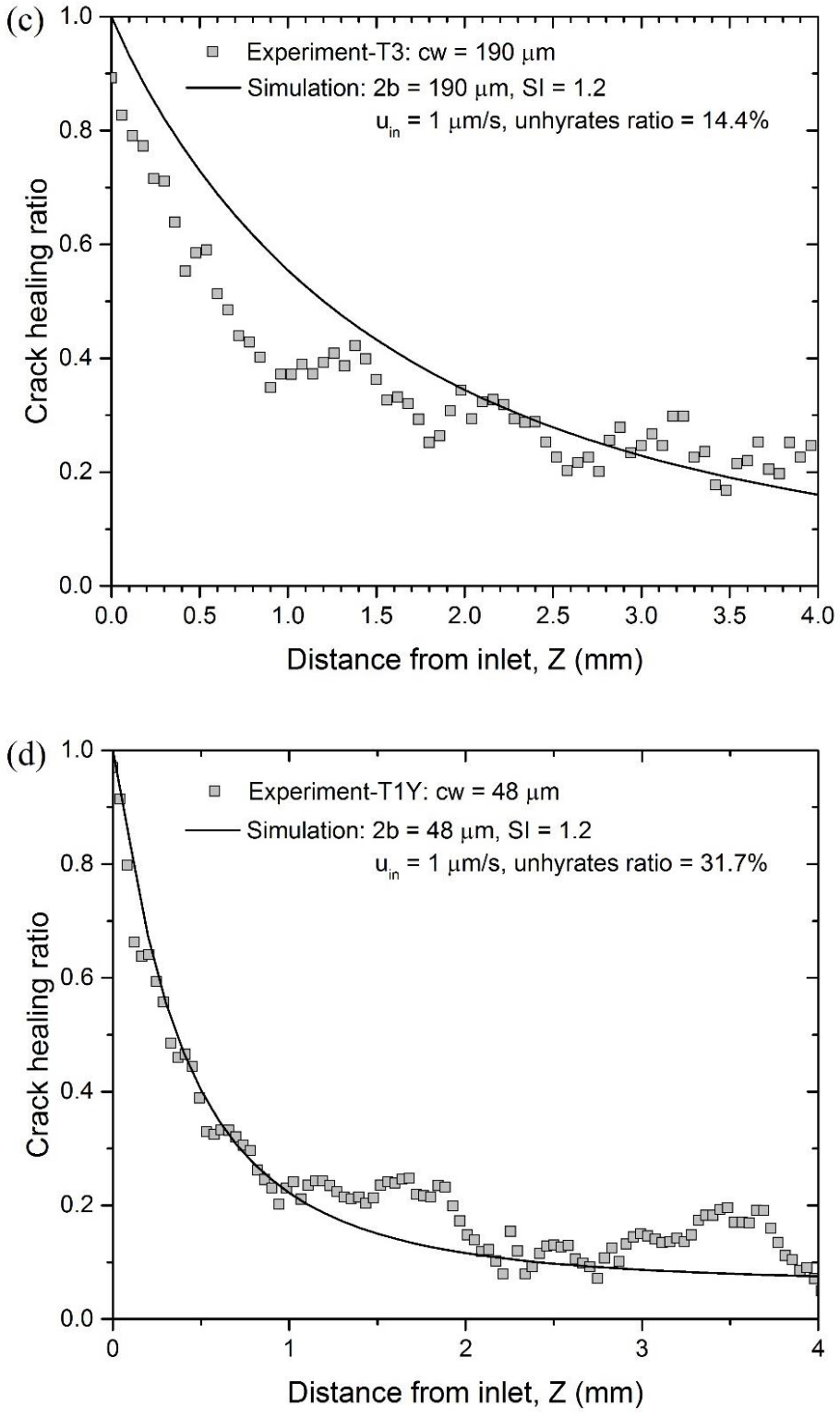

Figure 4.5 Experimental measured (dots) and simulated (lines) crack healing ratios along the crack depth direction.

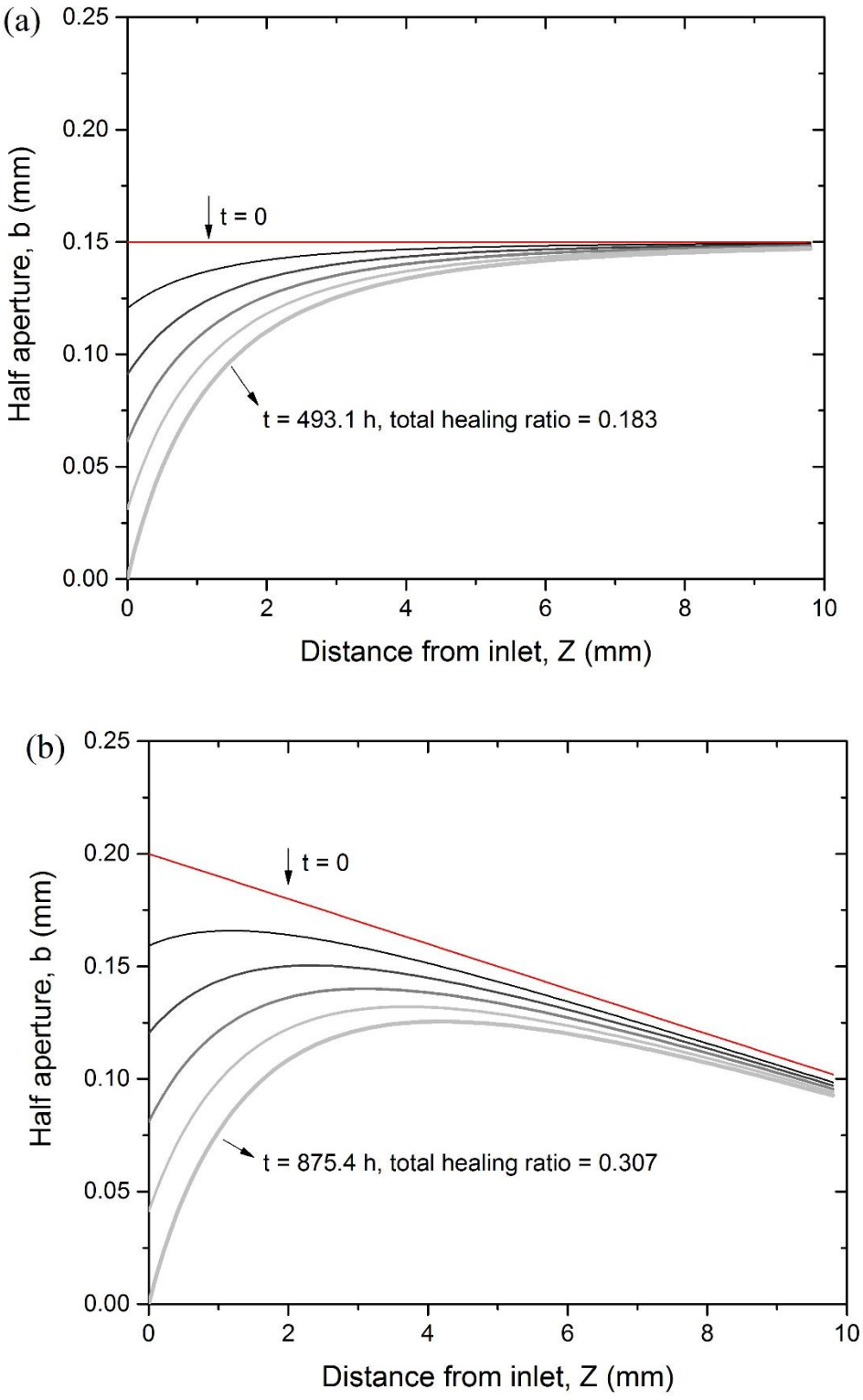

Figure 4.6 Numerical simulation of changes in fracture aperture for (a) flat tension crack and (b) constricted bending crack at the conditions of SI = 1.2, u_{in} = 1 μm/s.

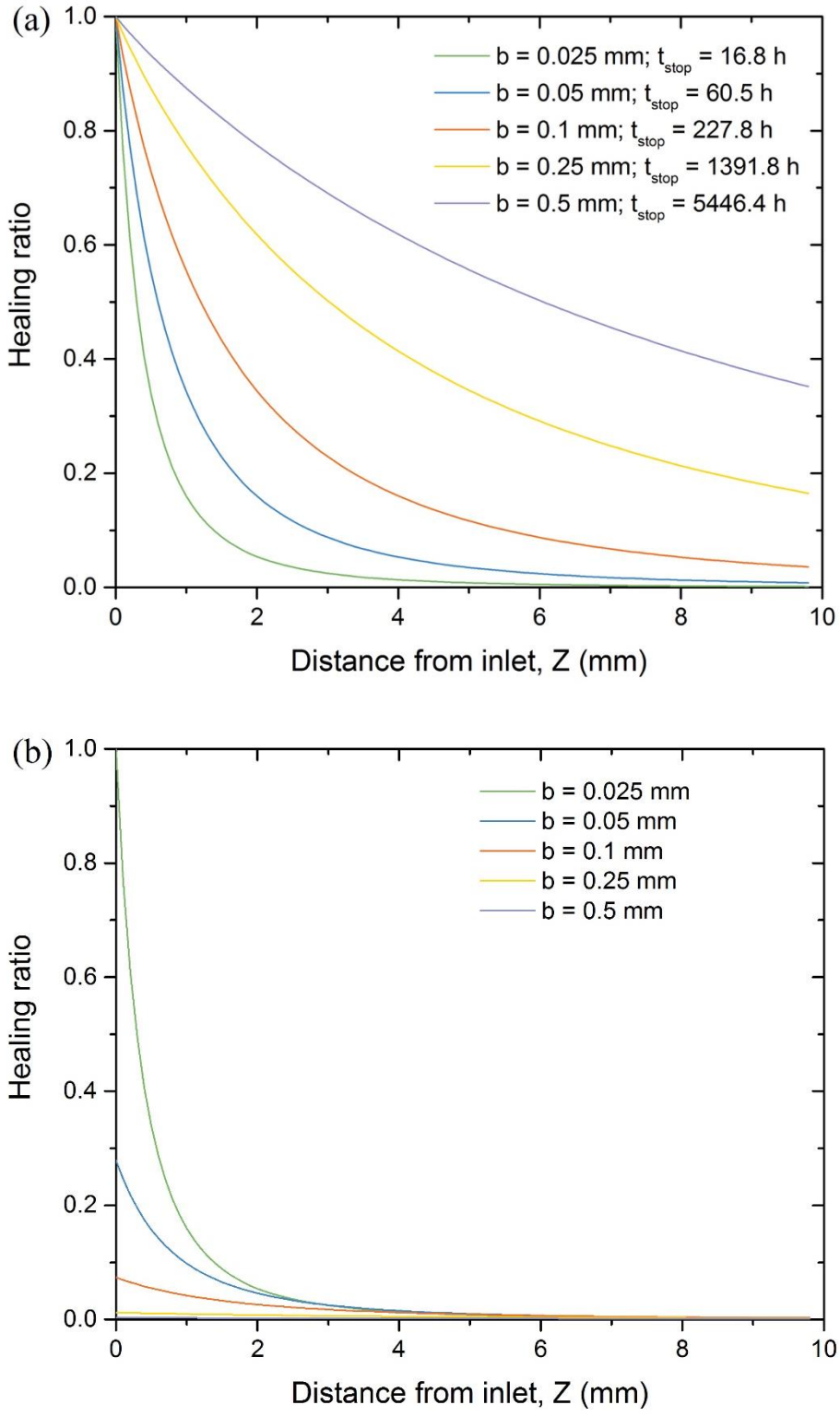

Figure 4.7 The influence of change of initial crack width on the healing ratio (u_{in} = 1 μm/s, *SI* = 1.2): (a) at the end of simulation; (b) at the same stop time (t_{stop} = 16.8 h).

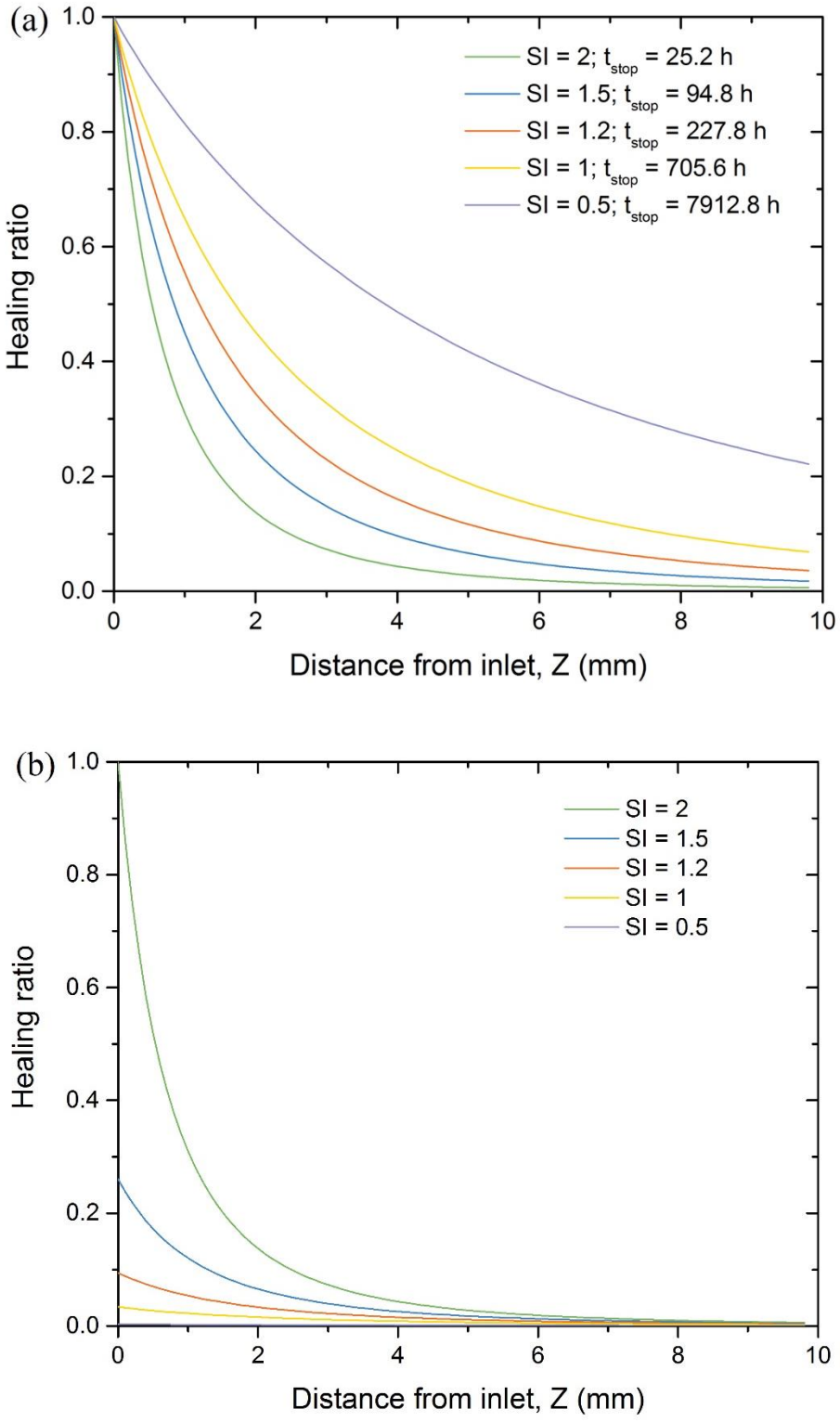

Figure 4.8 The influence of change of initial supersaturation on the healing ratio (b_0 = 0.1 mm, u_{in} = 1 μm/s): at the end of simulation; (b) at the same stop time (t_{stop} = 25.2 h).

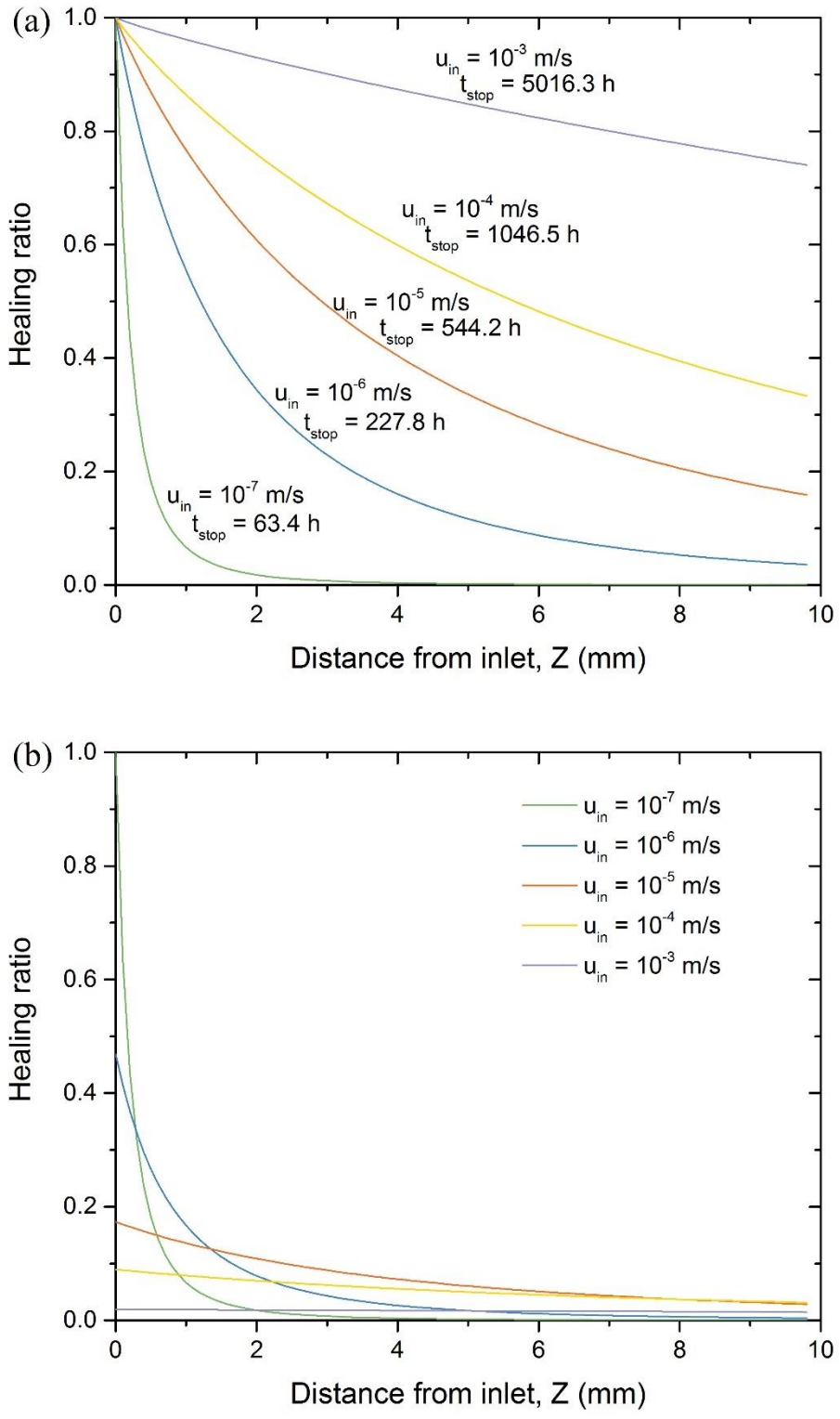

Figure 4.9 The influence of change of initial flow velocity on the healing ratio (b_0 = 0.1 mm, *SI* = 1.2): at the end of simulation; (b) at the same stop time (t_{stop} = 63.4 h).

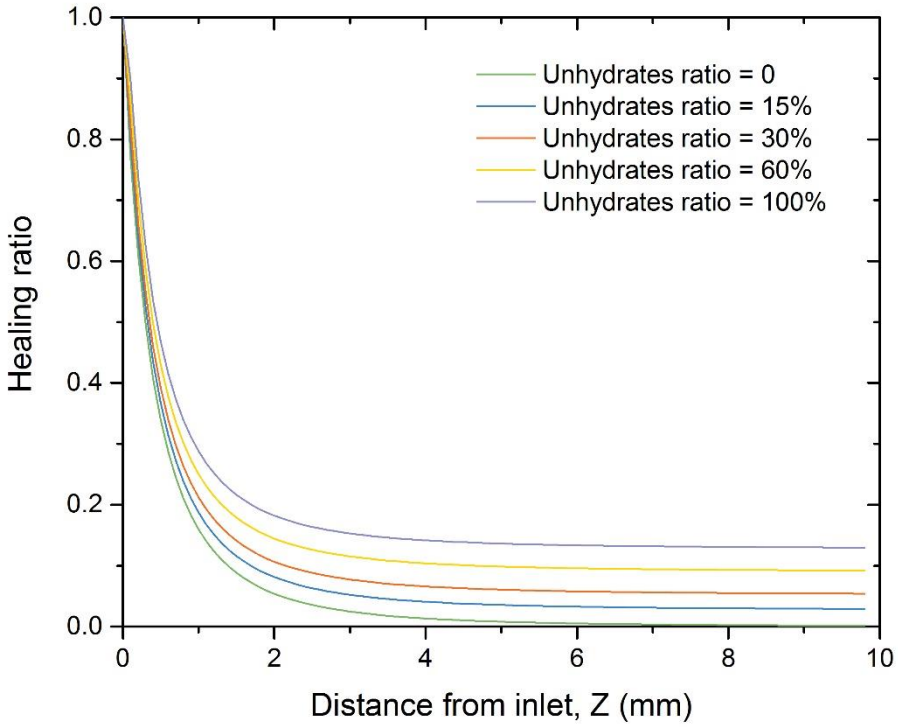

Figure 4.10 The influence of the undyrated cement ratio (b_0 = 0.025 mm, SI = 1.2, u_{in} = 1 μm/s).

References

[1] Huang, H., Ye, G., & Damidot, D. (2013). Characterization and quantification of self-healing behaviors of microcracks due to further hydration in cement paste. Cement and Concrete Research, 52, 71-81.

[2] Chitez, A. S., & Jefferson, A. D. (2016). A coupled thermo-hygro-chemical model for characterising autogenous healing in ordinary cementitious materials. Cement and Concrete Research, 88, 184-197.

[3] Edvardsen, C. (1999). Water permeability and autogenous healing of cracks in concrete, ACI Materials Journal, 96(4), 448-454.

[4] Fan, S., & Li, M. (2014). X-ray computed microtomography of three-dimensional microcracks and self-healing in engineered cementitious composites. Smart Materials and Structures, 24(1), 015021.

[5] Van Tittelboom, K., Gruyaert, E., Rahier, H., & De Belie, N. (2012). Influence of mix composition on the extent of autogenous crack healing by continued hydration or calcium carbonate formation. Construction and Building materials, 37, 349-359.

[6] ter Heide, N., & Schlangen, E. (2007, April). Self-healing of early age cracks in concrete. In First international conference on self-healing materials. Springer, Dordrecht.

[7] Rothstein, D., Thomas, J. J., Christensen, B. J., & Jennings, H. M. (2002). Solubility behavior of Ca-, S-, Al-, and Si-bearing solid phases in Portland cement pore solutions as a function of hydration time. Cement and Concrete Research, 32(10), 1663-1671.

[8] Bekri, S., Thovert, J. F., & Adler, P. M. (1997). Dissolution and deposition in fractures. Engineering Geology, 48(3), 283-308.

[9] Dijk, P., & Berkowitz, B. (1998). Precipitation and dissolution of reactive solutes in fractures. Water Resources Research, 34(3), 457-470.

[10] Fox, R. W., McDonald, A. T., & Pritchard, P. J. (1985). Introduction to fluid mechanics (Vol. 7). New York: John Wiley & Sons.

[11] Roos, H. G., Stynes, M., & Tobiska, L. (2008). Robust numerical methods for singularly perturbed differential equations: convection-diffusion-reaction and flow problems (Vol. 24). Springer Science & Business Media.

[12] Detwiler, R. L., & Rajaram, H. (2007). Predicting dissolution patterns in variable aperture fractures: Evaluation of an enhanced depthed depth (Vol. 24). Springer Science & Business Media.Busi& Bus

[13] Nancollas G. H. and Reddy M. M. (1971) The crystallization of calcium carbonate II: Calcite growth mechanism. J. Colloid Interface Sci.37, 843–830.

[14] Wiechers, H. N. S., P. Sturrock, and G. V. R. Marais. (1975). Calcium carbonate crystallization kinetics. Water Research, 9(9), 835-845.

[15] Kazmierczak, T. F., Tomson, M. B., & Nancollas, G. H. (1982). Crystal growth of calcium carbonate. A controlled composition kinetic study. The Journal of Physical Chemistry, 86(1), 103-107.

[16] Inskeep, W. P., & Bloom, P. R. (1985). An evaluation of rate equations for calcite precipitation kinetics at pCO2 less than 0.01 atm and pH greater than 8. Geochimica et Cosmochimica Acta, 49(10), 2165-2180.

[17] Plummer, L. N., & Busenberg, E. (1982). The solubilities of calcite, aragonite and vaterite in CO2-H2O solutions between 0 and 90 C, and an evaluation of the aqueous model for the system CaCO3-CO2-H2O. Geochimica et cosmochimica acta, 46(6), 1011-1040.

[18] R. Grossier and K.J. Van Vliet: Visualizing hydration products. Concrete Sustainability Hub Research Profile Letter. (MIT, Cambridge, MA, 2012).
[19] Ferralis, N., Jagannathan, D., Grossman, J. C., & Van Vliet, K. J. (2015). Unintended consequences: Why carbonation can dominate in microscale hydration of calcium silicates. Journal of Materials Research, 30(16), 2425-2433.
[20] Lasaga, A. C. (2014). Kinetic theory in the earth sciences. Princeton University Press.
[21] Ferreira, V. G., De Queiroz, R. A. B., Lima, G. A. B., Cuenca, R. G., Oishi, C. M., Azevedo, J. L. F., & McKee, S. (2012). A bounded upwinding scheme for computing convection-dominated transport problems. Computers & Fluids, 57, 208-224.

CHAPTER 5 MATERIALS DESIGN FOR ROBUST SELF-HEALING CAPACITY

5.1 Introduction

The development of self-healing cementitious materials can open a new world of opportunities for resilient concrete infrastructure under various service loading conditions. However, the self-healing potential in conventional concrete is significantly limited by the localized fracture, the unsatisfactory healing extent, and the non-homogenous healing kinetics. A key motivation of this dissertation is to develop novel self-healing cementitious materials with enhanced intrinsic healing capacity, allowing for self-repair after multiple damage events.

Guided by the findings from the previous chapters about healing mechanisms, this work combined the micromechanics-based strain-hardening material design theory with cement chemistry to design new cementitious composites uniquely featuring robust and repeatable self-healing capacity. The fundamental hypothesis (**Figure 5.1**) is that robust and repeatable self-healing in cementitious materials can be possible if a combination of conditions are met: (1) the presence of a multitude of essential chemical species that are spatially available through the entire crack region and can react with natural actuators upon cracking, (2) the material exhibits a self-controlled, distributed multiple cracking behavior that provides greater chance for more healing compounds contributing to the healing process, and (3) the healing process and reaction kinetics can lead to the formation of high strength and high toughness healing products with sufficiently large volume, leading to recovery of both mechanical and transport properties.

In order to boost the intrinsic healing potential in cementitious materials, this study strategically tailored fly ash and Nano $MgCO_3$ into fiber reinforced strain-hardening system. The

addition of reactive particles is to provide sufficient chemical compounds to form profound healing products deep inside the crack. The strain-hardening behavior of the fiber reinforced cementitious composites system is achieved by tailoring the synergistic interaction between fiber, matrix, and interface using a micromechanics theory to ensure the formation of multiple microcracking. In this study, the tensile stress-strain response and the change in permeability as well as 3D damage pattern were measured and evaluated during the loading and self-healing cycle. The surface tomography and chemical composition of the healing products within microcracks were analyzed by scanning electron microscopy and energy-dispersive X-ray spectroscopy.

5.2 Material Design Framework

5.2.1 The Incorporation of Nano $MgCO_3$ to Promote the Homogenous Healing

The minerals dissolution and precipitation induced crack aperture alteration is a ubiquitous feature in cementitious materials when they are exposed to water. This intrinsic process, is controlled by a wide range of microscale processes, such as the mass transport mechanism and reaction kinetics at mineral surface. Such a complex system controls the local autogenous healing rate and extent at various temporal and spatial scales. Among different healing products, the previous studies have suggested that the carbonation products $CaCO_3$ is the most dominant precipitate in terms of size and volume, especially in mature concrete when there is not sufficient amount of anhydrate cement. In presence of atmospheric carbon dioxide, it can dissolve in water to form carbonic acid:

$$CO_2\,(g) \rightleftharpoons CO_2\,(l) \tag{5.1}$$

$$CO_2\,(l) + H_2O \rightleftharpoons H_2CO_3 \tag{5.2}$$

The carbonic acid a weak acid that dissociates in two steps, leading to the formation of bicarbonate and carbonate ions:

$$H_2CO_3 \rightleftharpoons HCO_3^- + H^+ \quad (5.3)$$

$$HCO_3^- \rightleftharpoons CO_3^{2-} + H^+ \quad (5.4)$$

The formation of solid calcium carbonates results from the reaction of these dissociated CO_3^{2-} carbonate ions with free Ca^{2+} ions from the dissolution and leaching of the unreacted cement clinkers and hydration products such as calcium hydroxide and CSH:

$$C_3S + 3H_2O \longrightarrow 3Ca^{2+} + H_2SiO_4^{2-} + 4OH^- \quad (5.5)$$

$$Ca(OH)_2 \rightleftharpoons Ca^{2+} + 2(OH)^- \quad (5.6)$$

$$Ca^{2+} + CO_3^{2-} \rightleftharpoons CaCO_3\,(s) \quad (5.7)$$

The above reactions can be presented more schematically:

$$\underset{}{CO_2(g) \rightleftharpoons CO_2\,(l)} \overset{+\,H_2O}{\rightleftharpoons} \underset{}{H_2CO_3} \overset{+\,H_2O}{\rightleftharpoons} \underset{}{HCO_3} \overset{+\,H_2O}{\rightleftharpoons} \underset{}{CO_3^{2-}} \overset{+\,Ca^{2+}}{\rightleftharpoons} \underset{}{CaCO_3(s)} \quad (5.8)$$

The local reaction rate of $CaCO_3$ deposition is primarily controlled by the ionic concentrations of $[Ca^{2+}][CO_3^{2-}]$ in the crack. While Ca^{2+} is rich in the cementitious system, the solubility of CO_2 at natural condition is very low and the transition from CO_2(l) to CO_3^{2-} is kinetically slow. At equilibrium, only a small fraction (~0.2 - 1%) of the dissolved CO_2 is converted to H_2CO_3. Most of the CO_2 remains as solvated molecular CO_2. In addition, when the water flow carrying Ca^{2+} and CO_3^{2-} percolates through a crack, the mass flux at the sample surface is large to the advective flux deep inside the crack, resulting in the precipitation mainly accumulated at crack shallow region. At the time of crack shallow region sealing, large portions of the deep region remain devoid of healing products. This quick sealing process further isolates the crack deep region from the surroundings environment. It thus becomes more difficult for carbon dioxide in the environment to transport through the sealed layer and reach the interior

region of the crack. Therefore, the self-healing in normal cementitious materials usually shows non-uniform pattern along the crack depth, and the overall healing extent is significantly limited.

In order to overcome these limitations and promote the homogenous healing, the incorporation of carbonate salts ($M_x(CO_3)_y$) into cementitious system during the process of mixing could provide a potential path toward the enhanced carbonation rate deep inside the crack. When crack occurs, the carbonate salts around the crack walls are exposed to the humid or water environment, leading to the salts dissolution. The dissolved carbonate ions can thus serve as additional healing agent to react with Ca^{2+} ions, yielding new $CaCO_3$ precipitation inside the crack. Rather than the healing in normal concrete, the extent of which severely limited by the move of carbon dioxide (equation 5.8) in the environment, this new system can rely on the pre-embedded carbonate phase in the material as healing resource to maximize the healing potential in the crack interior region.

$$M_x(CO_3)_y(s) \xrightleftharpoons{+H_2O} CO_3^{2-} \xrightleftharpoons{+Ca^{2+}} C_aCO_3(s) \quad (5.9)$$

To pull the equilibrium condition more to the right in equation 5.9, the carbonate salts ($M_x(CO_3)_y$) should have higher solubility than $CaCO_3$. Based on the solubility rules, carbonate salts containing the common metal cations can be ranked in the following sequence for solubility at room temperature:

$$Na_2CO_3\ (340.7\ g/L) > K_2CO_3\ (31.1\ g/L) > MgCO_3\ (0.139\ g/L) > CaCO_3(0.013\ g/L) \quad (5.10)$$

Despite the high solubility of Na_2CO_3 and K_2CO_3, they are not suitable for using as healing agents in the cement based matrix because most of the carbonate ions will be activated and consumed during the mixing or initial hardening by the moist calcium silicate minerals, resulting in the shortage of healing materials when the crack occurs. Therefore, from the perspective of solubility, $MgCO_3$ becomes a potential candidate. **Figure 5.2** summarizes the hypothesis that the

addition of carbonate salt can enhance intrinsic healing in the cementitious system by providing extra healing resource. This study aims to test this hypothesis. Furthermore, the influence of the influence of addition of $MgCO_3$ on the cementitious composites behaviors was also investigated in terms of hydration kinetics, mechanical properties, and chemical evolution.

5.2.2 Micromechanics Based Strain-Hardening Composite Design to Control the Cracking Behavior

The strain-hardening behavior of the fiber reinforced brittle matrix composites is achieved by tailoring the synergistic interaction between fiber, matrix, and fiber/matrix interface using a micromechanics theory to ensure the formation of multiple cracking [1]. One of the most important conditions for multiple cracking failure mode is the presence of steady state cracking [2]. In fiber reinforced composites, during crack opening, the fiber bridging stress increase as fiber/matrix interfaces debond and the debonded segments of fibers stretch. If the maximum bridging stress can exceed the matrix tensile stress, the crack flanks will not result in catastrophic loss of loading capacity but flatten to maintain the applied stress level, which is termed as the steady state cracking. As a result, load can be transferred from this crack plan back into the matrix and cause the formation of another new crack. Repeating this process creates the behavior of multiple cracking. Based on the J-integral analysis, a steady state crack requires the crack tip toughness J_{tip} must satisfy

$$J_{tip} = \sigma_{SS}\delta_{SS} - \int_0^{\delta_{SS}} \sigma(\delta)d\delta \tag{5.11}$$

$$J_{tip} = \frac{K_m^{\ 2}}{E_m} \tag{5.12}$$

where δ_{ss} is the constant cracking opening corresponding to steady state crack stress σ_{ss}. J_{tip} can be approximately expressed by K_m^2/E_m at small fiber content. K_m is the matrix fracture toughness and E_m is the matrix elastic modulus, both of which are sensitive to the mixture design, such as the aggregates content and water/ binder ratio. The condition for steady state then can be expressed as

$$J_{tip} \leq \sigma_0 \delta_0 - \int_0^{\delta_0} \sigma(\delta) d\delta \equiv J_b' \tag{5.13}$$

where δ_0 is the cracking opening corresponding to maximum bridging stress σ_0. The complementary energy J_b' can be calculated from the fiber bridging stress versus crack opening $\sigma(\delta)$ curve, as illustrated in **Figure 5.3**. The $\sigma(\delta)$ relationship, viewed as the constitutive law of fiber bridging behavior, is expressible as a function of micromechanics parameters, including fiber properties such as volume content V_f, fiber diameter d_f, length L_f, and Young's modulus E_f, and fiber/matrix interface properties like interface chemical bond G_d, frictional bond τ_0, and slip-hardening coefficient β accounting for the slip-hardening behavior during fiber pullout. It is clear from Equation (5.13) that the successful composite design for robust strain-hardening requires a high ratio of J_b'/J_{tip}. Based on the theoretical discussions presented above, in this investigation we tailored the cementitious composite with different fly ash and $MgCO_3$ replacement ratios to find moderate matrix toughness and high complementary energy, result in sufficient compressive and tensile strength, meanwhile adequate margin between J_b' and J_{tip} to activate a large number of microcracks.

5.3 Experimental Procedures

5.3.1 Effect of $MgCO_3$ Addition on Cement Hydration

A. Calorimeter

To study the effects of $MgCO_3$ on cement hydration rate and hydration degree, isothermal calorimetry (TAM AIR) tests were performed at 25 °C with a time resolution of 1 min. This instrument has a precision of ± 20 μW and an accuracy > 95 %. Preblended mixture of hematite nanoparticles and water were added to cement to achieve $MgCO_3$-cement mass ratios of 5.0%, 10.0%, and 20.0%, and a water/(cement+fly ash+$MgCO_3$) ratio of 0.30. Right after mixing, 2.0 g of mixture was tightly sealed inside the glass ampule and placed into the calorimetry immediately.

To exclude the exothermic effect of early rapid dissolution of cement, the calorimetry data from the initial 15 min were not recorded for the sample temperature to become completely equilibrated with the instrument. Triplicate samples were measured for each mixture design.

B. Compression test

The effects of $MgCO_3$ on the mechanical properties of cementitious samples were studied through uniaxial compression tests. Uniaxial compression tests were conducted on cylinder specimens (5 cm in diameter, 10 cm in height) using a hydraulic testing frame with a data acquisition system. The compression tests were performed at different specimen ages of 1, 7, 14 and 28 days, to measure the strength development of each mixture. The specimens were prepared following the ASTM Standard 192/C 192 M. Before testing, the top and bottom surfaces of each cylinder specimen were capped with sulfur to ensure more evenly distributed stress under loading and to minimize lateral confinement effect. The test was conducted under displacement control at a quasi-static condition with a loading rate of 0.025 mm/s. Each specimen was loaded till there was a 20% drop of the peak load. The compressive strength was calculated by dividing the failure load (i.e. the peak load) by the initial cross-sectional area of the cylinder. For each age and mixture design, three specimens were tested and the results were averaged.

C. XRD

To study the potential effects of $MgCO_3$ nanoparticle addition on cement hydration products, preblended mixture of $MgCO_3$ and water were added to Portland cement to achieve $MgCO_3$-cement mass ratios of 0.0%, 5.0%, 10.0% and 20.0% and a water-cement ratio of 0.40. After curing for 3 and 28 days, the cementitious specimens were ground into powders, and Fourier transform infrared spectroscopy (FTIR, IS50, Nicolet) and X-ray diffraction (XRD, Miniflex600, Rigaku) measurements were conducted to identify the hydration products.

5.3.2 Verify the Enhanced Self-Healing Property

A. Materials and Sample Preparation

The mix compositions of all the matrixes used in this study are listed in **Table 5.1**. All the mixtures were prepared and cured at room temperature 25 ± 5 °C and relative humidity of 70 ± 20 %. In a typical procedure, the solid powders such as cement, fly ash, $MgCO_3$, and sand were firstly blended in a paddle mixer for 2 min, and then the water and superplasticizer were poured and continued mixing for 2 min until the mortar fluidized and stabilized. For fiber reinforced composites, polyvinyl alcohol (PVA) fibers with a surface oil coating of 1.2% by weight were incorporated into the matrix system. The main properties of the fiber are presented in **Table 5.2**. The PVA fibers were added manually into the mortar matrix very slowly to ensure proper distribution, and keep mixing for several minutes until no additional improvement in workability was observed. Upon mixing, the mixture was then cast into various modes for compression and toughness tests. The specimens were covered with plastic sheets and stored at room temperature for 24 hours; then they were demoded and cured in the laboratory until the age for testing.

B. Crack Scale: Micro CT, Microscopy, and SEM

After the preloading test, prismatic sample of 10 by 10 by 32mm contained cracks were sawn from the big coupon specimens for SEM inspections. The SEM sections were cleaned in an ultrasonic bath for about 1 min and then prepared by carbon coating under vacuum. Studies of the fractured surfaces were performed at 1000 × using a JeolJSM-6010LV SEM with EDX detector. The SEM scanning was carried out before and after self-healing treatment for multiple damage-healing times.

C. Sample Scale: uniaxial tension and water permeability.

Unlike conventional concrete, tensile strain-hardening behavior represents one of the most significant features of strain hardening material. To assess the quality of self-healing in the new materials, the magnitude of recovered mechanical properties were measured under uniaxial tension test. Firstly, the deliberate damage should be induced by tensioning a coupon specimen (6 in. by 2 in.) to pre-determined strain levels called preloading. To develop multiple cracking, a displacement-controlled uniaxial tensile test was applied. Tests were carried out on an electromechanical system under 0.0025 mm/s rate. Extension meter with a gauge length of 3 in. was attached to the specimen to measure the elongation. The tensile specimen dimensions and testing setup are shown in **Figure 5.4**. The preloading for the samples was imposed to the strain of 1% to simulate in-service loading conditions. After unloading, specimens were exposed to water/dry environmental exposures for 5 cycles, allowing potential self-healing to occur. Subsequently, the specimens were undergone the reloading, using the same method and the same strain magnitudes described above for preloading. In the stress-strain curves of the reloading stages, the permanent residual strain introduced in the preloading stage was not accounted for, which gave a conservative measurement of the tensile strain capacities of re-healed specimens.

Cylindrical molds (3×6 in.) were used for casting the water permeability samples. After 24 hours, the demolded samples were stored in a controlled chamber at 25 °C and 100% relative humidity until the age of 28 days and then cut into 25-mm-thick slices for testing. After cutting, the slice samples were soaked in water for 7 days at room temperature to make it saturated and to avoid any further shrinkage microcracking. The saturated disks were clamped in the water permeability test setup as shown in **Figure 5.5**. The setup was based on the idea of axial water flow through the sample. The water drop was measured at regular time intervals, normally once a day, depending on the water flow rate of the specimen. After each measurement, water was restored to the original level by refilling the pipette with a syringe from top. The test results were plotted with a curve of the cumulative water flow versus time. To investigate the permeability behaviors of normal SHC and $MgCO_3$ enhanced SHC during self-healing process, the cylinder samples were first loaded to induce multiple microcracks using the standard split test setup. Then, the samples were installed in the water permeability apparatus to allow the healing to happen. The water head was monitored and recorded every 8 hours and up to 14 days for all the specimens tested.

Water permeability is commonly quantified by a permeability coefficient. Calculations assumed laminar flow, Darcy's law for the flow through the samples, and continuity of flow throughout the system. Thus, the permeability coefficient k can be expressed as:

$$\mathrm{k} = \left(\frac{A'd}{A\Delta t}\right) ln\left(\frac{h_0}{h_t}\right) \tag{5.14}$$

where A is cross-sectional area of concrete sample; A' is the area of the pipette; d is the thickness of the sample; Δt is the time between two successive readings; and h_0 and h_i are water head at the beginning and the end of the test, respectively.

5.4 Results and Discussion

5.4.1 Amount of MgCO3 Addition Affects Cement Hydration

Figure 5.6(a) shows the isothermal calorimetry data for Portland cement paste hydrated with $MgCO_3$ particles for the first 48 h after mixing. Compared with the cementitious samples without $MgCO_3$, all samples with the addition of $MgCO_3$ particles showed delayed rates of early hydration, and the height of the hydration peaks decreased. The corresponding total heat evolved at the end of the main hydration period, which represents the degree of hydration at 28 days, is presented in **Figure 5.6(b)**. The degree of hydration, α, was calculated by dividing the total amount of evolved heat at a given time (T) by the ultimate heat of reaction (Q_∞). Using a value of Q_∞ = 438 J/g reported in literature[3], 5.0% of $MgCO_3$ particles addition led to slightly higher hydration degree than pure cement paste. However, the mixtures with 10% and 20% $MgCO_3$ particles showed significantly lower hydration heat release. Although it is natural to hypothesize that higher addition of small particles in cementitious materials provide more additional nucleation sites for cement hydration, in practice, increasing the amount of nanoparticles added in cementitious materials makes nanoparticle dispersion more difficult, resulting in agglomerates that can reach a micrometer length scale. This dispersion difficulty depends on the nature and size of nanoparticles, rheology and properties of cementitious mixture, and the interactions between nanoparticles and cementitious mixture. In addition, the mixing of nanoparticles with the ultra-high surface area usually consumes large amount of water to dissolve the materials, leading to insufficient water for cement hydration. In this study, increasing $MgCO_3$ particles addition from 5% up to 10% did not lead to an increase in hydration; instead, negative impacts were observed. This result suggests that an upper limit of $MgCO_3$ dosage need to be considered on order to avoid the adverse effect on cement hydration.

The mechanical properties of cementitious materials are very important for their successful applications. The mechanical property evolution with age can also indirectly reflect the cement hydration process. In this study, the age-dependent development of compressive strength of cementitious specimens with 0%, 5%, 10%, and 20% $MgCO_3$ particles were compared (**Figure 5.7**). The addition of 5% hematite nanoparticles to cementitious samples led to the largest compressive strength at different ages up to 28 days. Compared with the cementitious samples without $MgCO_3$ particles, the increases in compressive strength were 7 % at 28-day with 5% $MgCO_3$ addition. It is known that the degrees of hydration of cement clinker phases and the microstructure (e.g. pore structure) of the hardened material determine its mechanical strength [4]. Higher degree of hydration leads to lower porosity or increases the proportion of fine pores, resulting in increased strength. In addition, the nano/micro-size particles can be adsorbed at the surfaces of sands due to Van der Waals forces, leading to a higher degree of hydration and an improved filling effect at the sand/binder interfacial transition zone [5]. This can result in a denser interfacial transition zone and higher compressive strength of the cementitious material. The mechanical test results further elucidated that the addition of optimized amount of $MgCO_3$ particles can modify the pore structure development of cementitious materials, leading to improved mechanical properties. However, excessive addition of $MgCO_3$ over 10% can cause the decline of mechanical strength.

The hydration products of cementitious samples with and without $MgCO_3$ addition after 28 days were characterized by XRD measurements. Based on X-ray diffraction patterns (**Figure 5.8**), it is shown that the major $Ca(OH)_2$ and CSH peaks can be observed for both samples, indicating that the addition of $MgCO_3$ did not significantly change the composition of cement hydration products. Another finding from the XRD result is that the $MgCO_3$ peaks can be clearly

detected in the sample with $MgCO_3$ addition after the major hydration stage. This confirms the hypothesis that the $MgCO_3$ can exit in the cementitious system during mixing and hardening, and be ready to provide healing species once the crack being initiated.

5.4.2 Improved Healing Property by the Addition of MgCO3

Micro-CT measurements and image analyses provided accurate (±2 μm) description of crack morphology and aperture field before and after self-healing. **Figure 5.9** and **Figure 5.10** show the mapping of the crack aperture field (in X-Z plane) of samples without and with $MgCO_3$ addition, respectively. Both samples contain one crack with similar initial crack width around 60 μm. The comparison between the initial and final aperture field in the two different samples reveals the three-dimensional self-healing extent of the crack. For both samples, a reduction in crack apertures due to self-healing was observed. But the extent of self-healing in normal SHC sample was lower than sample with $MgCO_3$ seeding, reflected by the transition from the green color to more blue color along the Z axis, as shown in **Figure 5.9(d)** and **Figure 5.10(d)**.

The quantitative self-healing ratios were calculated based on the CT image data. The results are presented in **Figure 5.11**. The self-healing ratio η is defined as:

$$\eta = \frac{Healed\ Crack\ Width}{Initial\ Crack\ Width} \tag{5.15}$$

Compared with the normal SHC sample without $MgCO_3$ particles, the increases in total healing ratio were 7 % at 7 cycles, 10% at 14 cycles, and 20% at 28 cycles with 5% $MgCO_3$ addition. **Figure 5.12** shows the typical microscopy images of the crack plane before healing (**Figure 5.12 (a)**) and after healing at different magnification factors (**Figure 5.12(b)-(d)**). The healing products refilled the crack are clearly visible. Most of the crack part were fully swelled with newly formed large crystals. The SEM image in **Figure 5.12(d)** shows that the single crystal size

within the crack can reach over 30 microns. The result revealed that the embedded and distributed $MgCO_3$ particles can provide extra CO_3^{2-} ions for the entire crack region to react with Ca^{2+} released from the dissolved concrete, yielding large calcite precipitates to fill the crack.

Figure 5.13 shows the typical 1% preloading tensile stress-strain curves of specimens with and without $MgCO_3$ addition. It can be distinctly seen that the self-healing functionality was achieved in the specimens. Comparing to the reloaded specimen without $MgCO_3$ addition, the most significant effect of $MgCO_3$ is the stiffness recovery which is defined by the slope of the initial linear segment on the stress-strain curve. the quantitative recovery of first crack strength that is defined as the stress value when the first crack opens, corresponding to the first stress drop, and the ultimate strength that is defined as the stress value corresponding to the maximum strain on the stress-strain curve. The first cracking strength of nearly all specimens after self-healing drops below the virgin specimens. However, the relative tensile stress after self-healing remains higher than preloading. It was found that about 95% of ultimate strength, 80% stiffness, and 75% first crack strength were regained.

Figure 5.14 shows the normalized flow rate as a function of the duration of exposure to water. The curves are the mean of all three relevant specimens. The flow rate is normalized with respect to the initial rate at the beginning of the healing test. The average crack width measured at the sample surface was about 50 μm for both mixtures. It can be seen that in ambient temperature, the characteristic flow curve shows significant decreasing trend because of self-healing. The initially high leakage dropped to a reduced level. **Figure 5.14** also shows a clear tendency to a faster and more robust self-healing in the case of samples with $MgCO_3$ addition. After only 50 h the flow rate dropped to about 30% of the initial flow rate, and after approximately 200 h a flow rate of just about 2% of the original flow rate can be measured.

While in the case of normal SHC sample without $MgCO_3$ seeding, the normalized flow rate was approximately 60% after 50 h and 20% after 200 h. The permeability test result further confirms the positive effect of the addition of $MgCO_3$ particles on both the rate and extent of autogenous healing in cementitious materials.

5.5 Summary

In this study, nano carbonate particles was strategically tailored into strain hardening cementitious composite system to promote the intrinsic self-healing. The effects of $MgCO_3$ addition on cement hydration and self-healing extent in cementitious materials were studied for the first time. The $MgCO_3$ addition did not change significantly the chemical composition of cement hydration products, but did affect the rate and degree of cement hydration, thus affecting the pore structure development and mechanical properties of the hardened cementitious material. Particularly, adding more than 5% $MgCO_3$ particles in cementitious materials resulted in negative impacts on hydration degree and compressive strength. The effect of $MgCO_3$ on self-healing behaviors in terms of crack volume recovery and transport property recovery were verified by the Micro-CT scanning and the water permeability test, respectively. The improved volumetric healing extent and the quickly decreased water flow rate indicated that the addition of $MgCO_3$ can be a promising strategy for enhanced intrinsic healing. Furthermore, robust self-healing phenomena was observed in $MgCO_3$ modified strain hardening cementitious composites after multiple loading events. These findings provided new insights for intrinsic self-healing cementitious materials design. Future studies are suggested to study the effect of different sizes and types healing agents addition to cementitious materials, with different mix design to improve the healing extent as well as the healing products quality.

Tables

Table 5.1 Mixture proportion of $MgCO_3$ enhanced SHC

Mix	W/(C+FA+M)	Cement	Sand	Fly ash	$MgCO_3$	Superplasticizer	Fiber
SHC	0.3	1	0.8	2.2	-	0.005	2%
SHC+5%M	0.3	1	0.8	2.2	0.05	0.005	2%
SHC+10%M	0.3	1	0.8	2.2	0.1	0.005	2%
SHC+20%M	0.3	1	0.8	2.2	0.2	0.005	2%

Table 5.2 PVA fiber properties

Parameter	Value
Nominal Strength (MPa)	1620
Density (kg/m^3)	1300
Diameter (μm)	39
Length (mm)	8
Young's modulus (GPa)	42.8
Elongation (%)	6

Figures

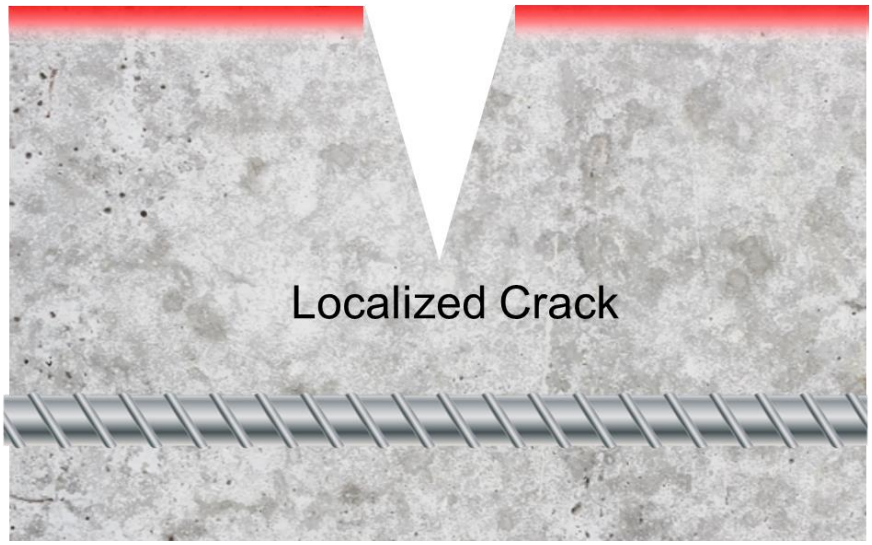

(a)

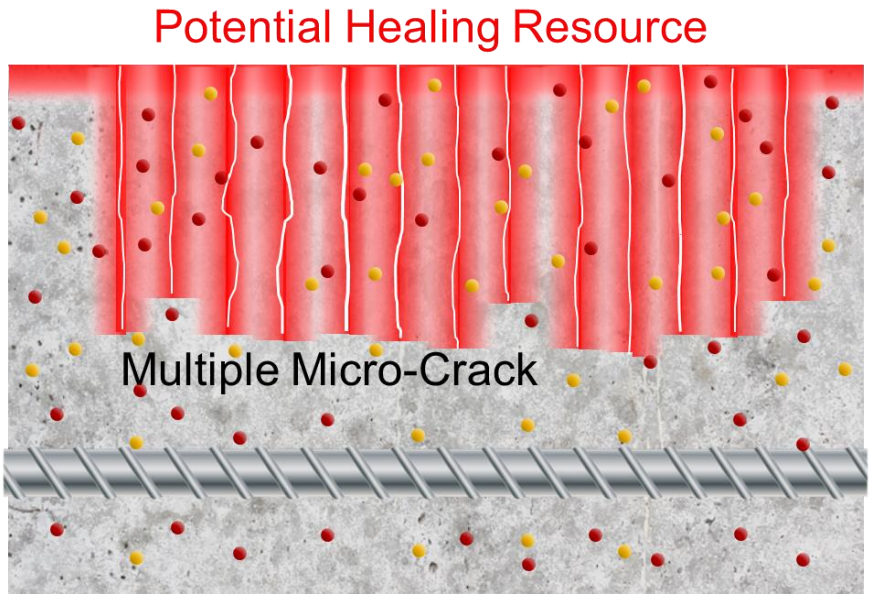

(b)

Figure 5.1 The schematic illustration of healing mechanism at composite scale for (a) conventional concrete and (b) proposed new cementitious composites.

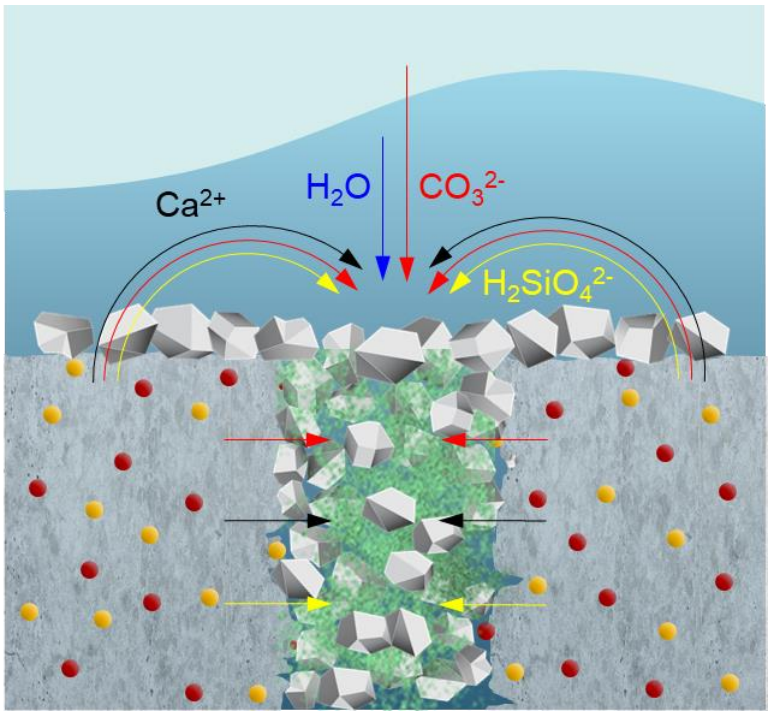

(a) Crack scale

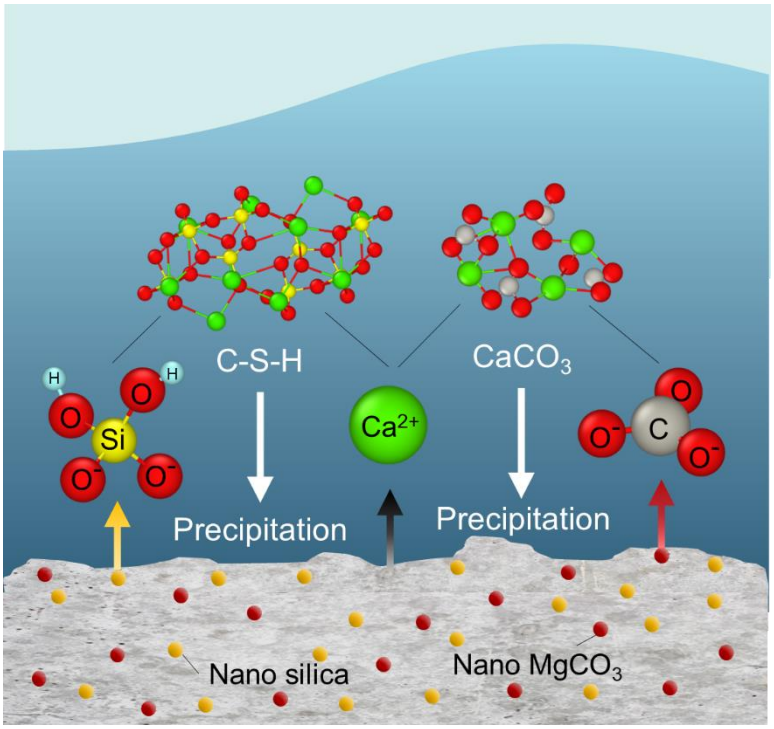

(b) Molecular scale

Figure 5.2 The proposed healing mechanism at (a) crack scale and (b) molecular scale.

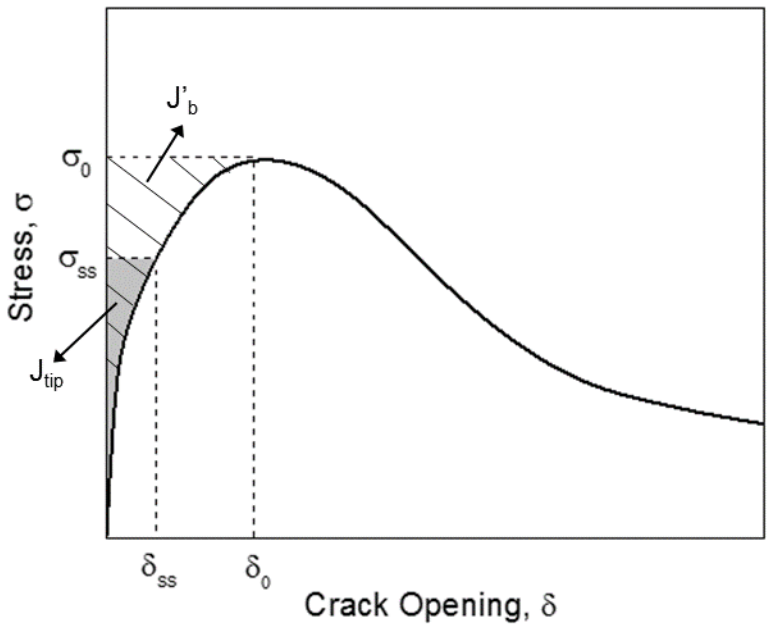

Figure 5.3 Typical fiber bridging stress vs. crack opening curve (Shaded area represents J_{tip} and hatched area represents maximum complementary energy J_b').

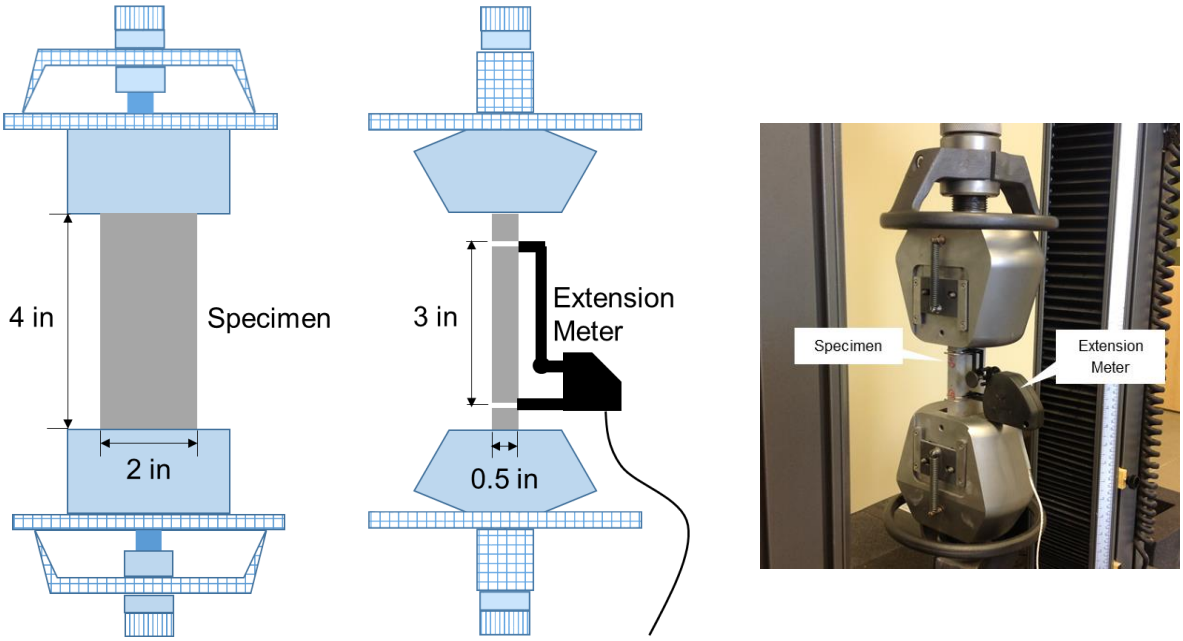

Figure 5.4 Experimental setup for uniaxial tension test.

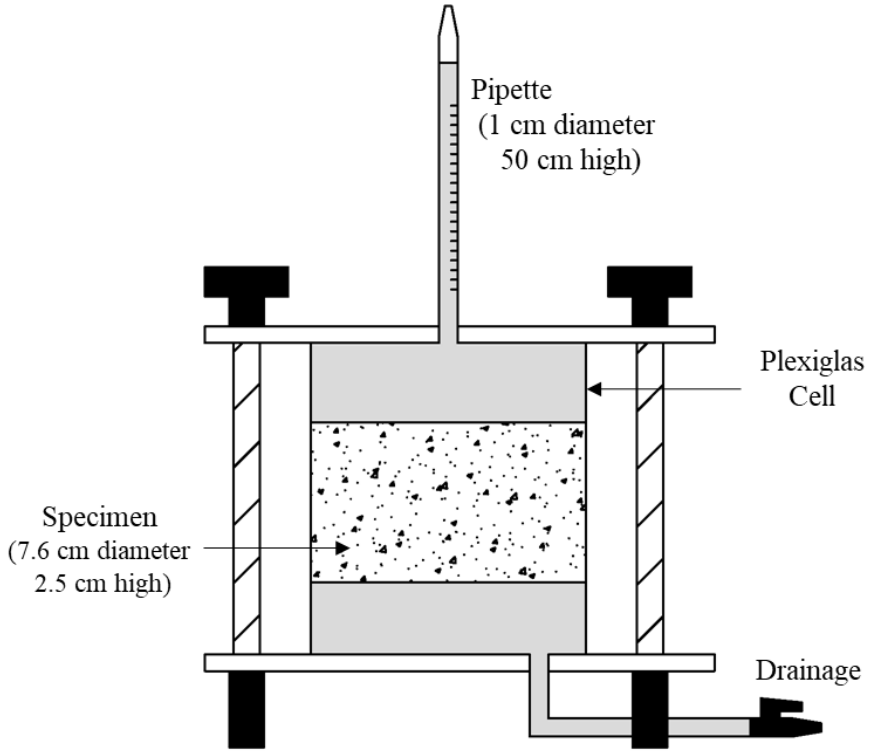

Figure 5.5 Schematic view of water permeability apparatus.

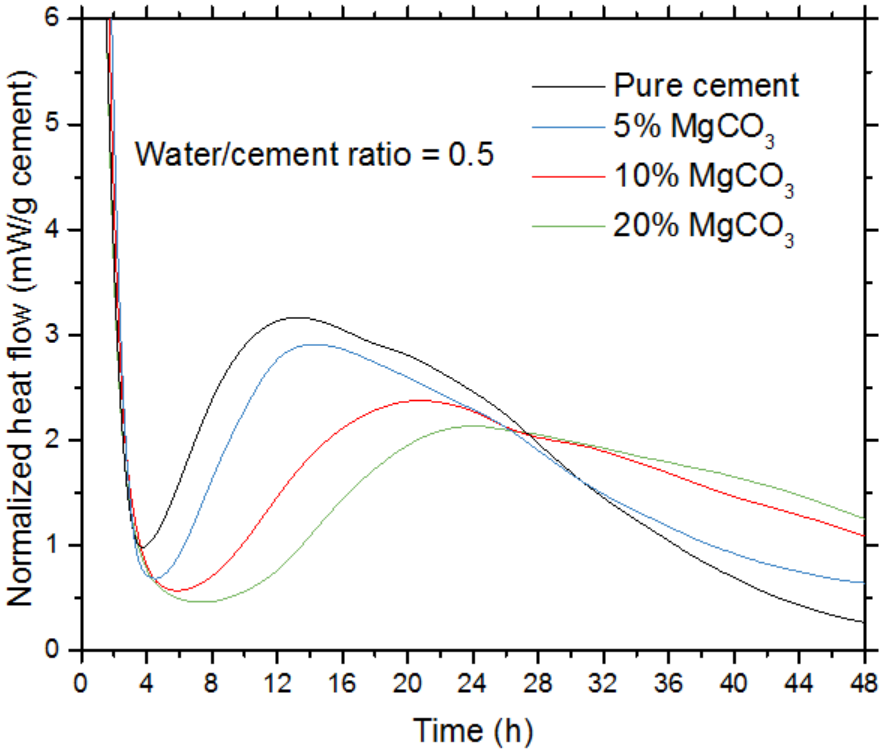

Figure 5.6(a) Rates of heat evolution during curing of cementitious samples with 0 %, 5 %, 10 %, and 20 wt % $MgCO_3$ additions

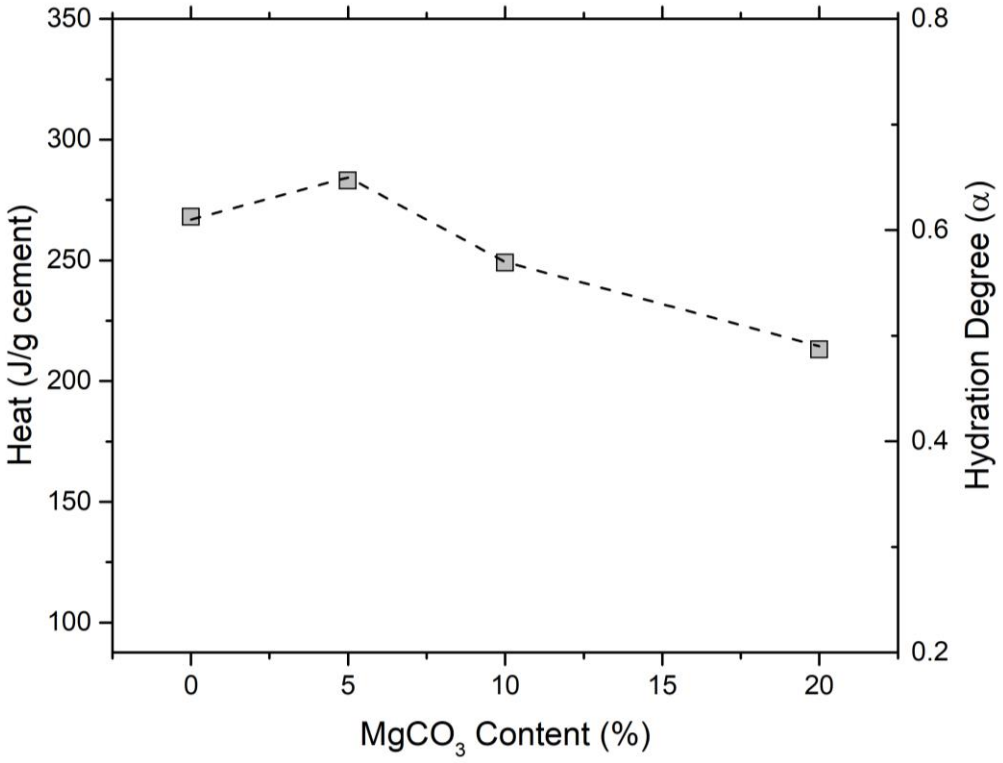

Figure 5.6(b) Hydration degree and total isothermal hydration heat as a function of the $MgCO_3$ dosage in cement pastes.

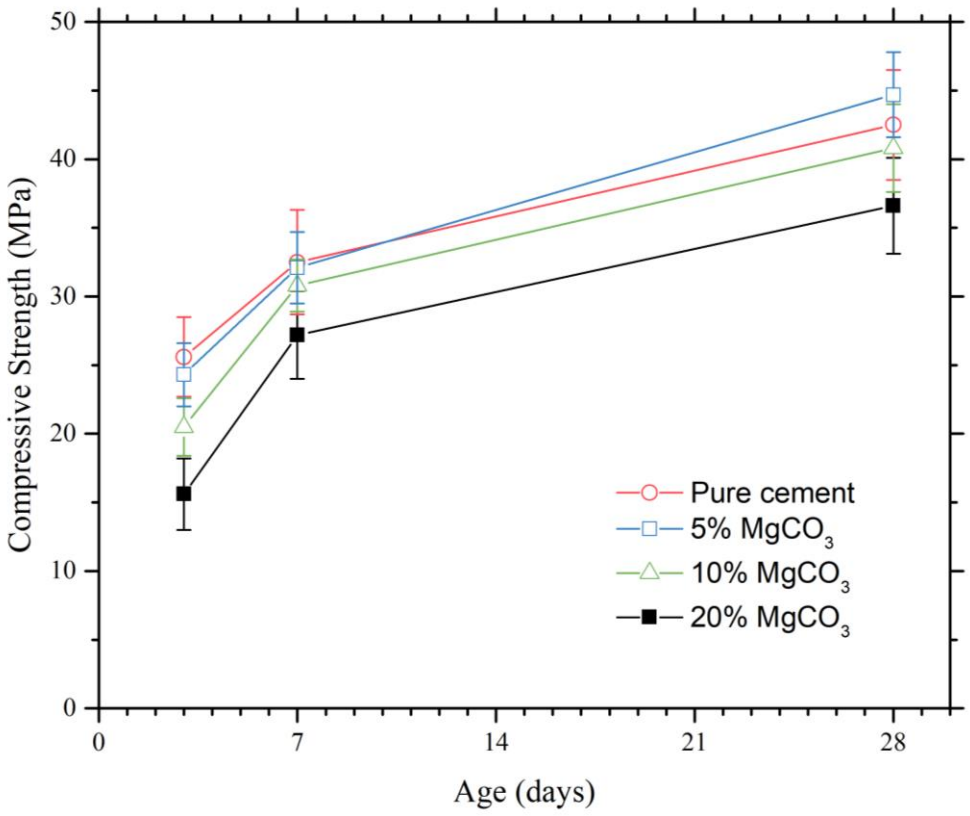

Figure 5.7 Compressive strength development of cement mortar made with 0 %, 5 %, 10 %, and 20 wt % $MgCO_3$ additions. Error bars show the standard deviation of three replicates.

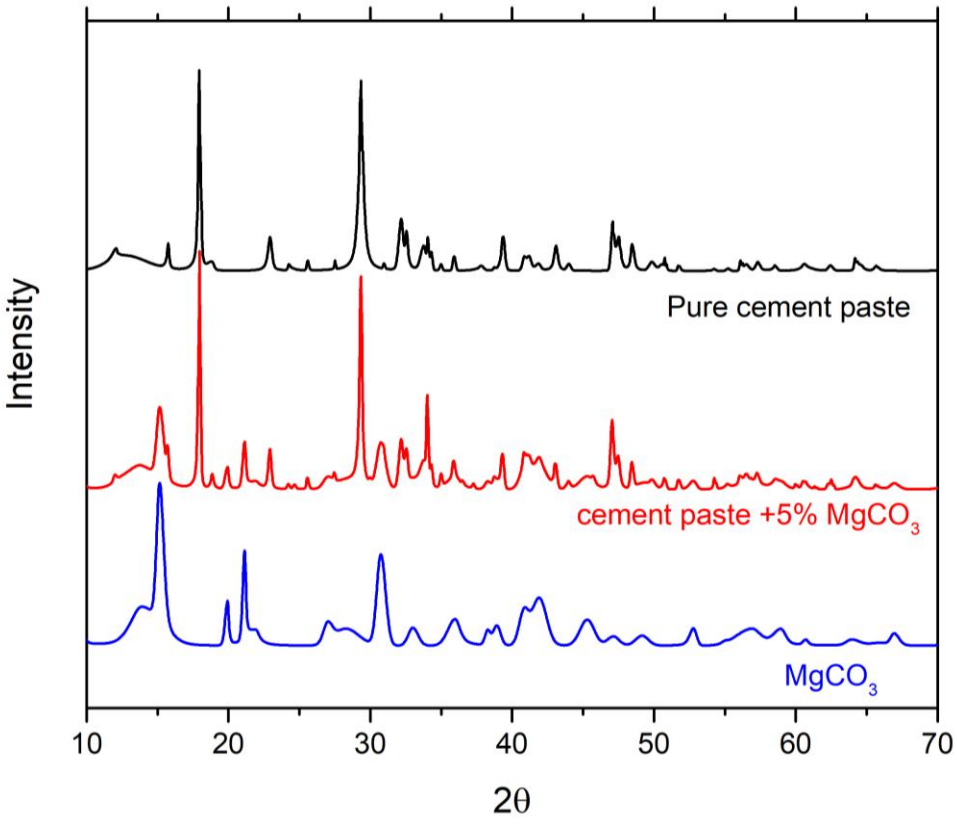

Figure 5.8 XRD spectra of cement samples at 28-day age.

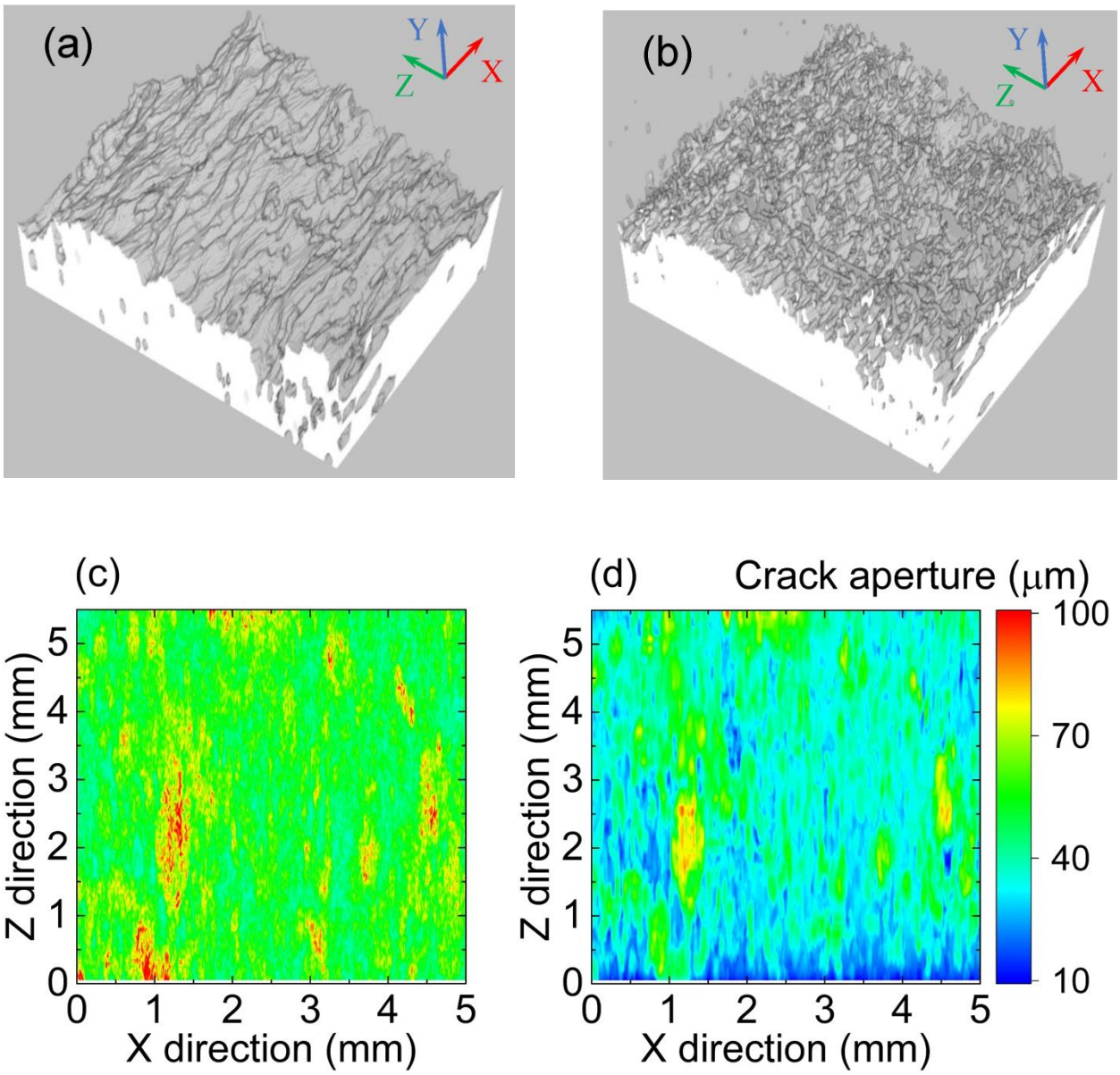

Figure 5.9 Sample SHC: (a) Crack morphology before healing, (b) Crack morphology after healing. (c) crack aperture field before healing, (d) crack aperture field after healing.

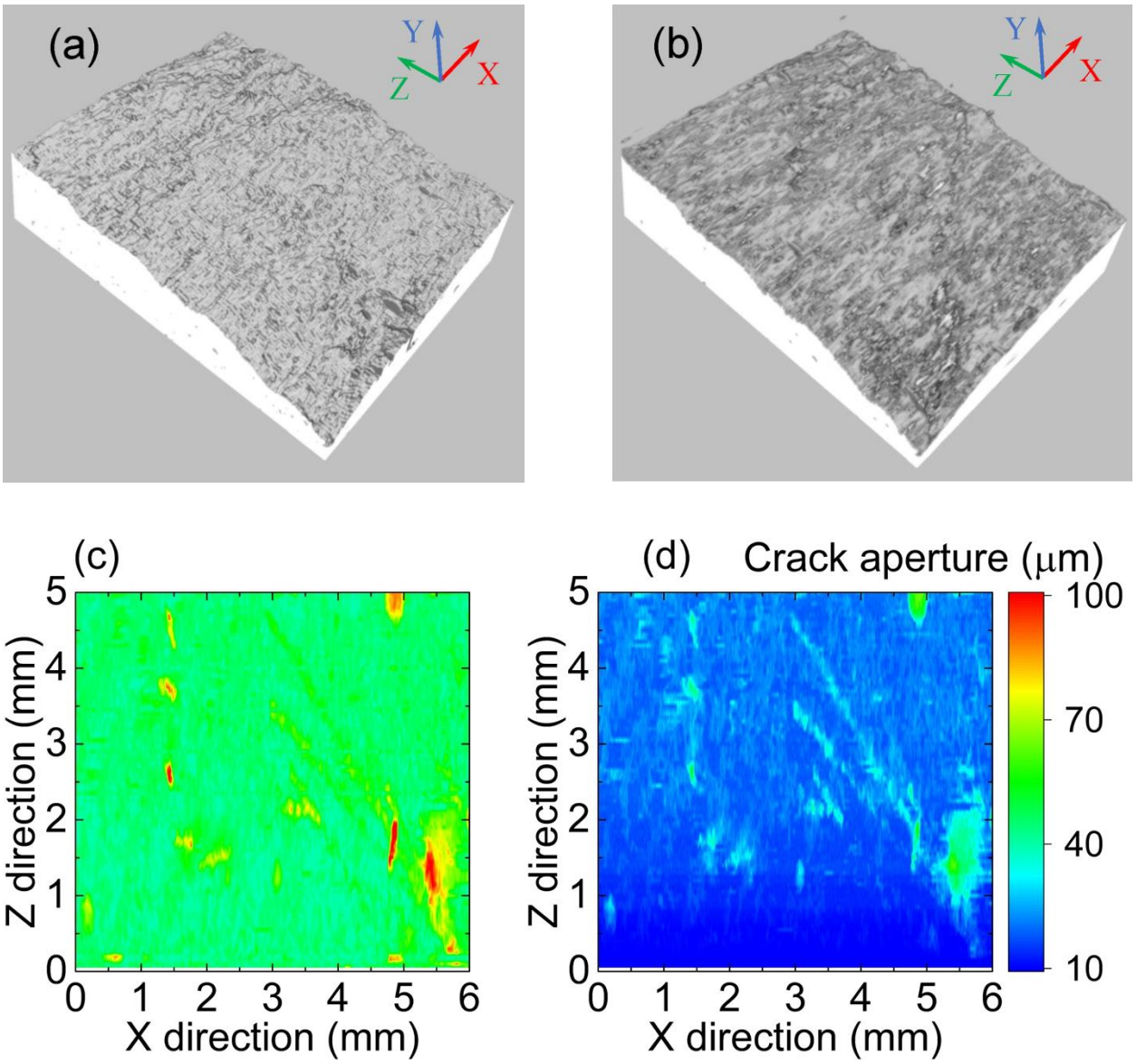

Figure 5.10 Sample SHC+5%M: (a) Crack morphology before healing, (b) Crack morphology after healing, (c) crack aperture field before healing, (d) crack aperture field after healing.

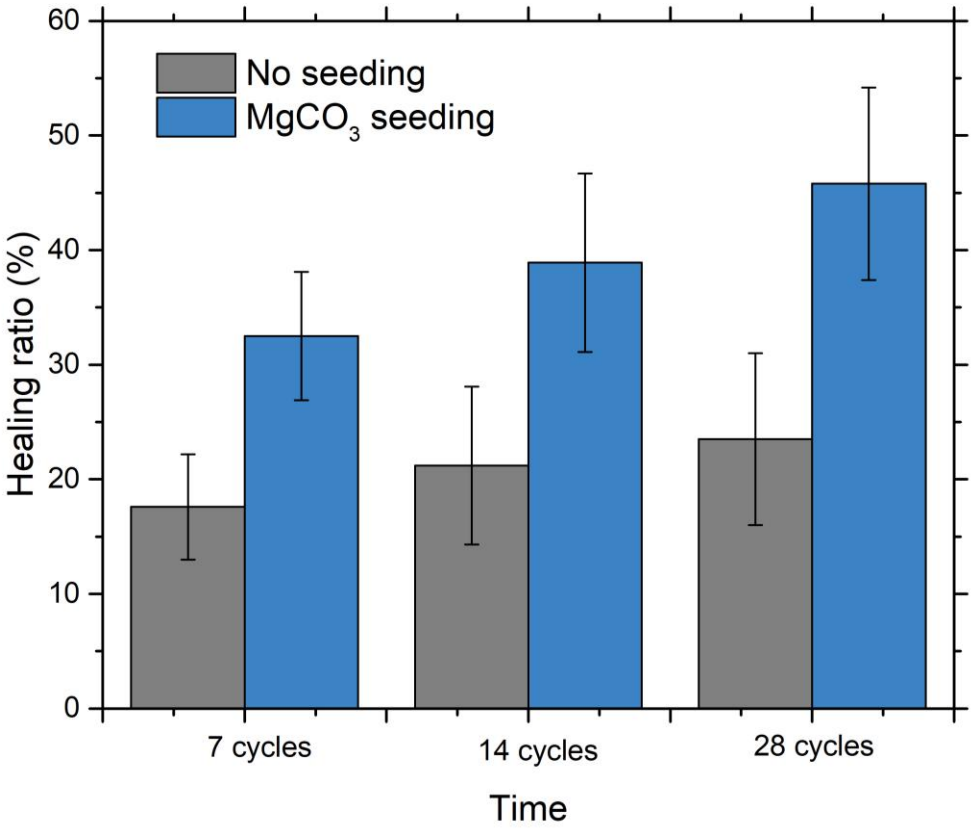

Figure 5.11 The total healing ratio for cementitious composites with and without $MgCO_3$ addition.

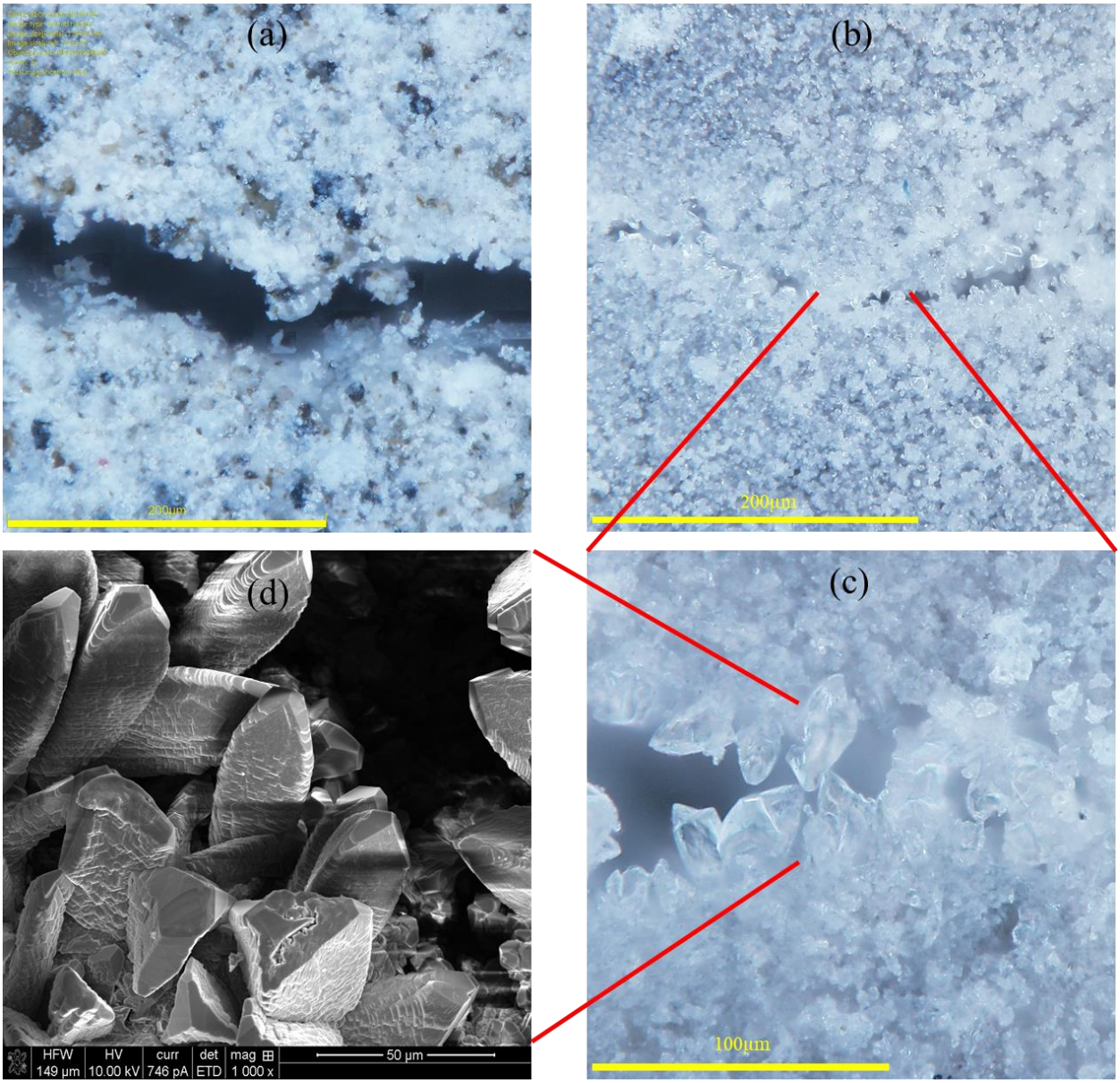

Figure 5.12 Microscopy images of crack region and healing products: (a) before healing, (b-d) after healing.

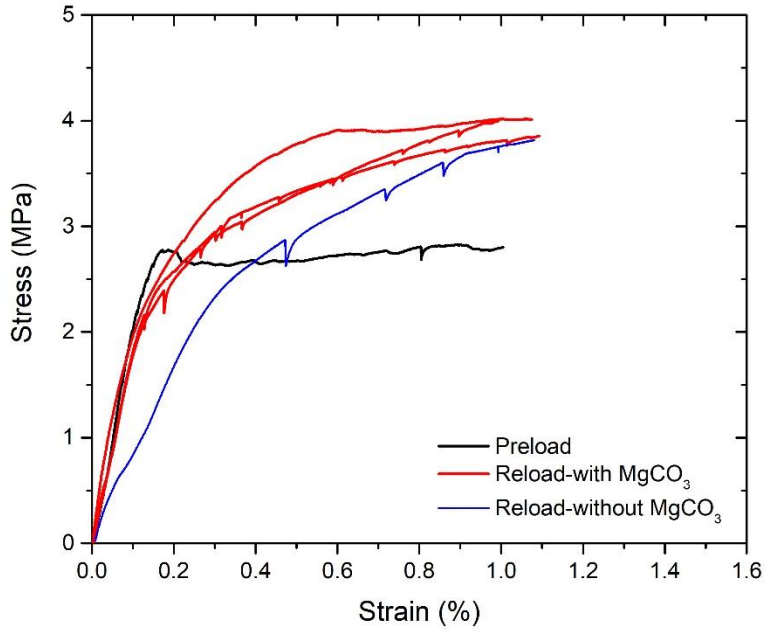

Figure 5.13 Typical reloading tensile stress-strain curves of specimens preloaded to 1%.

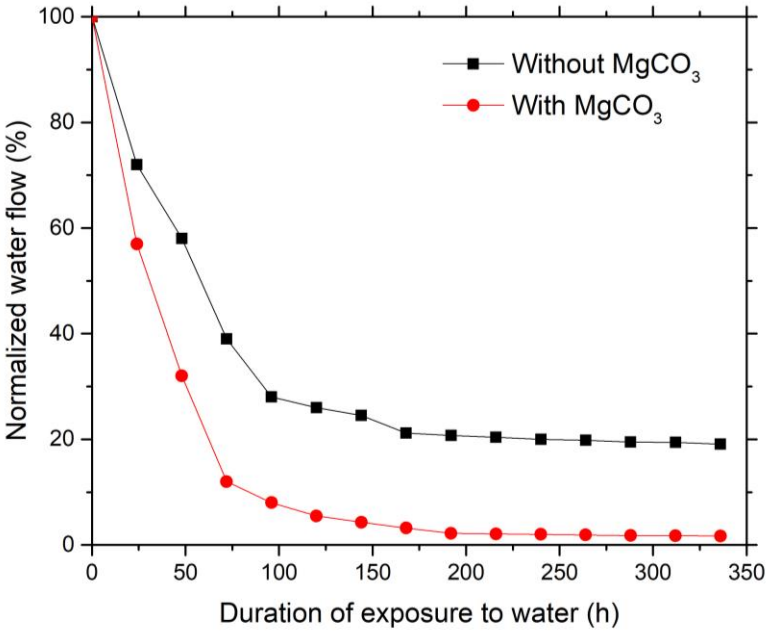

Figure 5.14 Decrease of the normalized flow rate because of the self-healing of the crack for samples with and without $MgCO_3$ addition (Average crack width level = 50 μm).

References

[1] Li, V. C., & Leung, C. K. Y. (1992). Theory of Steady State and Multiple Cracking of Random Discontinuous Fiber Reinforced Brittle Matrix Composites, Journal of Engineering Mechanics, 118(11), 2246-2264.

[2] Li, V.C. & Leung, C.K.Y. (1992). Steady State and Multiple Cracking of Short Random Fiber Composites, ASCE J. of Engineering Mechanics, 118(11), 2246-2264.

[3] Pane, I., & Hansen, W. (2005). Investigation of blended cement hydration by isothermal calorimetry and thermal analysis. Cement and concrete research, 35(6), 1155-1164.

[4] Taylor, H. F. (1997). Cement chemistry. Thomas Telford.

[5] Qing, Y., Zenan, Z., Deyu, K., & Rongshen, C. (2007). Influence of nano-SiO 2 addition on properties of hardened cement paste as compared with silica fume. Construction and building materials, 21(3), 539-545.

CHAPTER 6 DAMAGE SENSING OF SELF-HEALING CEMENTITIOUS MATERIALS

6.1 Introduction

Early detection of cracking and damage level in concrete is critical to provide timely maintenance and prolong structural service life. Current management practices of concrete structures rely on regular visual inspections that can be subjective and are limited to accessible locations [1] . Advanced structural health monitoring approaches mainly depend on point-based sensors that provide local measurements [2]. To identify spatially distributed damage such as cracking, a dense network of point-based sensors is needed, but highly costly and requires complex analytical models to extrapolate the point measurements to the damage state [3]. Emerging digital image correlation techniques applied to concrete structures can provide distributed information such as strain and displacement, but is limited to surface features [4]. These challenges can potentially be tackled by a new generation of multifunctional strain-hardening cementitious composite materials (multifunctional SHC), which are encoded with a distributed microcracking damage process coupled with damage self-sensing capacity [5]. The sequential formation of steady-state microcracks during material strain-hardening stage leads to a prolonged damage process, while allowing detection of microcracking damage level in the material long before localized fracture failure occurs. Through electrical probing and advanced tomography method, it is possible to achieve distributed damage sensing in SHC materials [6]. Nevertheless, advances in multifunctional SHC materials require a fundamental understanding on how the damage and healing process in SHC affects its frequency-dependent electrical response (i.e. complex impedance), and how such effects can be captured in analytical models

capable of explaining and predicting the electromechanical behavior of the material system containing cracks.

Resistivity (under DC) or impedance (under AC) of cementitious materials has been explored as a sensing functionality for hydration monitoring [7-14], composition and pore structure assessment [15-23], chloride penetration [16, 24, 25], and has recently emerged as a method for measuring the material's mechanical state [26-33]. Cementitious materials have a porous, heterogeneous microstructure. Under an applied steady electric field, the ions in pore water are mobilized to create current. The electrical response of a cementitious material strongly depends on its heterogeneous microstructure, such as the distribution and connectivity of pores, the interconnecting layers of C-S-H gels, their interfaces [18, 34-37], or any conductive particles or fibers as inclusions in the cementitious matrix [38-41]. Chung [42-46] explored multi-point DC probing of plain cementitious matrix and cementitious pastes with conductive carbon-based fibers, and revealed that the electrical properties of cementitious materials can be correlated to their mechanical behavior. Peled et al. [47] first reported AC electrical impedance spectroscopy characterization of carbon and steel fiber reinforced cementitious composites featuring a tension-softening post-cracking behavior. The electrical impedance spectroscopy method revealed the difference in the contribution of electrical response of conductive fibers vs. cementitious matrix phases. The work established the correlation between crack mouth opening displacement and impedance during the material fracture (i.e. localized cracking) process. Because this study focused on tension-softening cementitious composites reinforced with conductive fibers, the findings, despite their importance, are not applicable to SHC containing nonconductive polymeric fibers. Due to the fundamental difference in terms of the damage behavior between SHC and tension-softening fiber reinforced cementitious composites, the effects of SHC's

multiple cracking process and steady-state crack propagation on its frequency-dependent electrical impedance remain unknown. Tensile piezoresistive behavior of SHC was first experimentally studied by Hou and Lynch [48] and Li et al. [5, 6]. Their work showed that the resistivity of SHC can be correlated to mechanical strain during both elastic and strain-hardening stages. Most recently, Ranade et al. [49] experimentally and analytically studied the influence of microcracking patterns on the resistivity of SHC through 2-point DC probing. Based on the experimental measurements, the work correlated the bulk resistivity change with cracking characteristics such as crack number and crack width distribution.

Despite the recent advances, knowledge gaps remain. A fundamental question is whether the electrical response of cementitious materials, considering high material heterogeneity, can be fully represented by resistivity. A cementitious material is not an ideal resistor whose resistance value is independent of frequency. Therefore, AC current and voltage signals through a cementitious material are not in phase. This is further complicated when cracks are present in cementitious materials. These cracks introduce discontinuity to the existing inhomogeneity of the material, and the "impedance" of the cracks to electrical current is highly frequency-dependent. In this sense, frequency-dependent impedance is a rather correct measure than resistance for cementitious materials. It is also unclear how the cracking behavior of SHC affects its frequency-dependent impedance response. At single crack opening scale, the mechanics of single crack opening is known to be governed by tensile stress vs. crack opening relation ($\sigma \sim \delta$, the fiber bridging "spring law") [50]. The crack is bridged by polymeric fibers that are nonconductive. The electromechanical behavior of a single crack opening, i.e. the frequency-dependent complex impedance vs. crack opening relation ($Z \sim \delta$) is unknown. At multiple cracking scale, tensile stress vs. strain relation ($\sigma \sim \varepsilon$) describes the mechanical response of SHC under tension; the

strain represents a “smeared strain” due to the multiple cracking process. However, the electromechanical response of SHC under tension, the frequency-dependent complex impedance vs. strain relation ($Z \sim \varepsilon$), is not established. Furthermore, due to the tightly controlled crack width at micrometer scale within SHC, autogenous healing can naturally occur with time as a result of calcite precipitation and continued hydration reaction [51-53]. Autogenous healing of cracks in SHC represents a reversed damage process. It is important to understand whether and how this reversed damage process can lead to changes in material electrical response.

To answer these questions, frequency-dependent 4-point AC electrical impedance spectroscopy (EIS) and equivalent circuit analysis were performed on SHC specimens at single crack opening scale, at multiple cracking scale, and during self-healing of cracks, respectively. Impedance spectroscopy is a powerful method for characterizing electrical properties of materials and their interfaces with electrodes [54]. It can be adopted to investigate the dynamics of bound or mobile charge in the bulk or interfacial regions of solid materials, including ionic, semiconducting, dielectric and mixed electronic-ionic materials [54]. Through impedance spectroscopy, the frequency-dependent electrical behavior of the SHC can be represented by an idealized model circuit consisting of discrete electrical components, which describe the physical processes taking place in the material-crack system. Analyzing the changes of model parameters due to cracking and healing processes will reveal the mechanisms that contribute to the overall electromechanical response of SHC materials.

6.2 Experimental Investigation

6.2.1 Materials and Specimen Preparation

The designed SHC (**Table 6.1**) binder system contained water, a high-range water reducer, Type I ordinary Portland cement, ASTM standard Class F fly ash, and silica sand with mean grain size of 270 μm. The chemical compositions of the cement and fly ash are shown in **Table 6.2**. Polyvinyl alcohol (PVA) fibers were incorporated into the mixture at a volume fraction of 2.0%. The PVA fibers are 8 mm long and 39 μm in diameter, with nominal tensile strength of 1620 MPa and density of 1300 kg/m^3.

All dry particles such as cement, fly ash, and silica sand were firstly mixed for 1 minute. Water was then added with high-range water reducer to form a homogeneous mortar with optimum rheology favoring uniform dispersion of PVA fibers. Short PVA fibers were then added and mixed for 2 minutes until uniformly dispersed. The fresh mixture was cast into a series of coupon specimens with dimensions of 152×50×12.5 mm. The specimens were covered with plastic sheets and cured in laboratory air with a temperature of 20 ± 1°C and relative humidity of 45 ± 5% until the age of 3 days before demolding. Because the moisture content in the specimens can significantly affect electrical measurements, the demolded specimens were then cured in water until the age of 28 days for testing. By this means, the isolated effect of crack formation and self-healing on the electrical properties of SHC can be accurately measured without the noise caused by the variation in the moisture content in the uncracked region of the specimens.

6.2.2 Experimental Methods

An experimental program was devised for preloading the specimens under uniaxial tension to different damage levels, and then subjecting the specimens to different numbers of wet/dry cycles for self-healing to occur. Each complete cycle contained a 24-h dry cycle

followed a 24-h wet cycle. Under uniaxial tension, SHC exhibits a multiple microcracking behavior at macro-scale. The increasing level of applied tensile strain leads to an increasing number of microcracks formed in the material. Each microcrack, at the meso-scale, follows the fiber-bridging "spring law" describing the relation between the tensile stress across the crack and crack opening. Therefore, in terms of damage level, the tests in this study were performed at (1) single crack opening scale (meso-scale), to investigate the effect of single crack opening on material complex impedance, and (2) multiple cracking scale (macro-scale), to investigate the combined effects of crack opening and crack number increase on material complex impedance. Electrical impedance spectroscopy was conducted on undamaged specimens before loading, after different levels of damage, and after different cycles of self-healing.

6.2.2.1 Impedance spectroscopy

The frequency-dependent electrical responses of the specimens were measured by four-point AC electrical impedance spectroscopy (EIS) (**Figure 6.1**). Compared with DC resistance measurements, the results from AC EIS measurements can be correlated with many complex material variables, e.g. microstructure, inhomogeneity such as defects and cracks, dielectric properties, and compositional influences [54]. EIS explains fundamental electrical properties of materials, and provides means of analytical prediction of material electrical response through equivalent circuit modeling. Furthermore, four-point EIS avoids contact impedance and polarization which is evident during DC measurement. It provides critical insights into frequency-dependent electrical properties that cannot be obtained by resistance measurements.

Four electrodes made of copper tapes were attached to the specimen surface with conductive silver colloidal paste (**Figure 6.1)**. The two outer electrodes were used to inject AC current at various frequencies into the specimen. The two inner electrodes were used to measure

the in-situ voltage within the specimen. The electrodes were parallel to each other and spaced with sufficient distance in order for the current to be continuous and perpendicular to the electrodes. The EIS measurements were carried out using an impedance analyzer configured for a 100 mV amplitude excitation, which was slight enough to ensure that the material system was a linear system. A wide AC frequency ranging from 0.1 Hz to 1MHz was investigated. Impedance was measured at each frequency by applying a single-frequency current to the specimen through outer electrodes and measuring the amplitude and phase shift of the resulting voltage using Fast Fourier Transformation analysis of the response. Data were collected with 35 points per decade. The impedance as a function of frequency was then plotted, yielding the impedance spectrum. EIS were performed on specimens before tension and after various predetermined crack opening (for double-notched specimens) or tensile strain levels (for un-notched specimens). After damage the specimens were subjected to wet-dry cycles for self-healing to occur, EIS was performed on these specimens every 48 hours. All specimens were kept in saturated water condition before tests to eliminate the effect of moisture level on EIS measurements.

6.2.2.2 Uniaxial tension test

Uniaxial tension tests were conducted using a servo-hydraulic testing system at a fixed cross head displacement rate of 0.06 mm/min (**Figure 6.2(a)**). Two types of specimens were prepared: (i) un-notched specimens to investigate multiple microcracking at macro-scale, and (ii) double-notched specimens to investigate single crack opening at meso-scale. **Figure 6.2(b)** shows the configuration of un-notched specimens. The specimens were gripped at both ends by the testing system with a gripping length of 30 mm. Four copper tapes were attached onto the specimen surfaces through conductive silver paste to serve as electrodes for the EIS measurements. LVDTs were attached parallel to these electrodes with a gage length of 60 mm.

Figure 6.3 shows the measured tensile stress-strain curve of SHC loaded up to failure. In addition, six levels of loading conditions were carried out, corresponding to the maximum applied strain of 0.5%, 1%, 1.5%, 2%, 2.5%, and 3%, respectively, as marked in **Figure 6.3**. The electrical responses of these specimens were measured using EIS method before and after each level of loading, yielding the impedance vs. tensile strain ($Z \sim \varepsilon$) relation. Six specimens were tested for each loading scenario.

Uniaxial tension tests were also conducted on double-notched specimens to measure the fiber bridging stress vs. crack opening ($\sigma \sim \delta$) relation as well as the impedance vs. crack opening ($Z \sim \delta$) relation. The double notches were artificially created to ensure the initiation and propagation of a single crack along the notched cross section. The details of the specimen and notches are shown in **Figure 6.2(c)**. Four electrodes were attached to the specimen surface for injecting AC current at various frequencies and measuring voltage change during crack opening. The crack opening during loading was measured using LVDTs. The loading rate was reduced to 0.005 mm/min for the single crack opening test. **Figure 6.4** shows the $\sigma \sim \delta$ curve of SHC. The test was paused at different crack opening values at 10, 20, 50, 100, 200, 400 μm, denoted as a, b, c, d, e, f, respectively. Each time the test was paused, EIS was performed to measure the impedance spectrum at a fixed crack opening value.

6.2.2.3 Image documentation

A 16.1-megapixel camera was used to record images of crack propagation during uniaxial tension tests. The digital images were then post-processed to identify and characterize the cracks. The crack edges were marked according to the maximum changing slope on the gray level curve (**Figure 6.5)**, allowing for crack recognition. The images were then converted to binary images.

The change of crack opening during self-healing was observed and recorded each time before EIS measurement using a digital microscope (magnification ×200) with a CCD camera. The specimen was fixed on a movable micro-positioning stage to examine the cracks in the specimen. Based on the measurements, the change in statistical distribution of crack width due to increasing healing cycles was determined. In addition, the morphology of crack healed region was observed through a scanning electron microscope (FEI Quanta 3D FEG Dual Beam). Prismatic samples of 10 mm × 10 mm × 10 mm containing cracks were cut from the coupon specimen. The samples were firstly dried in vacuum chamber to remove the vapor inside the pore space. The sample surfaces were then coated with carbon for subsequent SEM imaging. The scanning was operated under low vacuum condition at 10 kV voltage using back-scattered electron signal.

6.3 Equivalent Circuit Model

An equivalent circuit model is proposed in this study to represent the electromechanical behavior of SHC. In equivalent circuit modeling, the experimental impedance data is approximated by the impedance of an equivalent circuit made of ideal resistors, capacitors and inductances, with various distributed circuit elements [55]. In this model, the bulk regions of the crack and the uncracked cementitious matrix are regarded as continuous media, for which the parameters are averages of the parameters appearing at microscopic and atomistic scales. The uncracked region of the cementitious material is represented by an equivalent parallel circuit containing a capacitor (C_{ml}) and a resistor (R_{m1}) connected in series, in parallel with a capacitor (C_{m2}), and a resistor (R_{m2}) (**Figure 6.6(a)**). C_{m1} and R_{m1} connected in series represent the overall electrical behavior of the partially conductive paths, for which the partially connected pores in the direction of the electrical current behave as a resistor (R_{m1}); the regions in between connected

pores behave as dielectrics in between conductors, providing a capacitor effect (C_{m1}). C_{m2} represents the overall capacitor effect of the nearly nonconductive paths along the direction of current in the cementitious material. The electrical insulation is attributed to the presence of calcium silicate hydrate gel binding silica aggregates and nonconductive polymeric fibers. R_{m2} represents the overall resistor effect of conductive paths in the direction of electrical current, that is, the well-connected pore structure where ions are mobilized to generate current.

When a crack is present in the cementitious material, the crack is idealized as a parallel circuit connecting a capacitor (C_c) and a resistor (R_c). It is hypothesized that if the crack only contains air phase (e.g. a dry crack), the capacitor effect dominates and the resistor effect becomes negligible. If the crack is connected by conductive path (e.g. conductive fibers, dissolved ions), the resistor effect becomes prominent. In this study, a crack in SHC is not traction-free; it is bridged by numerous nonconductive polymeric fibers with random orientation and embedment lengths. In addition to moisture level within the crack, the resistor R_c effect is also contributed by the contact impedance existing at the interfaces between fibers and the cementitious matrix. Consequently, the crack in SHC can be represented by the a capacitor C_c in parallel with a resistor R_c.

When SHC experiences multiple cracking under uniaxial tension, it is further assumed that a number of (N = the number of cracks) crack circuit elements are connected in series (**Figure 6.6(b)**) to represent the effect of multiple cracking process on the material electrical response. Each crack element (the ith element) is assigned with a pair of model parameters $C_{c,i}$ and $R_{c,i}$ whose values depend on the crack opening of the ith element. The total impedance of all cracks $Z_{c,total}$ (ε) at a given strain is thus the sum of the impedance of each individual crack $Z_{c,i}$.

In this model, a single-step charge transfer reaction in the presence of diffusion at the electrode-specimen interface is considered. The electrode-specimen interface is represented by a resistor $R_{\text{ele-inter}}$ and the Warburg diffusion element Z_{diff} connected in series, and then connected with a capacitor $C_{\text{ele-inter}}$ in parallel.

The total frequency-dependent impedance $Z(\omega)$ of the entire SHC material-crack-electrode system can be written as:

$$Z(\omega) = Z_{\text{m}} + Z_{\text{c}} + Z_{\text{e}} \tag{6.1}$$

where Z_{m}, Z_{c}, and Z_{e} denote the impedance of the SHC uncracked matrix, cracks, and electrode-interface, respectively, given as:

$$Z_{\text{m}} = \frac{1}{\frac{1}{R_{\text{m2}}} + \frac{1}{R_{\text{m1}} + \frac{1}{j\omega C_{\text{m1}}} + j\omega C_{\text{m2}}}} \tag{6.2}$$

$$Z_{\text{c},i} = \frac{1}{\frac{1}{R_{\text{c},i}} + j\omega C_{\text{c},i}} \tag{6.3}$$

$$Z_{\text{c,total}}(\varepsilon) = \sum_{i=1}^{n} Z_{\text{c},i} \tag{6.4}$$

$$Z_{e} = \frac{R_{\text{ele-inter}} + A_{\text{W}}\omega^{-\frac{1}{2}}(1-j)}{1 + j\omega(R_{\text{ele-inter}} + A_{\text{W}}\omega^{-\frac{1}{2}}(1-j))C_{\text{ele-inter}}} \tag{6.5}$$

where j is the imaginary number, ω is the angular frequency of the sinusoidal signal, and A_{W} is the Warburg constant.

Based on the impedance spectra measured by EIS, the parameters of the equivalent circuit model were determined and analyzed to reveal the impact of cracking and healing on the electrical properties of SHC. A representative Nyquist plot of the AC impedance response of the material-crack-electrode system and equivalent circuit model results are shown in **Figure 6.7**. The spectrum exhibits a high frequency semicircle arc (left) describing the electrical response of the bulk material and cracks, and a semi-infinite arc (right) ascribed to the electrode-interface behavior.

In this study, it was recognized that the impedance change of SHC during loading can arise from various mechanical, physical and chemical processes. For example, moisture can evaporate from the specimen during the mechanical testing, leading to an increase in the measured impedance. Continued hydration can also occur in the SHC specimens between tests, resulting in a change of the microstructure and consequently the bulk material electrical response. To remove the effects of these physical and chemical processes, and to probe the sole effect of mechanical cracking on the change of electrical parameters, EIS measurements were conducted on a set of control specimens. These control specimens were prepared from the same batch under the same curing conditions, had the same age as the other testing specimens when EIS was performed, but were not subjected to mechanical loading to induce cracks. For example, the single crack opening test took approximately 20 minutes to reach a crack opening of 0.1 mm. Correspondingly, EIS was performed on the control specimen 20 minutes (or the same duration as the single crack opening test) after the control specimen was taken out from water curing. The electrical parameters in Z_m were then calculated by employing the impedance spectra of the control specimens based on Equation (6.2). Once determined, these parameters were then input into the model described in Equation (6.1) to determine the cracking electrical parameters R_c and

C_c in Z_c based on the impedance spectra of the cracked specimens. The effects of cracking and self-healing on the electrical properties of SHC were thus determined by the changes of these parameters in Z_c. The role of each parameter (i.e. circuit element) in the overall conduction mechanism was also discussed.

6.4 Results and Discussion

6.4.1 Effect of Single Crack Opening

Figure 6.8 shows the binary images of a single crack (in white color) initiated and propagated from the notches in a SHC specimen during uniaxial tension test. The binary images were converted through post-processing from the raw images with a resolution of 4000×4000. Five crack opening levels, ranging from 20 μm to 400 μm, are shown to represent different stages of crack propagation. At different crack opening levels, the Nyquist plots of impedance spectra of the material-crack system in the complex plane are shown in **Figure 6.9**. The electrode-interface response data was removed from the plots because it was not related to the SHC material response. At each crack opening, the experimental data yield a depressed semicircular arc in the complex plane. The center of the arc is displaced below the real axis because the material-crack system contains distributed elements, leading to a relaxation time that is not single-valued but continuously distributed. The angle by which the semicircular arc is depressed below the real axis is related to the width of the relaxation time distribution [54]. The arcs do not pass through the origin on the real axis, showing that the resistance of the material at infinitely high frequency is larger than zero ($R_m > 0$). **Figure 6.9** also reveals that as the crack opening increases, the impedance spectrum shifts to the right along the real axis, and the impedance arc diameter increases. This indicates that the material impedance increases at both

very low and very high frequencies with increasing crack opening. At a low frequency (e.g. 0.5 kHz), such increase is dominated by increasing R_c, the circuit element that represents the resistor effect of the crack; at higher frequencies, this increase is due to the combined effects of increasing R_c and decreasing C_c as explained by Equation (3). Furthermore, the increase in the arc diameter indicates the increase in the imaginary part of material complex impedance during crack opening; the imaginary part represents the phase lag between voltage and current and also the energy storage of the circuit elements. The results in **Figure 6.9** suggest that the crack exhibits a strong capacitor effect, leading to the frequency-dependent change in the electrical response of the material during increasing crack opening.

The Nyquist plots in **Figure 6.9** depict the impedance response of the material-crack system. To quantify the isolated effect of crack opening on the changes in impedance magnitude $\Delta|Z_c|$ and phase angle $\Delta\theta_c$ $\Delta\theta_c$, the impedance data of uncracked control specimen ($Z^{test}_{control}$ $Z^{test}_{control}$) was subtracted from that of cracked specimens (Z^{test}_{crack}). By this means, the influence of moisture variation within specimens was removed. The changes in impedance magnitude and phase angle due to crack opening were calculated based on Equation (6.6), and are plotted in **Figure 6.10** at selected frequencies ranging from 0.5 kHz to 50 kHz.

$$\begin{cases} \Delta|Z|^{test} = |Z|^{test}_{crack} - |Z|^{test}_{control} \\ \Delta\theta^{test} = \theta^{test}_{crack} - \theta^{test}_{control} \end{cases} \quad (6.6)$$

Figure 6.10 shows that both the impedance magnitude and phase angle of the material increase with increasing crack opening. The increase in impedance magnitude is relatively slow when the crack opening is below 100 μm, and becomes faster afterwards (**Figure 6.10(a)**). This trend is obvious for most of the selected frequencies, except for the very high frequency 50 kHz. Based on the $\sigma \sim \delta$ relation in **Figure 6.4**, the critical crack opening δ_0 that defines the transition

from steady-state flat crack to Griffith elliptical-shape crack occurs approximately at 100 μm during crack propagation. These combined experimental evidences suggest that the change in crack type and geometry at approximate 100 μm, which is governed by the fiber bridging "spring law" across the crack, leads to a faster increase in impedance magnitude beyond 100 μm crack opening. This phenomenon, however, becomes less obvious at a very high frequency (e.g. 50 kHz), because the crack capacitor C_c exhibits less impedance to high-frequency AC current. Since the crack capacitor C_c more easily passes a very high frequency AC current, the rate of increase in impedance magnitude due to crack opening becomes less sensitive to crack type and geometry.

The results in **Figure 6.10** also reveal that the relation between impedance magnitude and crack opening is frequency-dependent. At low frequencies (e.g. 0.5 kHz), impedance magnitude increases more prominently during crack opening than at higher frequencies (e.g. 50 kHz). This is attributed to the capacitor effect C_c of the crack; a capacitor more easily passes high-frequency AC current but shows higher impedance to low-frequency AC.

The phase angle change is also frequency-dependent and crack opening-dependent, as shown in **Figure 6.10(b)**. At different frequencies except for at the very high frequency (50 kHz), the increase in phase angle is faster when the crack opening is below 100 μm, and becomes relatively slower afterwards. Interestingly, the most prominent increase in phase angle with crack opening does not occur at the highest or the lowest AC frequency; rather, it is found to be close to a frequency of 5 kHz, which is close to the maximum imaginary component of complex impedance and the maximum phase shift by which the current lags the voltage.

The above data strongly suggest that crack capacitance C_c is a critical parameter to characterize crack opening. This is because the impedance of crack resistor R_c is frequency-

independent, and will not lead to the change of imaginary part during crack opening. By fitting the experimental data with the equivalent circuit model described in Section 3, the electrical parameters C_c and R_c representing the crack impedance were extracted based on Equations (6.1-6.3). This allowed the quantification of the relations between crack capacitance C_c and crack opening δ, and between crack resistance R_c and crack opening δ (**Figure 6.11**). The data reveals a nearly linear relation between C_c and δ. This supports our hypothesis that a crack in cementitious materials exhibits a capacitor behavior following Equation (6.7):

$$C_c = \frac{\varepsilon_r \varepsilon_0 A}{\delta} \mathrm{C_c} = \varepsilon_r \varepsilon_0 \mathrm{A}/\delta \tag{6.7}$$

where C_c is the capactance of the crack, ε_r is the dielectric constant describing the relative static permittvity of the material between the plates that represent the two walls of the crack, ε_0 is the electric constant, and A is the area of overlap of the two crack walls. With constant values of ε_r, ε_0, and A, C_c linearly decreases with increasing crack opening, well describing the experimental data.

R_c describes the resistor effect of the crack, mainly due to the presence of moisture and fibers in cracks. If the crack is dry and traction-free, it behaves as a pure capacitor. The air between the two crack walls is nonconductive and thus behaves as an insulator. However, when the crack is not dry, the water or moisture inside the crack contains dissolved ions from cementitious matrix, acting as a conductor. Ion-containing moisture also exists at the surfaces of PVA fibers bridging the crack, and at the fiber/matrix interfaces, thus providing conductive paths across the crack despite that the fibers are nonconductive. These "conducting" effects result in the resistor behavior of the crack, characterized by R_c. In **Figure 6.11**, the $R_c \sim \delta$ relation is found to be nonlinear, following a second-order polynomial relation. Because the specimens were in moisture-saturated conditions till testing, this nonlinearity is attributed to the combined effects of

the loss of moisture content during testing, and the reduction of the number of fibers bridging the crack resulting from fibers debonding, pullout or rupture during increasing crack opening.

The results show that a crack in cementitious material can be treated as a capacitor C_c in parallel with a resistor R_c. While R_c depends on various parameters, such as crack opening, moisture condition, presence of conductive fibers (e.g. carbon fibers, steel fibers) or nonconductive fibers (e.g. polymeric fibers), C_c is dominated by crack opening δ. This suggests that C_c is a more suitable parameter to characterize crack opening in cementititious materials. Compared with C_c, R_c involves more uncertainties related to mix design and moisture condition of the cementitious material. The beauty of the impedance spectroscopy approach and the equivalent circuit model established in this study is that it can extract data and quantify C_c as a crack characterization parameter.

6.4.2 Effect of Multiple Cracking

Built upon the understanding of the electrical behavior of a single crack, the equivalent circuit model describing the multiple cracking behavior in SHC (**Figure 6.6(b)**) was used to predict the effect of multiple cracking on the complex impedance of the material system. Equations (1-4) were used. This model used crack opening of each crack as the input parameter, which was experimentally measured, and predicted frequency-dependent impedance magnitude and phase angle as the output parameters for the material system containing multiple cracks at different damage levels, which were experimentally validated.

Uniaxial tension tests and impedance spectroscopy were conducted on SHC specimens. The images of crack pattern at different tensile strain levels (0.5%, 1%, 2%, and 3%) are shown in **Figure 6.12**. Higher strain level led to more microcracks formed in the SHC material. The crack number and statistical distribution of crack width were quantified using the image

processing method described in Section 2.2.4. The crack width distribution at different tensile strain levels are shown in **Figure 6.13(a)**. The total crack number, mean crack width and maximum crack width at different tensile strain levels are summarized in **Figure 6.13(b)**. It is observed that when the tensile strain increased, the number of cracks increased, and the mean crack width slightly increased. High strain level led to the formation of more microcracks with larger crack width. The multiple cracking process resulted in the pseudo-strain-hardening behavior of SHC. It was assumed that mechanical behavior of each crack follows the fiber bridging spring law (the $\sigma \sim \delta$ relation) and its electrical response followed the frequency-dependent impedance vs. crack opening ($Z \sim \delta$) relation established in the section above. Based on **Figure 6.11**, the capacitance $C_{c,i}$ and resistance $R_{c,i}$ of the ith crack with known crack width were determined. Then, Equations (3) and (4) were used to predict the frequency-dependent complex impedance of the material at different tensile strain levels. The results are plotted in **Figure 6.14** in terms of the relation between impedance magnitude, or phase degree change, and tensile strain, at three different AC frequencies.

To verify the modeling results, the material's complex impedance was experimentally measured at different strain levels and plotted in **Figure 6.15**. The electrode-interface response data that appeared at high frequencies was removed from the Nyquist plots based on Equation (5), because it was not related to the SHC material response. The experimental data yields a depressed semicircular arc in the complex plane. As the tensile strain increases and the multiple cracking process progresses, the impedance spectrum shifts to the right along the real axis, and the impedance arc diameter increases, showing that material impedance increases at low and also high frequencies. Based on the experimental data collected from six specimens, the change in impedance magnitude and phase angle due to multiple cracking at different tensile strain levels

are plotted in **Figure 6.14** for three different AC frequencies (0.5, 5, and 50 kHz). **Figure 6.14** shows that despite the variation in experimental data among specimens, the model-predicted results closely match the experimental data at different frequencies for both magnitude change and phase angle shift. The increase in impedance magnitude and phase angle with increasing tensile strain is contributed by the increase in crack number and the change of crack width distribution (**Figure 6.13**), which lead to a change in $R_{c,i}$ and $C_{c,i}$ distribution during material strain-hardening stage.

The model comparison with experimental data shows that the present model can predict the electrical response of SHC reasonably well at different strain and multiple cracking levels. The present model is able to capture the frequency-dependency of the relation between material complex impedance and its multiple cracking process, which is essential for understanding the electromechanical behavior of SHC. It should also be pointed out that fiber dispersion in SHC specimens cannot be absolutely uniform in reality. Non-uniform fiber dispersion leads to a variation in the $\sigma \sim \delta$ relation and also in the $Z \sim \sigma$ relation at different cracking region along each specimen; It also leads to a variation in material electromechanical properties among different specimens. This explains the difference between the experimental data and model prediction, because we assumed the same $Z \sim \sigma$ relation for all cracks in the model.

6.4.3 Effect of Crack Self-healing

Self-healing of the microcracks in SHC can be viewed as a reversed damage process. It is hypothesized that this reversed damage process can be captured by the change in the complex impedance of the material. Experiments were conducted on SHC specimens preloaded to 2% tensile strain, and then subjected to different wet-dry cycles for self-healing to take place. **Figure 6.16(a)** shows the optical microscopy of a crack, with the original crack width of 34 μm which

decreased to 21 μm after 2 days and to 0 after 14 days. **Figure 6.16(b)** shows the higher-resolution SEM image of a region of the crack in the original condition and after 14 days of self-healing. It is observed that the surface of the crack has been fully closed. **Figure 6.17** shows the change in the statistical distribution of crack width in SHC specimens due to self-healing, characterized by microscopy from sample surface. With increasing wet/dry exposure cycles, both the crack number and mean crack width decreased in the SHC specimens. With the information on crack width distribution in **Figure 6.17**, the capacitance $C_{c,i}$ and resistance $R_{c,i}$ of the ith crack with known crack width were determined according to **Figure 6.11**, and were inputted into the equivalent circuit model to predict the frequency-dependent complex impedance of the material at different self-healing cycles. The results are plotted in **Figure 6.18** in terms of the relation between impedance magnitude, or phase degree change, and healing time, at three different AC frequencies.

The material complex impedance before cracking, after multiple cracking when loaded to a 2% tensile strain, and after different self-healing cycles were measured using EIS. The experimental results are shown in terms of impedance magnitude and phase angle in **Figure 6.18** and in Nyquist plots in **Figure 6.19**. It is observed that multiple cracking in SHC at 2% tensile strain leads to a significant shift of the impedance spectrum to the right long the real axis, and a significantly increase in arc diameter along the imaginary axis (**Figure 6.19**). Self-healing causes an opposite effect. With increasing healing time, the impedance spectrum moves backward to the left along the real axis, and the arc diameter decreases. This indicates that self-healing of the microcracks leads to a reduction in resistance at high and low frequencies, due to the decrease in the damage level reflected as the decrease in crack number and average crack width.

Furthermore, the decrease in arc diameter indicates a reduction in the capacitor effects of the microcracks.

The model prediction results are compared with EIS measurements in **Figure 6.18** at deferent frequencies. Both model prediction and experimental data show the same trend of decreasing impedance magnitude with healing time, and decreasing phase degree with healing time. The trend is prominent at lower frequencies (e.g. 0.5 kHz and 5 kHz), and becomes less obvious at higher frequencies (e.g. 50 kHz). This is because the cracks capacitors more easily pass higher frequency current; therefore, at a very high frequency the impedance of the cracks capacitors become less sensitive to the change in crack width distribution due to self-healing. It is also observed that the impedance magnitude decreases faster during earlier healing cycles (i.e. the initial 4 days), and becomes slower during later healing cycles. This suggests that the conductive paths inside the cracks were quickly re-established during the early time of self-healing. As water containing dissolved ions transports through a crack from outside environment, calcite precipitation occurs fast at the shallower region of the crack, because this region is at first in contact with ion-containing water. This healing process leads to an increased resistor effect of the crack, due to the partial closing of the crack that re-establishes the conductive path, and a decreased capacitor effect, due to the reduction in plate area; both effects take place in all the microcracks, resulting in a fast decrease in the material impedance magnitude during early healing cycles. During later healing cycles, the healing process becomes slower for the deeper region of the crack, because the fast closure of the shallower region of the crack makes it more difficult for ion-containing water to transport into the deeper region. This leads to a slower reduction in impedance magnitude. The decrease in phase degree with increasing healing cycles also suggests a reduction in the capacitor effect (which is responsible for the imaginary values of

the complex impedance) and an increase in the resistor effect with time due to self-healing of the microcracks.

The comparison in **Figure 6.18** shows that the present model reasonably predicts the decreasing trend of impedance magnitude and phase angle with healing time, indicating that the model captures the important mechanisms underlying the relation between damage level and frequency-dependent complex impedance. However, a larger discrepancy exits between the predicted values and experimental measurements (**Figure 6.18**) than the differences between the multiple cracking data and model results in **Figure 6.14**. This indicates that in addition to the variation in the $Z \sim \delta$ relation among different microcracks, which is assumed to be equal in the present model, there are other factor(s) contributing to this discrepancy. Experimental evidences from previous chapters obtained by X-ray microtomography show that the healing extent is not homogeneous along the depth of a crack in SHC; although the crack appears to be fully healed from top surface, very often its deeper region remains less healed. In the present model, the input crack width values were obtained from microscopic observations from the surfaces of the cracks, with the assumption that the healing extent is the same along the crack depth. Therefore, the actual volumetric healing conditions of the cracks are not considered in the model. This leads to an overestimation of the decrease in impedance magnitude and phase degree with increasing healing time, as shown in **Figure 6.18**. In addition to the change in physical properties (e.g. crack width and volume), the change in chemical properties of the healing products can also lead to a difference in the model prediction and experimental data. The chemical compositions of the newly formed healing products within cracks are quite different from the original bulk material; the former contains more calcite crystals and less porous calcium silicate hydrate. This mechanism can also result in a divergence between the model prediction and the real electrical

response of the material. This study suggests an interesting future research to refine the present model by considering the 3-dimensional healing profile of the cracks, and by considering the electrochemical properties of the self-healing products.

6.5 Summary

This study combines four-point electrical impedance spectroscopy measurements with equivalent circuit modeling to study the electrical response of strain-hardening cementitious materials at single crack propagation scale, multiple cracking scale, and during time-dependent self-healing process. The following conclusions are drawn:

(1) SHC exhibits a frequency-dependent electrical response, which can be captured by complex impedance measurements through 4-point AC impedance spectroscopy.

(2) The frequency-dependent electrical response of SHC can be approximated by an equivalent circuit made of ideal resistors, capacitors and Warburg diffusion element, with various distributed circuit elements representing the conductive, partial conductive and nonconductive paths in the SHC material-crack system, and at the material-electrode interface.

(3) The change in SHC complex impedance due to the propagation of a single crack is governed by the crack complex impedance vs. crack opening ($Z \sim \delta$) relation, which is experimentally determined in this study. This relation is frequency-dependent, and is contributed in parallel by the crack capacitor effect C_c as well as crack resistor effect R_c.

(4) The crack capacitance C_c nearly linearly decreases with increasing single crack opening, following the equation describing the capacitance of a capacitor constructed of two parallel plates separated by a distance. The relation between R_c and crack opening is nonlinear, following a second-order polynomial relation. As R_c is mainly contributed by the conductive

media (e.g. moisture and fibers) present within the crack, C_c is a more suitable parameter to characterize crack opening.

(5) The transition from a slower increase in impedance magnitude to faster increase occurs at approximately 100 μm crack opening, which is consistent with the transition from steady-state crack propagation to Griffith-type crack propagation. This phenomenon is frequency-dependent.

(6) The frequency-dependent effect of multiple cracking on the complex impedance of SHC material is well predicted by the equivalent circuit model, which accounts for statistical distribution of crack width as well as C_c and R_c contribution of each individual crack.

(7) The frequency-dependent effect of self-healing on the complex impedance of SHC material is reasonably explained by the equivalent circuit model. Self-healing leads to the change in crack number and crack width distribution, which is captured by the changes in $C_{c,i}$ and $R_{c,i}$ in the model. In order to more accurately predict the self-healing effect, the present model needs to be refined to take into account nonhomogeneous crack healing phenomena and the chemical composition of the self-healing products.

Tables

Table 6.1 Mixing proportion of SHC.

Cement	Water	Sand	Fly ash	Superplasticizer	PVA Fiber	Compressive strength (28d)
kg/m^3	kg/m^3	kg/m^3	kg/m^3	kg/m^3	Vol-%	MPa
266	309	456	956	2.7	2	47±4.6

Table 6.2 Chemical compositions of fly ash and cement.

Chemical composition, %	Fly ash	Cement
SiO_2	55.93	19.68
Al_2O_3	26.52	5.23
CaO	1.24	60.57
Fe_2O_3	5.82	2.47
MgO	2.74	1.12
Na_2O	1.18	0.22
K_2O	1.20	1.25

Figures

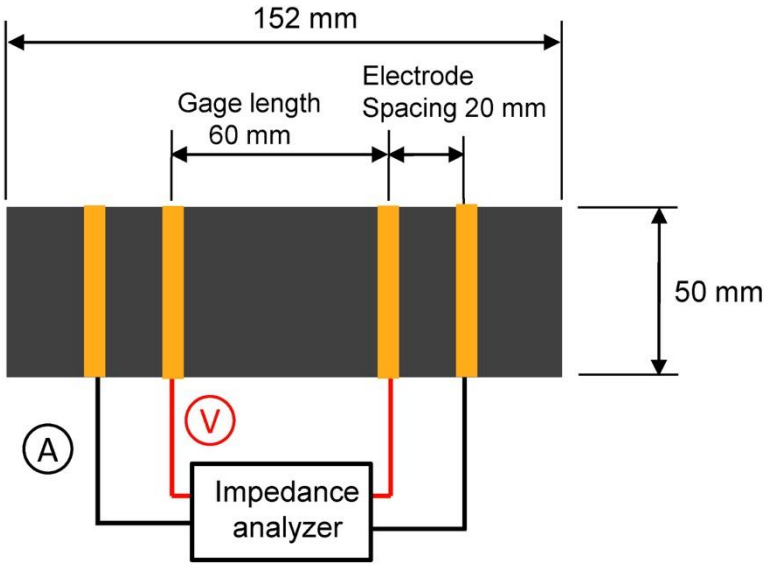

(a)

(b)

Figure 6.1 Four-Point electrical impedance spectroscopy: (a) specimen details; and (b) EIS measurement.

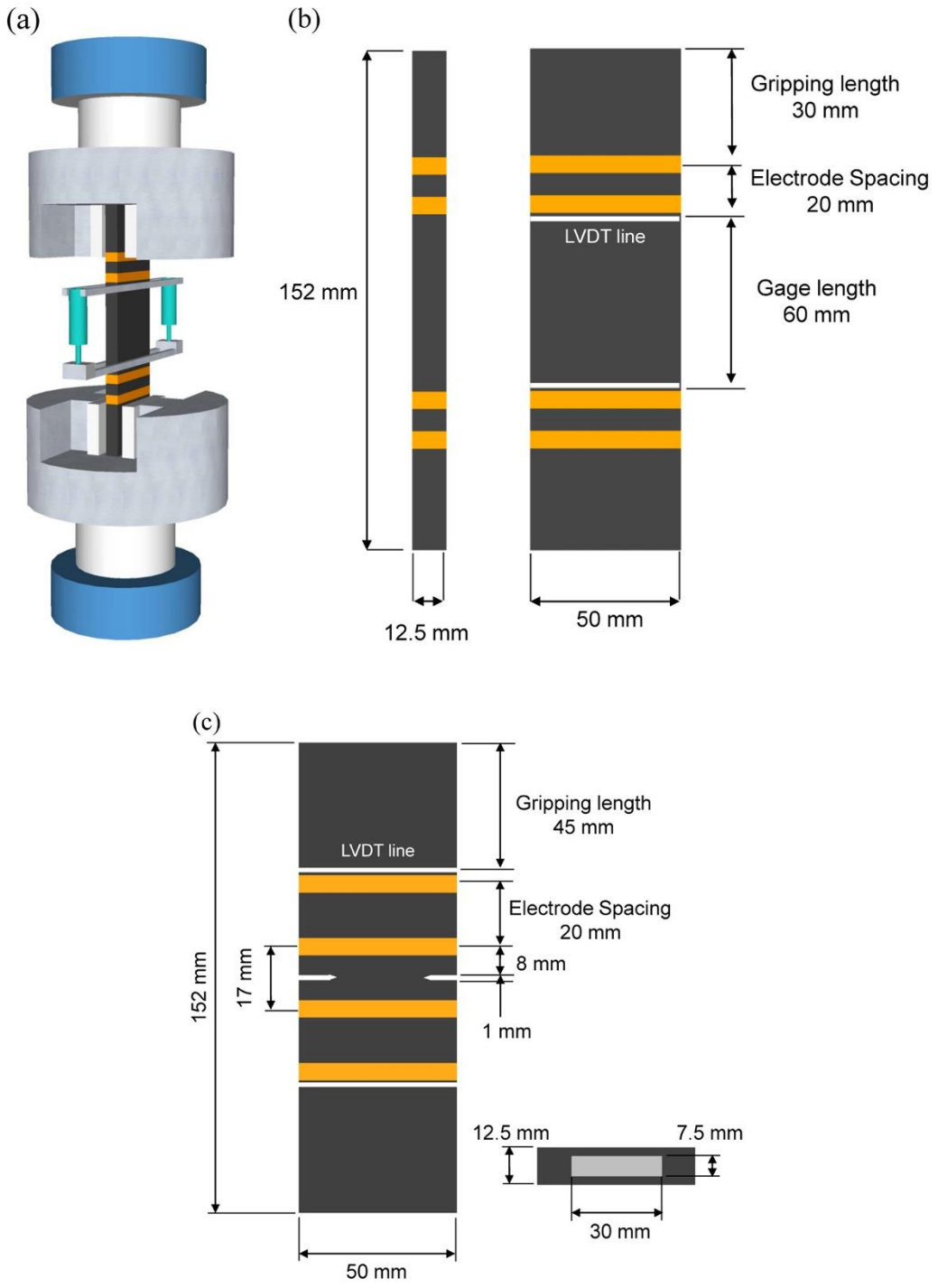

Figure 6.2 Uniaxial tension test: (a) test setup; (b) un-notched specimen details; and (c) double-notched specimen details.

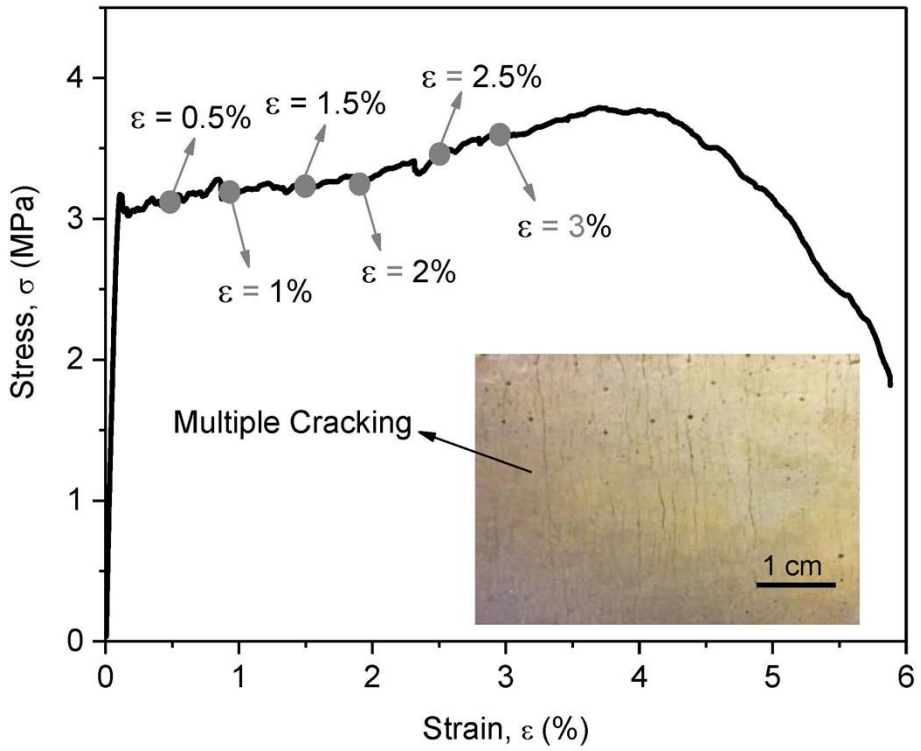

Figure 6.3 Tensile stress-strain curve ($\sigma \sim \varepsilon$ relation) and multiple microcracking behavior of SHC. EIS was performed at different strain values as marked, corresponding to different damage levels within SHC.

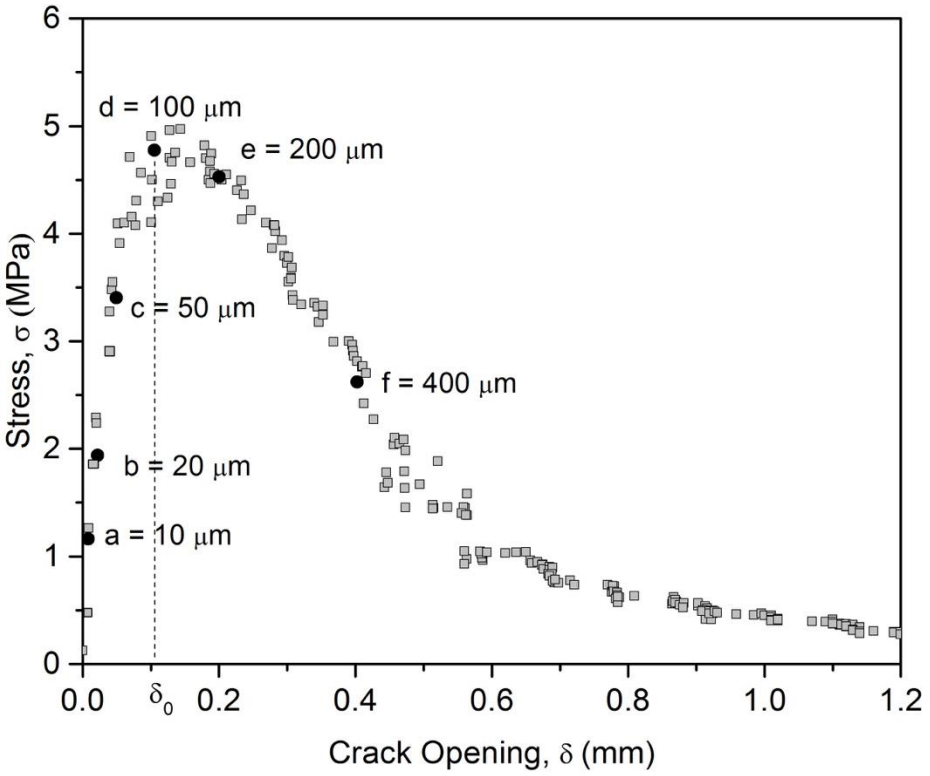

Figure 6.4 Single crack opening behavior ($\sigma \sim \delta$ relation) of SHC. EIS was performed at different crack opening values as marked on the curve.

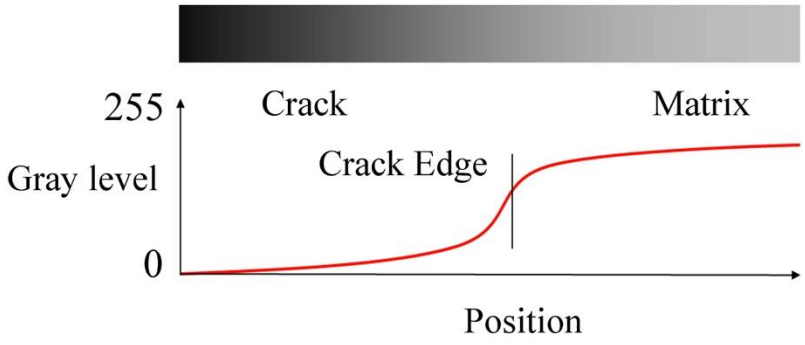

Figure 6.5 Gray level distribution for detecting the crack edge.

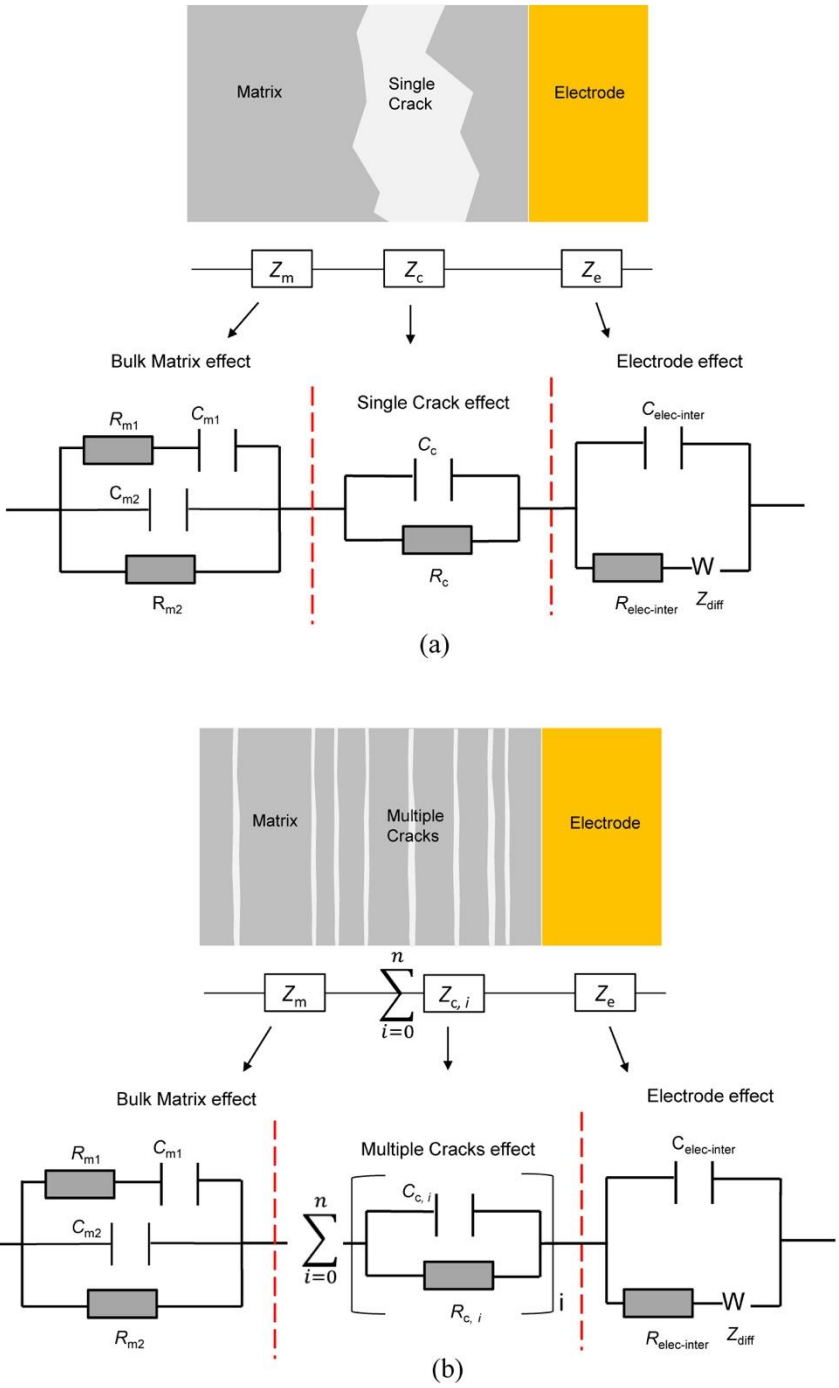

Figure 6.6 Equivalent circuit model of the material-crack-electrode system: (a) single crack opening; and (b) multiple cracking.

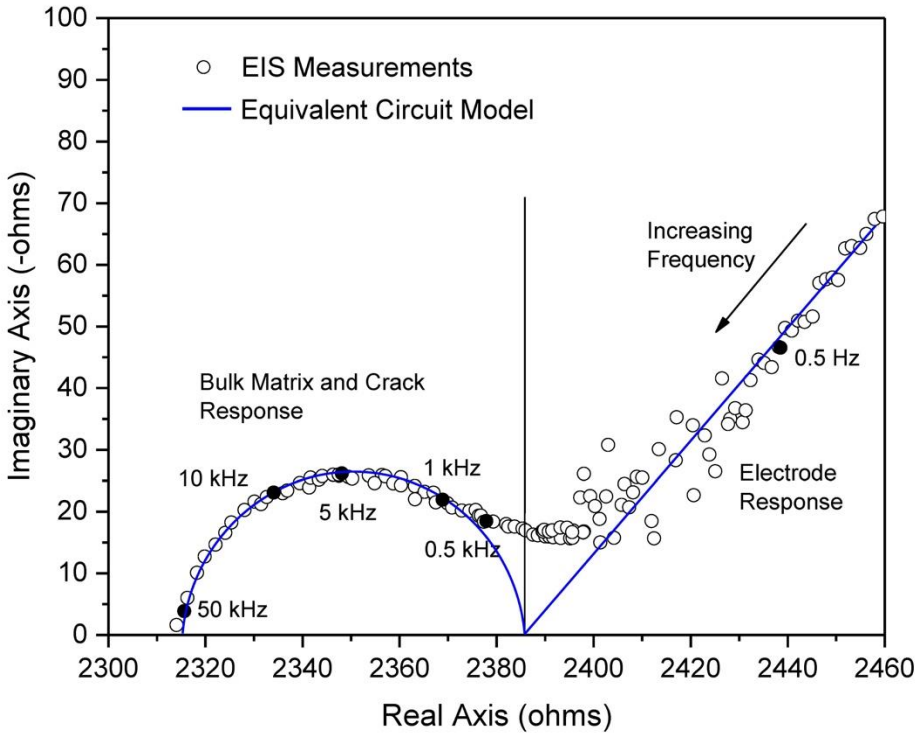

Figure 6.7 EIS Nyquist plot and fitted data by the equivalent circuit model.

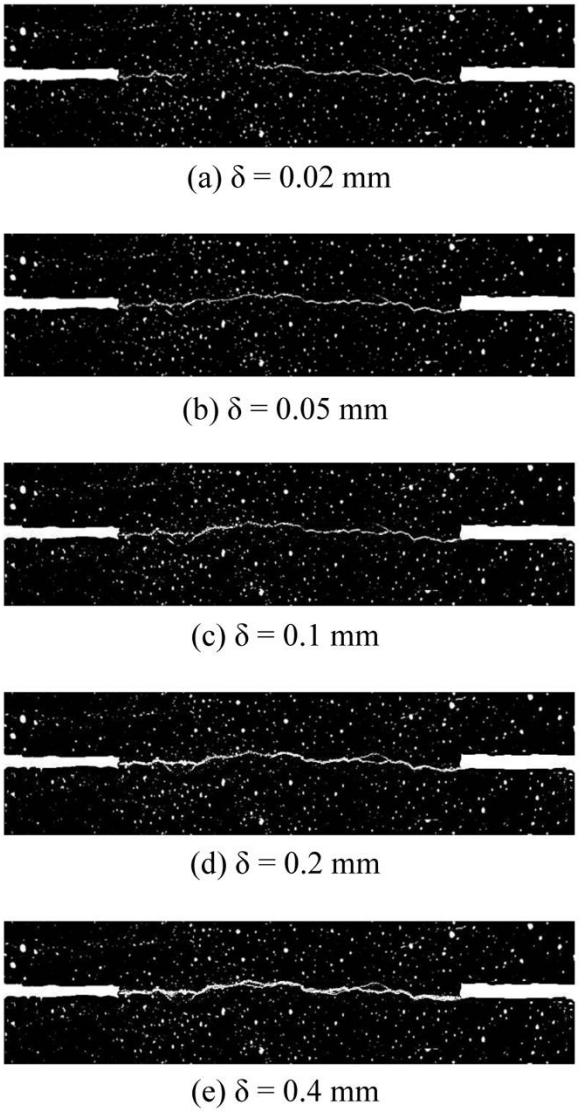

Figure 6.8 Binary images of a crack at different crack openings during uniaxial tension test.

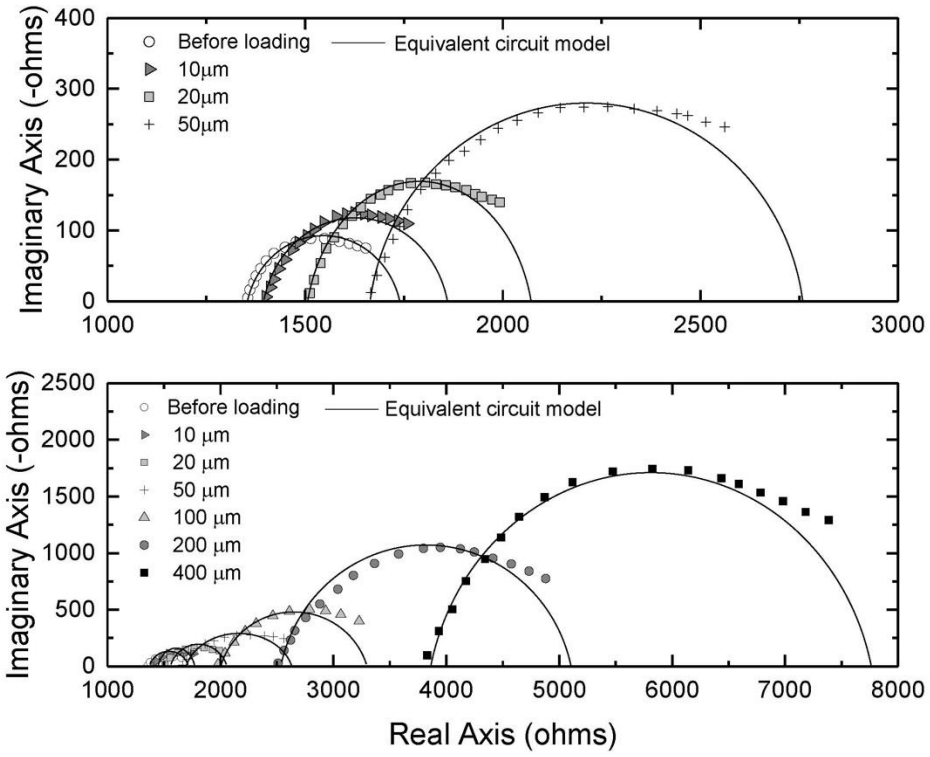

Figure 6.9 EIS Nyquist plots of SHC at different crack openings.

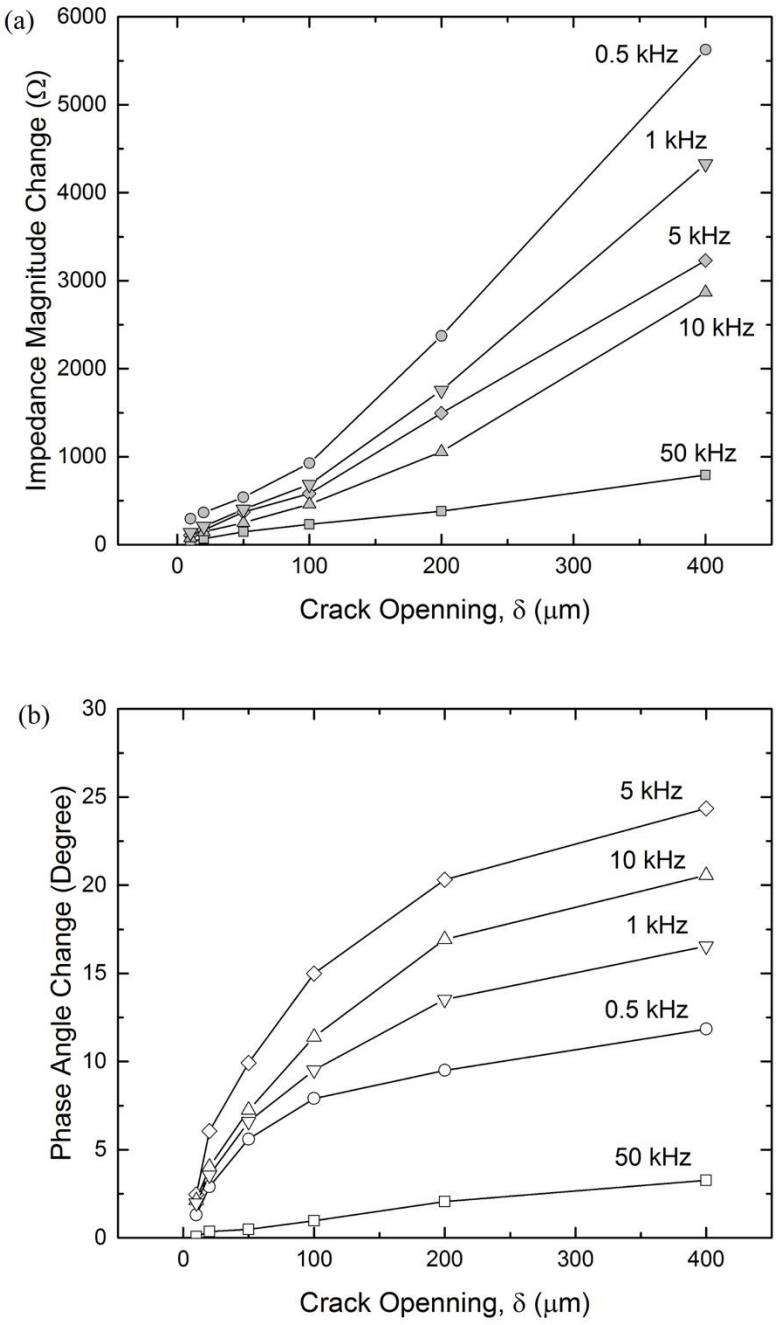

Figure 6.10 Effects of single crack opening on (a) impedance magnitude and (b) phase angle at different AC.

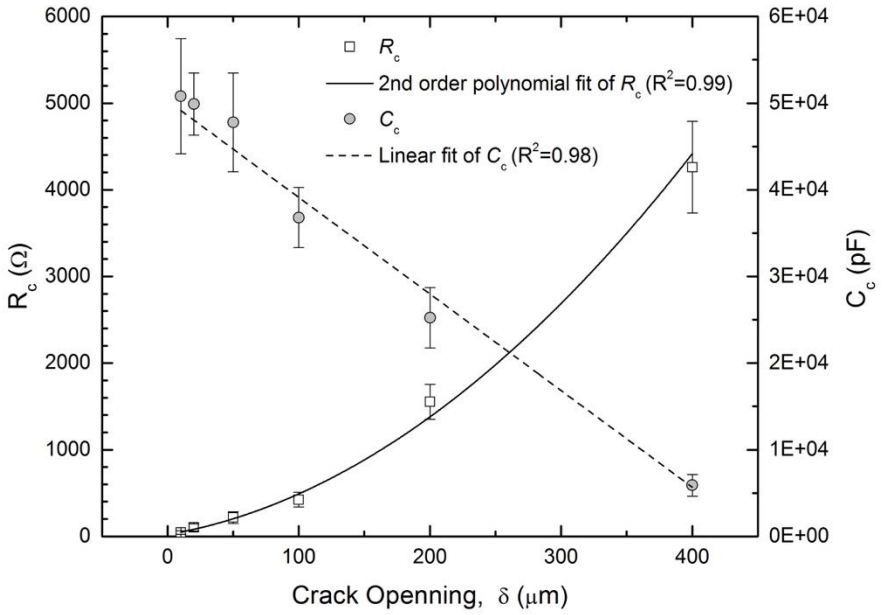

Figure 6.11 Effects of single crack opening on R_c and C_c.

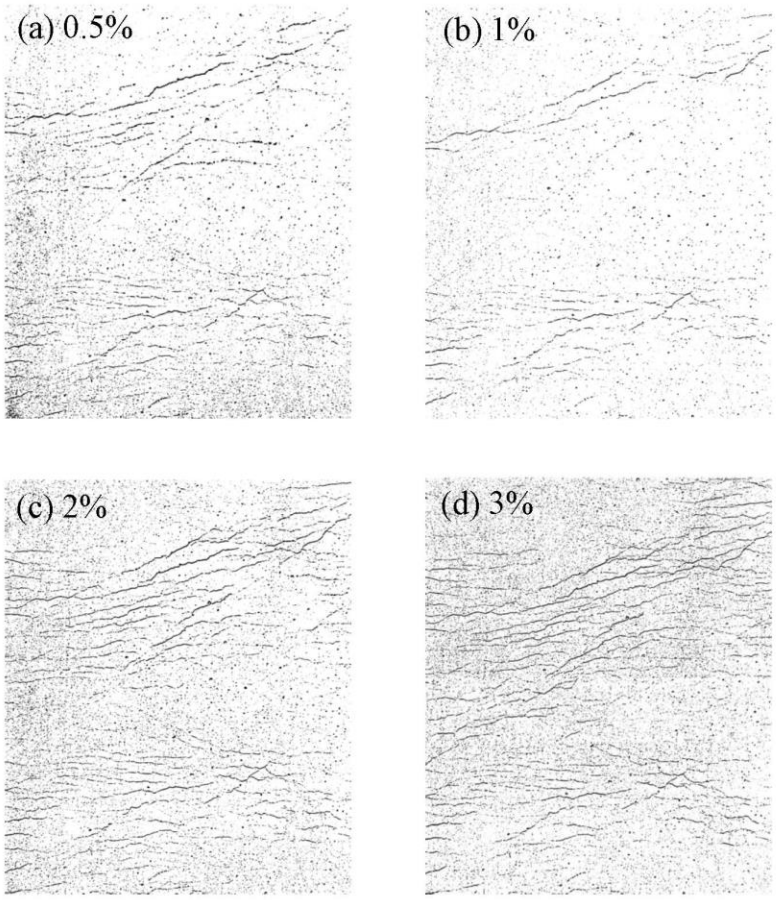

Figure 6.12 Multiple microcracking patterns in SHC at different tensile strain levels.

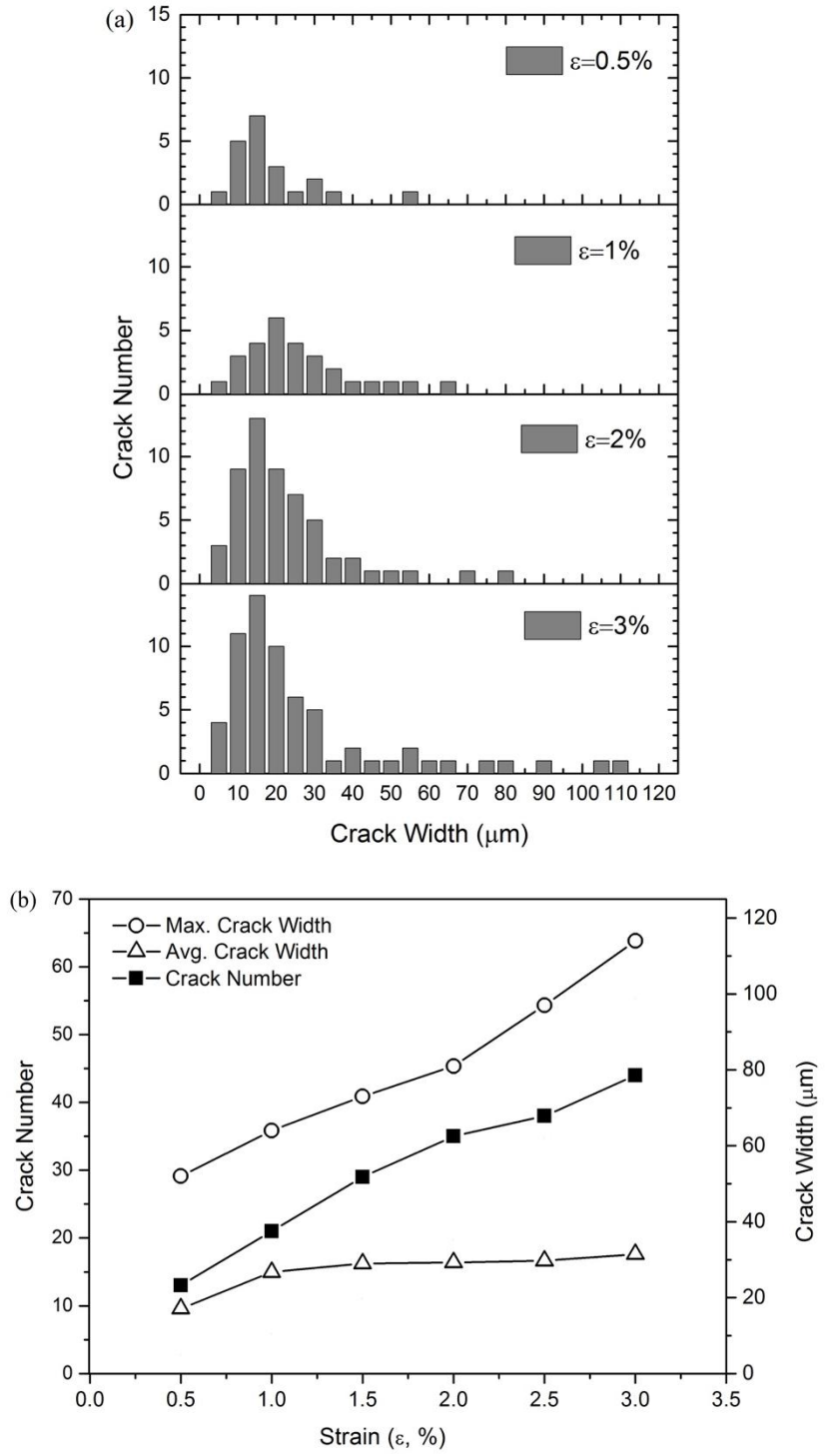

Figure 6.13 Effect of tensile strain on statistical distribution of crack width: (a) frequency distribution; and (b) statistical parameters.

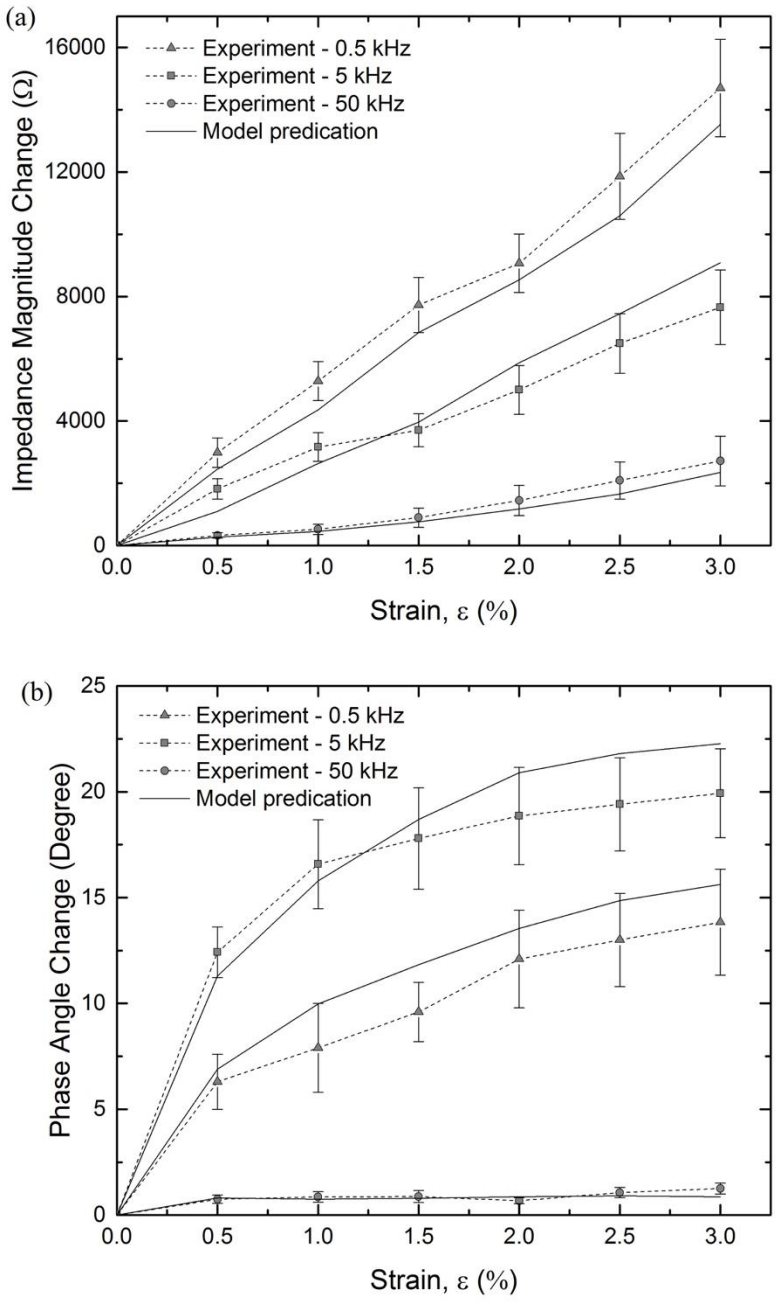

Figure 6.14 Effects of tensile strain on (a) impedance magnitude and (b) phase angle at different AC frequencies.

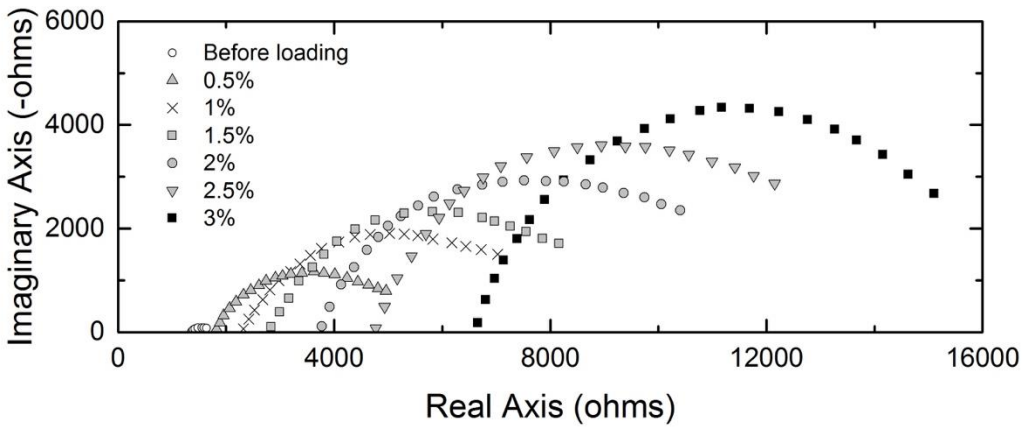

Figure 6.15 EIS Nyquist plots of SHC at different tensile strain levels.

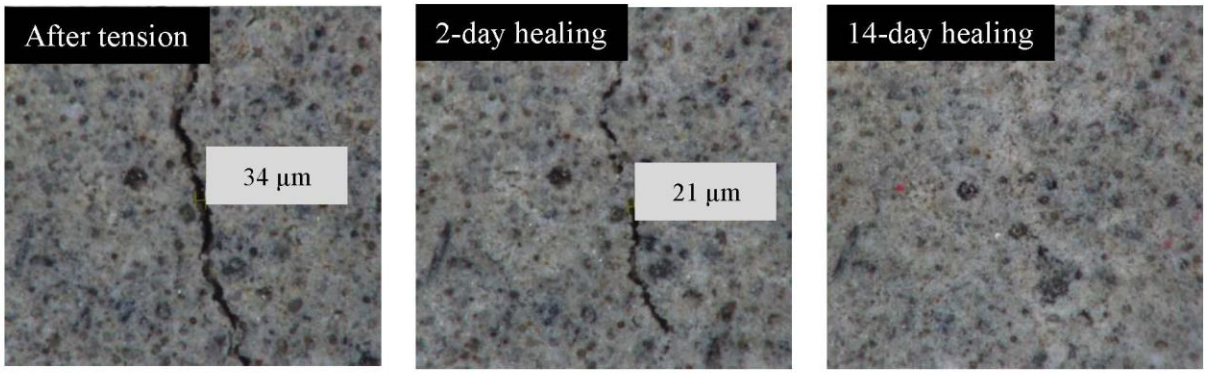

(a) Microscopy images

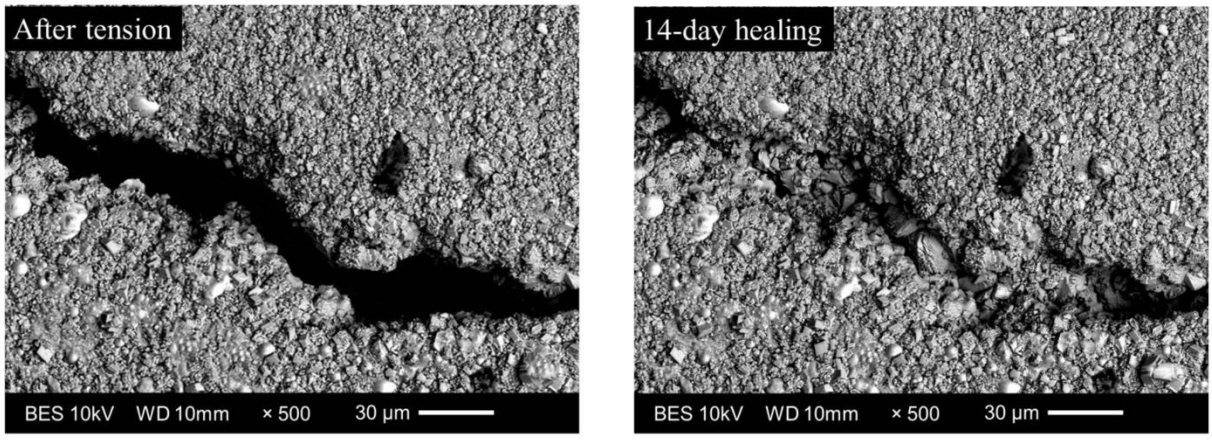

(b) SEM images

Figure 6.16 Optical microscopy and SEM images of self-healing phenomenon in SHC.

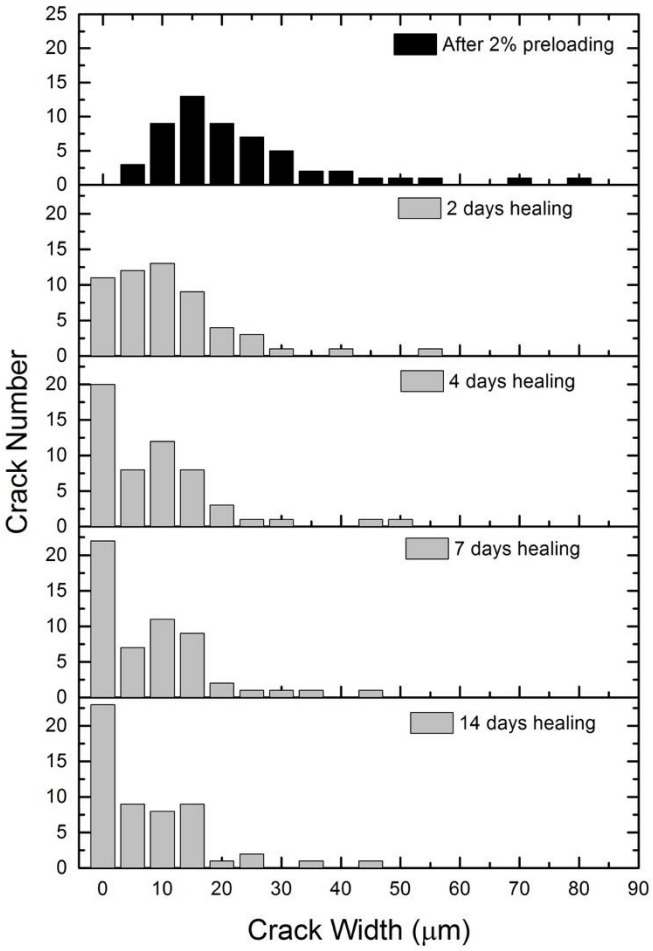

Figure 6.17 Effect of self-healing on statistical distribution of crack width.

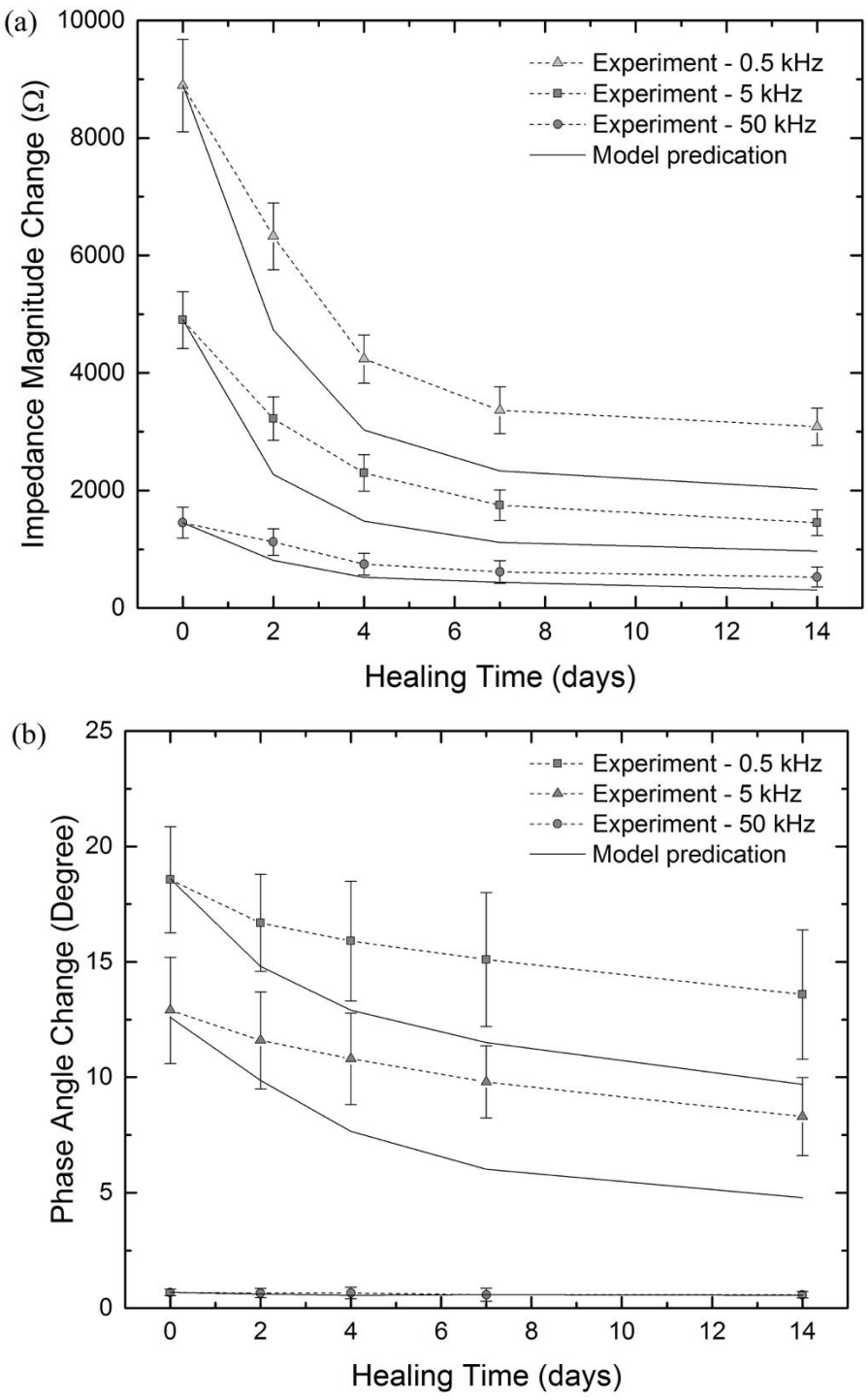

Figure 6.18 Effects of self-healing on (a) impedance magnitude and (b) phase angle at different AC frequencies.

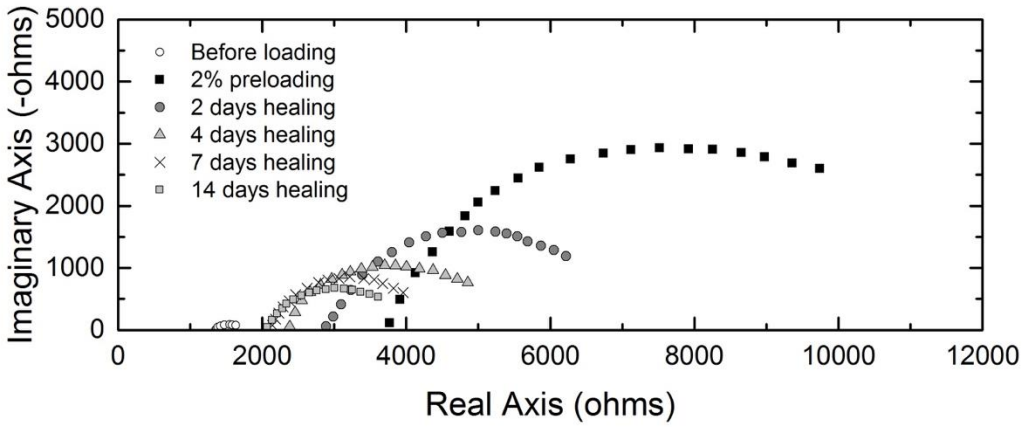

Figure 6.19 EIS Nyquist plots of SHC before loading, after preloading to 2% tensile strain, during self-healing.

References

[1] National Bridge Inspection Standards, Federal Highway Administration 2004.

[2] D. Adams, Health Monitoring of Structural Materials and Components: Methods with Applications, John Wiley& Sons, Ltd, Chichester, UK, 2007.

[3] J.P. Lynch, V. Kamat, V.C. Li, M. Flynn, D. Sylvester, K. Najafi, T. Gordon, M. Lepech, A. Emami-Naeini, A. Krimotat, M. Ettouney, S. Alampalli, T. Ozdemir, Overview of a cyber-enabled wireless monitoring system for the protection and management of critical infrastructure systems, SPIE Smart Structures and Materials + Nondestructive Characterization for Composite Materials, International Society for Optics and Photonics, 2009.

[4] D. Corr, M. Accardi, L. Graham-Brady, S. Shah, Digital image correlation analysis of interfacial debonding properties and fracture behavior in concrete, Eng. Fract. Mech. 74 (2007) 109-121.

[5] M. Li, V. Lin, J. Lynch, V.C. Li, Multifunctional carbon black Engineered Cementitious Composites for the protection of critical infrastructure, in: G.J. Parra-Montesinos, H.W. Reinhardt, A.E. Naaman (Eds.) High Performance Fiber Reinforced Cement Composites 6: HPFRCC 6, Springer Netherlands, Dordrecht, 2012, pp. 99-106.

[6] M. Li, V.W.J. Lin, J.P. Lynch, V.C. Li, Carbon black Engineered Cementitious Composites - mechanical and electrical characterization, ACI Special Publication, 292 (2013) 1-16.

[7] W.J. McCarter, The a.c. impedance response of concrete during early hydration, J. Mater. Sci. 31 (1996) 6285-6292.

[8] P. Gu, P. Xie, J.J. Beaudoin, R. Brousseau, AC impedance spectroscopy II micostructual characterization of hydration cement silica fume systems, Cem. Concr. Res. 23 (1993) 157-168.

[9] G. Dotelli, C.M. Mari, The evolution of cement paste hydration process by impedance spectroscopy, Mat. Sci. Eng. A 303 (2001) 54-59.

[10] S.W. Tang, Z.J. Li, H.Y. Shao, E. Chen, Characterization of early-age hydration process of cement pastes based on impedance measurement, Constr. Build Mater. 68 (2014) 491-500.

[11] J.M. Cruz, I.C. Fita, L. Soriano, J. Payá, M.V. Borrachero, The use of electrical impedance spectroscopy for monitoring the hydration products of Portland cement mortars with high percentage of pozzolans, Cem. Concr. Res. 50 (2013) 51-61.

[12] L. Xiao, Z. Li, Early-age hydration of fresh concrete monitored by non-contact electrical resistivity measurement, Cem. Concr. Res. 38 (2008) 312-319.

[13] L. Xiao, Z. Li, New understanding of cement hydration mechanism through electrical resistivity measurement and microstructure investigations, J. Mater. Civ. Eng. 21 (2009) 368-373.

[14] B.J. Christensen, T.O. Mason, H.M. Jennings, Influence of silica fume on the early hydration of portland cements using impedance spectroscopy, J. Am. Ceram. Soc. 75 (1992) 939-945.

[15] M. Cabeza, M. Keddam, X.R. Nóvoa, I. Sánchez, H. Takenouti, Impedance spectroscopy to characterize the pore structure during the hardening process of Portland cement paste, Electrochim. Acta 51 (2006) 1831-1841.

[16] D.A. Koleva, J.H.W. de Wit, K. van Breugel, L.P. Veleva, E. van Westing, O. Copuroglu, A.L.A. Fraaij, Correlation of microstructure, electrical properties and electrochemical phenomena in reinforced mortar. Breakdown to multi-phase interface structures. Part II: Pore network, electrical properties and electrochemical response, Mater. Charact. 59 (2008) 801-815.

[17] W.J. McCarter, R. Brousseau, The A.C. response of hardened cement paste, Cem. Concr. Res. 20 (1990) 891-900.
[18] N. Schwarz, M. DuBois, N. Neithalath, Electrical conductivity based characterization of plain and coarse glass powder modified cement pastes, Cement Concrete Comp. 29 (2007) 656-666.
[19] S.W. Tang, Z.J. Li, E. Chen, H.Y. Shao, Impedance measurement to characterize the pore structure in Portland cement paste, Constr. Build Mater. 51 (2014) 106-112.
[20] S.W. Tang, Z.J. Li, H.G. Zhu, H.Y. Shao, E. Chen, Permeability interpretation for young cement paste based on impedance measurement, Constr. Build Mater. 59 (2014) 120-128.
[21] I. Sánchez, C. Antón, G. de Vera, J.M. Ortega, M.A. Climent, Moisture distribution in partially saturated concrete studied by impedance spectroscopy, J. Nondestruct.Eval. 32 (2013) 362-371.
[22] I. Sánchez, X.R. Nóvoa, G. de Vera, M.A. Climent, Microstructural modifications in portland cement concrete due to forced ionic migration tests. study by impedance spectroscopy, Cem. Concr. Res. 38 (2008) 1015-1025.
[23] N. Neithalath, J. Weiss, J. Olek, Characterizing enhanced porosity concrete using electrical impedance to predict acoustic and hydraulic performance, Cem. Concr. Res. 36 (2006) 2074-2085.
[24] J.M. Loche, A. Ammar, P. Dumargue, Influence of the migration of chloride ions on the electrochemical impedance spectroscopy of mortar paste, Cem. Concr. Res. 35 (2005) 1797-1803.
[25] I. Sánchez, M.P. López, J.M. Ortega, M.Á. Climent, Impedance spectroscopy: An efficient tool to determine the non-steady-state chloride diffusion coefficient in building materials, Mater. Corros. 62 (2011) 139-145.
[26] P.-W. Chen, D.D.L. Chung, Improving the electrical conductivity of composites comprised of short conducting fibers in a nonconducting matrix: The addition of a nonconducting particulate filler, J. Electron. Mater. 24 (1995) 47-51.
[27] J. Ou, B. Han, Piezoresistive cement-based strain sensors and self-sensing concrete components, J. Intel. Mat. Syst. Str. (2008) 1-8.
[28] F. Reza, G. Batson, J. Yamamuro, J. Lee, Resistance changes during compression of carbon fiber cement composites, J. Mater. Civ. Eng. 15 (2003) 476-483.
[29] H. Ammari, J.K. Seo, T. Zhang, L. Zhou, Electrical Impedance Spectroscopy-based nondestructive testing for imaging defects in concrete structures, ARXIV (2014).
[30] Y. Li, C. Sui, Q. Ding, Study on the cracking process of cement-based materials by AC impedance method and ultrasonic method, J. Nondestruct.Eval. 31 (2012) 284-291.
[31] J.F. Lataste, C. Sirieix, D. Breysse, M. Frappa, Electrical resistivity measurement applied to cracking assessment on reinforced concrete structures in civil engineering, NDT&E Int. 36 (2003) 383-394.
[32] M. Cabeza, P. Merino, X.R. Nóvoa, I. Sánchez, Electrical effects generated by mechanical loading of hardened portland cement paste, Cement Concrete Comp. 25 (2003) 351-356.
[33] P. Chen, D.D.L. Chung, Carbon fiber reinforced concrete for smart structures capable of non-destructive flaw detection, Smart Mater. Struct. 2 (1993) 22.
[34] B.J. Christensen, T. Coverdale, R.A. Olson, S.J. Ford, E.J. Garboczi, H.M. Jennings, T.O. Mason, Impedance spectroscopy of hydrating cement based materials measurement, interpretation, and application, J. Am. Ceram. Soc. 7 (1994) 2789-2804.

[35] W.J. McCarter, H. Ezirim, AC impedance profiling within cover zone concrete: influence of water and ionic ingress, Adv. Cem. Res. 10 (1998) 57-66.
[36] B. Christensen, T. Mason, H. Jennings, Influence of silica fume on the early hydration of Portland cements using impedance spectroscopy, J. Am. Ceram. Soc. 75 (1992) 939-945.
[37] L. Kong, L. Hou, X. Bao, Application of AC impedance technique in study of lightweight aggregate-paste interface, Constr. Build Mater. 82 (2015) 332-340.
[38] X. Fu, D.D.L. Chung, Self-monitoring of fatigue damage in carbon fiber reinforced cement, Cem. Concr. Res. 26 (1996) 15-20.
[39] H. Li, H.-g. Xiao, J.-p. Ou, Effect of compressive strain on electrical resistivity of carbon black-filled cement-based composites, Cement Concrete Comp. 28 (2006) 824-828.
[40] T. Tombler, C. Zhou, L. Alexseyev, J. Kong, H. Dai, L. Liu, C.S. Jayanthi, M. Tang, S. Wu, Reversible electromechanical characteristics of carbon nanotubes under local-probe manipulation, Nature 405 (2000) 769-772.
[41] B. Han, B. Han, J. Ou, Experimental study on use of nickel powder-filled portland cement-based composite for fabrication of piezoresistive sensors with high sensitivity, Sensor. Actua. A-Phys. 149 (2009) 51-55.
[42] S. Wen, D.D.L. Chung, Partial replacement of carbon fiber by carbon black in multifunctional cement–matrix composites, Carbon 45 (2007) 505-513.
[43] S. Wen, D.D.L. Chung, Piezoresistivity-based strain sensing in carbon fiber-reinforced cement, ACI Mater. J., 104 (2007) 171-179.
[44] S. Zhu, D.D.L. Chung, Theory of piezoresistivity for strain sensing in carbon fiber reinforced cement under flexure, J. Mater. Sci. 42 (2007) 6222-6233.
[45] D.D.L. Chung, Carbon materials for structural self-sensing, electromagnetic shielding and thermal interfacing, Carbon 50 (2012) 3342-3353.
[46] D.G. Meehan, S. Wang, D.D.L. Chung, Electrical-resistance-based sensing of impact damage in carbon fiber reinforced cement-based materials, J. Intel. Mat. Syst. 21 (2009) 83-105.
[47] A. Peled, J. Torrents, T. Mason, S. Shah, E.J. Garboczi, Electrical impedance spectra to monitor damage during tensile loading of cement composites, ACI Mater. J. 98 (2001) 313-322.
[48] T.C. Hou, J. Lynch, Conductivity-based strain monitoring and damage characterization of fiber reinforced cementitious structural components, Proceedings of SPIE 12 Annual International Symposium on Smart Structures and Materials 5765 (2005) 419-429.
[49] R. Ranade, J. Zhang, J.P. Lynch, V.C. Li, Influence of micro-cracking on the composite resistivity of Engineered Cementitious Composites, Cem. Concr. Res. 58 (2014) 1-12.
[50] V.C. Li, H. Wu, Conditions for pseudo strain-hardening in fiber reinforced brittle matrix composites, Appl. Mech. Rev. 45 (1992) 390-398.
[51] Y. Yang, M.D. Lepech, E.-H. Yang, V.C. Li, Autogenous healing of engineered cementitious composites under wet–dry cycles, Cem. Concr. Res. 39 (2009) 382-390.
[52] M. Li, V.C. Li, Cracking and healing of Engineered Cementitious Composites under chloride environment, ACI Mater. J. 108 (2011).
[53] S. Fan, M. Li, X-ray computed microtomography of three-dimensional microcracks and self-healing in engineered cementitious composites, Smart Mater. Struct. 24 (2015) 015021.
[54] E. Barsoukov, J.R. Macdonald, Impedance Spectroscopy: Theory, Experiment, and Applications, 2nd Edition, 2005.
[55] G. Song, Equivalent circuit model for AC electrochemical impedance spectroscopy of concrete, Cem. Concr. Res. 30 (2000) 1723-1730.

CHAPTER 7 CONCLUDING REMARKS

7.1 Summary of Results

This dissertation has focused on: (1) the understanding of the fundamental mechanisms of intrinsic self-healing in cementitious materials; (2) the development of new cementitious composites with designed physical and chemical characteristics that favor robust self-healing. A collaborative framework integrating a variety of experimental and numerical modeling methods and tools has been developed to quantify, characterize, and analyze the self-healing behavior under the influence of different chemical, physical, and environmental factors. The comprehensive understanding about the control mechanisms enables us to specifically design and tailor the materials to promote pervasive self-healing function. This dissertation highlights the use of a "bottom-up" fabrication approach, where molecular species are assembled and incorporated at the micro-scale to dictate macro-scale bulk properties (e.g. multiple cracking, mechanical strength, healing extent.).

Five main research activities have been divided into individual chapters. In chapter 2, X-Ray Computed Micro-Tomography (μCT) technique was adopted to quantitatively characterize the microstructure evolution of cracks during the healing process. This work showed that μCT is an effective technique to directly and quantitatively probe self-healing extent in three dimensions. This is extremely important when the cracks do not have a uniform geometry along their depth, such as bending cracks, so that self-healing characterization from the surface is not sufficient. Furthermore, compared to other techniques that provide bulk information of the self-healing extent, μCT can offer direct measurement of each crack in three dimensions, and can isolate the effect of pore network development from the self-healing of cracks under certain environmental

exposure. This chapter established a systematic method for mathematically quantifying the morphological evolution of microcracks and pore structure within cementitious materials. The μCT-based approach provides new knowledge on the true self-healing condition of the entire crack within a cementitious material. μCT together with other self-healing characterization techniques, provide a powerful set of tools at both the mechanisms study and the materials development stages.

On the basis of the experimental methods developed in previous chapter, Chapter 3 elucidated the influence of different chemical (e.g. materials composition, sample age, supplementary cementitious materials), physical (e.g. crack width, crack depth), and environmental parameters (e.g. flow rate, saturation index) on the healing products precipitation and crack evolution during the autogenous healing process. μCT was applied to quantitatively characterize the self-healing patterns in natural, rough-walled, water-saturated concrete cracks. The morphology and minerology of the healing products were analyzed by SEM, EDS, and Raman Spectroscopy. It has been shown that the intrinsic healing profile is nonhomogeneous along the crack depth, and strongly controlled by the relative rates of dissolved ion transport and reaction kinetics at the fractural surfaces. Because the mass flux (e.g. CO_3^{2-} and Ca^{2+}) at the sample surface is large to the advective flux through the crack, precipitation is found to mainly focused near the crack inlet. At the time of crack surface sealing, large portions of the deep region of the crack remains devoid of healing products, which suggest that the quickly sealing part significantly reduces long range fluxes to deliver enough dissolved minerals to uniformly fill the crack downstream. The thickness of this quickly sealed region is about 50~200 microns. The chemical analysis revealed that the healing products are mainly the mixture of $Ca(OH)_2$ and $CaCO_3$, especially at crack shallow region. For crack deep region, small amounts of CSH and

sulfate phases were detected in the healing products. Comparing with pure cement paste, the supplementary cementitious materials generally have negative effect on the healing extent, especially at the crack shallow region. The replacement of 50% silica fume caused the most significant reduction from ~70% to ~30%, followed by fly ash to ~50%. Slag had the least effect on healing ratio at shallow region, only about 5% decrease was observed. For the healing ratio at crack deep region. after 28 cycles of healing, pastes containing silica fume showed a lower healing extent than pure cement pastes, while the fly ash and slag systems showed slightly enhanced healing extent. The chemical compositional data for healing products in three different types of SCMs-cement systems with 50% replacement ratio have been determined from EDS mapping. The blending of cement with fly ash or silica fume leads to a decrease of the amount of portlandite and calcite, but the formation of more C-S-H with higher Si/Ca and Al/Ca ratios. Blending with slag has little effect on the change of portlandite and calcite phases inside the crack. However, because of the higher overall Si/Ca ratio of the system, more C-S-H with higher Si/Ca was formed.

The experiments provide quantitative measures of the precipitation induced crack aperture alterations. However, the complicated and various boundary conditions, and the small length- or time-scale of the experiments, limit our ability to interpret and quantify the complex healing networks. Chapter 4 presents a hydro-thermodynamics model to mathematically predict the mineral precipitation along the crack, together with finite difference numerical solutions. This semi-analytical model considered the coupled hydrodynamic flow, solute transport, continued hydration, precipitation process, and the feedback between crack aperture evolution and fluid transmissibility. The numerical study shows that the initial crack aperture, the fluid velocity, and the supersaturation condition have profound influences on the healing patterns. A

large initial crack width, low saturation content, and fast flow rate can enhance the potential to heal a crack greatly and homogenously, but require a much larger volume of mineral resource in the solution and longer temporal scale. The contribution of the continued hydration on the crack volume change is depending on the unhydrated cement ratio. But even for very young sample, the healing ratio change due to hydration products growth is still insignificant.

Guided by the new findings from the previous chapters about healing mechanisms, details regarding new cementitious composites fabrication featuring robust self-healing capacity using micromechanics-based strain-hardening material design theory and cement chemistry are presented in Chapter 5. In particular, magnesium carbonate particles have been selected as the material of choice to provide extra healing resources. Upon materials fabrication, the inherent mechanical and healing properties of these novel composites are characterized. Meanwhile, the influence of the addition of magnesium carbonate particles on the cement hydration was investigated. It has been experimentally demonstrated that the magnesium carbonate addition did not change significantly the chemical composition of cement hydration products, but did affect the rate and degree of cement early hydration, thus affecting the pore structure development and mechanical properties of the hardened cementitious material. Particularly, adding more than 5% magnesium carbonate particles in cementitious materials resulted in delayed hydration and reduced compressive strength. The effect of magnesium carbonate on self-healing behavior in terms of crack volume recovery and transport property recovery were verified by the Micro-CT scanning and the water permeability test, respectively.

Chapter 6 combines four-point electrical impedance spectroscopy measurements with equivalent circuit modeling to study the electrical response of strain-hardening cementitious

materials at single crack propagation scale, multiple cracking scale, and during time-dependent self-healing process.

7.2 Future Work

The ultimate goal for the proposed self-healing cementitious materials is to be applied on actual structural components to significantly improve the concrete long-term safety, sustainability, and economic efficiency. This has never been demonstrated and need to be further validated under field condition to illustrate their potential for real infrastructure applications. However, prior to field implementation, the multiscale experiments and modeling need to be conducted for a better understanding of the self-healing kinetics and further assurance of robust self-healing.

At nano-scale, the healing related mineral dissolution and precipitation rate on the crack wall need to be measured through a combination of in situ atomic-force microscopy (AFM) and 3D digital microscope. The mechanical properties of the precipitated minerals can be measured using the nano indentation or scratch tester. This analysis will be able to investigate how the crack surface heterogeneity (e.g. mineral distribution and aperture roughness) and local environments (e.g. pH and temperature) control the healing reaction chemistry and the mechanical properties of constituents of healing products. In addition, the measured healing reaction kinetic data will be used to refine the mechanistic simulation model.

At crack-scale, the long-term healing stability need to be investigated. The impacts of various outdoor environmental conditions on the healing performance need to be identified. In addition, plane-strain toughness test on the single edge notched compact tension specimens can be used to determine the fracture toughness of the healed crack. The knowledge generated from the fracture toughness measurement will be utilized as input microstructure and micromechanical

parameters to construct the finite element model at the composite level. The robustness and repeatability of self-healing function at structural level need to be studied by standard mechanical and durability tests.

In addition to experimental validation, the multiscale computational modeling is also necessary to enhance the fundamental theoretical understanding of self-healing behavior, and therefore facilitate the tailoring of new composite materials that simultaneously optimize mechanical and durability properties. Here, molecular dynamics simulations can be employed as a powerful tool to study the chemical and physical properties of the healing reaction at nanoscale. In addition, the transport hydro-thermodynamic modeling applied in this dissertation needs further modification to improve the accuracy and take account more parameters. Furthermore, at the composite or structural level, finite element analysis can be carried out to explore the effect of self-healing on the material properties (e.g. permeability and elasticity) regain and structural response recovery. All the computational model will be validated by comparing the predicted values with actual measured material behaviors through experimentation.

The new-generation self-healing material aim to significantly improved sustainability of concrete infrastructure with reduced life cycle costs and environmental impacts. Such improvements need to be elucidated and rationally quantified by industrial ecology approaches. Industrial ecology is a scientific basis for assessing infrastructure sustainability by systematic analysis of global, regional and local material and energy flows associated with products, processes, economic sectors and other complex systems. Life cycle assessment (LCA) quantifies these flows and evaluates impacts that occur during materials production, manufacturing, use, and end-of-life stages. LCA will be an integral part of the development process, identifying

factors that will increase the sustainability of the final products. The bulk of the effort in performing LCA studies lies in collecting data (energy consumption and carbon production of each reactant, energy consumed during processing, etc.). In addition, the potential deterioration process of self-healing materials in a given infrastructure application is important in determining maintenance schedules that affect resource use and emissions. Such service life models of self-healing materials do not yet exist, and need to be established based on future durability studies. Once data inventory has been created and the general composition and durability properties of the formulae are known, sustainability of the infrastructure system with self-healing materials will be assessed using environmental, economic and social indicators. It will lead to future insights on succeeding material design and improvements for more sustainable development with a holistic approach.